Influence of Conventional Heat Treatment and Thermomechanical Processing on the Microstructure and Hardness of Two Tungsten Hot Working Tool Steels

Meilinda Nurbanasari

Thesis Submitted for the Degree of Doctor of Philosophy

The Department of Materials Science and Engineering
The University of Sheffield

June 2013

Contents i

Acknowledgements..... v

Abstract……..... vi

Chapter 1 Introduction……..... 1

1.1 Background……..... 1

1.2 Objectives……..... 2

1.3 Thesis Layout…… 3

Chapter 2 Literature Review…… 4

2.1 Development of Tool Steels…….. 4

2.2 Tool Steels……..... 6

2.2.1 Classification of Tool Steels……..... 6

2.2.2 Role of Alloying Elements……... 8

2.3 Heat Treatment of Tool Steels…….. 13

2.3.1 Hardening……..... 13

2.3.2 Tempering……..... 15

2.4 Carbides in Tool Steels…….. 19

2.4.1 Identification of Carbide Type……..... 21

2.4.2 Sequence of Carbide Precipitation…… 22

2.5 Martensite and Bainite Formation……..... 23

2.5.1 Martensitic Transformation…….. 23

2.5.2 Thermodynamics of Martensitic Transformation……..... 25

2.5.3 Morphology of Martensite…… 25

2.5.4 Crystallography of Martensitic Transformation…….. 27

2.5.5 Bainite Formation……..... 27

2.5.6 Bainite Morphology……. 28

2.5.7 Stress-Induced Transformation……..... 30

2.6 Microstructure of the H21 and H23 Tool Steels……. 30

2.7 Controlled Thermomechanical Processing…… 32

2.7.1 Work Hardening…… 34

2.7.2 Flow Stress and Activation Energy…….. 35
2.7.3 Restoration Processes…… 39
2.7.4 Factors Affecting Restoration Processes …… 45
2.8 Summary…… 48

Chapter 3 Experimental Methods……... 50
3.1 Investigated Materials…….. 50
3.2 The Experimental Process……... 52
3.2.1 Hot Deformation and Double Tempering Process…….. 53
3.2.2 Double Tempering Process after Hot Deformation…… 63
3.2.3 Conventional Heat Treatment……. 64
3.3 Characterisation of Microstructure…….. 65
3.3.1 Sample Preparation for Optical Microscopy and SEM…….. 65
3.3.2 Optical Microscopy……. 66
3.3.3 Scanning Electron Microscopy……... 66
3.3.4 Transmission Electron Microscopy…… 66
3.3.5 Quantitative Metallography…… 68
3.4 X-ray Diffraction……... 70
3.5 Hardness Test…….. 72
3.6 Thermodynamic Calculations……. 72

Chapter 4 The Microstructures of the As Cast H21 and H23 Tool Steels… 73
4.1 Introduction…….. 73
4.2 Grain Structure and Casting Defects…….....**.** 73
4.3 X-ray Diffraction……. 75
4.4 Carbide Types in the Tool Steels…….. 76
4.5 The Distribution of Primary Carbides…….**.....** 76
4.6 Identification of Primary Carbides and Solidification Path of the As Cast H21 Tool Steel…… 78
4.6.1 Identification of Primary M_6C Carbides…….**.....** 78
4.6.2 Identification of the Fine Primary Carbides …….. 80

4.6.3 Solidification Path of the H21 Tool Steel……. 80

4.7 Identification of Primary Carbides and Solidification Path of the As Cast H23 Tool Steel……..... 88

4.7.1 Identification of Primary M_6C Carbides…….. 88

4.7.2 The Fine Carbides of the As Cast H23 Tool Steel……... 92

4.7.3 Solidification Path of the H23 Tool Steel……. 94

4.8 Hardness of the As Cast Tool Steels…….. 102

4.9 Conclusions……..... 104

Chapter 5 Conventional Heat Treatment of the H21 and H23 Tool Steels……. 105

5.1 Introduction…… 105

5.2 The Effect of Solutioning Temperature……. 105

5.2.1 The Effect of Solutioning Temperature on Microstructure…… 105

5.2.2 Identification of Carbides …….. 112

5.2.3 The Effect of Solutioning Temperature on Hardness. …….. 118

5.2.4 X-ray Diffraction of the As Quenched H21 and H23 Tool Steels…. 120

5.3 Double Tempering of the H21 Tool Steel……... 125

5.3.1 The Effect of Double Tempering Temperature on Microstructure… 125

5.3.2 Identification of Carbides…….……. 129

5.3.3 X-ray Diffraction of the Double Tempered H21 Tool Steel…..…… 135

5.3.4 Carbide Evolution…….. 137

5.4 Double Tempering of the H23 Tool Steel……...…… 141

5.4.1 The Effect of Double Tempering Temperature on Microstructure… 141

5.4.2 Identification of Carbides …….…….. 143

5.4.3 Carbide Evolution…… 148

5.4.4 X-ray Diffraction of the Double Tempered H23 Tool Steel……... 149

5.5 The Effect of Double Tempering Temperature on Hardness of the H21 and H23 Tool Steels…….. 150

5.6 The Tempering Parameter of the H21 and H23 Tool Steels……. 153

5.7 Comparison the Experimental Results with Theoretical Prediction…… 154

5.8 Conclusions……... 156

Chapter 6 The Controlled Thermomechanical Processing and Double Temper of the Tool Steels…… 159

6.1 Introduction……. 159

6.2 Controlled Thermomechanical Processing……... 160

6.2.1 Validity of Axisymmetric Compression Test……. 160

6.2.2 Flow Stress Behavior…….. 161

6.2.3 The Effect of Solutioning and Hot Deformation Temperatures on Microstructure…….**.....** 164

6.2.4 X-ray Diffraction of the H21 and H23 Tool Steels after Hot Deformation……. 182

6.2.5 The Effect of Hot Deformation on Hardness…….. 184

6.3 The Effect of Double Temper in the H21 Tool Steel after Hot Deformation…….. 186

6.3.1 The Effect of Double Tempering Temperature on Microstructure.. 186

6.3.2 X-ray Diffraction of the Double Tempered H21 Tool Steel…….. 193

6.3.3 The Effect of Double Tempering Temperature on Hardness……. 196

6.4 Conclusions …….. 197

Chapter 7 Conclusions and Future Work…….. 200

7.1 Conclusions ……. 200

7.1.1 The As Cast H21 and H23 Tool Steels……..……. 200

7.1.2 Conventional Heat Treatment……..…… 201

7.1.3 Controlled Thermomechanical Processing……..…… 202

7.2 Industrial Implications…….. 203

7.3 Limitation of the Study……. 204

7.4 Future Work.…… 204

Publications……... 205

References……..... 206

Acknowledgements

I would like to express my greatest gratitude to Professor Panos Tsakiropoulos for his valuable guidance and encouragement he provided during my study, and for giving me the opportunity to study on interesting topic in tungsten hot working tool steels. I also gratefully acknowledge to Dr. E.J. Palmiere for his support and important suggestion in every aspect of my study.

I would like to thank Directorate of Higher Education, Indonesian Government and Institut Teknologi Nasional, Bandung, which helped greatly for their financial support to accomplish my study.

I am also grateful to many members of technical staffs within the Sorby Centre, IMMPETUS and the Department of Materials Science and Engineering in general for all of their assistance during my study. I thank also to my friends in the department who encouraged me.

Most importantly, I would like to express my deepest thanks to my parents, my husband, Setiyo Suprastiyoko, and my lovely daughters, Shafira Sari and Nadhira Ratnasari for their endless encouragement, support and love.

ABSTRACT

The H21 and H23 tungsten hot working tool steels are used at elevated working temperatures due to their resistance to softening, high hot hardness, and high compressive strength. The mechanical properties of these tool steels are strongly affected by the presence of carbides. High concentration of carbide forming elements in these tool steels tends to form brittle eutectic carbide networks. Carbide networks in the as cast condition are detrimental to their mechanical properties. The objective of this study was to identify controlled thermomechanical processing (TMP) parameter, namely deformation temperature at two different solutioning temperatures to break down carbide networks and improve hardness. The primary focus of this research was on the H21 tool steel owing to its promising hardness after TMP. The H21 tool steel was double tempered after TMP to improve its toughness. For comparison purposes, conventional heat treatment was also performed on both tool steels.

The TMP process was an axisymmetric compression test at a constant true strain rate of 0.01 s^{-1}, that was performed at 1000, 1050 and 1100 ^{o}C after solutioning at 1100 or 1250 ^{o}C. Double tempering was carried out at 650, 750 and 800 ^{o}C, with air cooling in between the first and second temper. The solutioning and double tempering temperatures in the conventional heat treatment were the same as for the TMP samples.

An overview of the flow curves and the characterisation of microstructures showed no evidence of dynamic recrystallisation. The increase in flow stress with decreasing solutioning and deformation temperatures was attributed to dislocation movement and the presence of fine and dispersed carbides causing a Zener pinning effect. The peak stress, microstructure and hardness data indicated that the optimum hot deformation condition was solutioning at 1250 ^{o}C and deformation at 1100 ^{o}C. No secondary hardening occurred after double tempering the H21 tool steel samples that were first subjected to hot deformation. The highest double tempered hardness (354 HV) of the H21 tool steel occurred after double temper at 650 ^{o}C following solutioning at 1250 ^{o}C and subsequent deformation at 1000 ^{o}C. It is suggested that the operating temperature for the H21 tool steel with the conditions used in this study should be less than 650 ^{o}C.

Chapter 1
Introduction

1.1 Background

The tungsten hot working tool steels are widely used in high working temperature applications, such as die-casting dies and hammer and forging dies due to their resistance to deformation at elevated temperature, high hot hardness, and high compressive strength (Roberts *et al.*, 1998). These tool steels contain high concentration of carbide forming elements that tend to promote segregation and form brittle eutectic carbide networks, which consequently decrease toughness and make easy crack formation and propagation (Brick *et al.*, 1977). The carbides in the tool steels play an important role in the mechanical properties of these materials.

The tool steels are usually used in the heat treated condition. The heat treatment involves solutioning to dissolve the carbides followed by water or oil quench, which transforms the austenite to martensite. Finally, these steels are tempered to produce a secondary hardening effect, which provides high strength at both ambient and elevated temperatures. Previous works (Kheirandish and Noorian, 2008, Wu *et al.*, 1996) have reported that it is difficult to dissolve the carbides during the solutioning process due to their thermodynamic stability. Thus, the undissolved carbide networks are still present after austenisation, which is detrimental to mechanical properties.

Earlier investigations (Jandova *et al.*, 2004, Ghomashchi and Sellars, 1993, Lee and Chun, 1981) reported that controlled thermomechanical processing is an effective method to control the microstructure, break up the carbide network and optimise the mechanical properties owing to refinement of the carbides and their uniform

distribution. Furthermore, through TMP the austenite grain size will be refined as a result of strain accumulation producing a higher density of nucleation sites and consequently refinement of final microstructure, as reported by Isasti *et al* (2011), Van-Leeuwen and Sietsma (2007), and Hanlon *et al* (2001). However, the carbide forming elements in the tool steels present problems to hot deformation in terms of a narrow hot working temperature range (Imbert and McQueen, 2001). The lower limit of the hot working range is defined by the type, size and morphology of carbides located along the grain boundaries and within grain interiors that can dissolve into the matrix. The presence of undissolved carbides in the hot working range temperature makes the tool steels more difficult to deform (Imbert and McQueen, 2001, Liu *et al.*, 2000, Imbert *et al.*, 1984). The upper limit is determined by the incipient melting of eutectic carbides and by segregation of low melting point phases along the grain boundaries (Imbert *et al.*, 1984, Roberts, 1984). The type of eutectic carbide, their volume fraction, morphology, size and distribution, depend on the composition of tool steels and result to different hot workability of tool steels.

Though the studies on tool steels are extensive (Pirtovšek *et al.*, 2011, Imbert and McQueen, 2000, Dobrzański, 1993, Ryan and McQueen, 1986b, Imbert *et al.*, 1984), the study of the effect of combining TMP and a double tempering process on the tungsten hot working tool steels is still limited. It is intended that this data will add to the existing knowledge base regarding the choice of appropriate hot deformation and heat treatment parameters to achieve desired microstructure and properties and to satisfy the required specifications for high temperature applications.

1.2 Objectives

The aim of this study is to provide data that would allow the design of tungsten hot working tool steels with improved performance. The objective is to study the effect of heat treatment and TMP on the microstructures and hardness and toughness of tungsten hot working tool steels. The strategy to achieve the aim and objective is as follows:

a) Obtain and compare mechanical property data after conventional heat treatment and controlled thermomechanical processing

b) Choose the best parameter of controlled thermomechanical processing, which breaks the carbide network and gives a combination of satisfactory hardness and toughness

c) Analyse microstructure evolution during conventional heat treatment and controlled thermomechanical processing

1.3 Thesis Layout

The structure of this thesis is as follows. Chapter 1 explains the background of the problem addressed by the thesis and the aim and objective of the study. It also explains the thesis layout. Chapter 2 provides an introduction to tool steels, the heat treatment of steels, controlled thermomechanical processing, work hardening and the restoration mechanisms. Chapter 3 introduces the experimental methods used in this study, and the main tools for microstructural investigation. Chapter 4 reports on the as cast microstructures and solidification paths of the H21 and H23 tool steels. Chapter 5 is dedicated to the microstructural aspects of the conventional heat treatment of the H21 and H23 tool steels. Chapter 6 covers the effect of controlled thermomechanical processing on the H21 and H23 tool steels. The microstructure investigations are reported and discussed, and compared with the conventional heat treatment results. This chapter 6 reports on the selected tool steel, based on hardness after hot deformation, to proceed to double temper. The pertinent variables of controlled thermomechanical processing and double tempering are concluded. Chapter 7 summarises the whole study and draws some key areas that could be usefully investigated if any future work was undertaken. The limitations of this study are also reported in this chapter.

Chapter 2
Literature Review

2.1 Development of Tool Steels

The history of the development of tool steels closely corresponds to the evolution of steels in general. It started when Benjamin Huntsman, a clock maker from Sheffield, England, casted pieces of blister steel in a crucible in 1740. He found that the steel was more homogeneous and stronger compared with iron that had been heated in charcoal, which provided carbon to diffuse into the iron. The production of modern tool steels with high content of alloying elements and combination of heat treatment processes started gradually in the 19th century when Robert Mushet in 1868 deliberately added tungsten to high carbon steel, producing Fe-2C-2.5Mn-7W-0.5Cr-1.1Si (wt.%) (Roberts *et al.*, 1998). The steel had better properties compared with high carbon steels, as it became hard when air cooled from a high temperature while steels required water quenching for hardening. It was regarded as the first high speed steel. The next investigation of tool steel was with the addition of chromium as an alloying element after its discovery in 1797. Julius Baur, in 1865, was the first who claimed in an American patent the benefits of hardening and toughening of steels by alloying with chromium. However, the addition of chromium did not always give better properties due to the role of carbon in hardening and solid state phase transformations were not properly understood at that time. A dramatic period of high speed steel development occurred from 1894 to 1898 when Taylor and White discovered that very high temperature heating and subsequent air cooling of chromium-tungsten steels produced remarkable effect, e.g., excellent hardness during machining at high speeds, even at red heat. The development was continued and by 1920 many types of tool steels were produced including the tungsten base and chromium base hot working die steels. Much progress has been made since then in

alloy development and the significant developments were linked with alloying with cobalt, molybdenum, chromium, tungsten, vanadium, niobium and nitrogen.

Nowadays, tool steels are produced using casting processes or powder metallurgy (P/M). Good quality and performance of tool steels are very important and are affected by composition tolerance, cleanliness and accurate control of the process. Most tool steels are processed using electric arc furnace or induction furnace. The secondary refining process to improve the cleanliness of the liquid steel and the control of the chemistry are performed in ladle furnace with vacuum arc degassing process (VAD). Electro slag remelting (ESR) and vacuum arc remelting (VAR) have been employed to improve cleanliness with homogeneous microstructure and better mechanical properties. In the VAR process, the steel ingot obtained from VAD is remelted under vacuum into a water-cooled copper crucible. The advantages of this process are the removal of dissolved gases and improved cleanliness. The ESR process is carried out if a high degree of cleanliness of tool steel is required by decreasing the sulphur content and removing the inclusions (Totten, 2006). Unfortunately, the ESR process is expensive and it is optionally applied.

Tool steels can also be made by powder metallurgy, which produces segregation free microstructure with more uniform size and distribution of carbides (Rosso *et al.*, 2006, Davis, 1995). The powder process involves melting the steel to the desired chemistry and then producing the powder by impinging a thin stream of molten steel with jets of water or gas. Pre-alloyed or elemental powders are then mixed, and the mixing is followed by hot compression or cold compression and sintering. The powder metallurgy processes and technology have rapidly grown in recent years. Miller (2010) reported that through powder atomising technology, new high nitrogen tool steels have been produced with excellent wear resistance and high mechanical strength, which make them suitable for high pressure applications. However, there are some limitations in producing tool steels through powder metallurgy, such as limitation on shapes and sizes.

In summary, continuing development and progress in manufacturing, heat treatment and alloy modification of tool steels have been made in line with great advances in microstructure characterisation, and scientific understanding of phase transformations and microstructures. Tool steels are expected to offer the best properties in service and tool life. To meet the demands for tool steels further investigations of alloy development and processing technology are required.

2.2 Tool Steels

2.2.1 Classification of Tool Steels

There are many types of tool steels and their classification is usually based on the main alloying elements, heat treatment and application. The American and Iron Steel Institute (AISI) and Society of Automotive Engineers (SAE) have divided tool steels into seven groups and some of those groups are further classified into subgroups regarding alloy composition or mechanical property similarities. In this literature review, the discussion will focus on hot working tool steels, especially tungsten base tool steels. Table 2.1 shows classification of tool steels based on AISI and SAE standard.

Table 2.1 Classification of Tool Steels (Campbell, 2008).

Classification	Grade	Significant Characteristic
Water hardening	W	Low alloy steel
Shock resisting	S	Varying alloy content
Cold work	A	Air hardening
	D	High C and high Cr
	O	Oil hardening
Hot work	H	H1 - H19: Cr-base
		H21-H26: W-base
		H42-H43: Mo-base
High Speed	M	Mo-base
	T	W-base
Special purpose	L	High C steels with varying W
Mould	P	P1-P6: very low C steels

Tungsten hot working tool steels have low or medium concentration of carbon, and contain tungsten from 9 to 18 wt% plus additions of other alloying elements. The alloying of these steels qualitatively and quantitatively is similar to the group of high speed steels, but they have a lower concentration of carbon. Table 2.2 shows the nominal chemical compositions of tungsten hot working tool steels.

Table 2.2 Approximate alloying element concentrations (wt%) of tungsten hot working tool steels (Campbell, 2008).

AISI	C	Mn	Si	Cr	Ni	Mo	W	V	Co
H21	0.28-0.36	0.15-0.40	0.15-0.50	3.00-3.75	0.30 max	...	8.50-10.00	0.30-0.60	...
H22	0.30-0.40	0.15-0.40	0.15-0.40	1.75-3.75	0.30 max	...	10.00-11.75	0.25-0.50	...
H23	0.25-0.35	0.15-0.40	0.15-0.60	11.00-12.75	0.30 max	...	11.00-12.75	0.75-1.25	...
H24	0.42-0.53	0.15-0.40	0.15-0.40	2.50-3.50	0.30 max	...	14.00-16.00	0.40-0.60	...
H25	0.22-0.32	0.15-0.40	0.15-0.40	3.75-4.50	0.30 max	...	14.00-16.00	0.40-0.60	...
H26	0.45-0.55	0.15-0.40	0.15-0.40	3.75-4.50	0.30 max	...	17.25-19.00	0.75-1.25	...

There are some specific properties that must be fulfilled by hot working tool steels because they are used at high temperatures. The following characteristics are very important (Totten, 2006, Roberts *et al.*, 1998):

a. Resistance to shock

   Toughness is a crucial property for avoiding cracks and for increasing their life time.

b. Resistance to wear at the working temperature

   This property is related to resistance to the loss of material from surfaces due to mechanical action at high temperature

c. High hot strength and red hardness

   Hot strength is the ability of tool steels to retain their strength during long time exposure at high temperature and red or hot hardness is the ability of material to maintain their hardness at high temperature.

d. Resistance to heat checking or fire checking

   This could be defined as resistance to thermal fatigue. Heat checking is the formation of a fine crack on the surface of metal due to high cyclical thermal loads.

e. Good machinability in the annealed condition

   Good machinability is important in shaping tool steels. Tool steels are normally machined in a ferrite-pearlite microstructure but if their carbon content is high, machining is carried out in the spheroidised carbide condition.

The recommended working hardness of hot working tool steels depends on their application. The tungsten hot working tool steels have greater hot hardness than any group of hot working tool steels. Among the tungsten hot working tool steels, the H21 tool steel is widely used for die-casting dies such as short runs on brass die casting with the required hardness in the range 38-42 HRC, and hot extrusion dies with the required hardness between 41-45 HRC. The application of the H23 tool steel is for die-casting dies such as medium runs on brass die casting with the required hardness between 32-39 HRC (Roberts *et al.*, 1998). The toughness of tungsten hot working tool steels is not as good as that of the molybdenum hot working tool steels and the former tend to distort during hardening and develop chill crack sensitivity (Brick *et al.*, 1977).

2.2.2 Role of Alloying Elements

In hot working tool steels the presence of an alloying element has an important effect on the final mechanical properties. Carbon in steels is the most substantial alloying element for affecting the hardness and it will encourage the formation of carbides. Hot working tool steels should have at least 0.2 wt% carbon dissolved in the matrix. The alloying elements usually found in tool steels are chromium, tungsten, molybdenum and vanadium. Figure 2.1 shows the relationship between alloying element and hardness.

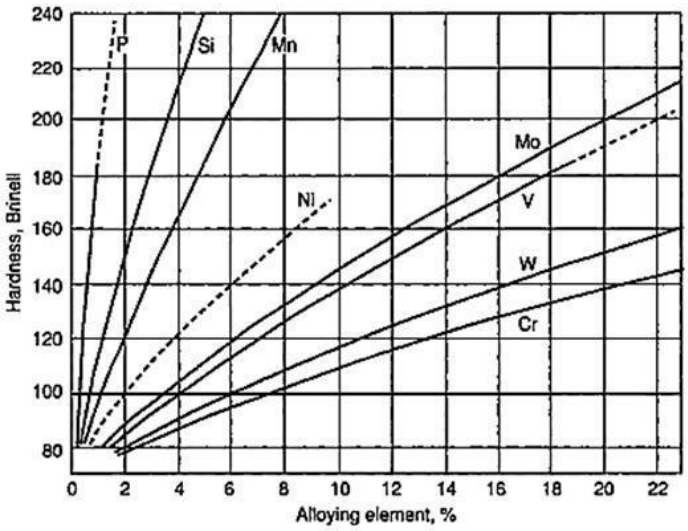

Figure 2.1 The effect of alloying elements on the hardness of steel (Bain and Paxton, 1966) .

In tool steels the alloying elements are added to promote greater toughness, hot hardness and hot strength at high temperature, wear resistance, depth hardening at high temperature and secondary hardening, and to reduce the risk of distortion and crack formation during hardening process. The functions of alloying elements in tool steels are as follows:

- Carbon

Carbon is the most important alloying element, which contributes to hardness, abrasion and wear resistance in tool steels. However, the higher C content increases the brittleness due to the formation of carbides. Therefore, in hot work tool steels the C content is kept below 0.45 wt.% (Davis, 1995).

- Chromium

Besides being a ferrite stabiliser, Cr is strong carbide former. In tool steels, Cr increases the hardenability, wear resistance and improves the resistance to high temperature softening. Fischmeister *et al* (1988) reported that Cr had an important role to produce secondary carbides, and provided strong synergistic enhancement of the hardening effect to any of the stronger carbide formers. Shu-qi *et al* (2006) found that by increasing the Cr content from 3 to 4 wt%, the wear rate decreased.

However, high Cr tended to promote the formation of delta ferrite, which decreased the toughness of steel (Abe and Nakazawa, 1992).

- Tungsten and molybdenum

Tungsten and Mo have similar lattice parameter and atomic radii. The atomic weight of Mo is approximately half the atomic weight of W. The W equivalent (W_{eq}) can be expressed as Mo:W = 1:2 or Mo contributes twice as many alloying atoms to the steel when added in the same weight percentage as W (Roberts *et al.*, 1998). Tungsten in tool steels prohibits grain growth, reduces the risk of decarburization during exposure at elevated temperatures, increases wear resistance at high temperatures, develops hot hardness, and improves depth of hardenability. Molybdenum, as well as W, will improve hot hardness, hot strength, wear resistance, and decrease temper brittleness. Ma *et al* (2012) showed that W and Mo in a Cr-W-Mo-V high alloy carbon steel had positive effect on secondary hardening during tempering, which increased the hardness up to 66.8 HRC. However, Shu-qi *et al* (2006) reported that excessive Mo (more than 4 wt%) in cast hot-forging die steels deteriorated their wear resistance resulting to high wear rates and concluded that Mo must not exceed this level.

- Vanadium

Vanadium is powerful carbide former and will form MC type carbide. It will increase hot strength, and hot hardness and the resistance to tempering and wear, and provide good cutting performance tool steel. Many investigations confirmed that the presence of V in tool steels produced excellent wear resistance (Liujie *et al.*, 2006, Shu-qi *et al.*, 2006, Wei *et al.*, 2006).

- Niobium

Like vanadium, Nb is strong carbide former and will produce MC type carbide that does not dissolve completely in austenite at high temperature (Kesri and Durand-Charre, 1987). Kheirandish *et al* (2008) showed that the addition of Nb in as cast H13 hot working tool steel increased the maximum hardness and the microstructure was more homogeneous.

- Manganese

Manganese is an austenite stabiliser. The presence of Mn in steels will improve their strength, hardness and hardenability and reduce the risk of brittleness caused by S. Kishore *et al* (2005) observed that an addition of 5 wt% Mn to Fe-Cr alloys increased their hardness and wear resistance, while 10 wt% Mn decreased their hardness and wear resistance.

- Nickel

Nickel is an austenite stabiliser and not carbide former. Nickel will improve corrosion resistance, strength, hardenability and machinability of tool steel. Medvedeva *et al* (2011) reported that by increasing the Ni content, the machinability of hot work tool steel was improved and the tool life increased.

- Silicon

In steel production, Si is added as deoxidiser. Silicon could provide high hardenability, toughness and hardness. However, the Si content in tool steel must not exceed at a certain level to avoid decreasing the impact toughness (Opal'chuk *et al.*, 1995). Mesquita and Kestenbach (2011) showed that lower Si content in H11 hot working tool steel resulted to higher toughness due to more homogeneous and finer particle distributions.

- Cobalt

Cobalt makes tool steels thermally stable up to 650 ^{o}C and gives high hardness up to 70 HRC. According to Dobrzanski *et al* (2003) the addition of 5 wt% Co in W-Mo-V and W-V tool steels increased the secondary hardness effect, improved their life time and increased cutting speed up to 50 %, compared with the same grade tool steels without Co addition.

- Nitrogen

Nitrogen is an austenite stabiliser and occupies interstitial sites in the Fe lattice. The addition of N in steel produces fine precipitate dispersions of nitrides and carbonitrides. Halfa *et al* (2012) and Li *et al* (2012) observed that addition of N in tool steels produced good tempering stability, and increased the secondary hardening

effect. France *et al* (1997) found that the N addition in strengthening of the H13 tool steel is most effective below 1 wt%.

The presence of alloying elements in a tool steel will influence phase equilibrium, which may produce some new phases, transformation kinetics and the interaction between substitutional and interstitial solutes. The impact of some alloying elements on phase equilibrium in steel can be seen in Figure 2.2.

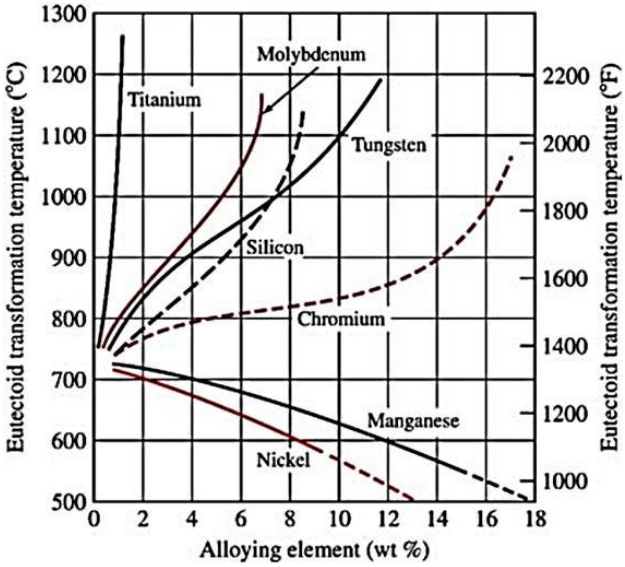

Figure 2.2 Eutectoid temperature as affected by several alloying elements (Bain and Paxton, 1966).

Figure 2.2 shows that W, Cr, Mo, Si and Ti are ferrite stabilisers. They increase the eutectoid temperature of steel and broaden the ferrite region. Manganese and Ni are austenite stabilisers and increase the austenite region. The hardening temperatures decrease by adding Mn and Ni, whereas the hardening temperatures increase to varying degrees by other elements. With the exception of Si as an alloying element, the powerful carbide forming alloying additions tend to increase the eutectoid temperature. Therefore, the equilibrium phase diagram for tool steel systems differs significantly from the Fe-C phase diagram and will affect hardening, change the nature and amount of the carbide phase and the tempering characteristics of the tool

steels. Due to high alloying content, the phase diagram of tool steels must be represented with more than three components.

2.3 Heat Treatment of Tool Steels

Heat treatment is a process combining heating and cooling to obtain an optimal combination of high hardness, good wear resistance and toughness for a given application. Heat treatment of tool steels consists of two steps, namely hardening, which provides high hardness through martensitic transformation, and tempering, which produces secondary hardening and improves the toughness of tool steels.

2.3.1 Hardening

The hardening process involves austenisation or solid solution and water or oil quenching or air cooling. During austenisation, tool steels are heated above the critical range in the austenite region (temperatures at which the phase transformation happens) where some carbides will dissolve and consequently the austenite becomes rich in carbon and alloying element content. The choice of austenisation temperature and holding time are important to get homogeneous austenite. The higher the austenisation temperature and the longer soaking time, the more homogeneous the austenite, but care must be taken to avoid coarse grain formation, which will decrease the hardness of the tool steel. If a lower austenisation temperature is employed, less diffusion of alloy element into the matrix may occur and the matrix becomes tougher but may not develop high hardness. During quenching, austenite will transform to martensite and the hardness will increase significantly. The choice of cooling rate depends on the type of tool steel, quenching medium and the desired final mechanical properties. Slow quenching rate will reduce the risk of distortion and cracking but the hardness will become lower, and high quenching rate will increase the hardness of tool steel and the risk of distortion and crack formation. Fares *et al* (2012) reported that higher level carbon content (~ 0.52 wt%) with oil bath cooling gave unsatisfactory results and led to the formation of cracks.

Alloying elements can influence the austenite decomposition process to pearlite, bainite and martensite. Figure 2.3 shows the effect of alloying elements on isothermal transformation diagrams.

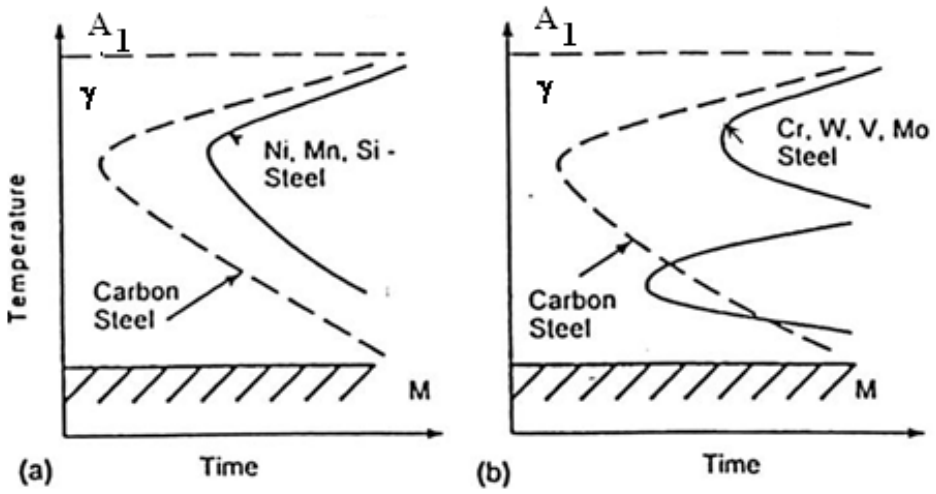

Figure 2.3 Isothermal transformation diagrams, (a) carbon steel and alloyed steel with non-carbide forming elements; (b) carbon steel and alloyed steel with carbide forming elements (Totten and Howes, 1997)

The alloying elements that dissolve only in ferrite without carbide formation such as Ni, Mn and Si tend to slow down the austenite transformation process (Figure 2.3a). Meanwhile, carbide forming elements such as Cr, Mo, W, and V affect kinetics of isothermal transformations. They affect the austenite decomposition differently at different temperatures. Figure 2.3b shows that steels with carbide forming elements have two regions of austenite isothermal decomposition separated by a region of stable undercooled austenite. The first region corresponds to the pearlite transformation, which has lamellar structure, and the other one to the bainite transformation, which has a needle-like structure. At temperature below the M_s temperature the martensite transformation occurs producing a supersaturated solutioning. In alloy steels, alloying elements may even cause the arrest of the bainite transformation, causing incomplete transformation.

2.3.2 Tempering

Martensite produced from quenching has very poor mechanical properties. Furthermore, the matrix may not be completely transformed to martensite, thus retained austenite may be present (Roberts *et al.*, 1998). The tempering process aims to improve the toughness, to achieve the stable phase, and to produce a secondary hardening effect, which provides high strength at elevated temperatures. The selection of tempering temperature is related to the maximum temperature expected in service to avoid the decrease of hardness in the surface more rapidly than the body of the die.

Tempering involves the reheating of tool steel to a certain temperature and soaking for a certain time, followed by cooling to room temperature. Due to the high alloying content, it is strongly recommended to temper the hardened tool steel at least twice. The double tempering process increases the secondary hardness by allowing the amount of retained austenite to transform to martensite or lower bainite, as well as increasing the volume fraction of secondary carbides. Hufenbach *et al* (2012) studied the double tempering of high-strength 84.3Fe-4.3Cr-4.6Mo-2.2V-4.6C (at%) and the results showed that the hardness of two-stage tempered samples was higher than the one-stage tempered samples due to precipitation hardening being more dominant and no retained austenite. Fares *et al* (2012) reported that double tempering affected the secondary hardness, decreased the amount of retained austenite and increased the volume fraction of carbide. Bakhsheshi-Rad *et al* (2011) reported that the maximum hardness of a 3Cr~Mo steel was achieved through triple tempering at 520 ^{o}C and that the amount of retained austenite decreased by about 2 %.

During tempering, a number of solid state reactions take place and the crystal structure of quenched martensite will change from bct to bcc as tempered martensite. There are three or five stages of tempering in steels, depending on their chemical composition, even though the temperature ranges overlap (Totten, 2006). These stages are:

stage 1: in the temperature range 50 – 200 ^{o}C, the transition ε (epsilon) carbide is formed. This stage is proceeded by redistribution of C atoms and other structural changes occur due to the rearrangement of C atoms (Krauss, 1984).

stage 2: during this stage, the retained austenite transforms to cementite and ferrite and the temperatures between 200 – 350 ^{o}C.

stage 3: in this stage, dissolution of epsilon carbide take place and formation of cementite carbide within martensite with decreasing hardness. The tetragonality of martensite is decreasing. The temperature range of this stage depends on the composition of the steel, which starts from 250 ^{o}C for high alloyed tool steels.

stage 4 and 5: the fourth stage exists for high alloy tool steels in which there is an exchange of carbon between cementite and other carbides. It occurs at temperatures above 500 ^{o}C and results to the precipitation of dispersed alloy carbides and increase of the hardness, known as secondary hardening. The fifth stage also corresponds to high alloy steels and starts at 600 ^{o}C producing the coalescence of carbides and annealed microstructure.

The presence of carbide forming elements in tool steels affects the carbide formation during tempering (stage 4 and 5). The alloying elements Cr, Mo, V, W and Ti when present at sufficient concentration will form carbides, which are thermodynamically more stable than cementite. The secondary hardening phenomenon occurs when relatively coarse cementite is replaced by finer alloy carbides, which give higher hardness. This phenomenon correlates strongly with time and tempering parameter. At the higher tempering temperatures and longer tempering times, the carbide coarsens and as a result the hardness decreases (Ma *et al.*, 2012, Bakhsheshi-Rad *et al.*, 2011, Zhou *et al.*, 2011).

The nucleation of secondary carbides during tempering can occur in three ways; firstly, the nucleation occurs on the interfaces between cementite particles and ferrite, secondly, nucleation occurs on dislocations inherited from the former martensite structure and thirdly, at grain boundaries and/or subgrain boundaries including the prior austenite grain boundaries (Bhadeshia and Honeycombe, 2006). In high alloyed steels, the first carbide to form is not the equilibrium carbide and the equilibrium carbide usually starts to nucleate along the grain boundaries and grows rapidly replacing the non-equilibrium carbide within the grains. The nucleation of secondary carbides at various types of boundaries is expected due to the latter being energetically favourable sites that allow rapid diffusion of solute.

The determination of the tempering parameters temperature and time is crucial to get the final desired mechanical properties. There is a correlation between the hardness and tempering temperature and time (Hollomon and Jaffe, 1945).

$$\text{Hardness} = f\ P' = f\ T\ [\ C + \log t\ )\ ] \qquad (2.1)$$

where P' is the tempering parameter, T is the tempering temperature (K), t is the tempering time (s) and C is a constant.

$$C = 21.3 - 5.8 \times (\text{mass \% C}) \qquad (2.2)$$

The equation (2.1) shows that the tempering temperature has stronger effect than time on the mechanical properties, as indicated by the log t. This equation shows that the same hardness can be achieved with a short tempering time and a high tempering temperature and with a long tempering time and a low tempering temperature as long as the tempering parameter C is constant. The value of the parameter C increases with decreasing C content. Hollomon and Jaffe (1945) proposed C = 19.5 for carbon and alloy steels with carbon content 0.25 - 0.24 wt% and C = 15 for tool steels with carbon content 0.9 – 1.2 wt%.

Janjušević *et al* (2009) investigated the applicability of the Hollomon-Jaffe equation on tempering a HSLA steel. Their results showed good agreement with the tempering

parameters included in the Hollomon-Jaffe equation. However, Furuhara *et al* (2004) reported that the correlation between hardness and the tempering parameters T and t was not good for short tempering period or low tempering temperature or for rapid heating and added the additional parameter in the formulae to describe the rapid heating and tempering behaviour.

$$P' = T \log (t_h + t_i) \quad (2.3)$$

where P' is the modified tempering parameter, t_i is the holding time and t_h is the tempering time, which is required to achieve the parameter P' at the final tempering temperature.

Another modification of the Hollomon-Jaffe equation 2.1 is the Larson-Miller equation. This equation was originally developed to predict creep-rupture times of steels and has been widely used for the stress rupture behaviour of various engineering materials. The Larson-Miller equation is (Larson and Miller, 1952, cited in Canale *et al.*, 2008):

$$LMP = T (C + \log t) \times 10^{-3} \quad (2.4)$$

where LMP is the tempering parameter (Larson-Miller Parameter = LMP), T is the absolute temperature in degree Kelvin (K), t is the heat treatment time in hours, and C is a material-dependent constant, which varies from 15-23 and for steels the value 20 is usually taken.

The Larson-Miller equation has also been used for tempering or ageing characterization of steels. Wignarajah *et al* (1990) used the LMP to simulate the microstructure, hardness, and notch toughness of a $2\frac{1}{4}$Cr-1Mo steel for elevated temperature treatment of a few thousand hours. Janovec *et al* (1992) studied the influence of tempering condition on phase transformation and carbide particles in a 2.7Cr-0.6Mo-0.3V steel by applying the Larson-Miller parameter.

2.4 Carbides in Tool Steels

In tool steels, the carbides play a very significant role, in terms of their type, distribution and morphology, in defining final mechanical properties. Carbides are compounds of carbon and transition metal elements and are characterised by very high hardness. The type and stability of carbide are affected by the presence of alloying elements. Carbides in steels are formed only by iron and the transition metals.

The carbide types in tool steels are the MC, M_2C, M_3C, M_6C, M_7C_3 and $M_{23}C_6$ where M represents the sum of carbide-forming elements (Roberts *et al.*, 1998). The carbide type depends on the presence and amount of alloying elements. The effectiveness of carbide in increasing the hardness depends on the volume fraction, the size and distribution of carbide. MC carbide, such as VC, NbC, TiC, TaC and HfC, form fine precipitates and the carbides M_7C_3, M_6C, and $M_{23}C_6$ are coarser (Porter and Easterling, 2004).

- MC carbide

The MC carbide has fcc crystal structure and plays an important role in grain refinement of the matrix. This carbide cannot dissolve completely during austenisation at high temperature due to its high thermal stability (Kheirandish *et al.*, 1997). In V containing steel only 50 % of the total V can be dissolved in austenite and the remaining V is in MC and M_6C carbides located along austenite grain boundaries and inhibiting the grain growth (Guimaraes *et al.*, 1986) and softening (Sawamoto *et al.*, 1986, cited in Kheirandish *et al.*, 1997).

- M_2C carbide

The M_2C carbide usually exists in hardened and tempered tool steels and does not appear in the equilibrium condition. This carbide has hexagonal crystal structure and is formed only in tool steels with medium up to high W content during tempering, near the top of secondary hardening. The metastable M_2C carbide will completely decompose into stable carbide at elevated temperatures, such as MC, M_6C (Dudova and Kaibyshev, 2011, Fischmeister *et al.*, 1989), $M_{23}C_6$ (Dudova and Kaibyshev,

2011, Vitek and Klueh, 1983) and M_7C_3 (Hashimoto *et al.*, 2004) depending on the alloying content.

- M_3C carbide

The M_3C carbide has orthorhombic crystal structure. It will exist in alloy steels after heat treatment. Depending on the tempering time and temperature and other alloying elements, tool steels with high Cr content cause the M_3C carbides to be replaced by $M_{23}C_6$ (Yu-Kipelova *et al.*, 2010) or M_7C_3 carbides (Thompson and Bhadeshia, 1992).

- M_7C_3 carbide

The M_7C_3 is chromium carbide with hexagonal crystal structure and can be found in tool steels with medium to high Cr content, with sufficient concentration of other alloying elements. This carbide cannot dissolve completely during the hardening process and leaves excess hard carbide to supply abrasion resistance to the tool steel.

- $M_{23}C_6$ carbide

The $M_{23}C_6$ is Cr rich carbide having fcc crystal structure. Molybdenum, W, V, and Fe can substitute partially for Cr. If the carbide has high W content, the Cr will be replaced by Fe with the formula $Fe_{21}W_2C_6$. Depending on the Cr content in the tool steel, this carbide can be found in the early stages of precipitation due to it nucleating easily on the grain boundaries or intergranular sites.

- M_6C carbide

The M_6C is W or Mo rich carbide in which Fe, Cr, V and Co may exist. It has a fcc crystal structure. The approximate formula for this carbide in tungsten hot working tool steels is Fe_4W_2C and/or Fe_3W_3C. The M_6C hard carbide particles improve the abrasion resistance of tool steel.

Table 2.3 summarises the six major carbide types found in tool steels and their hardness data.

Table 2.3 The type of carbide found in tool steels (Verhoeven, 2007)

Type	HRC	Element distribution in M	
		Most	Least
M_3C	70	Fe, Mn, Cr	W, Mo, V
$M_{23}C_6$	73	Cr	Mo, V, W
M_6C	75	Fe, Mo, W	Cr, V, Co
M_7C_3	79	Cr	….
M_2C	79	W, Mo	Cr
MC	84	V	W, Mo

2.4.1 Identification of Carbide Type

Each type of carbide may form with a specific morphology. The M_6C carbide is easy to be identified when the fish bone morphology appears in the microstructure. Previous studies (Fredriksson and Nica, 1979, Fredriksson and Brising, 1976, cited in Boccalini and Goldenstein, 2001) reported that the morphology of carbide type was affected by the chemical composition of the steel and the cooling rate and minor additions of certain elements such as Al and N. However, the fish bone morphology of the eutectic M_6C is not influenced by chemical composition nor cooling rate, but the distance between platelets is decreased under faster cooling rates. Ghomashchi and Sellars (1993) reported that the morphology of M_6C carbide was very sensitive to deformation and that the MC carbide morphology was not as sensitive as that of the M_6C carbide.

It should be emphasized that sometimes it is difficult to distinguish the carbide type based on the morphology. The type of carbide in tool steels can be identified from its EDS spectrum and quantitative analysis, since each type of carbide has different chemical composition. The following criteria have been used in the literature (Hashimoto *et al.*, 2004, Mébarki *et al.*, 2004, Li, 1996, Elrakayby and Mills, 1986, Todd, 1986) :

- The spectrum with just one high peak corresponding to V or Nb is from MC carbides

- M_7C_3 is distinguished by the presence of Cr peak higher than Fe peak or vice versa
- $M_{23}C_6$ is distinguished by the high Cr peaks and another high peak of Fe or the ratio Fe/Cr is about 1
- M_6C has a spectrum with a high Mo or W peak and a high Fe peak
- M_3C has a spectrum with a high Fe peak and/or a high Cr peak
- M_2C has a high Mo or W peak, but is distinguished from M_6C by the absence or small peak of Fe and the presence of considerable peaks of V and Cr

Diffraction patterns obtained from TEM are also used to identify the type of carbide, especially for fine carbide. However, both the $M_{23}C_6$ and M_6C carbides have fcc crystal structure and their lattice parameters are very close, therefore careful TEM work is required to distinguish the carbide type from diffraction patterns.

2.4.2 Sequence of Carbide Precipitation

It is well known that one or more metastable (transitional) carbide may form during the tempering of steels. Many investigations have studied the sequence of carbide precipitation in tool steels, which was found to depend strongly on the alloying elements and the processing, such as heat treatment and hot deformation. Bhadeshia and Honeycombe (2006) gave the sequence of carbide formation in high Cr steels, as follows:

$$\text{Matrix} \rightarrow M_3C \rightarrow M_7C_3 \rightarrow M_{23}C_6$$

This sequence was also reported by Thomson and Bhadsehia (1992). The $M_{23}C_6$ carbide can also form as a transient carbide that partially transforms to M_6C carbide when Mo is added, as observed in a type 316 stainless steel (Sourmail, 2001).

Dudova and Kaibyshev (2011) reported that the carbide sequence in a 10 % chromium steel was martensite $\rightarrow M_3C \rightarrow M_2C \rightarrow M_{23}C_6$ and M_6C and was attributed to the W and B addition to the steel. Asadabad *et al* (2010) studied the tempering of a 4.5Cr-2W-0.25V (wt%) steel and found that M_3C and M_2C carbides

formed in the first stages of tempering and transformed to the M_7C_3 and $M_{23}C_6$ carbides.

In steels with W content in the range 4 to 6 wt. % the carbide sequence is $M_3C \rightarrow M_2C \rightarrow M_6C$ (Roberts *et al.*, 1998). According to Kuo (1957, cited in Roberts *et al.*, 1998), the M_2C carbide is mainly responsible for the secondary hardening in W and/ or Mo steel. This carbide nucleates at prior austenite grain boundaries and ferrite lath boundaries during tempering of the quenched steels. After longer tempering at 700 ^oC the M_6C carbide formed at grain boundaries and grew quickly while the M_2C carbide dissolved.

Shtansky and Inden (1997) reported that the sequence of carbide precipitation in Fe-W-C steels containing W in the range 1.0 to 2.5 wt% during tempering at 700 ^oC was $Fe_3C \rightarrow M_6C \rightarrow M_{23}C_6$. They also reported that the MC carbide was not found even after tempering for 3000 hours.

The literature would thus suggest that the precipitation process during tempering can be complicated when steels contain more than one carbide forming element. The most stable thermodynamically carbides will predominate in the equilibrium (Bhadeshia and Honeycombe, 2006).

2.5 Martensite and Bainite Formation

2.5.1 Martensitic Transformation

The presence of martensite（ά） in hot working tool steel is very important. The formation of martensite starts at the M_s temperature and finishes at the M_f temperature. Both temperatures are affected by alloying and the processing of the steel. There are some empirical formulae giving the M_s temperature as a function of alloying elements. Some are given below.

M_s (^oC) = 561 – 474 (C) – 33 (Mn) – 17 (Ni) – 17 (Cr) – 21 (Mo) (2.5)
concentrations in wt% (Steven and Haynes, 1956, cited in Krauss, 2005)

M_s (^oC) = 539 – 423 (C) – 30.4 (Mn) – 17.7 (Ni) – 12.1 (Cr) – 7.5 (Mo) (2.6)
concentrations in wt% (Andrews, 1965, cited in Krauss, 2005)

M_s (^oC) = 539 – 423 (C) – 30.4 (Mn) - 7.5 (Si) + 30 (Al) concentrations in (2.7)
mass % (Mahieu *et al.*, 2002)

The equation 2.5 is valid if all the alloying elements are completely dissolved in the austenite, the equation 2.6 is based on data from very large number of steels and is suitable for most steels, and the equation 2.7 is valid for C-Mn-Al TRIP steels.

Figure 2.4 shows the effect of C and alloying element content on the M_s temperature. The latter decreases with increasing C and alloying element content except for Al and Co, with C and Mn having the stronger effect (Figure 2.4a). Figure 2.4b shows that at 1 wt% C the M_f is 300 ^{o}C below the M_s (Pickering, 1978).

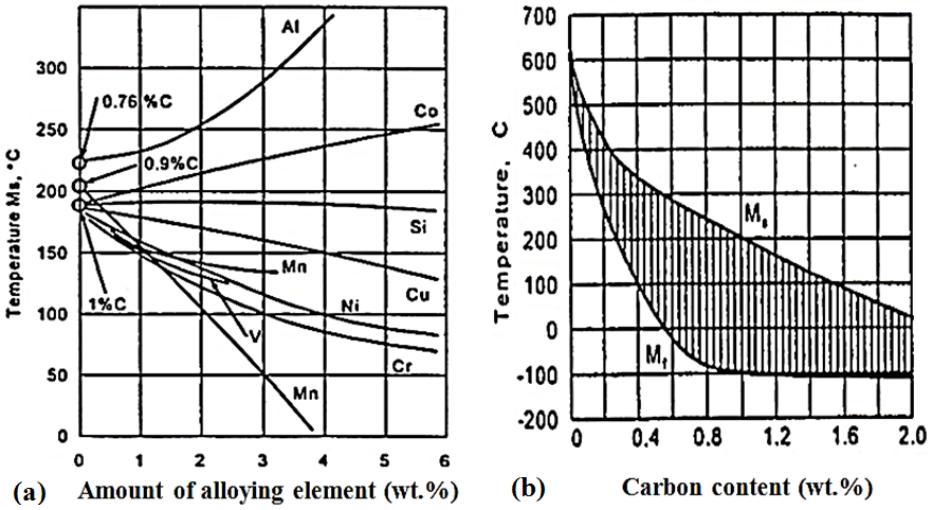

Figures 2.4: The effect of alloying elements (a) and carbon content (b) on the M_s temperature (Totten and Howes, 1997).

Yang and Bhadeshia (2009) and Lee and Lee (2005) also reported that the M_s temperature is influenced by the austenite grain size and that the M_s increased with increasing austenite grain size.

2.5.2 Thermodynamics of Martensitic Transformation

The martensitic transformation is a diffusionless or displacive transformation and martensite is not present in an equilibrium phase diagram. According to Bhadeshia (2002), martensite deviates from equilibrium owing (i) to it fast growth (up to 1100 m/s) and consequently its chemical composition being the same at that of the prior austenite due to insufficient time for diffusion and (ii) to the shape deformation producing strains.

The martensitic transformation does not depend on time but depends only on the degree of undercooling below the M_s temperature. Koistinen and Marburger (1959) proposed the equations 2.8 and 2.9 to describe quantitatively the progress of transformation from austenite to martensite in carbon steels.

$$V_\gamma = \exp [-1.1 \times 10^{-2} (M_s - T)] \quad (2.8)$$

$$V_{\alpha'} = 1 - V_\gamma \quad (2.9)$$

Here V_γ is the volume fraction of retained austenite, $V_{\alpha'}$ is the volume fraction of martensite, T is the quenching temperature, and M_s is the martensite start temperature. Since time does not contribute in this relationship, the $V_{\alpha'}$ depends only on the difference between M_s and T. This transformation is of athermal character. In contrast, the isothermal transformations are diffusion controlled and time dependent (Bhadeshia, 2002).

2.5.3 Morphology of Martensite

The martensite morphology in steels can be of two basic types, namely lath and plate (Wilson, 1994). The two morphologies differ in shape, mutual arrangement of crystals substructure and habit plane. Figure 2.5 shows the relationship between M_s, carbon content and martensite morphology.

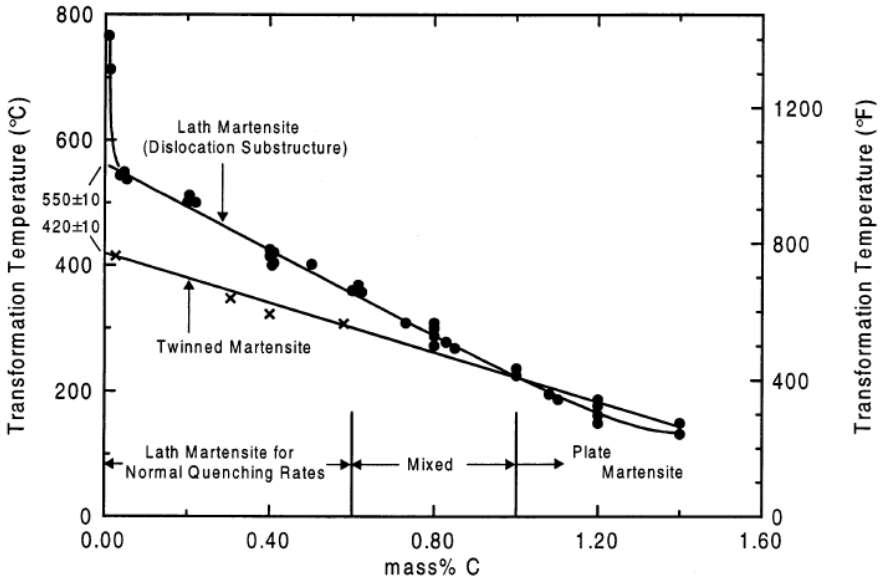

Figure 2.5 The relationship between M_s temperature, martensite morphology and carbon content in Fe–C alloys (Krauss, 1999).

It can be seen from Figure 2.5 that the lath morphology of martensite occurs in low and medium carbon martensite with relatively high M_s temperature. It is characterised by packets of parallel arrays of lath-shaped crystals. There is a high density of dislocations inside the laths produced by water or oil quenching, which reflects lattice invariant deformation and volume accommodation effects during athermal transformation (Krauss, 1999). The M_s temperature was depressed to 420 ^{o}C from 550 ^{o}C by increasing the cooling rate as shown in Figure 2.5. The amount of twining increased with decreasing M_s temperature and increasing carbon content (Krauss, 2005).

Plate martensite occurs in high carbon steels and is characterised by irrational habit planes. The formation of plate martensite at low M_s temperature leads the plate martensite crystals to form at temperatures where the lattice invariant deformation is accomplished by twinning and limited dislocation motion. The presence of large amounts of retained austenite is typical for plate martensite.

2.5.4 Crystallography of Martensitic Transformation

The formation of martensite involves the coordinated movement of atoms as a result of which the austenite and martensite lattices are closely related. There are two crystallographic parameters in ferrous alloys to show the interrelationship between austenite with an fcc crystal structure and martensite with bct crystal structure. One is the orientation relationship between the crystal structure of austenite and martensite, and the other one is the habit plane, which is the planar interface between any retained austenite and the martensite crystal (Krauss, 2005). The habit plane is affected by alloy composition, especially C content. Bhadeshia (2002) summarised the three well known preferred orientation relationships in steels, namely:

a . The Kurdjumov – Sachs (K-S) orientation relationship:

$$\{1\,1\,1\}\gamma \parallel \{0\,1\,1\}\alpha \;\; ; \;\; \langle 1\,0\,\bar{1}\rangle\,\gamma \parallel \langle 1\,1\,\bar{1}\rangle\alpha$$

b . The Nishiyama – Wasserman (N-W) orientation relationship:

$$\{1\,1\,1\}\gamma \parallel \{0\,1\,1\}\alpha$$
$$\langle 1\,0\,\bar{1}\rangle\gamma \quad \text{about } 5.3^{\circ} \text{ from } \langle 1\,1\,\bar{1}\rangle\alpha \quad \text{towards} \quad \langle \bar{1}\,1\,\bar{1}\rangle\alpha$$

c . The Treninger–Trojano relationship

$$\{1\,1\,1\}\gamma \quad \text{about } 0.2^{\circ} \quad \text{from } \{0\,1\,1\}\alpha$$
$$\langle 1\,0\,\bar{1}\rangle\gamma \quad \text{about } 2.7^{\circ} \quad \text{from } \langle 1\,1\,\bar{1}\rangle\alpha \quad \text{towards } \langle \bar{1}\,1\,\bar{1}\rangle\alpha$$

The KS or NW orientations enable for the existence of a semi coherent boundary between austenite and ferrite and thus minimise the surface energy required to nucleate the ferrite at the austenite boundary.

2.5.5 Bainite Formation

According to Bhadeshia (2001) bainite forms from the decomposition of austenite at a certain temperature above M_s but below the temperature where fine pearlite forms. As with the martensite start temperature, the bainite start temperature (B_s) is affected by alloying elements. Some empirical equations correlating the B_s temperature with the chemical composition of steels have been developed, for example:

B_s (^oC) = 830 – 270 (C) – 90 (Mn) – 37 (Ni) – 70 (Cr) – 83 (Mo) in wt% (Steven and Haynes, 1956) (2.10)

B_s (^oC) = 732 – 202 (C) + 216 (Si) – 85 (Mn) – 37 (Ni) – 47 (Cr) – 39 (Mo) in wt% (Kunitake and Okada, 1998) (2.11)

B_s (^oC) = 745 −110 (C) – 59 (Mn) – 39 (Ni) – 68 (Cr) – 106 (Mo) + 17 (Mn) (Ni) + 6 $(Cr)^2$ + 29 $(Mo)^2$ in wt % (Lee, 2002) (2.12)

There are controversies regarding the effect of austenite grain size on the bainite transformation temperature under continuous cooling. Yamamoto *et al* (1995) reported that the austenite grain size does not affect the bainite transformation temperature. Lee *et al* (2008) reported that both the B_s and B_f temperatures decreased with decreasing austenite grain size and the bainite transformation rate was accelerated by decreasing the austenite grain size. However, they observed that the transition temperature between upper and lower bainite remained almost constant, irrespective of austenite grain size. Zhang and Boyd (2010) observed in deformed austenite of low carbon steel that decreasing the prior austenite grain size increased the bainite transformation temperature range but had little effect on the transformation rate.

The bainite formation has been attributed to diffusionless (displacive). Bhadeshia and Edmons (1980) summarised that the bainite formation is a diffusionless transformation in which carbon atoms partition into retained austenite or carbide shortly after growth is arrested.

2.5.6 Bainite Morphology

Bainite consists of ferrite and carbides and its formation depends on the diffusion controlled partitioning of carbon between ferrite and cementite (Krauss, 2005). Each ferrite plates is10 μm in length and 0.2 μm in thickness and therefore it is invisible by optical microscopy. There are two morphologies of bainite that have been identified by Mehl (1939, cited in Bhadeshia, 2001), depending on the temperature ranges of bainite formation, namely upper bainite and lower bainite. They consist of

ferrite plate aggregates separated by retained austenite, martensite or cementite. Upper bainite occurs typically below 500 ^{o}C and lower bainite occurs in the temperature range 400-250 ^{o}C. Bhadeshia (2001) explained the microstructure of upper and lower bainite with the schematic diagram presented in Figure 2.6.

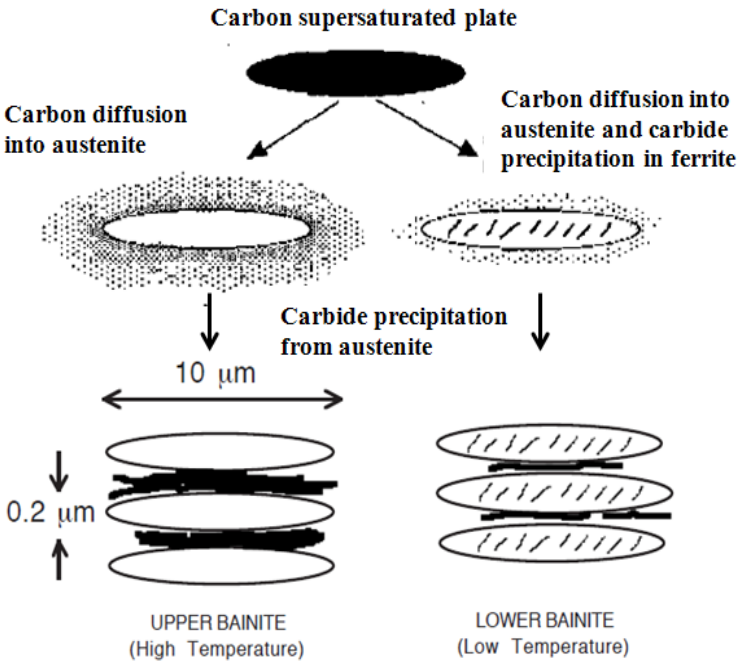

Figure 2.6 An overview illustration of differentiation between upper and lower bainite (Bhadeshia, 2001).

The microstructure of upper bainite is developed by packets or sheaves (cluster of ferrites) adjacent to each other growing across austenite grain with the orientation relationship between ferrite and austenite being of Kurdjumov-Sachs type. Elongated cementite is present between the platelets and the amount and continuity of cementite layers are affected by the carbon content of the steel. Lower bainite consists of large ferrite plates and interlath carbide significantly finer than that of the upper bainite. The carbide in the ferrite plates of lower bainite typically makes an angle around 60^{o} to the long axis of lath ferrite. These carbides are invisible in the light microscope (Krauss, 2005). In some cases, multi variants have been observed although the 60^{o} variant is still dominant (Bhadeshia and Edmonds, 1979).

2.5.7 Stress-Induced Transformation

The external stress applied to a steel can influence the free energy change driving martensite and bainite transformation. The martensite or bainite formed due to deformation is named strain induced martensite or bainite. The temperature at which martensite or bainite formed by deformation, M_d or B_d respectively, normally is higher than the M_s or B_s temperature. Bhadeshia and Honeycombe (2006) argued that it is highly possible that deformation of the austenite above M_d will change the M_s on subsequent cooling through the martensite range with the M_s temperature decreased, thus increasing the austenite stability, which is known as mechanical stabilisation. Others researchers (Alvarado-Meza *et al.*, 2012, Fan *et al.*, 2009, Xiao *et al.*, 2006, Nishiyama *et al.*, 1978) reported that the effect of deformation on austenite is to increase the M_s temperature.

The effect of hot deformation on the bainite transformation in Fe-0.45C-2.08Si-2.69Mn wt% has also been reported that the high external stress enhanced the bainite transformation (Shipway and Bhadeshia, 1995). A study by Yang *et al* (1995) of low carbon steels with bainite formation under continuous cooling showed that deformation of austenite increased the B_s temperature. Yamamoto *et al* (1995) also reported that hot deformation increased the B_s temperature by 20 to 60 ^{o}C. Lin-xiu *et al* (2006) observed that deformation accelerated the bainite transformation when it was carried out at high temperature.

2.6. Microstructure of the H21 and H23 Tool Steels

The solidification of tool steels starts with the precipitation of ferrite. During the subsequent cooling, the peritectic reaction occurs accompanied by segregation of alloying elements. As lower temperatures the carbides form by the eutectic reaction. The carbides formed during casting are referred to as primary carbides.

The H21 tool steel consists of a ferritic matrix (martensite or bainite) and carbides, formed by solutioning, quenching and tempering. The carbide types and their volume

fraction are dependent on tempering parameter and the alloying content of the tool steel. The choice of tempering parameter depends on the expected temperature in service. An increase of C content and carbide forming elements within the standard range can affect the volume fraction of carbide. The carbide types found in tempered H21 tool steels were the M_2C, M_6C and $M_{23}C_6$ carbides (Roberts *et al.*, 1998). Figure 2.7 shows an isothermal section of the Fe-W-C system at 1200 ^oC.

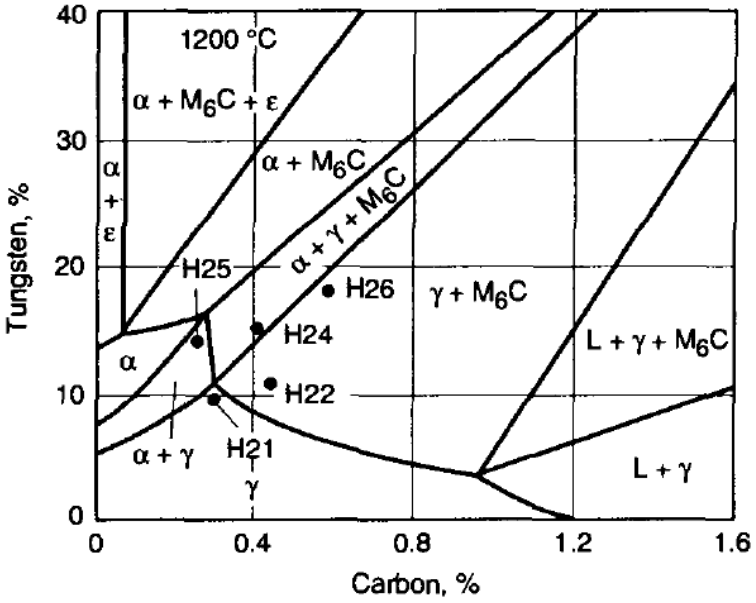

Figure 2.7 : Isothermal section of the Fe-W-C system at 1200 ^oC (Roberts *et al.*, 1998).

From Figure 2.7 it can be seen that the equilibrium phase in the H21 tool steel, when austenised at 1200 ^oC is the γ. However, the content of C and W within the standard range may shift the steel either in the $\alpha + \gamma + M_6C$ or the $\gamma + M_6C$ region.

The H23 tool steel has a ferritic structure and carbides, formed by solutioning, quenching and tempering. At the solutioning temperature of 1260 ^oC, this tool steel has a duplex structure, namely ferrite and austenite (Roberts *et al.*, 1998). When this tool steel is quenched to room temperature, the as quenched microstructure consists of ferrite, undissolved carbides and retained austenite due to the M_s temperature

being - 46 ^{o}C. Like the H21 tool steel, the formation of carbides and their volume fraction is strongly connected to the tempering parameter.

2.7 Controlled Thermomechanical Processing

Controlled thermomechanical processing (TMP) combines reheating, plastic deformation and cooling and is powerful for controlling the final grain size compared with what can be managed by conventional heat treatment. For the last several decades, thermomechanical processing has played an important part in the processing of many steels to improve their structure and mechanical properties through the refinement of the austenite grain structure. The presence of micro alloying elements (known as MAE) such as Nb, Ti, and V in small quantities in steels has made the goal of thermomechanical processing easy to achieve (DeArdo *et al.*, 1991). Many studies (Khlestov *et al.*, 2002, Liu *et al.*, 2000, Dobrzański, 1993) have reported that thermomechanical processing homogenises the microstructure, produces dispersed precipitates and refines the grain size resulting to improved toughness and hardness of tool steels.

The thermomechanical processing of steels can be divided into three types, which is based on where the deformation occurs relative to certain material critical temperatures and the condition of austenite (Dieter *et al.*, 2003, DeArdo *et al.*, 1991), namely:

1. Conventional controlled rolling, CCR,
2. Intensified controlled rolling, ICR, and
3. Recrystallisation controlled rolling, RCR

In the CCR process (indicated by B in Figure 2.8) the finish rolling takes place below the recrystallisation stop temperature, T_{RXN} or $T_{5\%}$, therefore during deformation the austenite grains are elongated (pancake-like) and afterwards transform into ferrite of fine grain size. In the ICR process (indicated by C in Figure 2.8) the finish rolling

extends to temperatures below T_{Ar_3} and the combination of the lower reheat and lower rolling temperature produce finer as-rolled austenite than in the CCR process. In the RCR process (indicated by D in Figure 2.8) the rough rolling and finish rolling occur above the recrystallisation stop temperature. The final microstructure consists of fine ferrite grain size formed by transforming fully recrystallised austenite.

There is a difference between thermomechanical processing and conventional hot rolling (CHR). In the CHR process (indicated by A in Figure 2.8), reheating, rough rolling, and finish rolling all occur at the highest possible temperatures and the primary goal of conventional hot rolling is to optimise productivity. Figure 2.8 shows schematically the deformations schedules for the aforementioned processes.

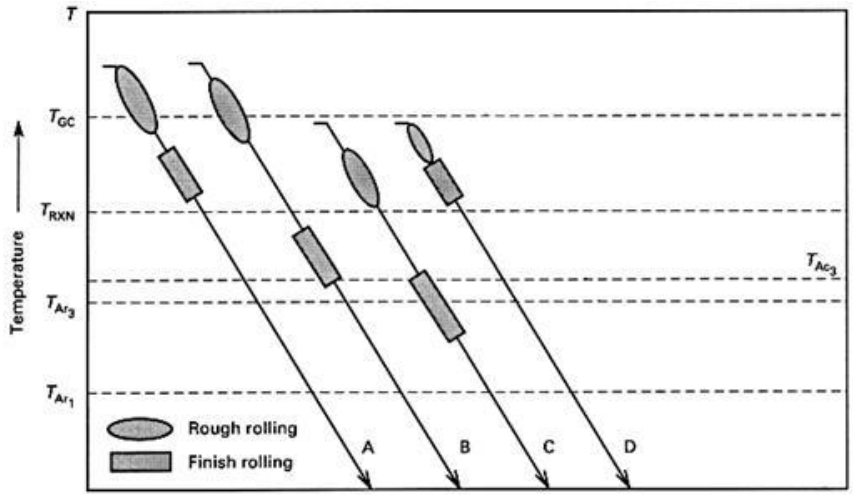

T_{GC} : Grain coarsening temperature
T_{RXN}: Recrystallisation stop temperature
T_{Ac_3}: The temperature at which transformation of ferrite to austenite is completed during heating
T_{Ar_1}: The temperature at which transformation of austenite to ferrite or to ferrite plus cementite is completed during cooling
T_{Ar_3}: The temperature at which austenite begins to transform to ferrite during cooling

Figure 2.8 Schematic of the difference between conventional hot rolling (CHR) and TMP (A: CHR, B: CCR, C: ICR, D: RCR) (Dieter *et al.*, 2003).

The critical temperatures and the changes in austenite microstructure as a function of deformation temperature and strain are schematically illustrated in Figure 2.9 for constant inter-pass time.

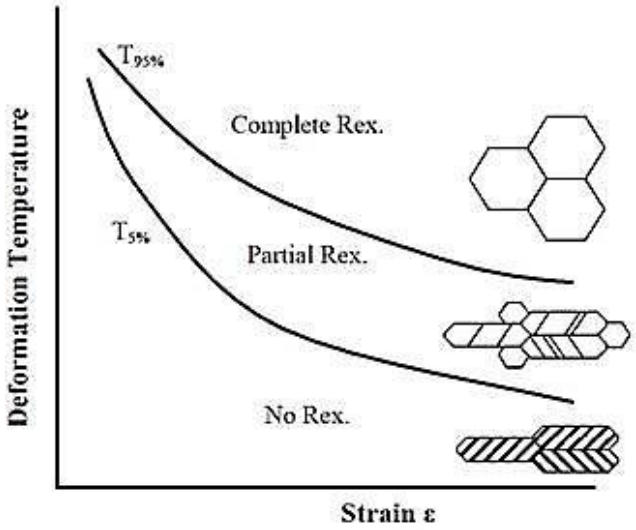

Figure 2.9 Schematic of austenite grains forming in various deformations (Palmiere *et al.*, 1993). $T_{95\%}$ is the recrystallisation-limit temperature and $T_{5\%}$ is the recrystallisation-stop temperature

2.7.1 Work Hardening

Work hardening or strain hardening is one of the strengthening mechanisms in metals and alloys and is linked with an increase of dislocation density and the creation of crystal defects during plastically deformation (Bhadeshia and Honeycombe, 2006). The increase of strength, which is indicated by an increase in the flow stress of a material, is due to the increased stress required for dislocation movement as the dislocations are hindered by microstructural obstacles. Dislocations are introduced by cold working, rapid cooling, differences in thermal expansion between phases, volume changes accompanying precipitation and strains produced during transformations (Pickering, 1978). Dislocation density and distribution are strongly affected by deformation temperature. A lower deformation temperature tends to produce higher dislocation densities.

In metals with fcc crystal structure and low stacking fault energy (SFE), typically less than 50 mJ/m^2, the dislocations will dissociate into partials due to their difficulty to cross slip, and thus deformation twinning may occur. Examples are austenitic stainless steels, and some Cu-Al or Cu-Zn alloys (Verlinden *et al.*, 2007, Humphreys and Hatherly, 2004). Cross slip occurs easily in bcc and fcc metals with medium and high SFE such as Cu and Al (Humphreys and Hatherly, 2004, Šesták and Seeger, 1971).

The work hardening behaviour is strongly influenced by alloying elements and in particular on whether the elements are in solid solution (solid solution hardening) or in a dispersion of second phase particles. Solid solution hardening occurs with alloying elements such as Mg and Cu in Al or C in Fe. The solute atoms interacted with dislocations and significantly decrease their movement, thus increasing the stress required for plastic flow. The second phase strengthening relates to the resistance offered by the second phase particles to dislocation movement and the dislocation either cutting fine particles (radius $\leq$ 10 nm) or by passing them via Orowan type mechanism (radius $\geq$ 20 nm) (Verlinden *et al.*, 2007).

2.7.2 Flow Stress and Activation Energy

Hot working refers to high temperature deformation at T > 0.6 T_m where T_m is the melting temperature in degrees Kelvin (Sellars and Tegart, 1972). Hot deformation tests produce flow stress data and information about structural changes that occur during or after deformation. At temperatures above 0.6 T_m, plastic deformation is strongly affected by thermally activated processes, thus the flow stress and structure changes are mainly functions of material, temperature and strain rate.

The constitutive equation to calculate the peak stress (σ_p) or steady state stress (σ_s), which depend on strain rate and temperature, can be analysed using the creep equation (Imbert *et al.*, 1984, Roberts, 1984):

$$Z = f(\sigma) = \varepsilon \exp (Q_{def}/RT) \quad (2.13)$$

where T is the absolute temperature (K), and ε is the strain rate (s^{-1}). Both T and ε can be grouped into a temperature-compensated strain rate, known as the Zener-Hollomon parameter (Z). In eq. 2.13 Q_{def} is an apparent activation evergy for deformation (J/mol), and R is the universal gas constat (8.314 J/mol K). The function $f(\sigma)$ is the stress function, which is expressed by the two following formulae (Sellars and Tegart, 1972):

$$Z = f_1(\sigma) = A\,\sigma^n \quad \text{(at low stress, usually } \sigma < 70 \text{ MPa)} \quad (2.14)$$

$$Z = f_2(\sigma) = B \exp(\beta\,\sigma) \quad \text{(at high stress)} \quad (2.15)$$

where A, B and β are constants, and n is the stress exponent.

The equation 2.14 is the power law description of stress preferred for creep and cannot be used when stresses are too high. Conversely, the exponential law (equation 2.15) is only suitable for low working temperatures and high strain rates. Sellars and Tegart (1966) combined the equations 2.14 and 2.15 to get the hyperbolic sine function given by equation 2.16, which is a more general equation and can be used for a wide range of temperatures and strain rates:

$$Z = f(\sigma) = C\,[\sinh(\alpha\,\sigma)]^n \quad (2.16)$$

where C and α are constants, and α, β and n are related via the equation 2.17:

$$\alpha = \frac{\beta}{n} \quad (2.17)$$

Imbert and McQueen (2001) calculated the peak stress using the hyperbolic sine equation and their results were in good agreement with data for A2 and M2 tool steels. Other studies by McQueen and Ryan (2002) and Imbert *et al* (1984) utilized the exponential law to calculate the peak stress of A2, M2 and H13 tool steels. The calculation gave Q_{def} between 350-450 kJ/mol for T > 1050 ^oC and carbide volume

fraction 1-12 % and Q_{def} > 500 kJ/m for carbide volume fraction 8-20 % and temperature below 1050 ^{o}C.

The activation energy for hot deformation Q_{def} is affected by alloying elements. The high alloying element content in tool steel will produce carbide precipitation and as a result affect the hot deformation behaviour. McQueen and Ryan (2002) and Ryan and McQueen (1986a) reported that solute addition, precipitates and inclusions resulted to increase of Q_{def} value by as much as 50 % due to alloying making the operation of restoration mechanisms such as dislocation climb, cross slip and grain boundary migration, more difficult. An increase of Q_{def} indicates increase in strength and decrease in ductility and workability of steel.

The increase in peak stress of tool steel is more sensitive to the presence of carbides than alloying elements in solution in the austenite matrix. The hard carbide precipitates cause increase in flow stress and Q_{def}. According to Milovic *et al* (1992) and Imbert *et al* (1984) the Q_{def} suddenly increases when $M_{23}C_6$ carbides precipitate around 1000 ^{o}C. Another study by Imbert and McQueen (2001) showed that the Q_{def} of a M2 tool steel was 14 % higher than that of a A2 tool steel due to greater alloy carbide content. The peak stress of tool steels is in general greater than that of carbon and HSLA steels due to greater amounts of alloying elements (Ryan and McQueen, 1986a). A decrease of flow stress indicates that a metal is more hot workable and ductile (McQueen and Jonas, 1984).

The Q_{def} value is also affected by strain and temperature. Liu *et al* (2000) concluded that the Q_{def} of a T1 tool steel depends on both deformation temperature and strain. They identified two regions, one at temperatures below 1000 ^{o}C where the Q_{def} value was high and decreased as the strain increased and another where the temperature was higher than 1000 ^{o}C and the Q_{def} value decreased and changed slightly as the strain increased. Table 2.4 gives a summary of Q_{def} values obtained from previous studies in terms of the different equations used and temperature ranges. Table 2.5 gives the chemical composition of some of the tool steels in Table 2.4.

Table 2.4 Summary of Q_{def} values for hot deformation of some tool steels

Type of tool steels	Q_{def} (kJ/mol)	T_D (^oC)	Strain rate (s^{-1})	Equation used to calculate Q_{def}	Reference
AISI T1	654	< 1000	0.001-10	(2.16)	(Liu *et al.*, 2000)
	467	>1000	0.001-10		
AISI M3:2	487	900-1100	0.1-10	(2.15)	(Rodenburg *et al.*, 2004)
M2	610	900-1100	0.1; 1	(2.14)	(Imbert *et al.*, 1984)
	590	900-1100	0.1; 1	(2.15)	
M2	455	900-1150	0.1; 1; 4	(2.16)	(Imbert and McQueen, 2001)
M2	608	900-1100	0.18-3.63	(2.15)	(Milovic *et al.*, 1992, cited in Pirtovšek *et al.*, 2011)
	422	1000-1100	0.18-3.63		
A2	530	900-1100	0.1; 1 ; 5	(2.14)	(Imbert *et al.*, 1984)
	578	900-1100	0.1; 1 ; 5	(2.15)	
	399	900-1150	0,1 ; 1; 4	(2.16)	(Imbert and McQueen, 2001)
A2	611	850-1000	0.001-10	(2.16)	(Pirtovšek *et al.*, 2008)
	400	1000-1150	0.001-10	(2.16)	
BRCMO HSS	607	900-1050	0.001-10	(2.16)	(Fajfar *et al.*, 2010)
H13	401	1000-1100	0.1; 1 ; 5	(2.15)	(Imbert *et al.*, 1984)
	830	900-1000	0.1; 1 ; 5		
	583	900-1100	0.1; 1 ; 5	(2.14)	
	585	900-1100	0.1; 1 ; 5	(2.15)	
Ledeburitic tool steel	554	950-1150	0.001-6	(2.16)	(Pirtovšek *et al.*, 2011)
	1125	850-950	0.001-0.1		
	1039	850-950	0.1-6		

Table 2.5 Chemical composition of some of tool steels listed in Table 2.4.

Type of tool steels	Chemical composition (wt%)				
	C	Cr	Mo	W	V
AISI T1	0.95	4.35	0.11	18.41	0.99
AISI M3:2	1.31	4.12	5.34	6.24	3.05
M2	0.84	4.00	5.00	6.50	1.90
H13	0.40	5.00	1.00	1.00	-
A2	1.00	5.00	1.15	-	0.30
BRCMO HSS	0.91	4.15	4.70	6.30	2.10
Ledeburitic tool steel	1.17	11.3	1.35	1.48	2.24

2.7.3 Restoration Processes

According to Verlinden *et al* (2007) and Humphreys and Hatherly (2004) when a metal is plastically deformed at a high temperature, most of the applied work will turn into heat and only ~1-10 % will remain as stored energy. The increase in stored energy during deformation is due to the increasing dislocation density and grain boundary area. The stored energy will act as a driving force for restoration processes.

Recovery, recrystallisation, and grain growth are processes, which decrease the stored energy. Recovery is a process where the dislocations in the deformed material rearrange to form a well-defined substructure in low energy configuration (Doherty *et al.*, 1997). During recovery, there is a series of events starting from random dislocation tangles, annihilation of dislocations within cells, and sub grain formation. The schematic of those events can be seen in Figure 2.10.

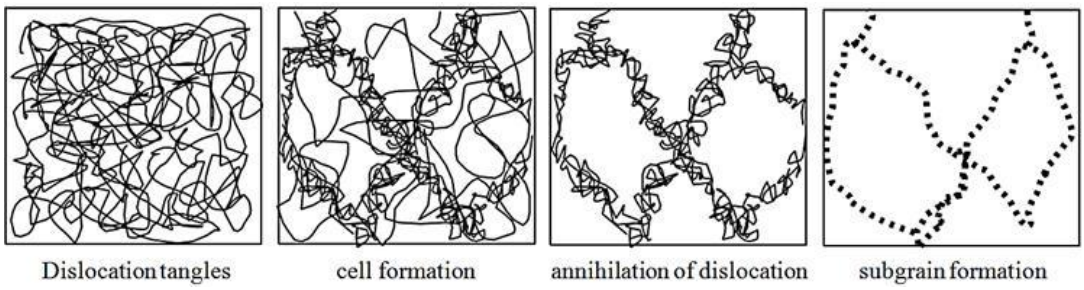

Figure 2.10 Schematic of structure changes during recovery (Verlinden *et al.*, 2007).

Recrystallisation is "the formation of a new grain structure in a deformed material by the formation and migration of high angle grain boundaries driven by the stored energy of deformation and grain growth is the growth of the mean grain size driven by the reduction in grain boundary area" (Doherty *et al.*, 1997). Figure 2.11 shows a schematic diagram of steps occurring during the formation of recrystallised grains. The latter starts with the formation of a necklace of new grains around the deformed grain (a and b) and continues by intragranular nucleation of new grains inside the grain (c and d).

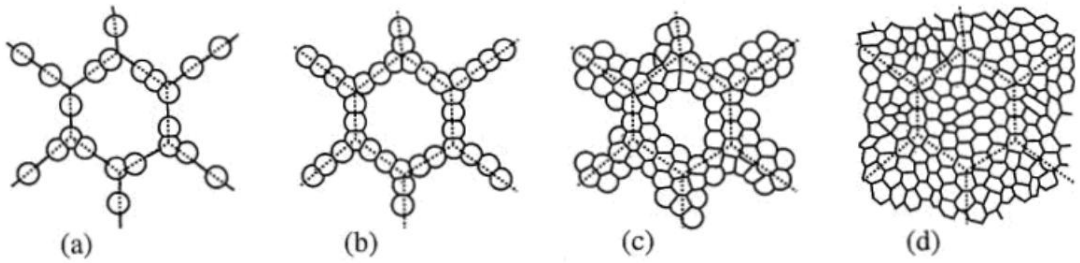

Figure 2.11 The sequence of the formation of recrystallising grains. The dotted lines indicate prior grain boundaries and the continuous lines represent new recrystallised grains (Humphreys and Hatherly, 2004).

The recovery and recrystallisation process are affected by temperature. At temperatures between 0.4 T_m to 0.5 T_m (T_m in degree Kelvin), the recovery process dominates, whereas at temperature above 0.7 T_m, recrystallisation occurs.

The restoration processes of recovery and recrystallisation can occur during and after hot deformation and to distinguish them they are called dynamic and static.

2.7.3.1 Dynamic Restoration Mechanisms

Two distinct dynamic restoration mechanisms have been established that operate during hot working, namely dynamic recovery (DRV) and dynamic recrystallisation (DRX) (McQueen and Jonas, 1984). Both dynamic restoration mechanisms increase the ductility of a material, therefore it becomes easier to deform the materials. The hot deformation behaviour of materials is usually determined from their flow curves

(σ – ε curves). The flow stress produced from hot working conditions tends to be lower than at room temperature. Furthermore, increase of ductility is usually observed at high working temperatures.

a. Dynamic recovery

Typical flow stress of a metal experiencing dynamic recovery and the corresponding microstructure changes can be seen in Figure 2.12. The flow curve exhibits an initial stage of strain or work hardening in which multiplication of dislocations take place and the dislocation density increases, and as a consequence the flow stress and the restoration driving force are increased. During this stage, subgrain formation in the microstructure will occur. However, the increase of dislocation density is limited. The flow stress becomes constant when the strain is greater than ε_m, which means the rate of strain hardening and recovery achieve a dynamic equilibrium, as a result the dislocation density becomes constant. The steady state value increases with increasing strain rate and decreasing deformation temperature.

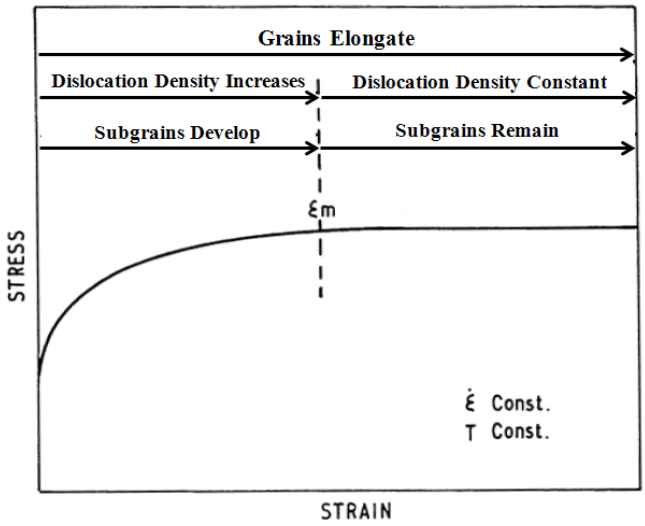

Figure 2.12 Schematic of stress-strain curve showing dynamic recovery formation and the corresponding microstructural changes (Sellars, 1990).

During dynamic recovery, the dislocations are annihilated due to the ease of cross slip, climb and dislocation unpinning during hot working. The microstructure

produced from dynamic recovery consists of elongated grains inside, which there are a well-developed, fine subgrains typically of the order of 1 to 10 μm (Dieter *et al.*, 2003). This behaviour is typical of metals with high SFE where the dislocations have high mobility. Roberts (1982) and Sellars and Tegart (1972) reported that metals with high SFE such as α-Fe, β-Ti alloys, Zr, Al and the bcc refractory metals undergo rapid dynamic recovery and do not experience dynamic recrystallisation due to dislocation climb being difficult.

b. Dynamic recrystallisation (DRX)

Dynamic recrystallisation has an important role to play, not only in reducing the flow stress but also in refining the grain size and improving the ductility. A typical stress-strain curve for dynamic recrystallisation shows the increase of flow stress to a peak value (σ_{peak}) and then followed by a lower steady state flow stress (σ_{ss}), as illustrated in Figure 2.13.

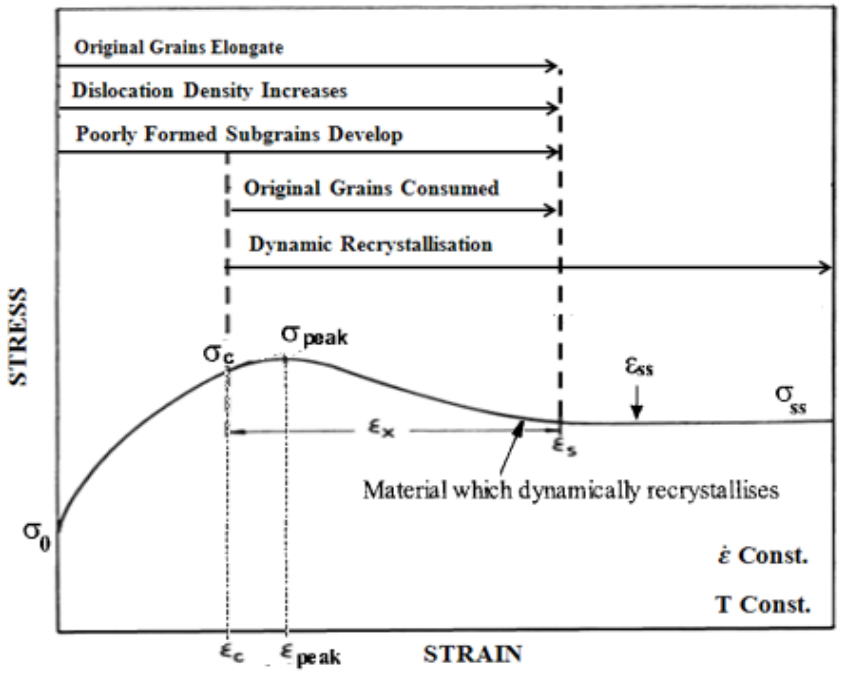

Figure 2.13 Schematic of stress-strain curve showing dynamic recrystallisation formation (Davenport *et al.*, 2000, Sellars, 1990). σ_o is the maximum stress when plastic strain $\varepsilon = 0$, σ_c is the stress when critical strain ε_c, and σ_{peak} and ε_{peak} are the peak positions.

Sellars (1980) concluded that dynamic recrystallisation occurs if a critical strain (ε_c) is reached. The critical strain required to initiate dynamic recrystallisation is lower than the peak strain, ε_p, in the stress-strain curve. Therefore, dynamic recrystallisation takes place before reaching the maximum flow stress at the peak strain. Luton and Sellars (1969) found that the strain at the peak flow stress varies with the stress. They explained that at high strain rate, subsequent cycles of recrystallisation start before the previous ones are finished, therefore the material is always in a partially recrystallised condition after the first peak, and the strain curve is smoothed out, producing a single broad peak. At low strain rate, regular oscillations of flow stress are visible due to the material having recrystallised completely before the next cycle of recrystallisation begins and this process is repeated.

In summary, dynamic recrystallisation occurs when dynamic recovery is unable to establish a stable substructure in which the density of dislocation substructure becomes high enough to give rise to the nucleation and growth of new grains (McQueen and Jonas, 1984).

2.7.3.2 Static Restoration Mechanisms

It has been established that recrystallisation does not only take place during deformation but can also occur after completing deformation and before cooling down to room temperature and between intervals of hot deformation (Imbert and McQueen, 2007, Ryan *et al.*, 1983). These mechanisms can be divided into three processes, namely static recovery, classical static recrystallisation (SRX) and metadynamic recrystallisation (MRX).

a. Static recovery

Static recovery involves the annihilation of dislocations within subgrains and their boundaries (Cahn and Haasen, 1996). According to McQueen and Jonas (1985), the static recovery usually will contribute 10-25 % to the initial softening. This

mechanism starts immediately after deformation when strains are smaller than the critical strain for SRX. The microstructural changes due to static recovery are not significant, because dynamic recovery has already occurred during deformation.

b. Static recrystallisation

SRX after hot working is very similar to the recrystallisation of cold worked materials during annealing (classic recrystallisation). The differences from classical recrystallisation arise due to much lower dislocation density of the hot deformed materials as a consequence of the dynamic restoration processes that occurred previously. The SRX nucleates and can complete the softening when the strain exceeds a critical value. The SRX can occur with strains as low as 0.05 and after an incubation period that depends on temperature and comes near to completion from fractions of seconds to hours (Imbert and McQueen, 2007, McQueen and Jonas, 1985). Metals that undergo full static recrystallisation will have equiaxed microstructure. Static recrystallisation occurs between passes in multistage hot working and can increase the overall ductility of the metal.

c. Metadynamic recrystallisation

According to Djaic and Jonas (1972) recrystallisation after deformation that is preceded by dynamic recrystallisation is called metadynamic. The nuclei for metadynamic recrystallisation already exist at the end of deformation, therefore MRX only occurs after dynamic recrystallisation has initiated and without any incubation period (McQueen and Jonas, 1985, Djaic and Jonas, 1973). The rate of metadynamic recrystallisation is fast and sometimes is completed during quenching after deformation. According to McQueen and Bergerson (1972) the metal experiencing MRX has equiaxed grains, fairly uniform and straight grain boundaries. The MRX grain size is slightly larger compared with the size of dynamically recrystallised grains due to there being no further nucleus formation after straining stops.

Morgridge (2002) found that metadynamic recrystallisation occurred at strains higher than a critical strain, showing strong dependence on strain rate and very weak dependence on temperature and strain. A weak dependence on composition was also detected but this occurred only at high temperature. This is in contrast from static recrystallisation where the rate of recrystallisation in austenite is influenced by temperature, strain, and grain size with little effect from strain rate.

2.7.4 Factors Affecting Restoration Processes

The alloying, deformation conditions such as temperature, strain and strain rate, and initial grain size are the parameters that influence the restoration processes.

2.7.4.1 Alloying Elements

The alloying elements in tool steels play an important role in the softening process. They can reduce the ability of metal to recover, and as a consequence increase the driving force and therefore increase the formation of dynamic recrystallisation. The alloying elements can also retard the softening process due to the formation of second phase particles or precipitate dispersion (Zener drag) or solute atoms segregating at the grain boundaries (solute drag).

a. Solute effect

In general, the addition of solutes decrease both the rate of dynamic recovery by hindering dislocations to leave their slip planes to undergo annihilation and the rate of dynamic recrystallisation through decreasing the mobility of grain boundaries (Ryan and McQueen, 1986a). Jonas and Weiss (1979) observed that the addition of Nb to steel retarded dynamic recrystallisation by the solute drag effect. A study by Andrade *et al* (1983) reported that the greatest retardation of static restoration by solute was produced by Nb, followed by Mo and V addition and the same effect was also found under dynamic softening conditions. Serajzadeh and Karimi Taheri (2002) concluded that higher Si content decreased the rate of both the dynamic recovery and recrystallisation due to the effect of solid solution hardening. The

solute drag effect of Nb and Ti on retarding dynamic recrystallisation in low carbon steel was also reported by Ma *et al* (2008). Another study by Miao *et al* (2012) found that in steels with high Mn content, Nb content higher than 0.1 %wt. could slow down the mobility of recrystallised grain boundaries.

b. Effect of precipitates

Carbides in tool steels have a great effect on their hot working behaviour depending on their size, distribution, solubility and hardness and the matrix (austenite or ferrite). The formation of fine precipitates before or during deformation reduces both the rate of recovery (by hindering dislocation motion) and the rate of recrystallisation (by stabilising the substructure, inhibiting nucleation and pinning grain boundaries) and as a result the ductility is decreased (McQueen and Jonas, 1985).

Shin *et al* (2003) attributed the increase of the recrystallisation temperature of the investigated steels to the pinning effect of fine precipitates that were smaller than 10 nm. Another study by Imbert and McQueen (2007) reported that carbon steels experienced rapid static recrystallisation whereas the presence of carbides in tool steels retarded the progress of recrystallisation and the retarding effect became more dominant when finer and harder carbides were present. Beladi and Hodgson (2007) reported that Nb at concentrations between 0.03 – 0037 wt.% reduced the recrystallisation rate due to the formation of Nb(C,N) precipitates, even at very high strains. Cao *et al* (2012) investigated the softening behaviour of high Nb microalloyed steel and observed that strain induced precipitation had stronger retarding effect on the recovery and static recrystallisation than the Nb atoms in solid solution. However, when the precipitates became coarser the retarding effect decreased rapidly.

Widely spaced large particles were observed to accelerate recrystallisation (Gao *et al.*, 2012, Longfei *et al.*, 2012, Lillywhite *et al.*, 2000). In general, coarse particles increase the density of dislocations and the concentration of dislocations surrounding

the precipitates' region, therefore enhancing nucleation of DRX. Lillywhite *et al* (2000) concluded that coarse particles with size more than 1 μm can promote recrystallisation through particle stimulated nucleation (PSN). Gao *et al* (2012) observed that large $M_{23}C_6$ carbides with size above 100 nm could promote recrystallisation due to the pile up of dislocations around the carbides producing high dislocation density and higher distortional energy. Longfei *et al* (2012) investigated DRX of ferrite in a low carbon steel with duplex microstructure and found that coarser particles with average size of 1.1 μm promoted DRX.

Zener (1948) was the first to produce quantitative formulae for the interaction of a moving grain boundary with dispersed particles. According to Rios (1987) Zener's formulae give a low value for the drag force for inhomogeneous particle distribution, such as when precipitates are located at grain boundaries.

2.7.4.2 Experimental Parameters and Prior Grain Size Effect

Deformation temperature, strain and strain rate affect the restoration process. In general, decreasing deformation temperature decreases the rate of softening, and increasing strain and strain rate lead to an increase in softening rate. Barraclough and Sellars (1979) observed that both the recrystallisation time and the recrystallised grain size of a 304 stainless steel decreased by increasing strain, strain rate and decreasing the original grain size. Queen and Vazquez (1986) reported that recovery occurred rapidly at the higher strain rate or temperature. Sun and Hawbolt (1995) concluded that increasing deformation temperature accelerated the initiation of static recrystallisation and the nucleation kinetics of static recrystallisation was accelerated either by strain rate or applied strain.

The rate of softening also depends on the microstructure present before deformation. Serajzadeh and Karimi Taheri (2002) observed that increasing the initial grain size (i.e., decreasing the grain boundary area) decreased the nucleation sites for new recrystallised grains and thus decreased the rate of dynamic recrystallisation, leading

to a higher flow stress. Zeng *et al* (2011) reported that static recrystallisation proceeds faster when the prior austenite grain size is smaller. Miao *et al* (2012) concluded that static recrystallisation can be accelerated by finer initial grain size.

2.8. Summary

Tungsten hot work tool steels are widely used for die-casting dies and hot forging dies due to having high hot hardness, and strength and resistance to softening at high working temperatures. The ability of these tool steels to meet the property requirements is strongly affected by the presence of carbides. The type of carbides, as well as their formation sequence in the tool steels depends on the chemical composition of the latter together with the heat treatment conditions.

A typical heat treatment for tool steels involves solution hardening to dissolve the carbide networks that formed during solidification and tempering to improve the toughness. However, it is difficult to dissolve the carbides during the solution hardening process due to the thermodynamic stability of the carbides. Controlled thermomechanical processing (TMP) is an effective method to control the microstructure, break up the carbide network and optimize the mechanical properties owing to refinement of the carbides and their uniform distribution.

In the group of tungsten hot work tool steels, the H21 tool steel is the most popular one. The highest alloying content in this tool steel is W, and is followed by Cr. The tempered microstructure of this tool steel is ferritic matrix (martensite or bainite) and carbides. The carbide types in the tempered H21 tool steel are the M_2C, M_6C and $M_{23}C_6$ carbides, with the M_6C carbide being the dominant one.

The H23 tool steel has the highest alloying content and hot hardness in the tungsten hot working group. The major alloying elements of this tool steel are W and Cr, each at around 12 wt%. Because of the high concentration of ferrite stabilisers, the microstructure of the H23 tool steel after solutioning, quenching and tempering

consists of a ferritic structure and carbides. After solutioning at 1260 ^{o}C, this tool steel has a duplex, which is ferrite and austenite structure (Roberts *et al.*, 1998). The formation of carbides and their volume fraction in the H21 and H23 tool steels is strongly dependent on the tempering parameter and their chemical composition.

Chapter 3

Experimental Methods

3.1 Investigated Materials

Two types of tungsten hot working tool steel were selected, namely the H21 and H23 tool steels contrasting the main alloying additions in this H grade of tool steels. The investigated materials were melted at 1590 ^{o}C using vacuum induction melting with slow cooling. Each steel was melted twice. Two ingots were produced for each tool steel. The weight of each ingot was around 12 kg and the dimensions were 280 x 75 x 70 (L x W x H), in mm. Figure 3.1 shows an ingot of the H23 tool steel investigated in this work and the top of the ingot showing the shrinkage cavity formed during solidification. Figure 3.2 shows how the ingot was sectioned to produce samples for various studies.

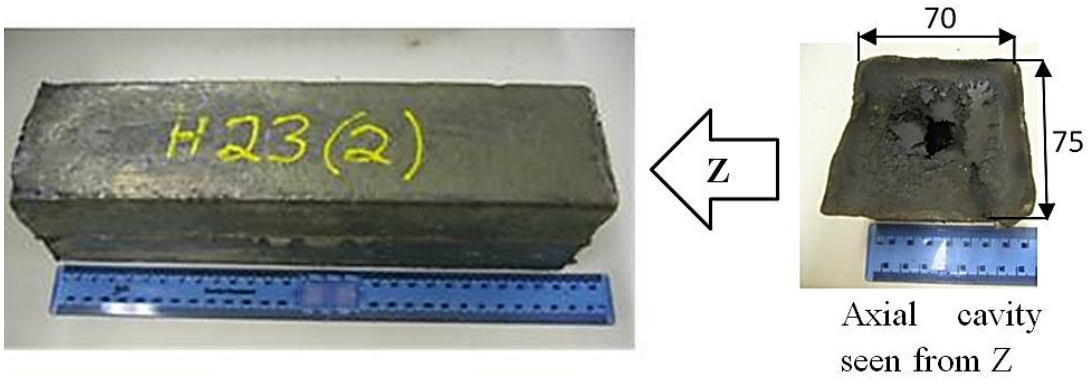

Figure 3.1 An ingot (left) of the investigated materials and shrinkage cavity in the top face of ingot (right). Dimensions in mm.

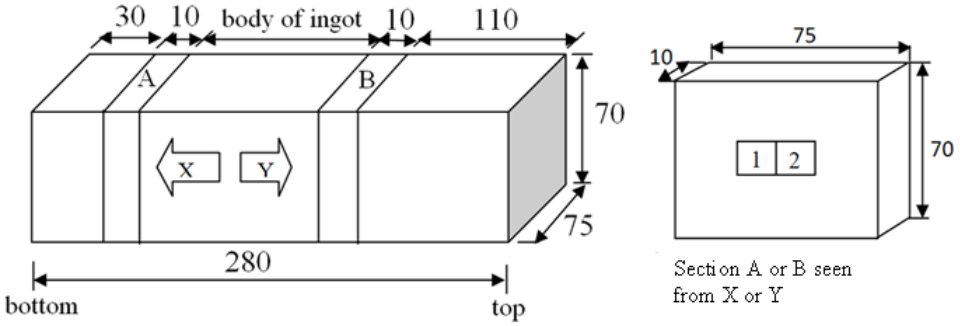

Figure 3.2 Schematic diagram showing how the ingot was sectioned to produce samples for chemical analysis, conventional heat treatment, and hot deformation. Dimensions in mm. Number 1 in right diagram for chemical composition and number 2 for microstructure analysis.

Each ingot was cut using EDM about 110 mm from the top and 30 mm from the bottom of ingot to remove the casting defects. Then, specimens 10 mm in thickness were cut to produce sections A and B. Cubic samples of size 1 cm^3 were cut from section B and section A for chemical composition (indicated by number 1 in the right diagram in Figure 3.2) and microstructure analysis (indicated by number 2). The microstructure samples were also used for hardness testing. The samples for XRD study of the as cast tool steels were taken from the middle top of the ingot (section B), adjacent to the samples for microstructure analysis. The remaining part of section B was used for conventional heat treatment samples with dimension 1 cm^3. The body of each ingot was used to prepare samples for axisymmetric compression. The chemical composition of each ingot was determined by XRF at the Sheffield Testing laboratories Ltd. The compositions of the tool steels are given in Tables 3.1 and 3.2.

Table 3.1 Chemical composition of the H21 tool steels (wt%).

Tool steels		C	Mn	Si	Cr	Ni	W	V	P	S	Co	Mo
H21 (1)	top	0.24	0.25	0.33	3.18	0.30	7.70	0.43	0.023	0.022	<0.02	<0.02
	bottom	0.27	0.25	0.32	3.13	0.30	7.43	0.42	0.028	0.022	<0.02	<0.02
H21 (2)	top	0.30	0.34	0.44	4.28	0.40	10.09	0.55	0.025	0.028	<0.02	<0.02
	bottom	0.33	0.34	0.43	4.31	0.42	10.12	0.56	0.028	0.034	<0.02	<0.02

Table 3.2 Chemical composition of the H23 tool steels (wt%).

Tool steel		C	Mn	Si	Cr	Ni	W	V	P	S	Co	Mo
H23 (1)	top	0.31	0.37	0.49	11.95	0.38	12.36	1.14	0.013	0.022	<0.02	<0.02
	Bottom	0.36	0.38	0.51	12.24	0.41	12.81	1.18	0.015	0.026	<0.02	<0.02
H23 (2)	top	0.33	0.36	0.49	12.35	0.40	12.30	1.16	0.014	0.029	<0.02	<0.02
	bottom	0.36	0.36	0.49	12.33	0.40	12.47	1.16	0.014	0.032	<0.02	<0.02

There were differences in the chemical compositions of the two ingots of the H21 tool steel for the C, Cr, Ni and W content. Both ingots of the H23 tool steel had very similar composition. Compared with the standard chemical compositions of the H21 and H23 grade tool steels in Table 2.2, some alloying elements were not in the range of the AISI standard; this is highlighted by shading in Tables 3.1 and 3.2. For example, the C and W contents in the first H21 ingot were lower than the standard and the Cr, Ni and W contents in the second H21 ingot were higher than the standard. In the H23 tool steel, the Ni content in both ingots and the W content in the first ingot were higher than the standard.

3.2 The Experimental Processes

The experimental processes in this research were hot deformation followed by double tempering, and conventional heat treatment, with a major focus of the research on the H21 tool steel regarding its hot deformation followed by double tempering. The flow chart of the processes can be seen in Figure 3.3.

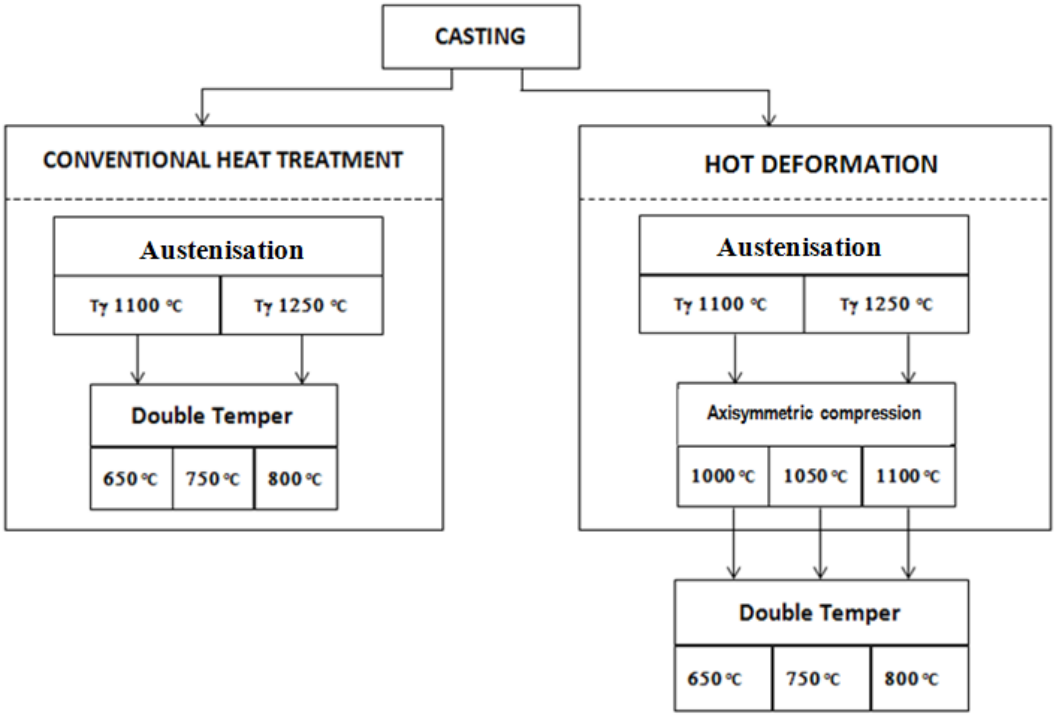

Figure 3.3 Flow chart of experimental processes.

The tool steel to proceed to double tempering after hot deformation was selected based on the hardness data.

3.2.1 Hot Deformation and Double Tempering Process

The investigation of hot deformation required a technique that can simulate the stresses experienced during forging under a range of conditions thus, a high axisymmetric compression test was chosen. Double tempering was selected to improve the toughness and thermal stability of the microstructure, which would not be achieved by single tempering due to the high alloying element content in the two tool steels. A schematic diagram showing the hot deformation and double tempering process can be seen in Figure 3.4.

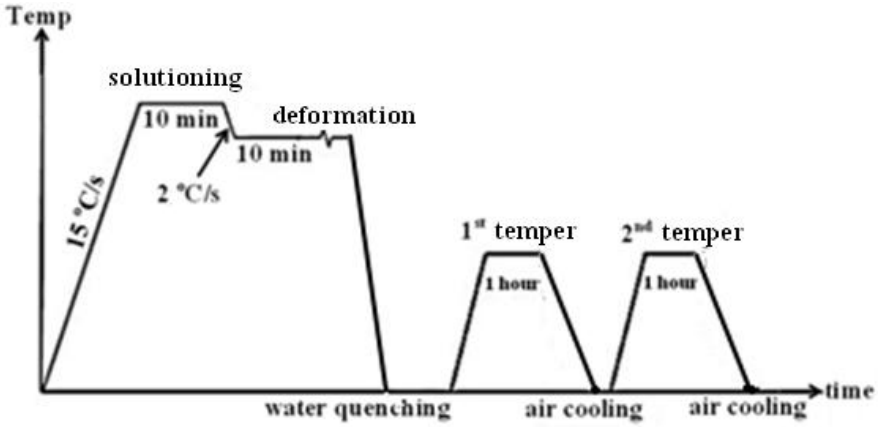

Figure 3.4 Schematic diagram of high axisymmetric compression and double tempering process.

3.2.1.1 Preparation of Axisymmetric Compression Sample

The axisymmetric compression samples were machined in the Ashmark Company in Sheffield. The position of axisymmetric samples taken from the body of ingot can be seen in Figure 3.5. The specification of the axisymmetric sample is shown in Figure 3.6. The sample was machined with thermocouple holes of 1.1 mm in diameter in the middle and 5 mm in depth for monitoring the temperature during deformation.

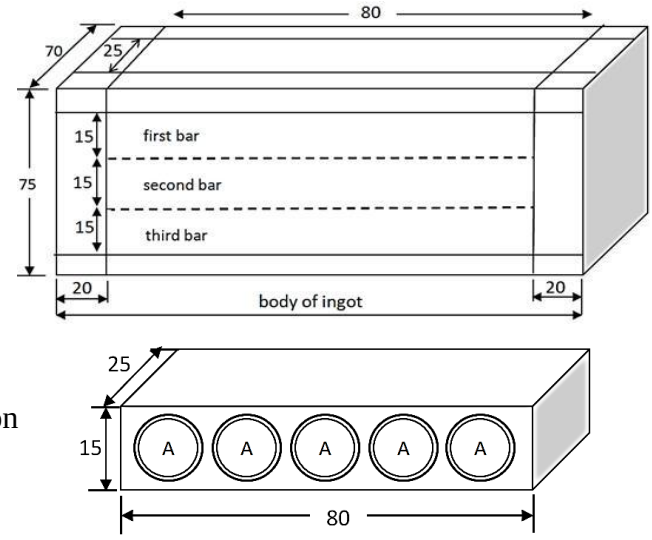

Bar dimension

Figure 3.5 Schematic illustration of the ingot body showing the location of the axisymmetric compression samples produced (indicated by A). Dimensions in mm.

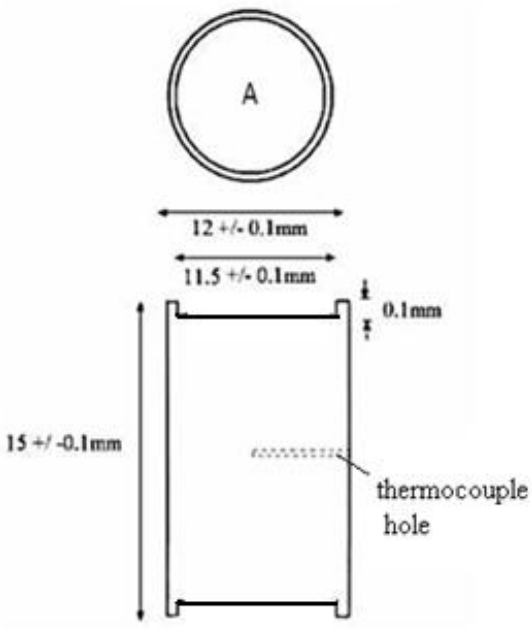

Figure 3.6 Specification of axisymmetric compression sample.

The body of ingot was divided into 3 bars and each bar produced 5 axisymmetric compression samples (indicated by A in Figure 3.5). The planned total number of axisymmetric samples for each of the H21 and H23 tool steels was 30. The number of valid axisymmetric compression samples from each ingot of tool steel was 10 due to casting defects in the body of each ingot. Figure 3.7 shows casting defects found in some axisymmetric samples and Figure 3.8 shows some axisymmetric samples without defects.

Figures 3.7 Casting defects found in axisymmetric compression samples.

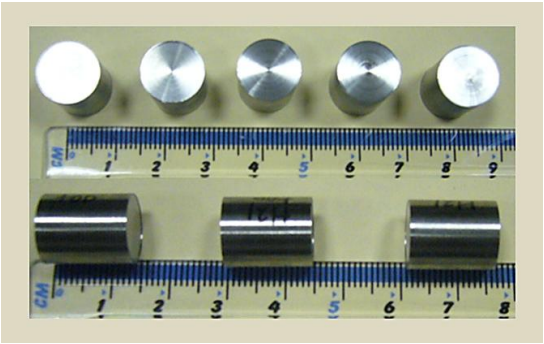

Figure 3.8 Some axisymmetric compression samples without visible casting defects.

3.2.1.2 High Axisymmetric Compression Tests

The high axisymmetric compressions tests were carried out on a SERVOTEST thermomechanical compression (TMC) machine available in the Institute for Microstructural and Mechanical Process Engineering The University of Sheffield – IMMPETUS, see Figure 3.9. The specification of the TMC machine is given in Table 3.3.

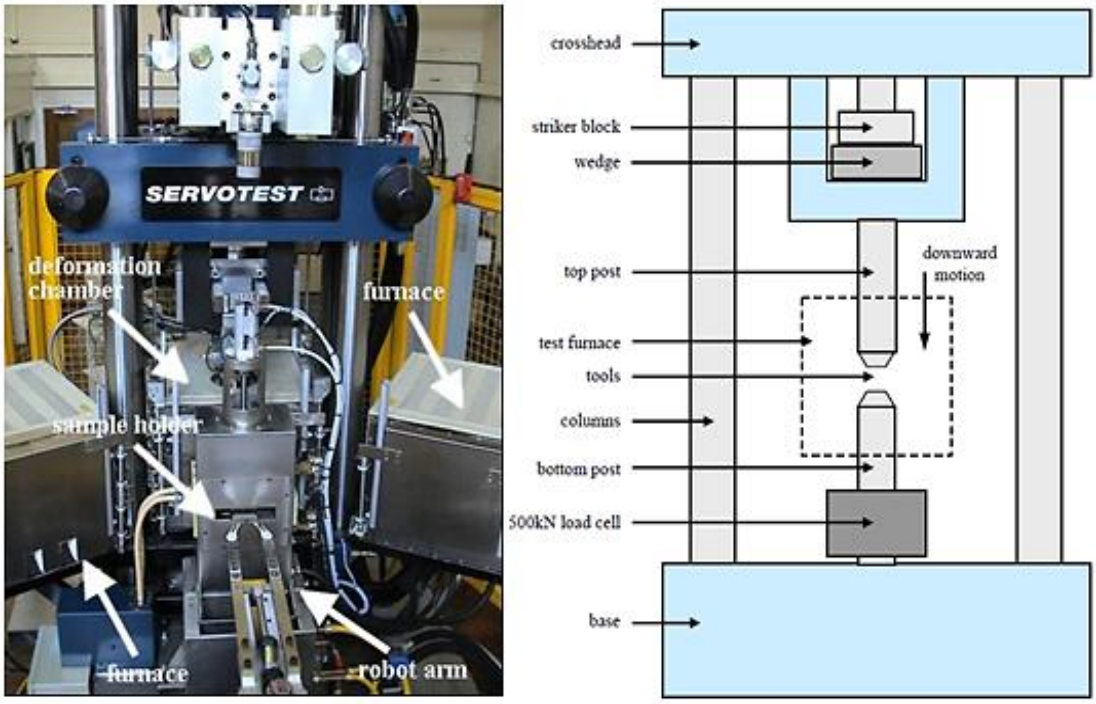

Figure 3.9 The TMC machine (left) and a schematic diagram of this machine (Hinton, 2006).

Table 3.3 Specification of the TMC machine of IMMPETUS.

Items	Machine Characteristics
Actuators	Servo hydraulic
Max strain	~ 2
Max strain rate	150 – 200 s^{-1}
Max temperature	1200 °C
Max load	500 kN
Quench	Either air/water cooled/quenched
Controllable variables	Load, displacement
Atmosphere control	None (air)
Temperature measurement	Up to 3 thermocouples in sample

The TMC machine records the load, displacement and temperature data, and can deform material at a constant true strain rate. The output data is produced as computer text files and must be changed in excel format for data processing.

Prior to high axisymmetric compression test, the top and bottom surface of the undeformed sample were lubricated with boron nitride lubricant (Lord and Loveday, 2001) to reduce the friction between sample and the anvil tool. A thermocouple was inserted in the centre of the sample, see Figure 3.6. The deformation temperature, true strain and strain rate were chosen, based on a combination of earlier investigations on tool steels and industrial heat treatment data. The testing schedule for high axisymmetric compression test can be seen in Figure 3.10.

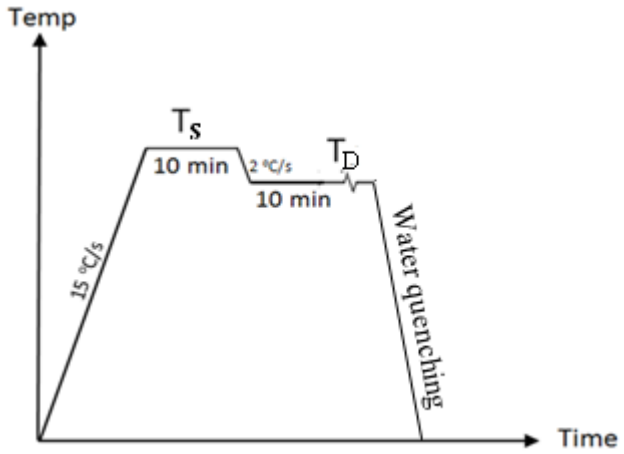

Figure 3.10 Schedule of high axisymmetric compression test.

The samples were heated up to the solutioning temperature (T_S) with rate 15 $^oC/s$ and then held at that temperature for 10 minutes for equilibration. Two solutioning temperatures was chosen, namely, 1100 ^oC and 1250 ^oC. Afterwards, the samples were cooled to the respective deformation temperature (T_D) at a rate 2 $^oC/s$ and held for 10 minutes, and then deformed to a true equivalent strain of 0.5 at a constant true strain rate of 0.01 s^{-1} followed by water quenching. The deformation was done at 3 different temperatures, namely 1000, 1050 and 1100 ^oC with solutioning temperatures 1100 and 1250 ^oC, respectively. Even though both grades of the investigated tool steels are not recommended to water quench (Roberts *et al.*, 1998), the samples were water quenched immediately on completion of the hot deformation in order to keep the deformed microstructure.

3.2.1.3 Validity Test

Roebuck *et al* (2006) reported the parameters to be measured to declare that a compression test is valid. The validity parameters are the barrelling coefficient (B), the aspect ratio (D_R) and the height coefficient (H). Barrelling is caused by friction at the sample tool interface and by temperature gradient in the specimen, and H indicates the parallelism of sample deformation. The formulae for the validity parameters are:

$$\text{Aspect ratio} = D_R = \frac{h_o}{d_o} \tag{3.1}$$

$$\text{Barrelling coefficient} = B = \frac{h_f {d_f}^2}{h_o {d_o}^2} \tag{3.2}$$

$$\text{Height coefficient} = H = \frac{Sh_f}{h_f} \tag{3.3}$$

where h_o and d_o are the height and diameter of the undeformed sample and h_f and d_f are the height and diameter of the deformed sample, Sh_f is the standard deviation of four measurements of the final height.

Before measuring the aforementioned dimensions, the deformed sample was cleaned to remove dried lubricant and scale. The height of the test piece was measured at the centre and at three points of the deformed sample and the diameter was measured at four different positions, as can be seen in Figure 3.11.

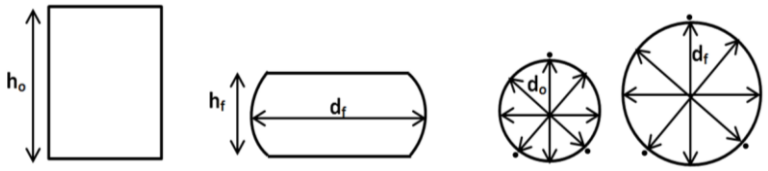

Figure 3.11 The positions for measuring parameters for the validity of an axisymmetric compression test (Roebuck *et al.*, 2006**)**.

The recommended value for aspect ratio is 1.5, but any value in the range 1-2 can be used. The recommendation for measured barrelling coefficient is maximum 1.10 and valid H must be below 0.04. The test is invalid if the validity parameters do not satisfy the recommended values.

3.2.1.4 Processing Raw Data of High Axisymmetric Compression Test

During compression test a large amount of data is logged in the computer. To process the raw data, the following steps were followed:

a. Sample measurement

The initial and final measurements of the sample thickness were measured as described in section 3.2.1.3. The initial height of the sample was corrected for linear thermal expansion using the following equation:

$$h_c = h_o + \alpha_1 h_c (T_D - T_o) \quad (3.4)$$

where h_c is the initial height of the sample corrected for thermal expansion, h_o is initial height, and α_1 is coefficient of linear thermal expansion of hot work tool steels (13.9×10^{-6} /^{o}C) (Roberts *et al.*, 1998), which is assumed to be constant in the temperature range. T_D is the deformation temperature and T_o is the room temperature (both temperatures are in degree Kelvin).

b. Zero error and machine compliance

The machine recorded the displacement data relative to the tool position. The displacement data needs to be converted to an instantaneous height by subtracting the displacement from the initial height. Figure 3.12 shows that when the load started to increase, which indicated there was a contact between the tool and sample, the displacement was not exactly in the zero position due to having discrepancy in the positions of tools and in addition the change of the sample's thickness owing to the lubricant. Hence, there is an error and a correction was applied to the raw data by adjusting the recorded ram displacement to the zero position. Figure 3.12 shows the load versus displacement before and after correction.

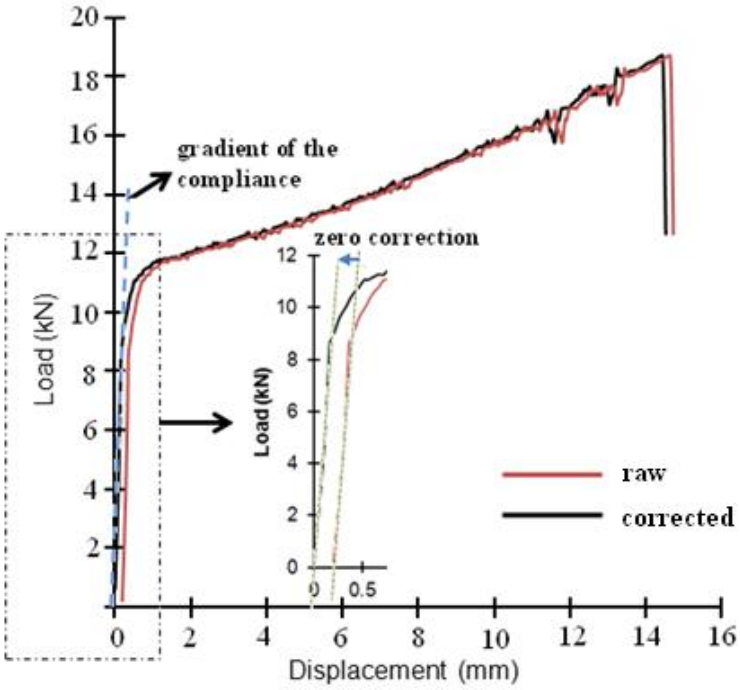

Figure 3.12 Load vs displacement before and after correction taken from data of the H21 tool steel for T_S = 1100 ^oC and T_D = 1000 ^oC.

Figure 3.12 also shows that in the early stage the load-displacement graph was slightly linear because of the compliance of the machine. As the concern of these tests is only plastic deformation, therefore the linear region needs to be removed. The machine compliance (the gradient of the load vs displacement curve, indicated by the blue dashed line in Figure 3.12) was measured by subtracting from the data to correct the displacement data at the beginning of the deformation.

c. Calculation of the pressure and true strain

The mean pressure (P) and true strain (ε) values were calculated using the following formulae:

$$\varepsilon = \ln \frac{h}{h_o} \tag{3.5}$$

$$P = \frac{F}{A} \tag{3.6}$$

where F is the applied load, A is the instantaneous cross sectional area and is calculated from the instantaneous height (h), and instantaneous diameter assuming a constant volume and that no barrelling of the sample had occurred.

d. Friction corrections

Ideally, the metal forming process should involve smooth and frictionless dies. However, in reality, the friction between die and sample surfaces is unavoidable and leads to scratches on the die surface, and inconsistency in the formed sample. The effects of surface roughness can be reduced by lubrication. The chosen friction coefficient (μ) value was 0.25 and was used to determine the equivalent isothermal flow-stress by reasoning that the change in the flow stress and the overall shape of flow curve did not vary greatly for μ value between 0.20 to 0.30, as can be seen in Figure 3.13.

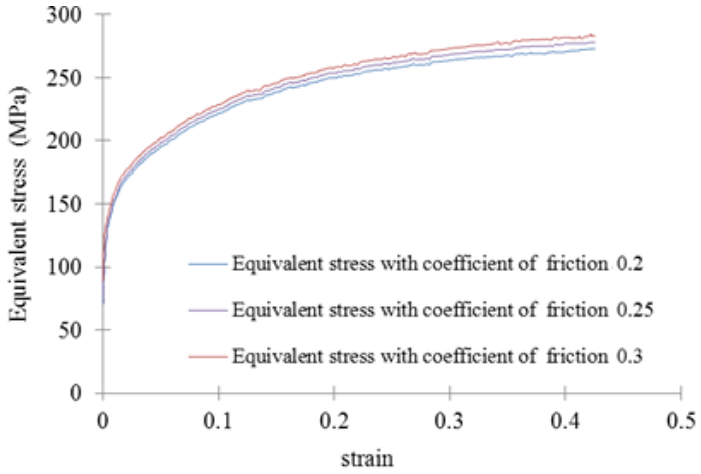

Figure 3.13 Effect of the friction coefficient on isothermal flow stress taken from data of the H21 tool steel for solutioning temperature (T_S) = 1100 ^oC and deformation temperature (T_D) = 1000 ^oC.

e. Deformational heating

The limited number of valid samples forced us to focus the axisymmetric compression test only on one value of strain rate for different deformation and solutioning temperatures and thus, the activation energy for hot deformation, Q_{def}, of the investigated material could not be calculated. To get an overview of the flow curve behaviour and to correct for the effects of deformational heating, the flow stress was calculated using Q_{def} = 607 kJ/mol, which was taken from Fajfar *et al* (2010) taking into account the similar hot working condition, chemical composition of steel and volume fraction of carbides.

The temperature correction arises from the fact that the sample temperature changes during deformation because of the work of deformation. The temperature corrected stress σ_{corr} (MPa) was calculated using the equation 3.7, which is derived from the exponential law, see equation 2.15 (Davenport *et al.*, 2000):

$$\sigma_{corr} = \sigma_1 + \frac{Q_{def}}{\beta R}\left(\frac{1}{T_2} - \frac{1}{T_1}\right) \tag{3.7}$$

where σ_1 is the uncorrected stress (MPa), Q_{def} is the activation energy for hot deformation (kJ/mol), R is the universal gas constant (8.314 J/mol/K), T_1 is the instantaneous temperature (in degree Kelvin), T_2 is the nominal test temperature (in degree Kelvin) and β = 0.03 MPa^{-1} (Fajfar *et al.*, 2010).

The procedure for the processing of the raw data is summarised in the Figure 3.14.

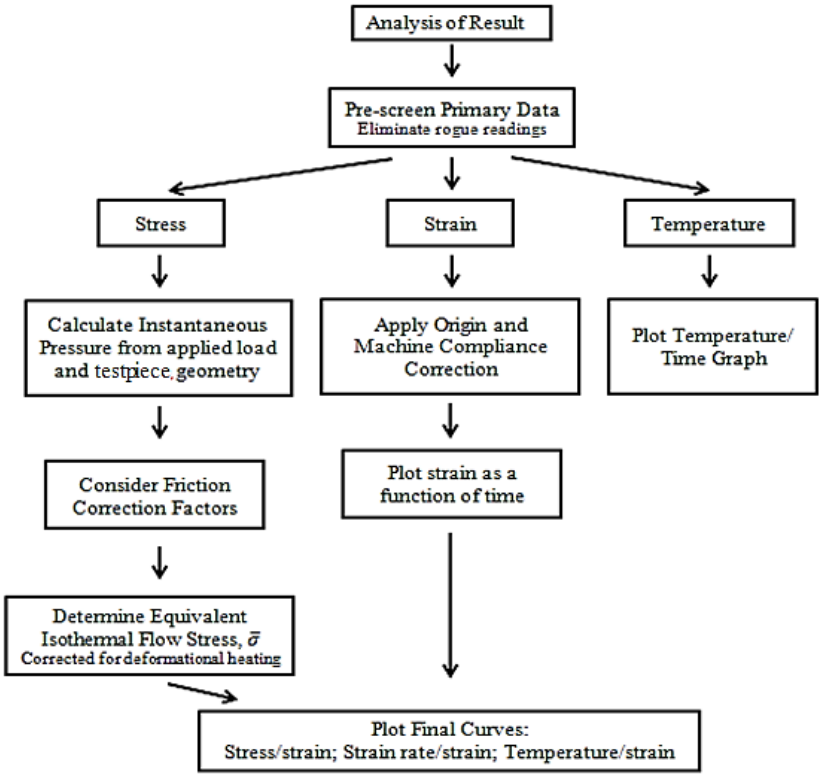

Figure 3.14 Flow chart of processing high temperature axisymmetric compression data (Roebuck *et al.*, 2006).

As mentioned before, in this study the hot compression tests were only performed on one value of strain rate for different deformation and solutioning temperatures, and therefore the plot of strain rate vs strain and temperature vs strain were not made.

3.2.2 Double Tempering Process after Hot Deformation

After hot deformation, the tool steel to proceed to double tempering was selected on the basis of hardness data. The deformed samples of the selected tool steel were cut along the longitudinal compression axes into 4 sections using Isomet 5000 and three of them were prepared for double tempering, and one was used for microstructural analysis, XRD and hardness testing. The sectioning of deformed samples is illustrated in Figure 3.15:

1: for microstructural analysis, XRD and hardness
2,3,4: prepared for double tempering process

Figure 3.15 The sectioning of deformed samples for microstructure and hardness analysis after deformation and double tempering (left) and the investigated area for microstructural analysis, XRD and hardness (right).

The double tempering was carried out isothermally at 650, 750 and 800 ^{o}C with holding time of one hour for the first and second temper respectively, and air cooling in between the first and second tempering.

3.2.3 Conventional Heat Treatment

The conventional heat treatment was hardening and double tempering process with the same parameter as in the hot deformation process. The heat treatment process was carried out using a muffle furnace. The data was collected for comparison purpose to observe the effect of hot deformation on microstructure changes and hardness behaviour. The schedule for conventional heat treatment can be seen in Figure 3.16.

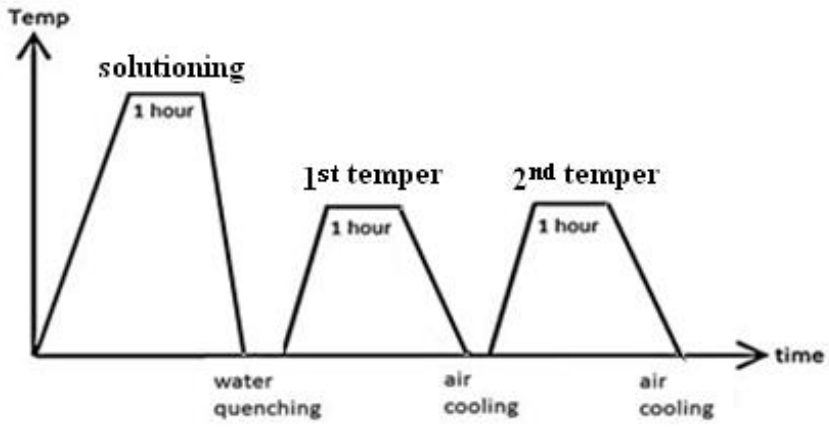

Figure 3.16 Schedule of conventional heat treatment.

For hardening, the samples were austenised at 1100 ^{o}C and 1250 ^{o}C in a furnace with holding time of 1 hour at each temperature, using argon atmosphere and followed by water quenching. Afterwards, double tempering was carried out isothermally at 650, 750 and 800 ^{o}C for 1 hour holding time at each temperature with air cooling in between the first and second tempering. The selected tempering temperature (650 ^{o}C) corresponds to maximum temperature expected in use (Roberts *et al.*, 1998). The two higher tempering temperatures (750 ^{o}C and 800 ^{o}C) were selected to increase the toughness of the tool steels.

3.3 Characterisation of Microstructure

The techniques used to study the evolution of microstructure were optical microscopy, scanning electron microscopy (SEM) and transmission electron microscopy (TEM). Both electron microscopes were equipped with EDS. The analysis of microstructure included measurements of grain size, carbide volume fraction and carbide mean size.

3.3.1 Sample Preparation for Optical Microscopy and SEM

Samples for optical microscopy were also used for scanning electron microscopy. They were mounted in conductive bakelite with the height of the mounting not more than 2 cm. Samples were grinded using manual grinding on silicon carbide papers gradually, starting from grit number 100, and followed by numbers 200, 400, 800 and 1200 under running water. Afterwards the samples were polished using diamond paste 6 μm and 1 μm and water based lubricant.

Several etchants with varying etching time and temperature were used due to difficulties with getting clear images and to reveal prior austenite grain boundaries for the heat treated and hot deformed conditions in the H21 tool steel. The preferred etchant to reveal the microstructure of the H21 tool steel was 5 % picral plus 2 % HCl and some drops of Teepol. The etching time was 20-30 seconds, due to the

etchant's quick response, and gave the most clear images. The prior austenite grain boundaries could be revealed only in some areas and experimental condition, compared with other etchants (Schafmeister's, Villelas, Nital 5 %, Picral 5 %, Ralph's, and Kalling No 2). The etchant used for the H23 tool steel was Groesbeck's (100 ml H_2O, 10 g NaOH, and 10 g $KMnO_4$) with etching time 5 – 10 seconds, showing clearly the carbides and the matrix. After etching, the samples were rinsed immediately with plenty of water and ethanol, and dried.

3.3.2 Optical Microscopy

Optical microscopy was used to provide qualitative and quantitative descriptions of microstructural evolution, before continuing to electron microscopy or nanoindentation at higher magnification. The images were also used for quantitative analysis of grain size, volume fraction of carbides and carbide mean size. Optical microscopy was carried out on a MET Polyvar microscope and images were taken at various magnifications.

3.3.3 Scanning Electron Microscopy

The optical microscopy samples were also used for SEM analysis. The SEM investigation was conducted on a JEOL 6400 that was operated at 20 kV and equipped with EDS and INCA software for chemical analysis. An Inspect F SEM was also used for some samples to show microstructural features at higher magnification (up to 80,000x). Secondary electron imaging in the SEM was used to show general microstructural features. The back-scatter mode in SEM was used to visualize the carbides via atomic number contrast. Quantitative chemical analysis was performed on JEOL 6400.

3.3.4 Transmission Electron Microscopy

The TEM was used for some sample conditions. The TEM study was performed mainly on a Philips 420 microscope operated at 120 kV and on a JEOL 2010F microscope operated at 200 kV. Both microscopes were equipped with an EDS

system. Selected area diffraction was used occasionally to identify the carbides and matrix. Qualitative EDS was applied to identify some carbides. The bright field and dark field imaging techniques were used to observe details of microstructures.

3.3.4.1 Sample Preparation for TEM Investigations

Two types of samples were examined using TEM, namely, thin foils and carbon extraction replicas.

a. Carbon extraction replicas

Optical microscopy samples were used to prepare carbon extraction replicas. Extraction replicas of carbides were obtained by etching the mirror polished sample surface with the same etchant used for optical microscopy and then coating the surface with a carbon thin layer using an Edwards speed device carbon coating machine operated at vacuum < $5x10^{-5}$ Torr. After carbon coating, the surface of bakelite was painted using Lacomite Varnish. The carbon coated samples were scratched using scalpel to form 2 mm squares. The replicas were stripped from the surface of samples by electrolytic etching using potential of approximately 30V and then immersed in methanol at an angle so that the carbon layers could lift off the sample. The carbon films were collected onto copper grids and dried on the filter paper. The electrolytic etching solution was 10 % Nital for the H21 tool steel and Villella's solution containing 1gr picric acid + 5 ml HCl + 100 ml ethanol for the H23 tool steel.

b. Thin foils

Thin foil samples were produced for microstructural study of the matrix and fine carbides. Samples 1 mm thick were cut from the optical microscopy samples using Isomet. Afterwards, they were mechanically grinded on silicon carbide papers to a thickness below 500 μm, and finished at 1200 grit. Samples were punched to make 3 mm diameter discs and continued to be manually grinded to a thickness of around 60 to 80 μm. The discs were then thinned by twin-jet electro polishing using a solution of 5 % perchloric acid, 35 % butoxyethanol and 65 % methanol. Operating conditions varied, but were nominally as follows: temperature between – 50 up to -

40 °C using liquid nitrogen, sensitivity 7-8, and operating current 30-35 mA. Foils were washed in methanol and stored in a glass bottle containing methanol prior to examination by TEM.

3.3.5 Quantitative Metallography

a. Carbide size and volume fraction of carbides

The average diameter and the volume fraction of the carbides (V_c) were measured in every condition using ImageJ software without carbide differentiation or type by type. Average equivalent diameters of the carbides were calculated by the length of the major and minor axes. More than 500 carbides for every condition were quantified to ensure reliability of the measurements. At least, a total of 6 optical and SEM images in different locations of each sample condition were taken to obtain representative measurements. Those images for measuring carbide size were also used for measuring the volume fraction of carbide. The distribution of carbides smaller than 0.1 μm was not calculated. An example of carbide size and volume fraction of carbide measurement using imageJ software is given in Figure 3.17.

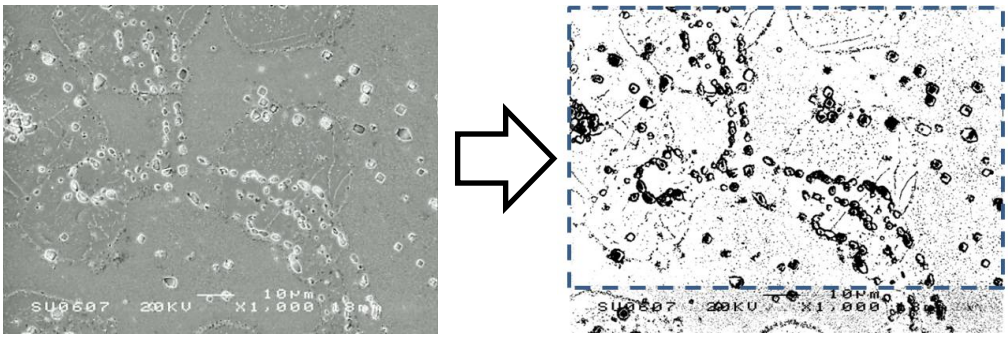

a.Secondary electron SEM image b.binary image (using ImageJ software)

Quantitative results using imageJ software

Count of measured carbides	Average carbide size (μm)	V_c (%)
677	0.3	12.3

Figure 3.17 Example showing carbide size measured in a binary image. The area measured for carbide quantitative analaysis is indicated by the dashed line.

b. Grain size

The grain size was measured using the mean linear intercept method (Higginson and Sellars, 2003) based on optical microscopy images. A line was drawn on the image and the number of grain boundaries which intercept a linear traverse of length were counted. A total of 6 optical images were measured for each sample and the total numbers of lines was 10 for each image. The mean linear intercept grain size (L_L) was obtained using the following equation:

$$L_L = \frac{L_T}{P} \tag{3.8}$$

$$S(L_L) = \frac{S}{\sqrt{n}} \tag{3.9}$$

$$\mu = L_L \pm (t_{95,n-1})\, S(L_L) \tag{3.10}$$

where:

L_T : the total length of the test lines

P : the total number of grain boundary intersections

n : the total number of lines

s : the standard deviation

$S(L_L)$: the standard error

C_L : Equal to $(t_{95,n-1})\, S(L_L)$ is the 95 % confidence limit on the value of the true population mean and the value of $(t_{95,n-1})$ is 2.0 for n=10

μ : to express the 95 % confidence limits on the value of the true population

Decolnet *et al* (2001) and Launeau and Robin (1996) reported that the grain size can be measured using the intercept method even when the grain boundaries are partially decorated by carbides. In this work the grain size was measured on binary images using the intercept method to produce an average intercept length inside grains, which was the average of intercept lengths measured at 0 and 90 degrees for each image, see Figure 3.18.

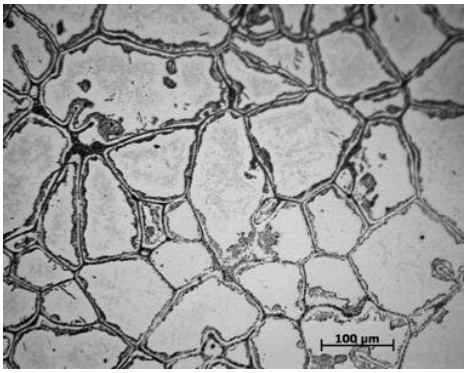

a.An optical image of the H23 tool steel.

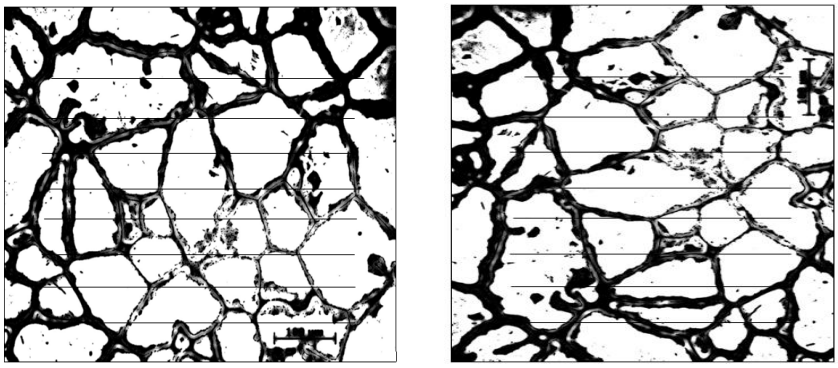

0^o position 90^o position

b. binary image using ImageJ software.

Figure 3.18 Example showing average intercept length measured inside grains in a binary image (indicated by lines in b), using the linear intercept method.

3.4 X-ray Diffraction

XRD was used to confirm the phase and carbide formation in the tool steels. The samples used for XRD analysis were the optical microscopy samples without bakelite mounting. All phases have a specific diffraction pattern. The Bragg law was used to calculate the d-spacing for different diffraction analysis:

$$\lambda = 2\, d \sin\theta \tag{3.11}$$

where λ is the wavelength of the x-rays, d is the lattice spacing and θ is the angle of reflection.

A Siemens D5000 diffractometer and Co radiation were used to obtain the X-ray diffraction patterns. The samples were scanned from 2θ angles ranging from 30^o through to 130^o. The patterns were achieved using step size of 0.02^o and a counting time 1^o per minute. The peaks were identified using the STOE WinXPow software program and the ICDD (International Centre for Diffraction Data) files.

Quantitative XRD analysis was used to calculate the volume fraction of retained austenite and ferrite after quenching based on ASTM E975-03 (2003). The formulae used to determine the volume fraction of retained austenite are given below.

$$V_\alpha + V_\gamma + V_c = 1 \tag{3.12}$$

$$V_\gamma = [(1 - V_c)]\left[\frac{(I_\gamma/R_\gamma)}{(I_\alpha/R_\alpha) + (I_\gamma/R_\gamma)}\right] \tag{3.13}$$

$$V_\gamma = [(1 - V_c)]\left(1/q\sum_{j=1}^{q}\left(I_{\gamma j}/R_{\gamma j} \Big/ 1/P\sum_{i=1}^{p} I_{\alpha i}/R_{\alpha i}\right) + 1/q\sum_{j=1}^{q}\left(I_{\gamma j}/R_{\gamma j}\right)\right) \tag{3.14}$$

where:

V_c, V_α and V_γ	the volume fraction of carbides, ferrite, and austenite, respectively
q and p	the numbers of austenite and ferrite diffraction peaks, respectively
j and i	the j^{th} and the i^{th} peak of austenite and ferrite, respectively
I_γ and I_α	the integrated peak intensities of each austenite or ferrite diffraction peak, which is equal to the area under the peak above the background
R_γ and R_α	the reflection factors of the austenite and ferrite peaks, respectively and these can be found in ASTM E975-03 (2003).

The volume fraction of carbides and the integrated peak intensities in this study were measured using ImageJ software.

3.5 Hardness Test

The hardness of all samples was measured at room temperature. The optical microscope samples were used for hardness testing. The Vickers hardness measurement was performed with 10 kg load and 15 s dwell time. At least six measurements per sample were made to calculate mean values and standard deviations.

Nano hardness (H) test were carried out using optical microscope samples to observe the heterogeneous microstructure in submicron scale. The test was performed using a Triboscope (Hysitron Inc.). A standard 142.35^{o} Berkovich indenter was employed and a load of 2000 μN was applied with a 5 s upload, a 5 s hold and a 5 s download at constant strain rate. The nanohardness was calculated using the following equation (Oliver and Pharr, 1992) :

$$H = \frac{P_{max}}{A} \tag{3.15}$$

where P_{max} is the maximum load, and A is the projected contact area.

3.6 Thermodynamic Calculations

The ThermoCalc software was used to calculate phase diagrams of both investigated tool steels using the TCEF6 database. The calculations provided data about the phase stability and the equilibrium dissolution temperature of carbides. The calculations were made in the temperature range 600 to 1500 ºC with constant pressure 101,325 Pa. The phases obtained from the experimental study were compared with the predictions of the ThermoCalc software.

Chapter 4
The Microstructures of
The As Cast H21 and H23 Tool Steels

4.1 Introduction

The solidification of tool steels can be complex due to the number and concentration of alloying elements. Casting defects and segregation are not uncommon. The properties of tool steels are usually determined by the type, distribution and size of carbides, which are closely related to the complex carbide pattern in the as-cast structure. Therefore, it is important to understand the solidification behaviour of tool steels as the type and morphology of carbides that form during casting affects the mechanical properties of the tool steels.

In this chapter, the formation, type, morphology and chemical composition of carbides in the cast H21 and H23 tool steels are discussed and the results were compared with predictions made using ThermoCalc software.

4.2 Grain Structure and Casting Defects

The as cast microstructures of both tool steels were coarse. The microstructure of the as cast H21 tool steel consisted of ferrite matrix and primary M_6C carbides that formed along grain boundaries. The microstructure of the as cast H23 tool steel consisted of ferrite matrix, primary M_6C carbides at grain boundaries and inside the grains. Figures 4.1 and 4.2 show optical images of the as cast H21 and H23 tool steels.

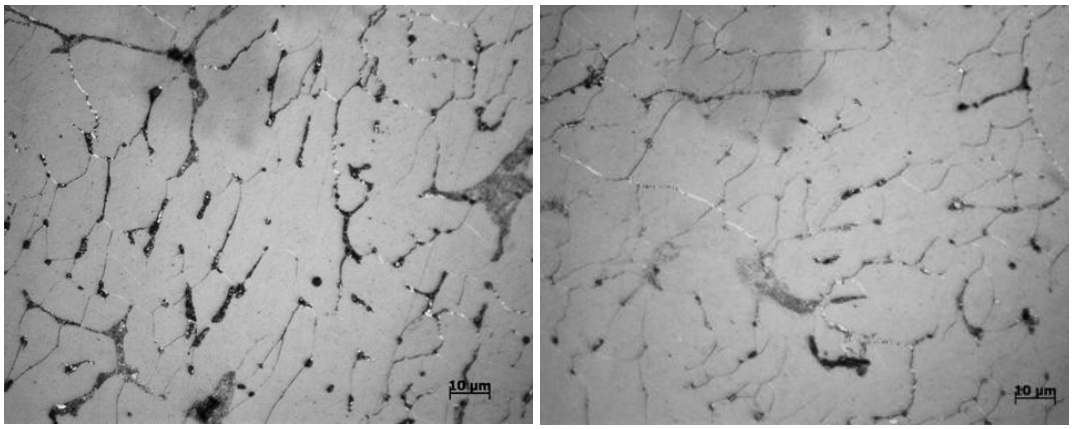

Figure 4.1 Optical images of the as cast H21 tool steel taken from sections A (left) and B (right) of ingot (see also Figure 3.2).

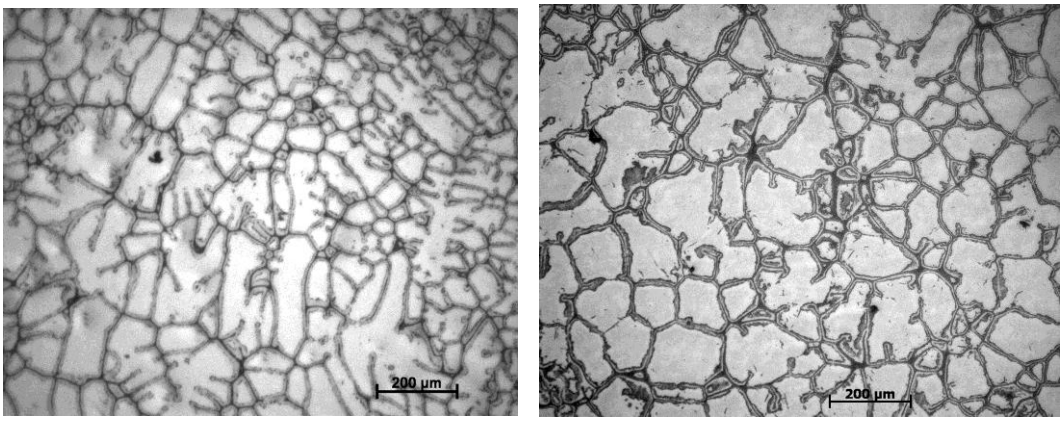

Figure 4.2 Optical images of the as cast H23 tool steel taken from sections A (left) and B (right) of ingot (see also Figure 3.2).

Figures 4.1 and 4.2 show that the grain structure in the sections B was more equiaxed compared with the grain structure in sections A. Therefore, the ingots had heterogeneous grain structures. Soon after pouring the melt into the mould, nuclei formed heterogeneously on the walls of the mould and began to grow into the melt. Crystals continued to grow dendritically and perpendicular to the mould walls and developed the columnar grains (Porter and Easterling, 2004). In the centre of the ingot the temperature was still high. Dendrite arms that were not completely melted, acted as nuclei and produced equiaxed grains in the centre of the ingot. The equiaxed grain structure in sections B would suggest that this section was in the equiaxed zone with randomly oriented grains. Sections A were in the columnar

regions near the bottom of the ingot. All ingots showed solidification shrinkage with a deep central cavity or pipe forming at the top, see Figure 3.1, due to insufficient feed metal during casting. The grain size of as cast tool steels was measured as described in section 3.3.5b using images taken from sections B and is given in Table 4.1 for the as cast H21 and H23 tool steels.

Table 4.11 Grain sizes of the as cast H21 and H23 tool steels.[1]

Tool steel	Position[2]	Total length, L_T, (μm)	*P*	L_L (μm)	$S(L_L)$	C_L	μ (μm)
H21	0^o	69,469	1204	57.7	0.7	1.4	57.7 ± 1.4
	90^o	69,766	1062	65.7	1.0	2.0	65.7 ± 2.0
H23	0^o	95,481	1152	82.9	0.9	1.8	82.9 ± 1.8
	90^o	95,379	1102	86.6	0.9	1.8	86.6 ± 1.8

[1]See equations 3.8 and 3.9 for symbols
[2]See Figure 3.18b

4.3 X-ray Diffraction

The presence of ferrite and M_6C carbides in the as cast H21 and H23 tool steels was confirmed by XRD, as shown in Figure 4.3.

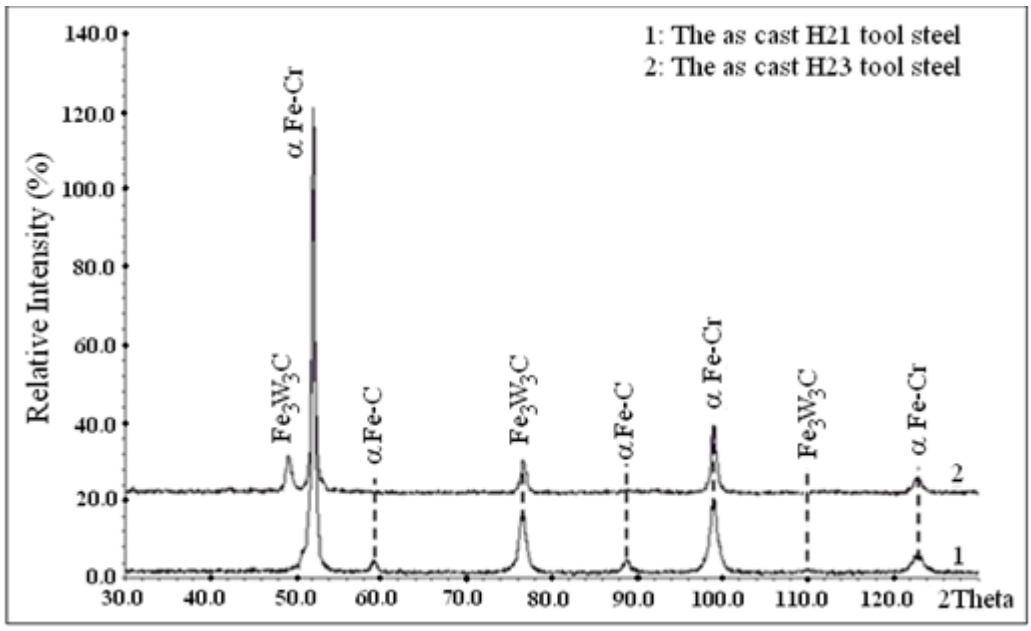

Figure 4.3 X-ray diffractograms of the as cast H21 and H23 tool steels.

The peak positions of α Fe-Cr, M_6C (Fe_3W_3C) carbides and Fe-C agreed well, respectively with the ICDD card numbers 34-396, 41-1351 and 52-512. No peaks of other carbide types were detected in both the as cast tool steels. The Fe-C and Fe–Cr peaks correspond to the solutioning of C and Cr in α-Fe.

4.4. Carbide Types in the Tool Steels

The carbides observed in the two tool steels of this study were (i) M_6C primary carbide that formed upon solidification in both tool steels and eutectoid M_6C carbide in the H23 tool steel (these were observed by SEM owing to their size), (ii) MC, which were present in the H21 and H23 tool steels and (iii) $M_{23}C_6$, which were present only in the H23 tool steel. The MC and $M_{23}C_6$ carbides were fine and were observed only by TEM. The following sections present and discuss data about the formation, size and chemistry of carbides using SEM-EDS and TEM (SADP, EDS).

To summarise, in the two tool steels the primary phase to form upon solidification was the delta ferrite and the first carbide to form (primary carbide) was the M_6C type. The MC and $M_{23}C_6$ carbide types formed from the liquid at a later stage. Using the terminology of the tool steel community the M_6C, MC and $M_{23}C_6$ carbides that were present in the cast tool steels will be also called primary carbide, to differentiate them from the carbides formed during subsequent heat treatment, which will be called secondary carbides.

4.5 The Distribution of Primary Carbides

The distribution of carbides in the solidified microstructure has a crucial influence on the properties of tool steels. Figure 4.4 shows secondary electron images of the as cast microstructures of the H21 and H23 tool steels**.**

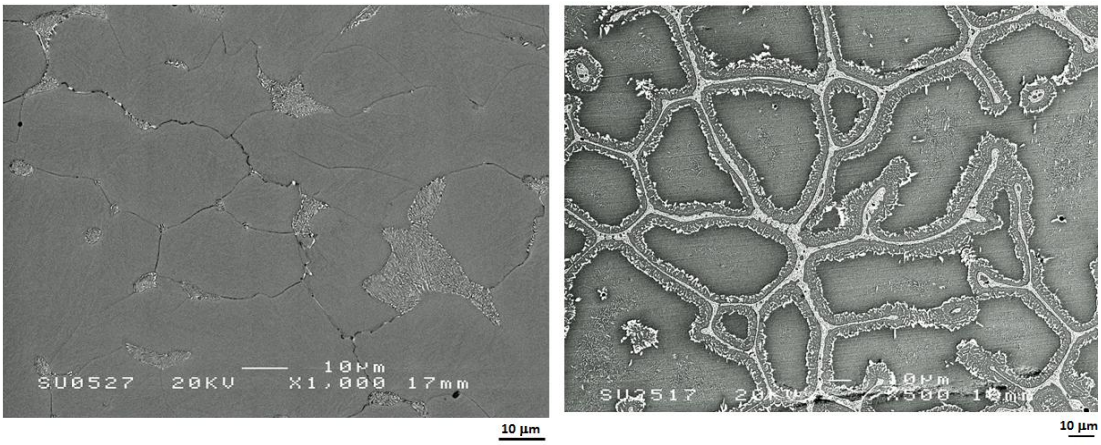

a. H21 tool steel b. H23 tool steel

Figure 4.4 SEM secondary electron images of the as cast H21 and H23 tool steels.

Figure 4.4a shows non-uniformly distributed carbides at the grain boundaries and triple junctions in the as cast H21 tool steel. No carbides inside the grains were observed by SEM. The ranking of various heterogeneous nucleation sites in order of increasing difficulty of nucleation is triple junctions, grain boundaries, inclusions, and dislocations (Zhao *et al.*, 2011, Fukino and Tsurekawa, 2008, Thewlis *et al.*, 1997, Speich *et al.*, 1984, Cahn, 1956). Therefore, the carbide formation preferentially at triple junctions and along grain boundaries occurred because of ease of nucleation at these sites compared with nucleation in the bulk of the grains as the diffusivity of C atoms is higher along grain boundaries than its volume diffusion.

On the contrary, in the as cast H23 tool steel although the carbides were predominantly formed along the grain boundaries and formed a continuous network, they were also formed inside the grains (Figure 4.4b). The formation and growth mechanism of the carbides were attributed to the alloying elements and solidification path of the H23 tool steel and will be discussed in Section 4.7.

4.6 Identification of Primary Carbides and Solidification Path of the As Cast H21 Tool Steel

4.6.1 Identification of Primary M_6C carbides

Figure 4.5 shows a SEM back scatter electron image of carbides and typical EDS spectra of matric and carbide in the as cast H21 tool steel.

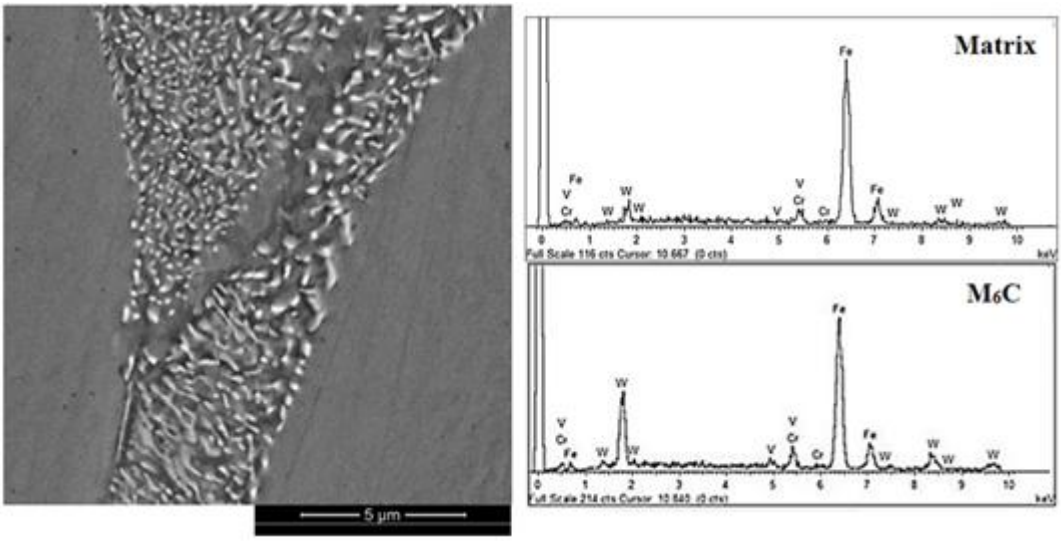

Figure 4.5 SEM back scatter electron image and typical EDS spectra of matrix and primary M_6C carbides of the as cast H21 tool steel (the black dots in the BSE image are cavities).

The accelerating voltage in EDS analysis controls the size of the interaction volume. The accelerating voltage for SEM-EDS analysis used in this study was 20 kV. The estimated dimensions of the interaction volume at 20 kV were ~ 1.1 µm in depth and ~ 0.9 µm in width, which means a spatial resolution of almost 1 µm for EDS analysis (Gharehbaghi, 2012, Wittke, 2008). The smaller the interaction volume the better the spatial resolution is. Hence, the quantitative data for the carbides should be considered with caution given their size due to interference of the interaction volume with the matrix. Table 4.2 shows the SEM-EDS analyses of the primary M_6C carbides and matrix of the steel.

Table 4.2 SEM-EDS data of the as cast H21 tool steel (wt%).

Tool steel	Phase	Element				Comment
		Fe	V	Cr	W	
H21	Matrix	86.2 ± 1.5	0.9 ± 0.3	4.1 ± 0.2	8.9 ± 1. 7	α^*
	Carbides	78.2 ± 7.8	1.0 ± 0.4	4.2 ± 0.4	16.6 ±7.3	M_6C

*see Figure 4.3

The SEM back scatter electron image in Figure 4.5 shows that there was only one type of carbide that exhibited white contrast (higher atomic number than the matrix). No other types of carbide were present, which should appear as black or grey areas (e.g. MC, M_7C_3 or $M_{23}C_6$ carbide). These carbides were identified by SEM-EDS as M_6C carbides with the typical EDS spectrum in Figure 4.5 showing the high W and Fe peaks and W content four times that of Cr. The primary M_6C carbides were rich in W and Fe. The morphology of the primary M_6C carbides in the as cast H21 tool steel was basically lamellar with very little or no interconnections between individual carbide platelets; there was neither a backbone at the center or carbide wall around the eutectic carbide-matrix interfaces, or the typical fishbone morphology of M_6C carbide. In general, the lamellar coarser carbides of rodlike, spherical and irregular morphologies (depending on sectioning) were M_6C carbides according to the XRD and SEM-EDS data. SEM-EDS analyses of the as cast H21 tool steel showed that the W, Cr, V and Fe content of the carbides and matrix were different (see Table 4.2). The quantitative data in Table 4.2 should be considered with caution given the size of the carbides. The mean size of the primary M_6C carbides of the as cast H21 tool steel was about 0.3 ±0.1 μm, and their % volume was 18.3 ± 2.2 %.

With respect to the M_6C carbide size, which is in the range 0.1 to 0.6 μm, interference between the interaction volume (~1 μm spatial resolution at 20 kV) and the matrix occurred when the carbides were analysed. Therefore, the analysis for the M_6C carbides could have slightly shifted to that of the matrix depending on the size of the carbides. The EDS result for the matrix was more accurate.

4.6.2 Identification of the Fine Primary Carbides

Figures 4.6 show fine carbides that were present in the as cast H21 tool steel. The carbides were identified by TEM as MC carbides having diameters between 5-10 nm.

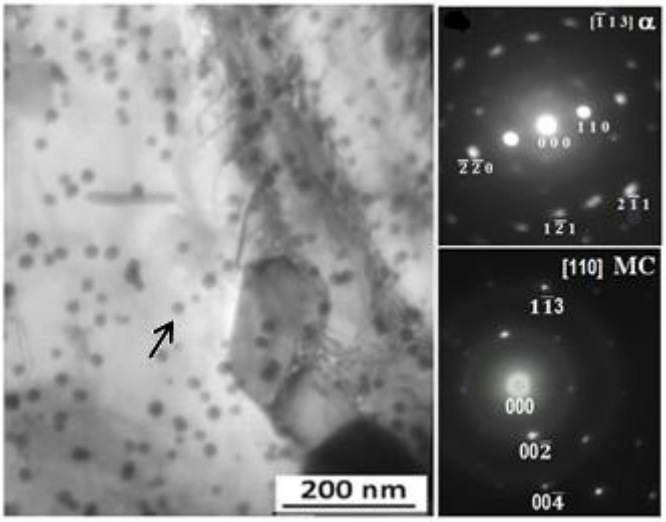

Figure 4.6 A bright field TEM image from thin foil showing the fine dispersed spherical MC carbides of the as cast H21 tool steel and SADPs of MC carbide (indicated by arrow) and matrix (ferrite).

Although, the V content in the H21 tool steel was low, the MC carbides formed due to V being a very strong carbide former. However, not all V was consumed in the formation of MC carbides. As shown in Table 4.2, V was present in the matrix of the as cast H21 tool steel.

4.6.3 Solidification Path of the H21 Tool Steel

Primary carbides in tool steels may have different morphologies, and different morphologies are produced by different growth mechanism, which is strongly affected by the solidification path and the chemical composition of the steel. The structure and carbide morphology at the concluding stages of solidification inherits all the features of the preceding phase transformations. ThermoCalc software was used to support the microstructural analyses. Because some of the alloying elements of the H21 tool steel were not in the range given in the AISI

standard (see Table 3.1), three isopleth phase diagrams with different chemical compositions of the investigated H21 tool steel were calculated to see what the effect of alloying elements to the equilibrium phase diagrams was namely:

a. Isopleth phase diagram taking into account four alloying elements, 0.3C – 3.2Cr – 7.6W – 0.4V (wt%), Figure 4.7.
b. Isopleth phase diagram taking into account six alloying elements, 0.3C – 0.25Mn – 3.2Cr – 0.3Ni – 7.6W – 0.4V (wt%), Figue 4.8
c. Isopleth phase diagram taking into account seven alloying elements, 0.3C – 0.25Mn – 0.3Si – 3.2Cr – 0.3Ni – 7.6W – 0.4V (wt%), Figure 4.9.

Those three calculated phase diagrams can be seen as follows:

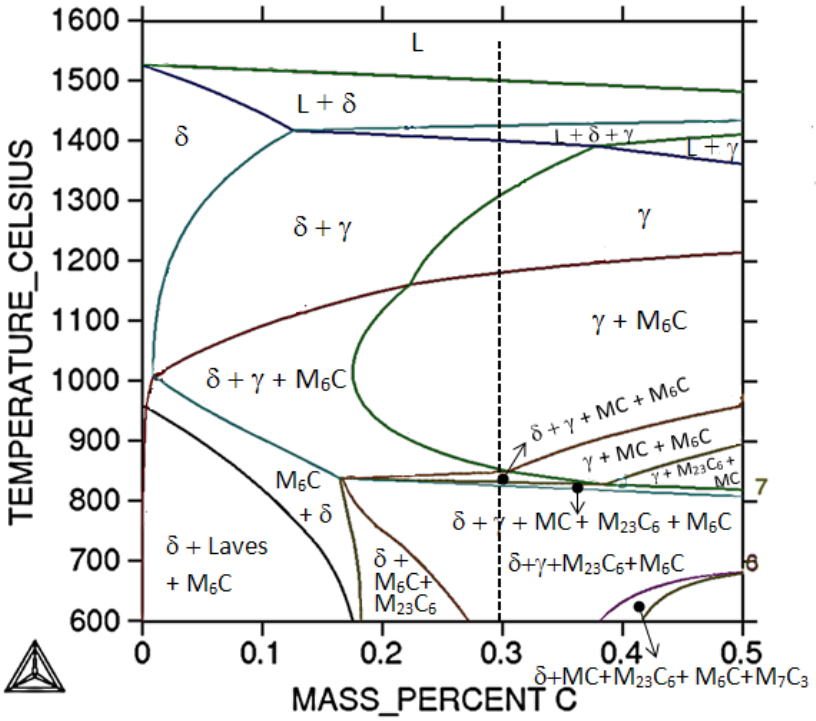

Figure 4.7 Isopleth phase diagram of the investigated H21 tool steel taking into account four alloying elements 0.3C–3.2Cr–7.6W–0.4V (wt%). The dashed line indicates the investigated tool steel.

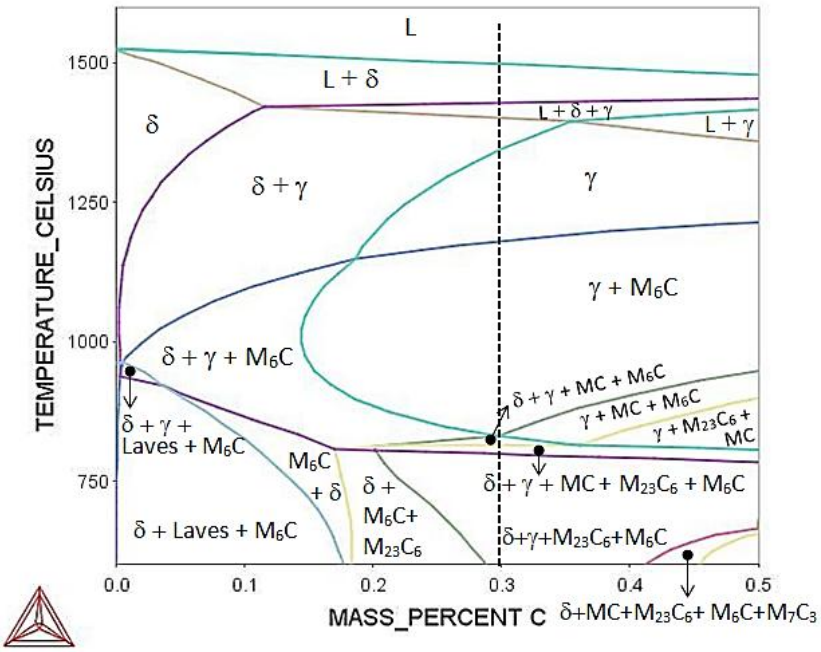

Figure 4.8 Isopleth phase diagram of the investigated H21 tool steel taking into account six alloying elements 0.3C–0.25Mn–3.2Cr–0.3Ni–7.6W–0.4V (wt%). The dashed line indicates the investigated tool steel.

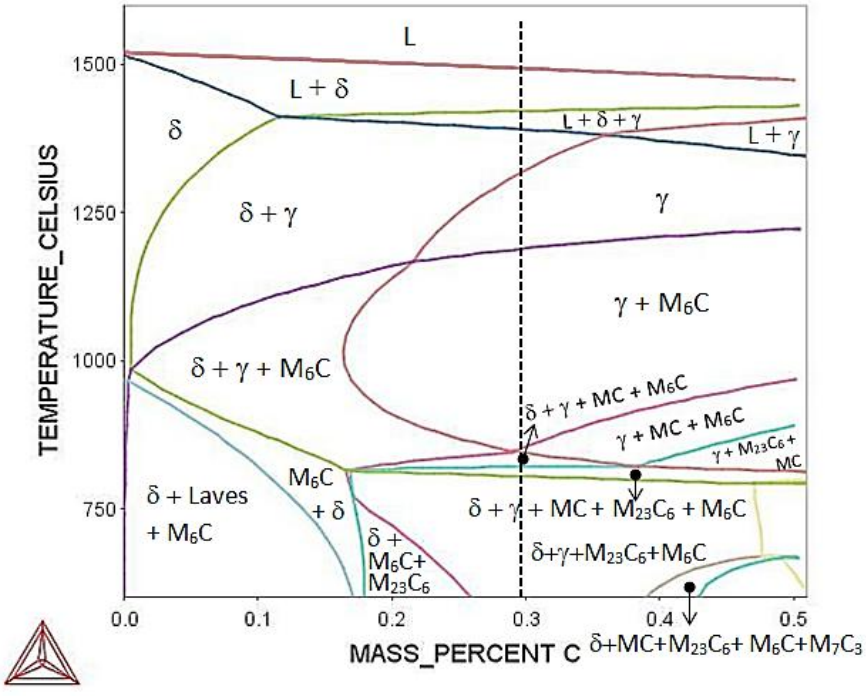

Figure 4.9 Isopleth phase diagram of the investigated H21 tool steel taking into account seven alloying elements 0.3C–0.25Mn–0.3Si–3.2Cr–0.3Ni–7.6W–0.4V (wt%). The dashed line indicates the investigated tool steel.

The presence of Ni and Mn, (Figures 4.8) as well as the addition of Si (Figure 4.9) in the H21 tool steel did not cause any significant change of the phase diagram when compared with the phase diagram calculated for four alloying elements only, Figure 4.7. Manganese is an austenite stabiliser and forms manganese carbide when the Mn content in the steel is at least 24 wt%. In tool steels, the Mn content is kept below 0.35 wt%, therefore manganese carbide does not form in tool steels (Sohar, 2011). Nickel is an austenite stabiliser and tends to increase the amount of retained austenite, whereas Si is a ferrite stabiliser.

The H21 tool steel of this study had 0.3 wt% C. According to the three calculated phase diagrams (Figures 4.7, 4.8 and 4.9) the addition of the austenite stabilisers (Ni and Mn) did not basically alter the microstructure formed after transformation. Considering that the H21 tool steel contains high carbide forming elements and that the presence of austenite stabilisers did not cause significant changes to the isopleth phase diagrams, the isopleth phase diagram with four carbide forming elements was selected to study the phase transformation and solidification path of the H21 tool steel.

It is important to note that the W content of the investigated H21 tool steel was lower than the standard (see Table 2.2). To see what the effect of W is on the equilibrium phase diagram, the isopleth phase diagram was calculated by taking into account the chemical composition of the standard H21 tool steel, namely (0.3C – 3.2Cr –8.5W – 0.4V (wt%). The isopleth phse diagram is shown in Figure 4.10.

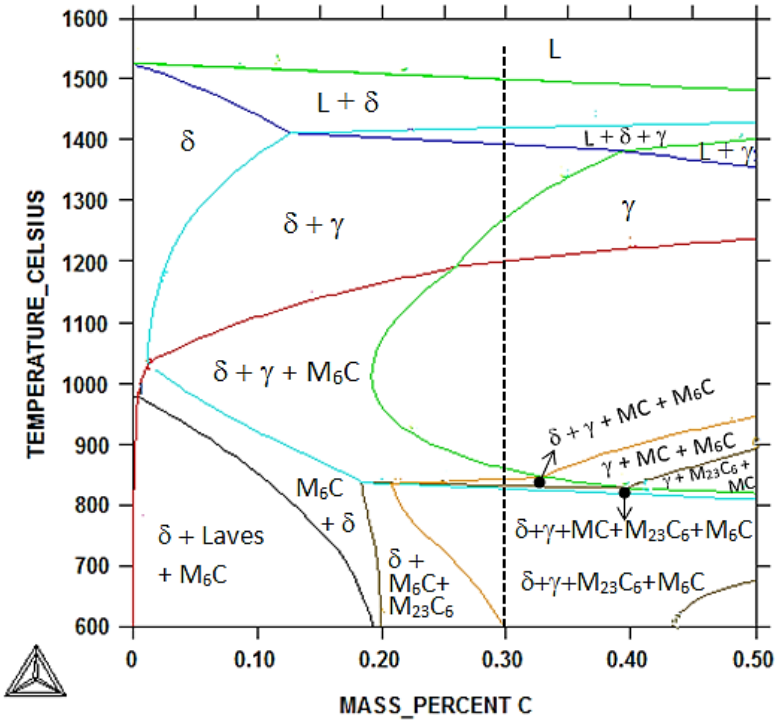

Figure 4.10 Isopleth phase diagram of the standard H21 tool steel taking into account four alloying elements 0.3C–3.2Cr-8.5W–0.4V (wt%). The dashed line indicates the investigated tool steel.

The higher W content widened the $\delta + M_6C + M_{23}C_6$ region in the range 600 – 850 ^{o}C (Figure 4.10) compared with Figure 4.7. However, this change did not affect the phase transformation of the investigated H21 tool steel, as indicated by the dashed line in Figure 4.10.

Figure 4.11 shows an isopleth phase diagram for the H21 tool steel and solidification path that was calculated using the Scheil-Gulliver simulation by assuming that C is fast diffusing. The chemical composition of the investigated tool steel is indicated by the dashed line in the calculated phase diagram.

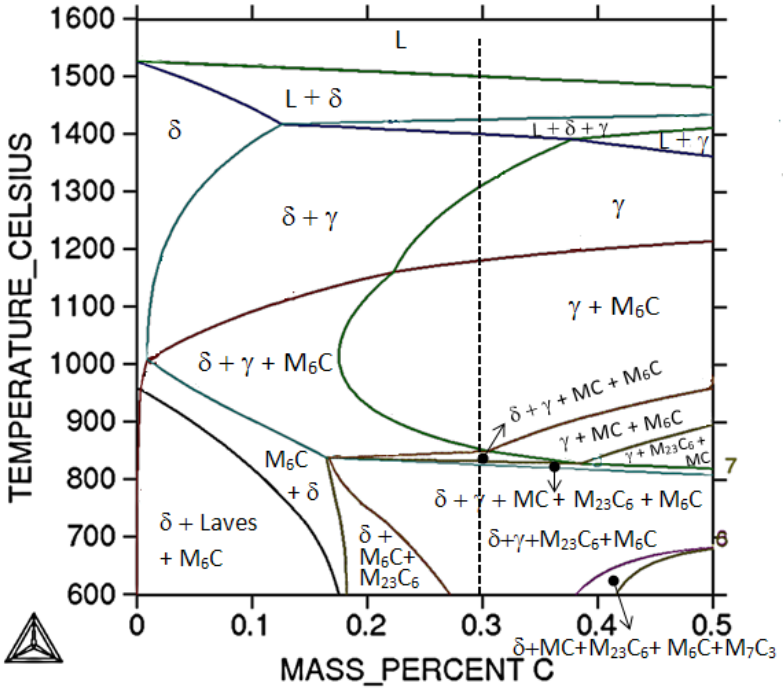

a. Isopleth of the H21 tool steel phase diagram.

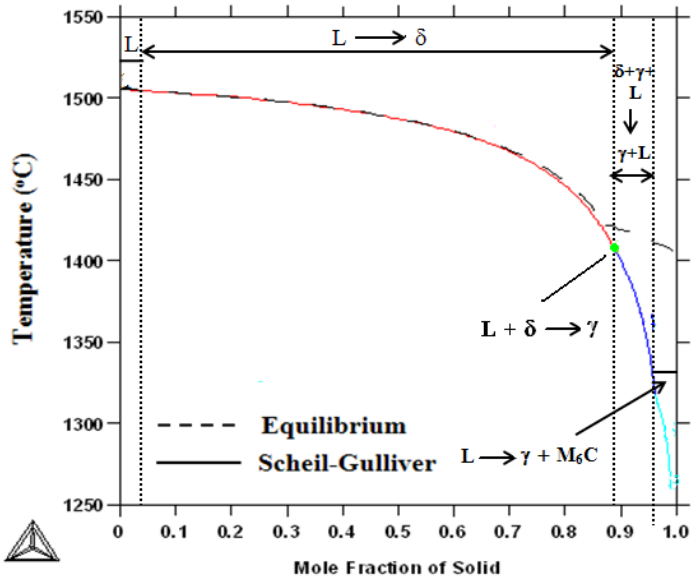

b. Scheil-Gulliver diagram of the H21 tool steel

Figure 4.11 Isopleth and solidification path of the investigated H21 tool steel.

The isopleth and solidification path of the H21 tool steel can be described as follows:

1) Stage 1: precipitation of delta ferrite from liquid (L → δ).

At this stage, δ (primary) ferrite started to crystallise from the liquid. The starting temperature of solidification is 1506 ^{o}C. From the Scheil-Gulliver diagram, Figure 4.11b, the fraction of δ ferrite increased until the γ phase begun forming or the starting temperature for the peritectic reaction was reached.

2) Stage 2: formation of austenite through peritectic reaction (L + δ → γ).
   At this stage, the δ ferrite was surrounded by austenite, which formed from the peritectic reaction. The ending temperature of the peritectic transformation was 1420 $^{\circ}$C. The Scheil-Gulliver diagram in Figure 4.11b shows that the solid fraction was in the range 0.89 – 0.96 and was a combination of δ and γ phases. As the temperature decreased, δ ferrite disappeared and additional γ was formed from the remaining liquid.

3) Stage 3: formation of eutectic carbides through eutectic reaction (L → γ + carbides). The eutectic reaction is the last phase transformation from liquid to solid during the solidification process. Therefore, the nucleation and growth of eutectic occurred in the remaining liquid, which was rich in C and carbide forming elements. Based on the Scheil-Gulliver diagram of the H21 tool steel, the M_6C carbide was the only eutectic carbide formed from the eutectic reaction at 1320 ^{o}C.

4) Stage 4: the eutectic transformation was complete at 1180 ^{o}C. During solid state phase transformation all austenite transformed to ferrite and formed new primary carbides types ($\gamma + M_6C \rightarrow \alpha + M_6C + MC + M_{23}C_6$).

It is well known that the phase diagrams do not provide details of phase transformation mechanisms and of primary carbide morphology under actual kinetic conditions. From the aforementioned solidification path and the observed as cast microstructure, the solidification of the H21 tool steel is shown schematically in Figure 4.12.

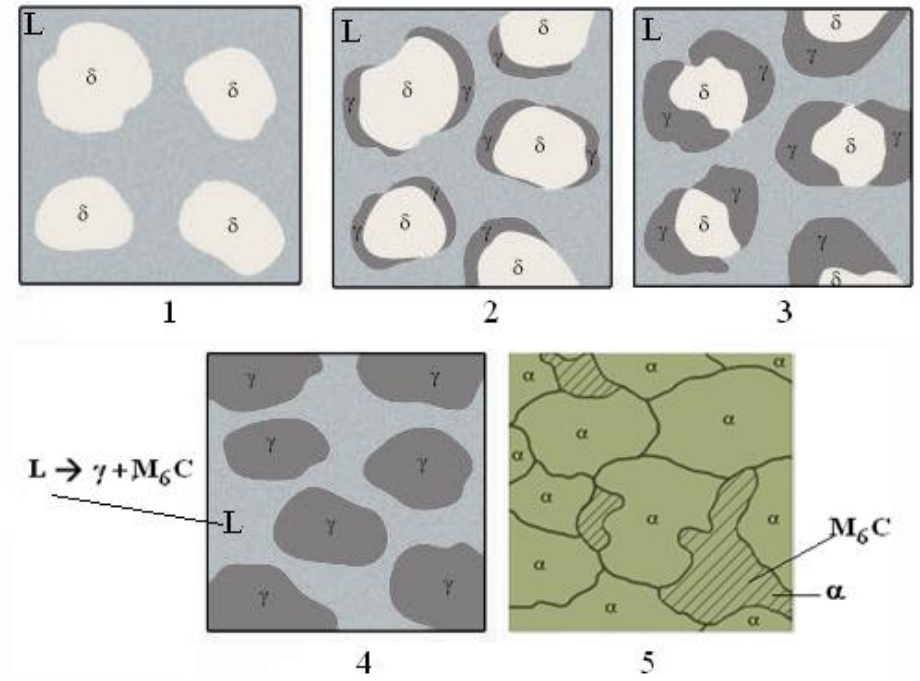

a. Multistage crystallisations in the H21 tool steel.

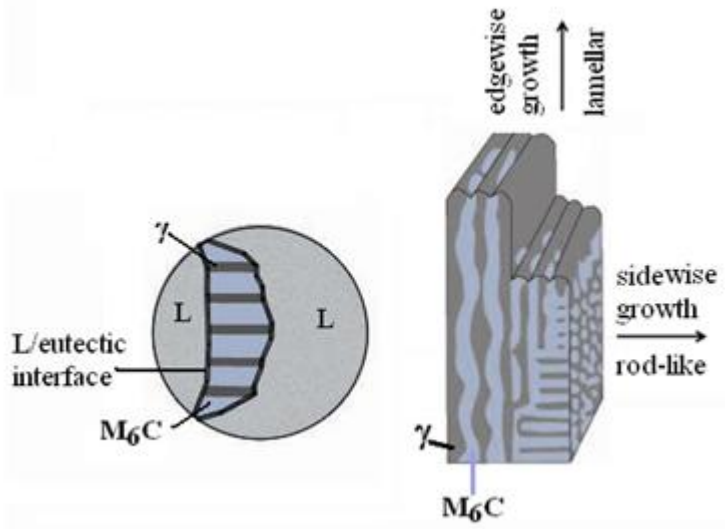

b. Formation of eutectic structure

Figure 4.12 A schematic representation of the solidification of the H21 tool steel.

Referring to Figure 4.12a, brief descriptions of each stage (indicated by number in the figure) are given below:

1. The primary δ ferrite grains nucleated and grew

2. The γ formed peritectically at the interface of δ and liquid, and covered δ ferrite grains.
3. The peritectic γ grew in the direction of δ ferrite via the peritectic transformation. The transfer of alloying components depended on the diffusivity of the substitutional alloying elements that is lower compared with that of C (Campbell, 2012).
4. Solidification of the remaining liquid occurred by the eutectic transformation L → γ + M_6C. The eutectic M_6C carbides were separated and surrounded by austenite with the latter being the leading phase (Peidao *et al.*, 1992). This reaction moved down a eutectic trough with continuously changing phase compositions, until the solidus temperature was reached. A lamellar eutectic in the edgewise direction, and rod eutectic in the sidewise direction (Trepczyńska-Łent, 2010) developed (Figure 4.12b).
5. The austenite transformed to ferrite below the solidus temperature.

Comparison between prediction and experimental results shows that the calculated phase diagram was not in agreement with the solidification microstructure of the H21 tool steel. The $M_{23}C_6$ carbides, predicted by the thermodynamic calculation were not observed by XRD, SEM-EDS and TEM and the MC carbides was observed by TEM but was not predicted by thermodynamic calculation.

4.7 Identification of Primary Carbides and Solidification Path of the As Cast H23 Tool Steel

4.7.1 Identification of Primary M_6C Carbides

Figure 4.12 shows a SEM back scatter electron image of carbides in the as cast H23 tool steel.

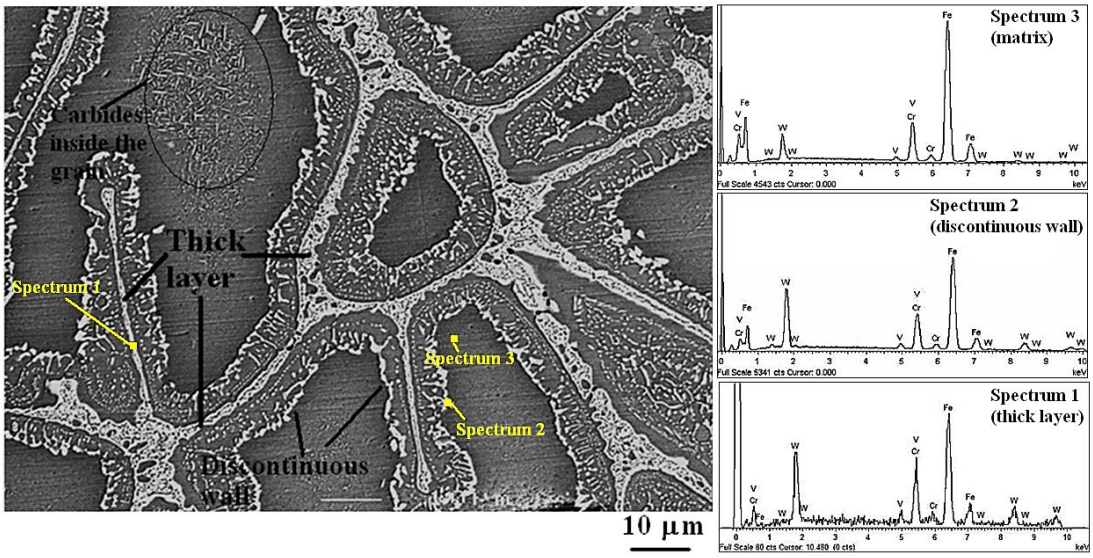

(a)

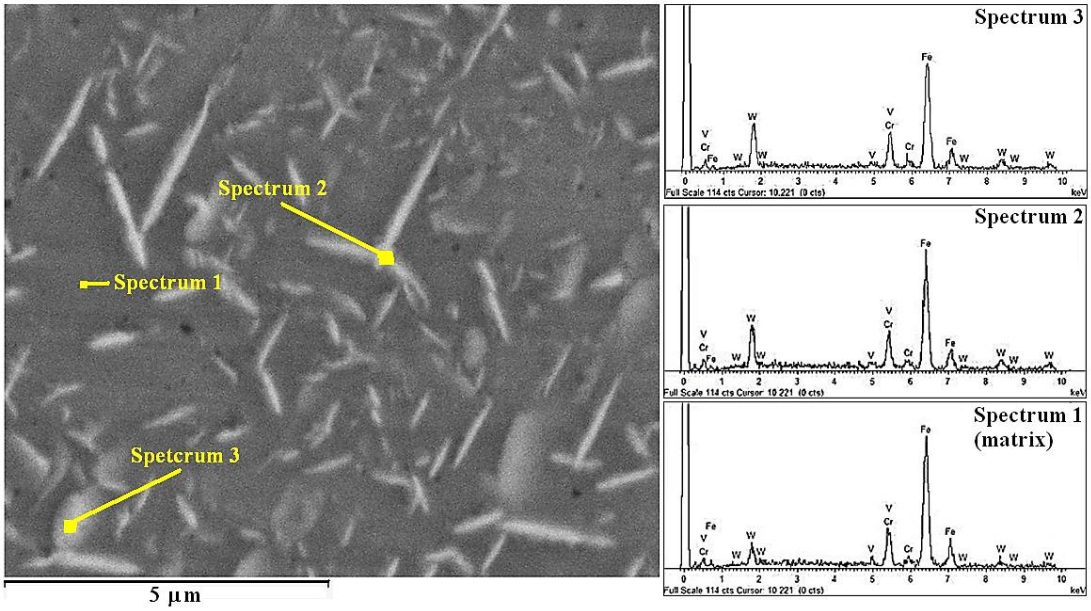

(b)

Figure 4.13 SEM back scatter electron images of the as cast H23 tool steel showing the carbides along the grain boundaries (a) and inside the grains (b) and EDS spectra of the M_6C carbide and matrix.

Figure 4.13 shows the EDS spectra of the carbides that were along the grain boundaries and inside the grains, and the EDS spectra of the matrix. The tungsten K_α peak of the carbides has intensified in their spectra when compared with the Cr peaks

relative to the matrix spectra. Table 4.3 shows the SEM-EDS analyses of the primary M_6C carbides and matrix of the steel.

Table 4.3 SEM-EDS data of the M_6C carbides and matrix in the as cast H23 tool steel (wt%).

Figure	Phase	Spectrum	Element				Comment
			Fe	Cr	V	W	
4.13.a	Carbides in the thick layer	1	55.9	18.6	2.8	22.7	M_6C
	Carbides in the discontinuous wall	2	52.2	16.2	2.5	29.1	M_6C
	Matrix	3	79.1	13.4	0.6	7.1	α^*
4.13.b	Carbides inside the grain	1	62.0	12.6	2.0	23.4	M_6C
		2	62.9	12.9	0.5	23.8	M_6C
		3	76.1	12.9	1.3	9.7	α^*

*See Figure 4.3

There was only one type of carbide that exhibited white contrast both along grain boundaries and grain interiors. These carbides were identified by XRD and SEM-EDS as M_6C carbides rich in W and Fe. There was a significant difference in carbide morphology between those formed on grain boundaries and those formed inside the grains. The morphology of the M_6C carbides inside the grains was rod-like, suggesting anisotropic growth. In contrast, the morphology of the M_6C carbides formed on the grain boundaries were thick layer carbides (skeleton) on the actual grain boundaries and carbides that formed a "discontinuous wall" around the outer edge of the eutectic colony that was formed on either side of the grain boundaries.

Table 4.3 shows that the M_6C carbides were essentially Fe and W rich. The M_6C carbides in the H23 tool steel were richer in W, Cr and V than those in the H21 tool steel. This is not surprising given the content of alloying elements in the two tool steels. The matrix was richer in Cr than W (spectrum 3 in Figure 4.13a,b) as the W was consumed to form the M_6C carbides. A slight difference in the chemical composition of the M_6C carbides was suggested by spectrum 1 taken from thick

layer, and spectrum 2 taken from discontinuous wall (Figure 4.13a). This was attributed to the shift of the composition point down a eutectic trough during the course of the eutectic reaction (Fischmeister *et al.*, 1989).

Figure 4.13 and Table 4.3 also show that the alloying element content of the M_6C carbides formed on the discontinuous wall (spectrum 2, in Figure 4.13a) was higher than that of the M_6C carbides formed inside the grains (spectrum 1 and 2 in Figure 4.13b). This was attributed to the M_6C carbides on the discontinuous wall having nucleated first on more energetically favourable site than the intragranular sites where the needle carbides formed inside the grains. Hence the size of the former carbides was bigger than that of the latter.

Figure 4.14 shows details the eutectoid M_6C carbide in the as cast H23 tool steel and Table 4.4 gives the SEM-EDS analysis of the eutectoid M_6C carbide of the same steel.

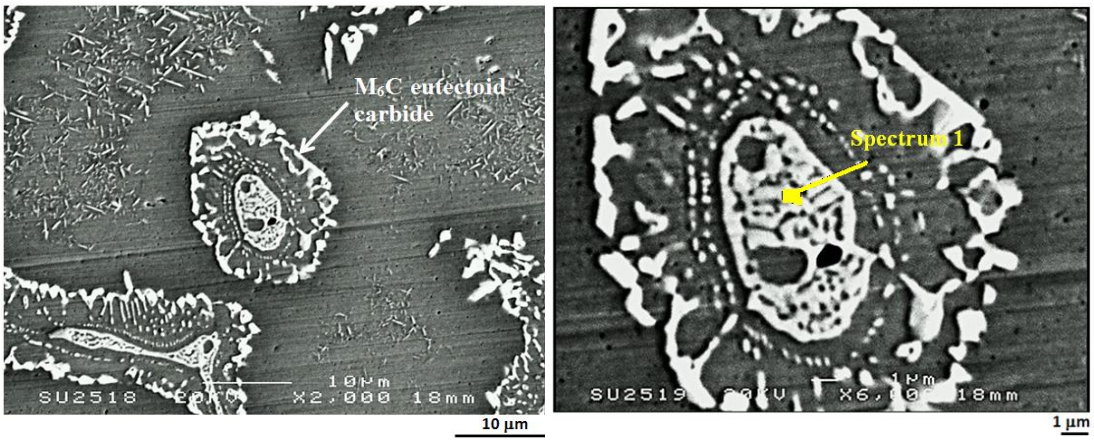

a.Low magnification b. High magnification

Figure 4.14 SEM secondary electron images of the as cast H23 tool steel showing eutectoid M_6C carbides.

Table 4.4 SEM-EDS data of the M_6C carbides in the as cast H23 tool steel (wt%).

Phase		Element				Comment
		Fe	Cr	V	W	
Carbide in Figure 4.14b	Spectrum 1	49.5	21.2	3.9	25.3	Eutectoid M_6C

The eutectoid carbide was identified by SEM-EDS as M_6C owing to its high W content. The morphology of the eutectoid carbide was irregular shape and exhibited features that were nearly the same as for the eutectic carbide. However, the alloying element content of eutectoid M_6C carbide was higher than that of eutectic M_6C carbide due to all the major carbide forming elements being ferrite formers and soluble in ferrite and the eutectoid M_6C being the product of the delta eutectoid transformation.

The mean size of the M_6C carbides in the as cast H23 tool steel could not be measured accurately. The M_6C carbide mean size inside the grains in the as cast H23 tool steel was about 0.4 ± 0.1 μm. The total volume fraction of coarse carbides was 21.5 ± 0.4 %.

Regarding the EDS analysis of the M_6C carbides in the as cast H23 tool steel that were located along grain boundaries and discontinuous wall, there carbides were coarser (0.1 to 1.5 μm) than those observed in the as cast H21 tool steel (see Section 4.6.1). Given that the spatial resolution of SEM-EDS was almost 1 μm, there was no interference between the interaction volume and the matrix for the larger M_6C carbides (> 1 μm) in the H23 tool steel. However, for the smaller M_6C carbides, there was interference between the interaction volume and the matrix, and thus the EDS analysis could have shifted to the matrix.

4.7.2 The Fine Carbides of the As Cast H23 Tool Steel

The presence of fine carbides was observed by TEM, as can be seen in Figures 4.15 and 4.16. The use of higher voltage and thinner sample than in the limit the interaction volume and X-ray absorpotion. The effective spatial resolution of TEM is considered to be between a few nanometers (Gauvin *et al.*, 2006) up to 0.1 μm, depending on the thickness of thin foil samples. As a result, the TEM-EDS became more sensitive to the sample surface due to the penetration depth of the electrons

being smaller. The carbide in Figure 4.15 was identified as MC carbide rich in V had diameter around 40 nm.

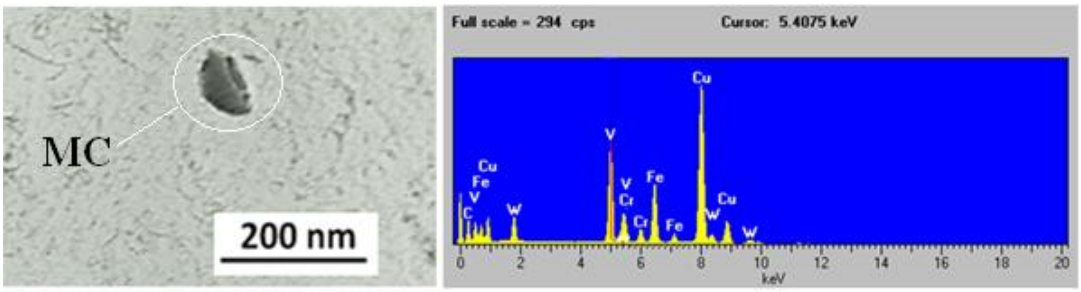

Figure 4.15 A bright field TEM image from replica showing a fine MC carbide of the as cast H23 tool steel and TEM-EDS spectrum of the same MC carbide, which was rich in vanadium (JEOL 2010F). The high Cu peaks in the EDS spectrum were from the Cu grid.

Another carbide observed by TEM was the $M_{23}C_6$ carbide located on grain boundary, see Figure 4.16. The $M_{23}C_6$ carbide was rich in Cr and Fe (Roberts *et al.*, 1998). The MC and $M_{23}C_6$ carbides have the same crystal structure (FCC) with different lattice parameters. The lattice parameter of the $M_{23}C_6$ carbide was ~ 1.06 nm and the lattice parameter of the MC carbide was 0.44 nm. The morphology of fine $M_{23}C_6$ carbide was nearly cuboid ellipsoidal with size below 80 nm in length.

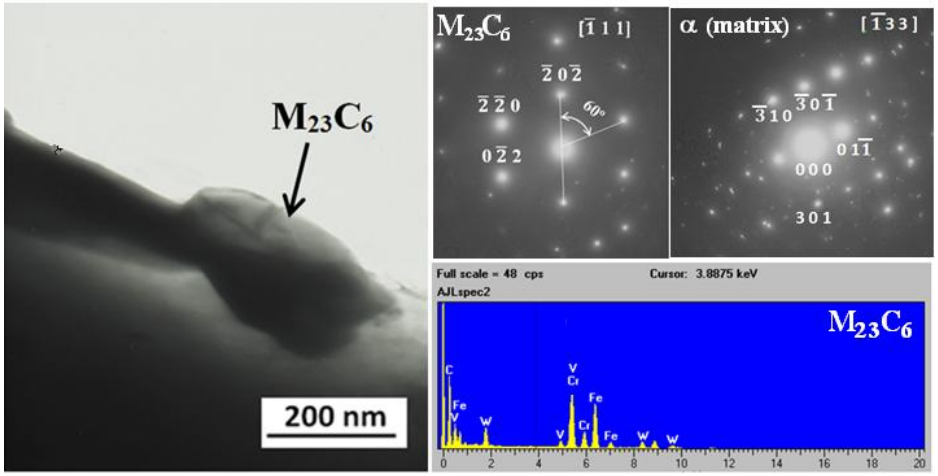

Figure 4.16: A bright field image TEM image and EDS spectrum of the $M_{23}C_6$ carbide and selected area diffraction pattern of the matrix and $M_{23}C_6$ carbide in the as cast H23 tool steel taken from thin foil (JEOL 2010F).

The MC carbides' size (~ 40 nm) in the as cast H21 tool steel and the corresponding intense Cu peak in the EDS spectrum indicated that the interaction volume was much larger than the submicron carbides, which led to interference from the sample holder. There was also interference from the matrix in the as cast H23 tool steel when the $M_{23}C_6$ carbides were analysed due to the spatial resolution of TEM-EDS being bigger than the size of the $M_{23}C_6$ carbides.

4.7.3 Solidification Path of the H23 Tool Steel

The formation and morphology of carbides in tool steels are strongly affected by the solidification path and the chemical composition of the steel. The ThermoCalc software was used to support the microstructure studies during solidification. The chemical composition of the H23 tool steel (Table 3.2) showed that the Ni content was higher than the standard. Three isopleth phase diagrams were calculated to study the effect of varying alloying contents, namely:

a. Isopleth phase diagram taking into account four alloying elements, 0.33C –12.2Cr -12.5W – 1.2V (wt%), Figure 4.17.
b. Isopleth phase diagram taking into account six alloying elements, 0.33C – 0.38Mn – 12.2Cr – 0.4Ni – 12.5W – 1.2V (wt%), Figure 4.18.
c. Isopleth phase diagram taking into account seven alloying elements, 0.33C – 0.38Mn – 0.5Si – 12.2Cr – 0.4Ni – 12.5W – 1.2V (wt%), Figure 4.19.

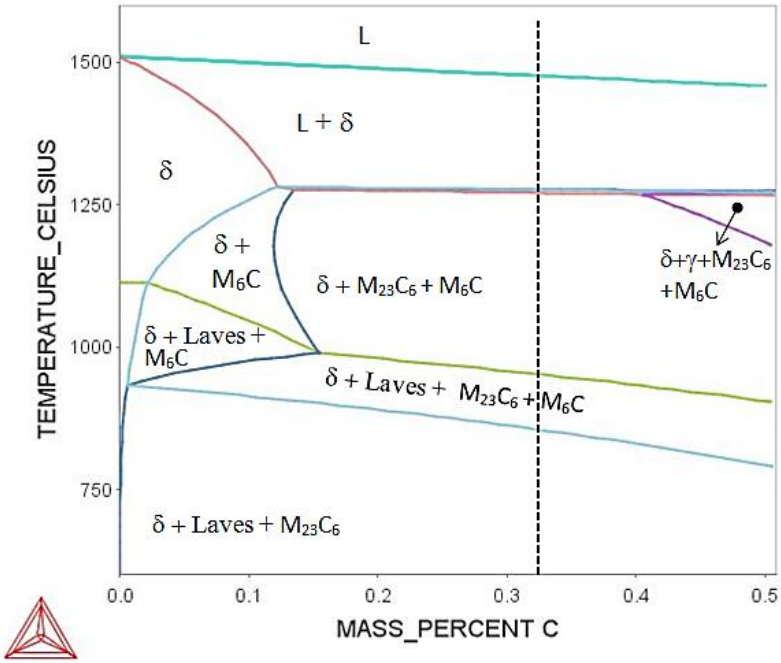

Figure 4.17 Isopleth phase diagram of the investigated H23 tool steel taking into account four alloying elements 0.33C–12.2Cr –12.5W–1.2V (wt%). The dashed line indicates the investigated tool steel.

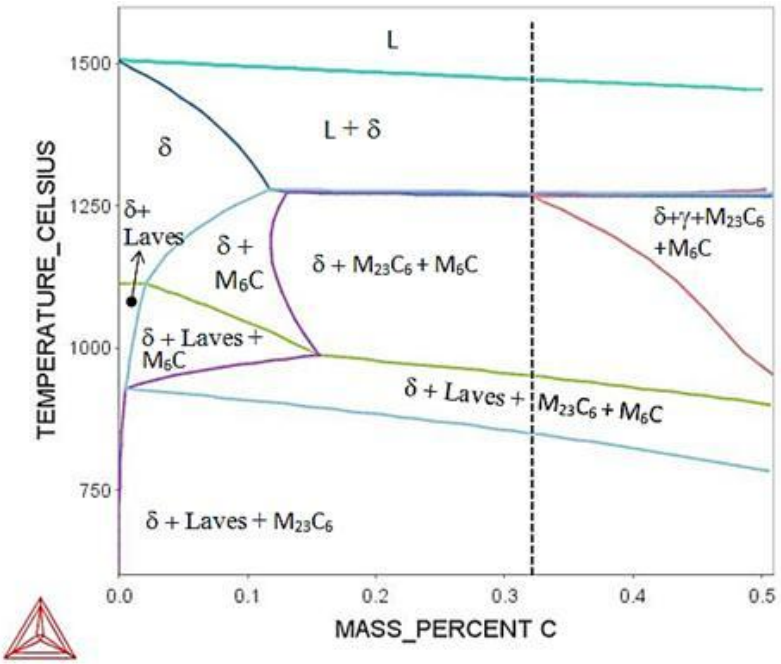

Figure 4.18 Isopleth phase diagram of the investigated H23 tool steel taking into account six alloying elements 0.33C–12.2Cr –12.5W–1.2V-0.38Mn-0.3Ni (wt%). The dashed line indicates the investigated tool steel.

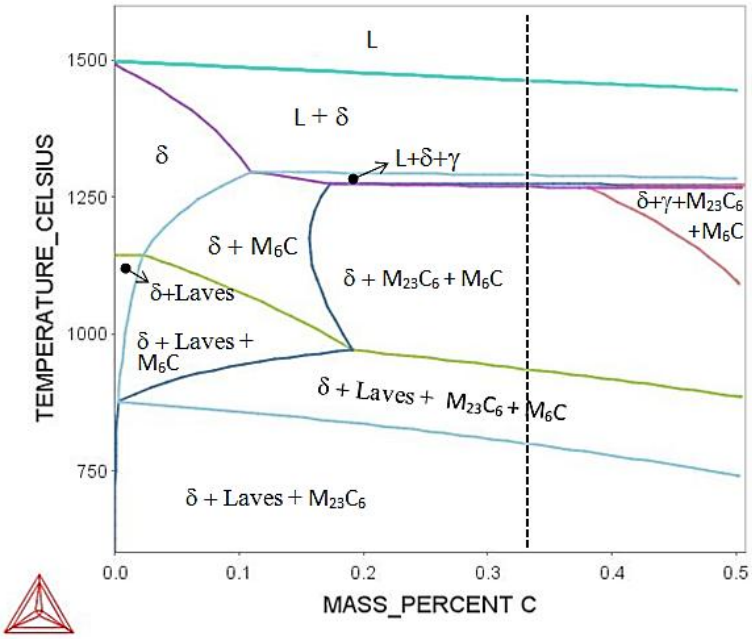

Figure 4.19 Isopleth phase diagram of the investigated H23 tool steel taking into account seven alloying elements 0.33C–12.2Cr –12.5W–1.2V-0.38Mn-0.3Ni-0.5Si (wt%). The dashed line indicates the investigated tool steel.

The addition of Ni and Mn in the calculated phase diagrams (Figures 4.18 and 4.19) widened the austenitic region compared with Figure 4.17 as both elements are austenite stabilisers. However, this change did not affect the phase transformation of the investigated H23 tool steel, as indicated by the dashed line in each figure.

To study the phase transformations in the H23 tool steel, the isopleth phase diagram calculated by taking into account four carbide forming elements was used and the solidification path was calculated using the Scheil-Gulliver simulation by assuming that C is fast diffusing, see Figure 4.20.

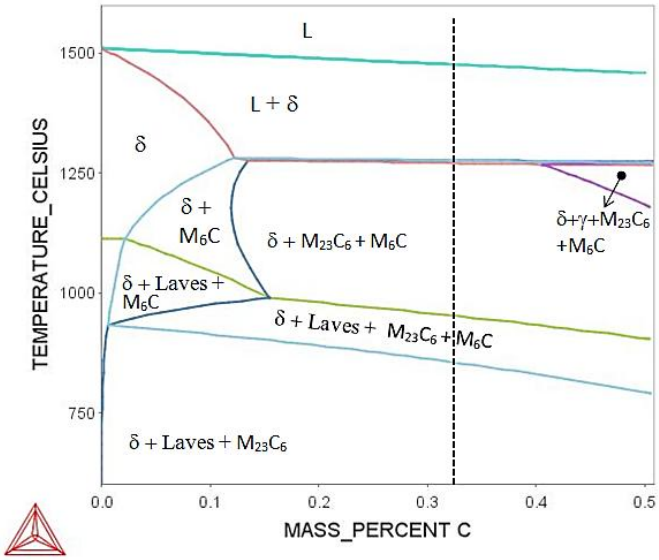

a.Isopleth of the H23 tool steel phase diagram.

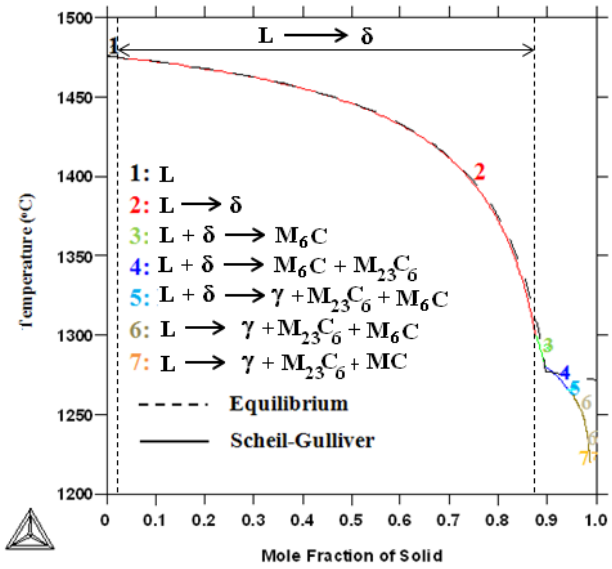

b.Scheil-Gulliver diagram of the H23 tool steel.

Figure 4.20: Isopleth and solidification path of the investigated H23 tool steel.

The isopleth and solidification path of the H23 tool steel would suggest the following solidification stages:

1) Stage 1 : precipitation of delta ferrite from liquid (L → δ)

   At this stage delta (primary) ferrite started to crystallize from the liquid. The starting temperature of solidification was 1476 ^{o}C.

2) Stage 2: formation of austenite through peritectic reaction

   The ending temperature of peritectic transformation was 1280 ^{o}C. The Scheil-Gulliver diagram for the H23 tool steel in Figure 4.20b, shows reactions with the order:

   a. $L + \delta \rightarrow M_6C$ (indicated by number 3)

   b. $L + \delta \rightarrow M_6C + M_{23}C_6$ (indicated by number 4)

   c. $L + \delta \rightarrow \gamma + M_6C + M_{23}C_6$ (indicated by number 5)

   Therefore, the M_6C and $M_{23}C_6$ carbides crystallized at different temperatures. The peritectic reaction, which produced austenite and carbides did not go to completion. The remaining liquid decomposed through the eutectic transformation. Compared with the calculated phase diagram of the H21 tool steel, the high W and Cr contents in the H23 tool steel depressed the peritectic temperature and reduced the γ phase region. As a consequence the gap between the liquidus and peritectic temperatures was widened. High W and Cr also increased the amount of the M_6C and $M_{23}C_6$ carbides.

3) Formation of carbides through eutectic reaction ($L \rightarrow \gamma$ + carbides).

   The eutectic reaction was the last phase transformation from liquid to solid during the solidification process. The nucleation and growth of eutectic phases occurred in the remaining liquid, which was rich in C and carbide forming elements. Based on the Scheil-Gulliver simulation of the H23 tool steel, the eutectic carbides in the H23 tool steel were M_6C, $M_{23}C_6$ and MC and formed in the temperature range 1295 to 1225 ^{o}C. The M_6C was the first eutectic carbide that formed at 1295 ^{o}C, followed by the formation of $M_{23}C_6$ at 1280 ^{o}C and MC at 1225 ^{o}C.

As discussed before, the differences in carbide morphology imply different growth mechanisms for the discontinuous wall carbide, the skeleton carbide, the carbides inside the grains and the delta eutectoid carbides. On the basis of the aforementioned solidification path and the as cast microstructure, it is suggested that the formation and growth of primary carbides in the H23 tool steel occurred as shown in the schematic diagram in Figure 4.21.

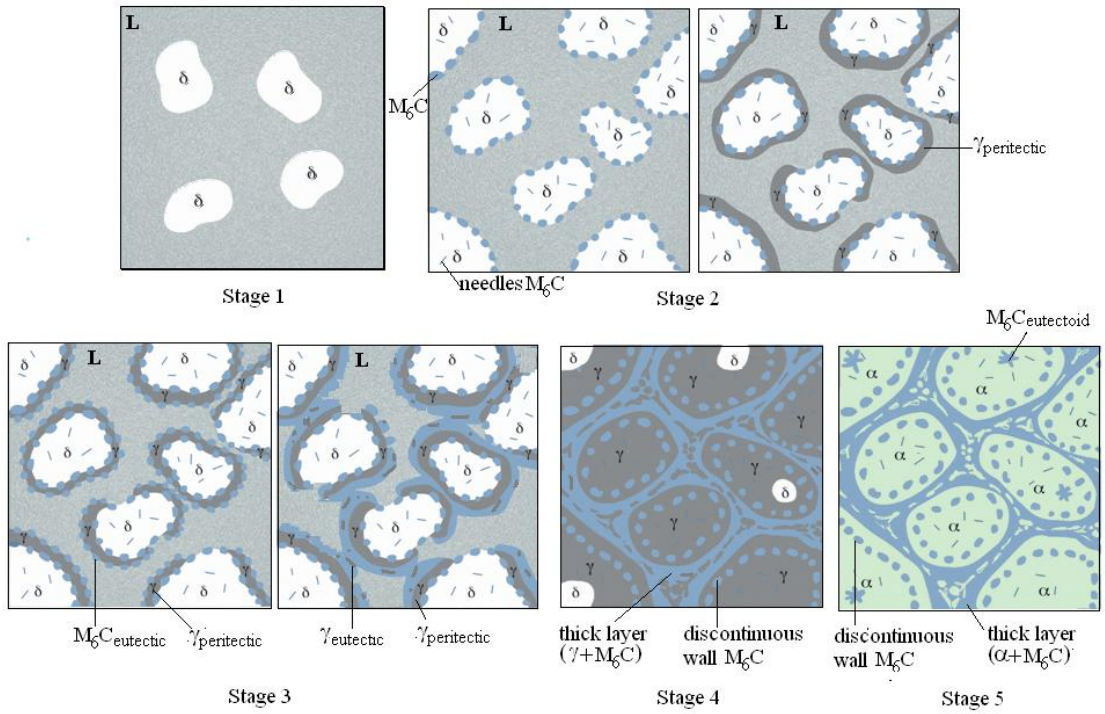

Figure 4.21 Schematic showing crystallisation stages of the H23 tool steel.

Figure 4.21 shows the different stages of crystallisation of the H23 tool steel.

1) Stage 1: L → δ

   The solidification started with the formation of primary δ ferrite at 1476 ^{o}C.

2) Stage 2: L + δ → M_6C + γ

   As the temperature decreased, the peritectic reaction occurred. Due to the high content of carbide forming elements in the tool steel, the M_6C carbides formed first through the peritectic reaction and then austenite. The as cast microstructure of the H23 tool steel suggested that there were two different sites of M_6C carbide formation.

   - First, the M_6C carbide was the leading phase of the peritectic transformation (Peidao *et al.*, 1992) and nucleated on the melt/δ ferrite interface to form discontinuous wall and thickened as solidification progressed.
   - Second, because of the high content of carbide forming elements the melt/ferrite interface could no longer accommodate all the carbide forming

elements and M_6C carbides nucleated independently in the less favourable intragranular sites of δ ferrite. Hence, at the end of the solidification process the M_6C carbides were distributed not only at the grain boundaries but also inside the grains.

The M_6C carbides, which formed first, grew cooperatively with the γ that formed from the peritectic transformation. The peritectic austenite grew and covered the δ ferrite and M_6C carbides.

3) Stage 3: $L \rightarrow \gamma + M_6C$

The peritectic reaction did not go to completion leaving the primary delta ferrite in the dendrite cores. This and the fact that the austenite formed a continuous shell around δ ferrite meant that further transformation was possible in the solid state transformation (Fischmeister *et al.*, 1989, Barkalow *et al.*, 1972). The remaining interdendritic liquid decomposed into a eutectic mixture of austenite and carbides. The eutectic transformation started at 1295 ^oC with the M_6C carbide being the leading phase of the eutectic transformation. The M_6C carbides nucleated on the surface of the peritectic austenite. The as cast microstructure in Figure 4.9a shows that the morphology of carbides formed along the grain boundary was a skeleton shape with characteristic midplane and regularly spaced lamellae.

4) The γ peritectic continued to grow in the direction of δ ferrite. The eutectic M_6C carbides grew simultaneously, and connected with others (Peidao *et al.*, 1992) and finally formed thick layer (skeleton) of M_6C carbides. Fischmeister *et al* (1989) observed that thickening of the lamellae towards the end of solidification of the inter-dendritic melt may, more or less, close the inter-lamellar gaps often forming a continuous coating on the metal dendrites. When the interdendritic melt area was big enough, from both sides of the eutectic M_6C carbides the skeletons grew out to form a secondary axis (Peidao *et al.*, 1992), and as a result the thick layer of the M_6C carbides became bigger. The high W content in the H23 tool steel must have played an important role in the formation of carbides. Kim *et al*

(2005) reported that W additions in a high speed steel accelerated the eutectic reaction forming M_6C carbides. The eutectic transformation terminated before the peritectic transformation and thus, there was residual delta ferrite (Nizhnikovskaya *et al.*, 1982).

5) Stage 5: Formation of delta eutectoid M_6C carbides via eutectoid transformation. Kagawa and Okamoto (1986) and Galda and Kraft (1974) reported that high W and Cr contents in steels depressed the peritectic reaction temperature. Thus, the H23 tool steel had a wide temperature range for delta (primary) ferrite crystallsation and caused delta ferrite to remain in the dendrite cores after the peritectic transformation. In this stage, the δ ferrite core was separated from the melt by wall of γ peritectic. Since the transformation is diffusion controlled, during the subsequent solidification the unconsumed delta ferrite in the dendrite cores transformed to austenite and carbide below the solidus temperature through the eutectoid transformation $\delta \rightarrow \gamma$ + carbides (known as delta eutectoid rection, Barkalow *et al.*, 1972) and upon further cooling to room temperature the austenite transformed to ferrite. The eutectoid transformation consumed a large quantity of C and as the delta ferrite is a C poor phase, the C could only be supplied by the C rich remaining liquid (Peidao *et al.*, 1992). Carbon must diffuse to the core through the peritectic austenite region. The substitutional alloying elements have much lower diffusion rates than C and as they had no time to diffuse to the delta ferrite in the dendrite core they segregated in the delta ferrite/austenite interface. Hence, precipitation of eutectoid carbides occurred at the austenite/delta-ferrite interface to accommodate the available carbide forming elements, which existed in the high temperature ferrite following the delta-eutectoid reaction. In the absence of the delta eutectoid carbide, as was observed in some areas, see Figure 4.4b, the peritectic austenite covered part of the delta ferrite and thus, both phases were in contact with the melt that supplied the alloying components, allowing the δ ferrite to transform completely to austenite.

In this study, the significantly different M_6C carbide morphology between the H21 and H23 tool steels was not affected by cooling rate as both tool steels solidified under the same conditions. Thus, the different morphologies were attributed to the content of alloying elements in the two tool steels. Peidao *et al* (1992) reported that differences in eutectic carbide morphology were influenced by different growth mechanisms and chemical compositions of steels. The W content was probably the major factor responsible for the significant difference in eutectic M_6C morphology between the as cast H21 and H23 tool steels. Lower W content in the H21 tool steel than in the H23 tool steel caused the eutectic carbide morphology to change from highly interconnected to little or no interconnection with short and thick rods.

In the H23 tool steel, the experimental results showed that the as cast microstructure consisted of ferrite, M_6C and fine MC and $M_{23}C_6$ carbides. The presence of Laves phase was not detected experimentally. Li (2006) and Weiss and Stickler (1972) reported that Laves phase formed after very long exposure at elevated temperature. Comparison between prediction and experimental results shows that the calculated phase diagram was not in agreement with the solidification microstructure of the H23 tool steel. The MC carbides, was not predicted by the thermodynamic calculation but observed by TEM due to V being a very strong carbide former.

4.8 Hardness of the As Cast Tool Steels

The hardness of tool steels is not only affected by the type and amount of carbides but also correlates strongly with the size and distribution of carbides and the matrix grain size. The hardness of the cast H21 and H23 tool steels was 483 ± 6 HV and 355 ± 4 HV, respectively. Although the volume fraction of carbides in the H23 tool steel was higher compared with the H21 tool steel, its hardness was lower. This is attributed to the size of carbides, which were coarser in the H23 tool steel than in the H21 tool steel and the type of fine carbides that existed in both tool steels. The hardness of $M_{23}C_6$ carbides (1200 HV) is well below the hardness of MC carbides (3000 HV) (Roberts *et al.*, 1998), therefore the formation of fine $M_{23}C_6$ carbides in the as cast H23 tool steel contributed to decrease in hardness.

Particular attention was given to the H21 tool steel by measuring the nanohardness of the as cast microstructure. A nanohardness profile of the as cast H21 tool steel in Figure 4.22 shows that the nanohardness values bulk grain to grain boundary precipitates varied between 4.8 to 8.9 GPa with an average value 6.2 ± 1.4 GPa. The ratio of the standard deviation to the average value was too large of 23 %. This indicated that there was inhomogeneity of the microstructure in submicron scale. This was attributed to the precipitation of fine carbides around grain boundaries.

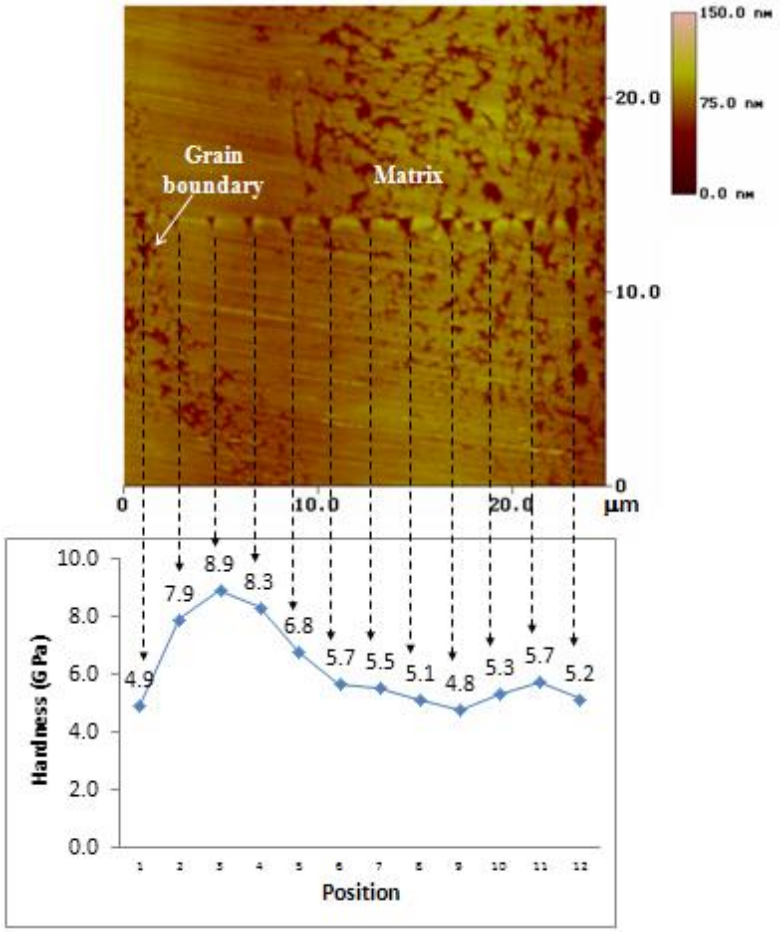

Figure 4.22 Nano hardness profile of the as cast H21 tool steel from grain boundary to matrix (the value of 4.9 GPa on the grain boundary does not refer to the hardness of the carbides).

4.9 Conclusions

1. The ingots of the H21 and H23 tool steels had porosity and heterogeneous grain structures.
2. The coarse eutectic carbides found in the H21 and H23 tool steels were M_6C carbides and had different morphologies due to the W content of the steels.
3. The morphology of the M_6C carbides in the as cast H21 tool steel was lamellar with very little or no interconections between individual carbide platelets; there was neither a backbone at the center or carbide wall around the eutectic carbide-matrix interfaces.
4. In the H23 tool steel, two different morphologies of peritectic M_6C carbides were observed by SEM. The M_6C carbides located inside the grains had a rod like morphology and carbide that formed a "discontinuous wall" of carbides around the outer edge of the eutectic colony had an irregular morphology. Grain boundary M_6C eutectic carbides were thick layer carbides (skeleton) on the grain boundary. Eutectoid M_6C carbides formed inside some grains and their features were nearly the same as for the eutectic carbide.
5. The fine carbides were observed only by TEM and were MC carbide in the H21 tool steel and MC and $M_{23}C_6$ carbides in the H23 tool steel.
6. The H21 and H23 tool steels basically had the same solidification path starting with the formation of delta ferrite from the melt and followed by the formation of austenite through peritectic reaction and then eutectic transformation.

Chapter 5
The Conventional Heat Treatment of the H21 and H23 Tool Steels

5.1. Introduction

Carbide forming elements in tool steels promote the formation of complex carbide network in the as cast condition, which is detrimental to the mechanical properties of tool steels. Thus, heat treatment is used to dissolve the carbide network and achieve the optimal combination of hardness and toughness. A typical heat treatment for tool steels involves hardening and tempering. In particular, the secondary carbides precipitated during subsequent tempering play an important role for the mechanical properties of tool steels.

Although thermomechanical processing is highly effective for improving the mechanical properties of tool steels, and has been used in this study, the study of conventional heat treatment was necessary for comparison purposes. This chapter is dedicated to the study of the effect of solutioning and double tempering temperatures on the microstructure evolution and hardness of the H21 and H23 tool steels.

5.2 The Effect of Solutioning Temperature

5.2.1 The Effect of Solutioning Temperature on Microstructure

The solid solution was carried out to homogenise the as cast microstructures and dissolve the primary carbide network. Figure 5.1 shows the as quenched microstructures of the H21 tool steel after solutioning at different temperatures.

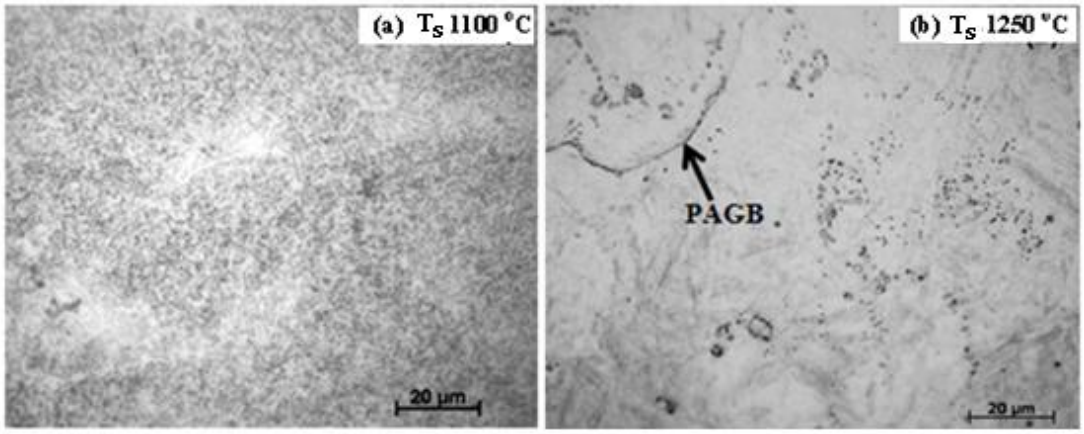

Figure 5.1 Optical images of the microstructures of the H21 tool steel after solutioning and water quenching (PAGB = Prior Austenite Grain Boundary).

The as quenched microstructure of the H21 tool steel consisted of lath martensite and carbides. After quenching from solutioning at 1100 ^{o}C the martensite matrix was not clear and the microstructure was dominated by a considerable volume fraction of dispersed carbides within martensite. At the higher solutioning temperature, the martensite was very clear and the carbides had coarsened. The prior austenite grain boundaries (PAGB) were only observed partially after solutioning at 1250 ^{o}C, thus the prior austenite grain size could not be estimated. The difficulty in imaging the PAGBs was probably due to the presence of thick martensite layer and the precipitation of carbides that covered the PAGBs. The solutioning temperature (T_s) did affect the dissolution of carbides as at the higher solutioning temperature the diffusion rate of the carbide forming elements increased and as a result more carbides dissolved enriching the matrix with alloying elements (Totten, 2006). However, a considerable volume fraction of primary carbides still existed even at the higher solutioning temperature, which indicated that the carbides did not dissolve completely during austenisation.

The microstructure of the H21 tool steel was characterised using TEM. Figure 5.2 shows the microstructure after solutioning and water quenching.

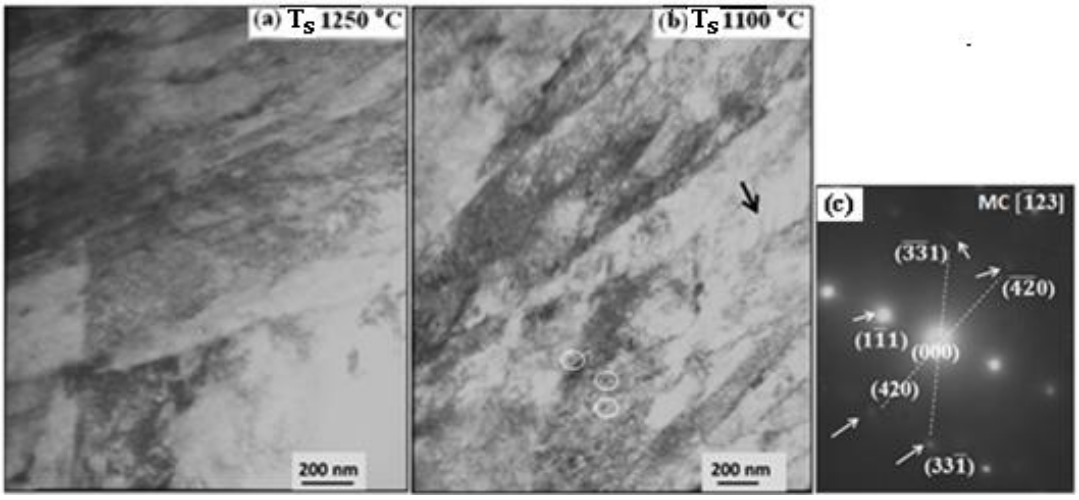

Figure 5.2 Bright field TEM images of the as quenched H21 tool steel showing (a) the presence of lath martensite, (b) lower bainite (indicated by arrow) and MC carbides (indicated by circles), and (c) diffraction pattern of MC carbide.

Figure 5.2 gives strong evidence that the microstructure of the H21 tool steel after solutioning and water quenching consisted of lath martensite and carbides. The presence of MC carbide is further discussed in Section 5.2.2.1. The morphology of the martensite was of lath type and was heavily dislocated, which is consistent with a previous investigation (Wilson, 1994). The width of martensite laths varied between 0.2 to 0.6 μm, and they were slightly parallel to each other. The morphology of martensite did not change significantly as the solutioning temperature increased from 1100 to 1250 ^{o}C. TEM studies also confirmed that lower bainite was present after solutioning at 1100 ^{o}C and water quenching (Figure 5.2b). The phase transformation during cooling from the solutioning temperature led to the formation of lower bainite in which fine carbides occurred in one direction across the laths and at an angle of 60^{o} to the lath axis. The internal stresses that built up during the transformation from austenite to martensite accelerated the formation of bainite (Radcliffe and Rollason, 1959, Howard and Cohen, 1948). The TEM investigation on the as quenched H21 tool steel after solutioning at 1250 ^{o}C found micro-twins in the lath martensite with spacing in the range 20 to 80 nm, as can be seen in Figure 5.3.

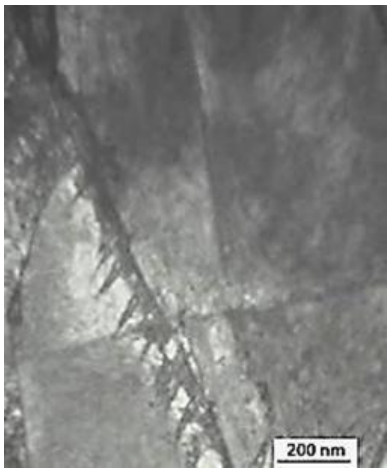

Figure 5.3 A bright field TEM image of the H21 tool steel after solutioning at 1250 ^{o}C and water quenching showing a lath martensite with micro-twins.

The formation of micro-twins can be explained as follows. During austenisation the carbides that dissolved into the matrix produced a local area of austenite enriched with C. When the rapid cooling was performed, this carbon was trapped in the retained austenite and the latter that was rich in C transformed to martensite with micro-twin formation.

Generally, the assessment of the M_s temperature is completed by means of the CCT diagram. However, several sources can be used to calculate that M_s temperature. The M_s temperature was calculated using equation 2.6 produced by Andrews (1965) by reason that it can be used for most types of steels. The volume fraction of martensite was calculated using equations 2.8 and 2.9 (Koistinen and Marburger, 1959). The M_s temperature of the H21 tool steel was 354 ^{o}C, which is lower than the 370 ^{o}C obtained from literature (Roberts *et al.*, 1998). The calculated volume fraction of martensite was 97.3 % and the volume fraction of retained austenite was 2.7 %. Note that the equations 2.8 and 2.9 do not have any correlation with solutioning temperature. The presence of retained austenite was observed by TEM using the dark field technique. Figure 5.4 shows the blocky retained austenite in the H21 tool steel after solutioning and water quenching.

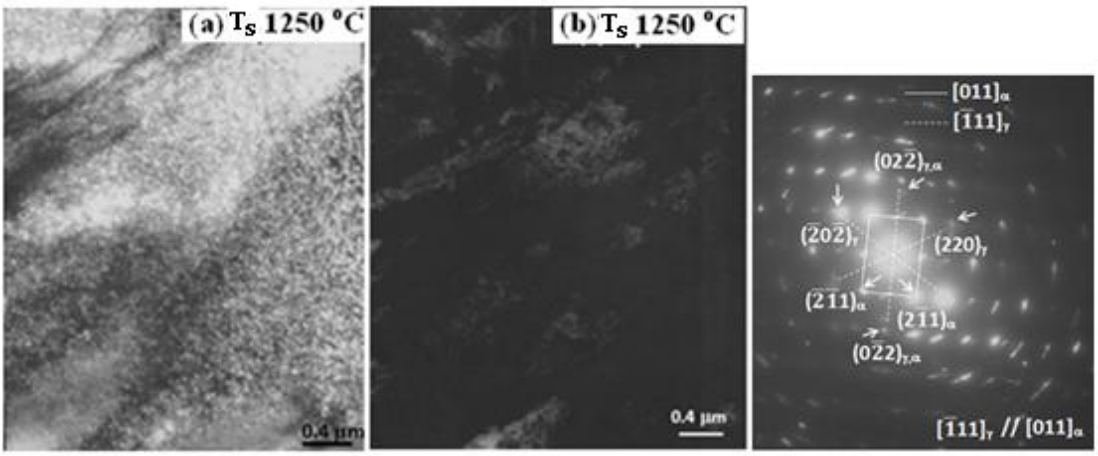

Figure 5.4 Bright field (a) and dark field (b) TEM images of the H21 tool steel after solutioning and water quenching showing retained austenite and the selected area diffraction pattern taken at the interface between retained austenite and martensite with $[111]_\gamma$ // $[011]_\alpha$.

The diffraction pattern in the Figure 5.4 shows that the orientation between martensite and austenite was in good agreement with a Kurdjumov-Sachs orientation relationship. Although quantitative measurements of the volume fraction of retained austenite were not made from the as quenched microstructure of the H21 tool steel, a qualitative assessment indicated that a larger volume fraction of retained austenite was associated with a higher solutioning temperature as a result of more carbides being put into solution leading to higher C content in austenite. The stability of retained austenite is considered to be related to the C content in the austenite phase, the higher the C content the more stable the retained austenite.

Turning now to the experimental evidence on the as quenched H23 tool steel, the Figure 5.5 shows the as quenched microstructures of the H23 tool steel from different solutioning temperatures.

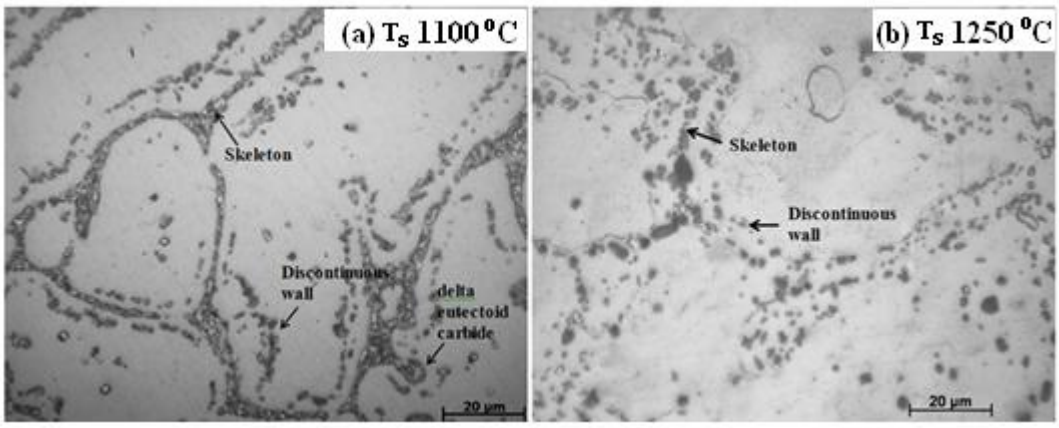

Figure 5.5 Optical images of the microstructure of the H23 tool steel after solutioning and water quenching.

The as quenched microstructures of the H23 tool steel, Figure 5.5, show that ferrite and carbide were present and no martensite was observed in both solutioning temperatures due to the M_s temperature of this tool steel being approximately - 46 ^oC (Roberts *et al.*, 1998). Compared with the as cast microstructure in Figure 4.4b the solutioning temperature affected the separation and dissolution of carbides. At the lower solutioning temperature, the carbides were still interconnected in the thick layer (skeleton), and there was dissolution of carbides in the discontinuous wall. At the higher solutioning temperature, the carbides in the skeleton were separated and coarser, and the carbides in the discontinuous wall had dissolved more into the matrix. The as quenched microstructures of the H23 tool steel exhibited the same trend as observed in the as quenched H21 tool steel, namely the higher solutioning temperature, the lower volume fraction of carbides owing to more carbide being dissolved into the matrix. At the higher solutioning temperature there was still a large volume fraction of undissolved carbides. There was no indication of carbide needles inside the grains in the as quenched microstructures of the H23 tool steel, as observed in the as cast condition, see Figure 4.9. It seems therefore that those small needle carbides dissolved easily into the matrix due to them having a higher surface to volume ratio than the larger carbides, in other words smaller carbides were less stable than larger carbides for the same type of carbide.

The prior ferrite grain size in the as quenched H23 tool steel could not be calculated because the discontinuous wall tended to disappear as well as skeleton, see Figures 4.2 and 5.5. It was thus impossible to determine the intersection when using the linear intercept method as done in the as cast microstructure. TEM study was carried out for the higher solutioning temperature sample to support the as quenched microstructure analyses, see Figure 5.6.

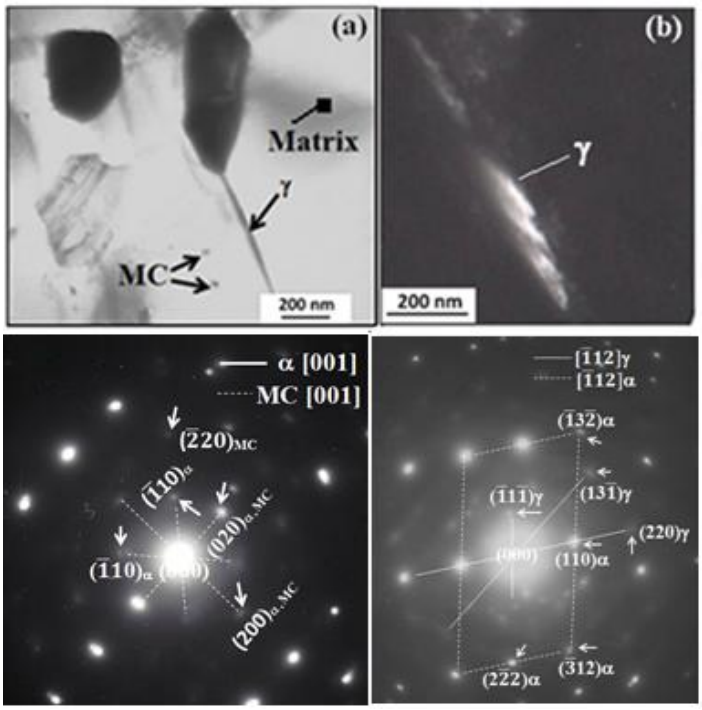

Figure 5.6 Top row: (a) a bright field TEM image taken from thin foil showing MC carbides, ferrite (matrix) and retained austenite in the H23 tool steel after solutioning at 1250 ^{o}C and water quenching and (b) a dark field TEM image showing retained austenite. Bottom row: the SADPs of MC carbide in the ferrite matrix and the SADPs of retained austenite and ferrite.

The diffraction patterns of the austenite, ferrite and MC carbide in Figure 5.6 confirmed that those phases existed in the as quenched microstructure. As this tool steel contained high ferrite stabilising elements (Cr and W), it is not surprising that the as quenched microstructure consisted of retained ferrite. In bright field TEM imaging, the retained austenite was of a film type with width 10 to 60 nm and located

at the ferrite lath boundaries. The formation of retained austenite was due to the dissolution of the carbides resulting locally in high C content in the matrix and the water quenching from the high solutioning temperature did not provide sufficient time for the austenite to transform to ferrite completely. Further discussion of the MC carbides in the as quenched H23 tool steel is given in Section 5.2.2.2 and the volume fraction of the retained austenite measured using XRD is discussed in Section 5.2.4.1.

5.2.2 Identification of Carbides

5.2.2.1 The H21 Tool Steel

Figures 5.7 and 5.8 show SEM images and EDS spectra of matrix and carbides for the as quenched H21 tool steel.

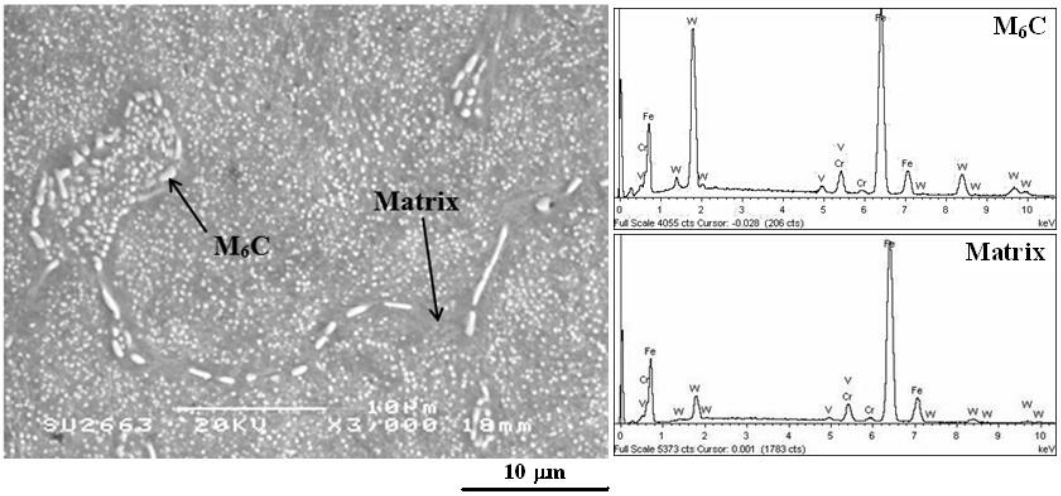

Figure 5.7 SEM secondary electron image of the H21 tool steel after water quenching from T_S = 1100 ^oC and EDS spectra of matrix and M_6C carbides.

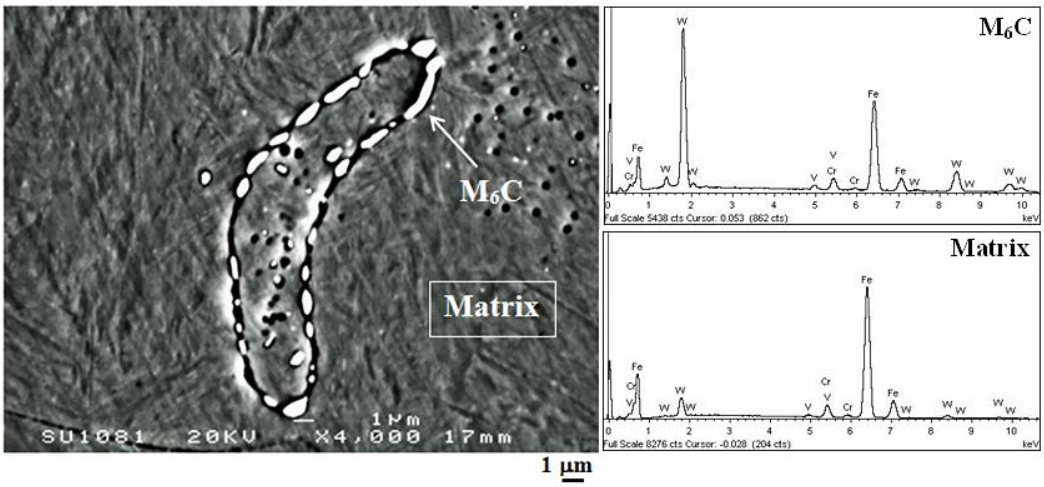

Figure 5.8 SEM secondary electron image of the H21 tool steel after water quenching from T_S = 1250 ^oC and EDS spectra of matrix and M_6C carbides.

The Figures 5.7 and 5.8 show that there was only one type of coarse carbide present in the as quenched H21 tool steel from both solutioning temperatures. These carbides were identified by SEM-EDS as M_6C carbides with their typical EDS spectra in Figures 5.7 and 5.8 showing the high W and Fe peaks. The morphology of coarse M_6C carbide was not significantly different compared with the as cast condition, where it had rodlike, spherical and irregular morphologies, see Figure 4.5. At the solutioning temperature (T_S) of 1100 ^oC, it was observed that a high volume fraction of fine spherical M_6C carbides existed in the matrix, Figure 5.7. This was attributed to the formation of secondary M_6C carbides. With SEM-EDS the presence of secondary M_6C carbides in the as quenched steel from 1250 ^oC was not observed. Therefore, two categories of the M_6C carbides existed in the as quenched H21 tool steel for 1100 ^oC solutioning temperature, one was the undissolved primary carbide with larger size and the other one was secondary carbide with finer size formed during austenisation.

The formation and growth of carbides is controlled by diffusion. At the lower solutioning temperature nucleation of carbides was possible, thus there were many more carbides but their growth was slower and as a result there was a high volume fraction of secondary fine carbides but with small size. These fine secondary

carbides were far from the equilibrium condition and less stable due to having higher surface to volume ratio than the larger carbides and hence they dissolved easily at the higher solutioning temperature. The primary M_6C carbides grew and became coarser at the higher solutioning temperature and did not dissolve completely during solutioning at 1250 ^oC, presumably because of the short solutioning period, see Figure 5.8. SEM-EDS quantitative data of the matrix and carbides is given in Table 5.1.

Table 5.1 SEM-EDS data of the as quenched H21 tool steel (wt%).

T_S (^oC)	Phase	Element				Comment
		Fe	Cr	V	W	
1100	Matrix	87.1 ± 1.4	3.7 ± 0.0	0.5 ± 0.1	8.8 ± 1.3	Martensite
	Carbide	60.2 ± 6.9	4.9 ± 0.1	1.6 ± 0.0	33.3 ± 7.0	M_6C^*
1250	Matrix	88.0 ±1.0	4.4 ± 0.1	0.6 ± 0.1	7.0 ± 0.9	Martensite
	Carbide	41.9 ± 5.9	3.6 ± 0.2	1.5 ± 0.1	53.0 ± 5.8	M_6C^*

Table 5.1 shows that the M_6C carbide was rich in W, and that the W content in M_6C increased with increasing solutioning temperature. As mentioned before, the spatial resolution for SEM-EDS in this study was almost 1 μm. In general, the average size of the carbides analysed by EDS was 0.5 μm and thus there was interference between the interaction volume and the matrix. Hence the quantitative data should be considered with caution given the size of the carbides. The composition of the matrix was in good agreement with that calculated using ThermoCalc (90.7Fe, 3.1Cr, 0.6V, 5.6W (wt%) at T_S = 1100 ^oC and 88.5Fe, 3.1Cr, 0.7V, 7.7W (wt%) at T_S = 1250 ^oC).

The TEM study also confirmed the presence of the MC carbide in the as quenched H21 tool steel from 1100 ^oC solutioning temperature, see Figure 5.2, that exhibited spherical morphology. According to Karagoz and Fischmeister (1987), the rate of carbide dissolution during austenisation increases in the sequence MC, M_6C, M_7C_3, $M_{23}C_6$. The MC carbide is thermodynamically stable and does not completely dissolve even at the high solutioning temperature (Totten, 2006). Therefore, it is

suggested that the MC carbide in the as quenched microstructure after austenisation was undissolved primary carbide.

5.2.2.2 The H23 Tool Steel

Figures 5.9 and 5.10 show SEM images and EDS spectra of matrix and carbides formed in the as quenched H23 tool steel.

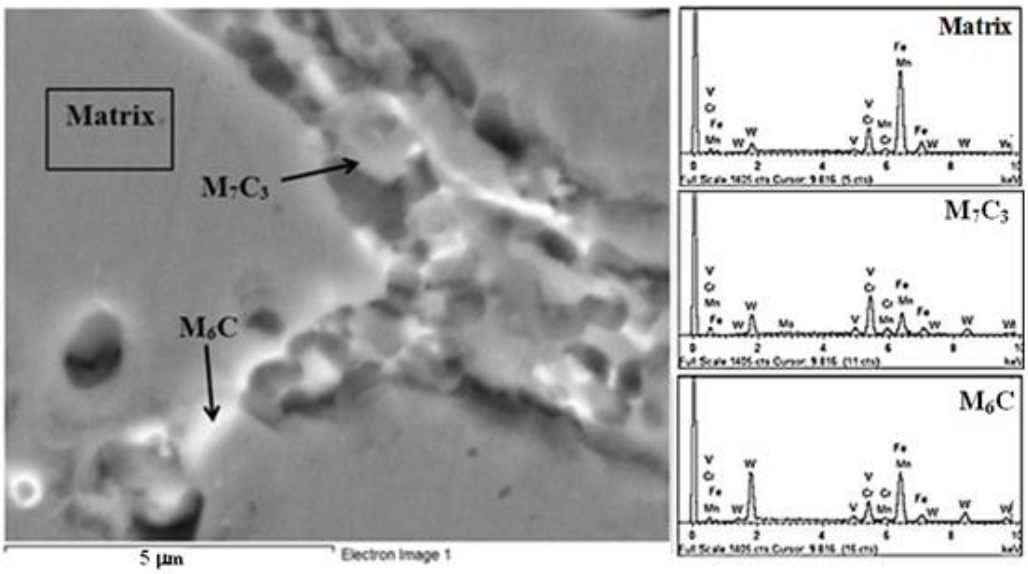

Figure 5.9 SEM back scatter electron image of the H23 tool steel after water quench from T_S = 1100 ^oC and EDS spectra of matrix and carbides.

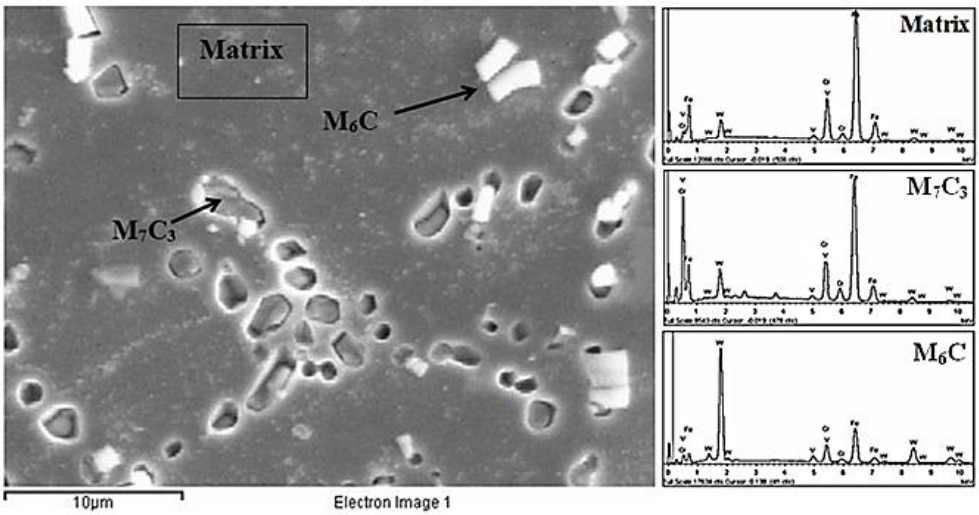

Figure 5.10 SEM back scatter electron image of the H23 tool steel after water quench from T_S = 1250 ^oC and EDS spectra of matrix and carbides.

Figures 5.9 and 5.10 show that there were carbides that exhibited two different colours under BSE imaging conditions. This indicated that two types of coarse carbides formed in the as quenched H23 tool steel and these were identified by XRD (see Section 5.2.4) and SEM-EDS as the M_6C (white) and M_7C_3 carbides (grey). The typical EDS spectrum of the M_7C_3 carbides is shown by the presence of Cr peak higher than Fe peak or vice versa. Both types of carbides had the same morphologies, e.g. rodlike, irregular and sphere. The presence of the $M_{23}C_6$ carbide in the as quenched H23 tool steel from both solutioning temperatures was not confirmed by SEM. The $M_{23}C_6$ carbides easily coalesce and coarsen during austenisation (Abe *et al.*, 1991, Pickering, 1987) and could dissolve completely at ~1095 ^oC (Krauss, 2005). It can be said that the primary $M_{23}C_6$ carbides (see Section 4.8.1) dissolved gradually during austenisation enriching the ferrite matrix with Cr and C, and as a result nucleation of the M_7C_3 carbide occurred, see Figures 5.9 and 5.10. The M_7C_3 carbide was rich in Cr and W (see Table 5.2). The M_7C_3 carbide dissolves at higher solutioning temperature than the $M_{23}C_6$ carbides (Wilson, 1975). The nucleation of M_7C_3 carbides directly from ferrite has been reported by Dyson and Andrews (1969) and Kuo (1953). The SEM-EDS quantitative data of the carbides is summarised in Table 5.2. The compositions of the matrix were in good agreement with those calculated using ThermoCalc (79.9Fe, 13.1Cr, 1.1V, 5.9W (wt%) at T_S = 1100 ^oC and 76.9Fe, 12.6Cr, 1.1V, 9.4W (wt%) at T_S = 1250 ^oC). The compositions of the M_6C carbides based on calculated using Thermocalc are 22.9Fe, 5.5Cr, 4.7V, 66.9W (wt%) at T_S = 1100 ^oC and 23.7Fe, 6.2Cr, 3.2V, 66.9W (wt%) at T_S = 1250 ^oC.

Table 5.2 SEM-EDS data of the as quenched H23 tool steel (wt%).

T_S(^oC)	Phase	Element				Comment*
		Fe	Cr	V	W	
1100	Matrix	78.7 ± 0.6	13.8 ± 0.6	1.1 ± 0.0	6.5 ± 0.2	Ferrite
	Carbide	51.9 ± 5.7	13.0 ± 1.1	2.8 ± 0.2	32.4 ± 3.4	M_6C*
	Carbide	50.0 ± 1.2	27.7 ± 0.3	3.3 ± 0.2	19.1 ± 0.3	M_7C_3*
1250	Matrix	75.0 ±0.9	14.0 ± 0.2	1.2 ± 0.0	9.8 ± 0.6	Ferrite
	Carbide	31.1 ± 6.6	9.1 ± 0.7	2.6 ± 0.2	56.9 ± 3.3	M_6C*
	Carbide	76.1 ± 1.9	11.2 ± 1.2	1.1 ± 0.1	11.6 ± 0.9	M_7C_3*

* The quantitative data should be considered with caution given the size of the carbides.

As T_S increased the volume fraction of M_7C_3 decreased and that of M_6C increased. Table 5.2 shows that the Cr content in the M_7C_3 carbide decreased with increasing solutioning temperature. The diffusion rate of alloying elements increases with increasing temperature, and the diffusion rate of Cr is higher than W. Since the M_7C_3 carbide was rich in Cr, its dissolution was affected by its Cr content that achieved its maximum value (and thus stability of this carbide) at the solutioning temperature of 1100 ^oC. The dissolution rate of M_7C_3 was faster than that of M_6C carbides, and the M_7C_3 continued to dissolve at the higher solutioning temperature. It can be seen from Table 5.2, that at solutioning at 1250 ^oC the Cr content in the M_7C_3 carbides decreased. This was in contrast with the M_6C carbides where the W content increased with increasing solutioning temperature.

Using SEM-EDS with accelerating voltage 20 kV requires size of the carbide to be analysed to be greater than 1 μm in order to obtain proper quantification without overlap from another constituent in the interaction volume. The quantitative data in Table 5.2 was taken from carbides with size in the range 0.3 – 1.5 μm. Thus, interference between the interaction volume and the matrix for the smaller carbides could not be avoided. In addition, from the data in Table 5.2, it can be seen that there was a minor deference in composition of alloying elements between the M_7C_3 carbides and the matrix at 1250 ^oC owing to the interference of the relatively large interaction volume with the matrix.

Fine MC carbides in the as quenched H23 tool steel after austenisation at 1250 ^{o}C were observed by TEM, see Figure 5.6. The size of MC carbide (~ 40 to 50 nm) was not significantly different compared with the as cast condition, which indicated that this carbide was undissolved primary carbide (see Figure 4.6) owing to its high thermal stability. The MC carbide and ferrite matrix exhibited the Baker-Nutting relationship. It should be noted that the primary MC carbide in the H23 tool steel was not predicted by the thermodynamic calculations, see Chapter 4, Section 4.7.3.

5.2.3 The Effect of Solutioning Temperature on Hardness

The hardness of the as quenched tool steels was controlled by the phase transformations that occurred during austenisation and water quenching. The hardness of the as quenched tool steels is given in Table 5.3.

Table 5.3 The as quenched hardness of the H21 and H23 tool steels.

Tool steel	Hardness (HV)	
	T_S 1100 ^{o}C	T_S 1250 ^{o}C
H21	536 ± 7	574 ± 1
H23	279 ± 1	302 ± 7

Table 5.3 shows that the hardness of the as quenched tool steels was increased at the higher solutioning temperature. This was attributed to the dissolution of carbides into the matrix thus enriching the latter with alloying elements. The volume fraction of carbides of the as quenched tool steels is summarised in Table 5.4. The significant difference in hardness of the as quenched H21 and H23 tool steels (Table 5.3) was also attributed to the coexistence of ferrite with austenite in the H23 tool steel. The high W and Cr contents in the H23 tool steel stabilised the ferrite at the high solutioning temperature. This ferrite was stable to room temperature and did not contribute to hardening. Thus the lower hardness with decreasing solutioning temperature was not only due to the lower dissolution of carbides but also due to the higher volume fraction of ferrite. In addition, the austenite did not transform to

martensite because the M_s temperature is far below room temperature. It can be said that the low as quenched hardness of the H23 tool steel was directly attributable to the high content of ferrite.

Table 5.4 The volume fraction of carbides (V_c) and their average size (μm) in the H21 and H23 tool steels after water quench from different solutioning temperatures**.**

Tool steel	As cast condition		As quenched condition			
			T_S 1250 ^oC		T_S 1100 ^oC	
	V_c (%)	Mean size (μm)	V_c (%)	Mean size (μm)	V_c (%)	Mean size (μm)
H21	18.3 ± 2.2	0.3 ±0.1	14.7 ± 0.4	0.4 ± 0.1	15.1 ± 0.7	0.2 ± 0.1
H23	21.5 ± 0.4	0.4 ± 0.1	13.9 ± 1.0	0.5 ± 0.1	15.3 ± 1.9	0.4 ± 0.2

From Table 5.4, it can be seen that the solutioning temperature had a strong influence on the volume fraction of carbides, which decreased with increasing solutioning temperature thus enriching the matrix with alloying elements. Compared with the volume fraction in the as cast condition, the percentage decrease of the volume fraction of carbides in the as quenched H23 tool steel was higher than in the H21 tool steel. This is linked with the Cr content in the H23 tool steel that was higher than in the H21 tool steel, which means that the H23 tool steel contained high volume fraction of Cr rich carbide, and the dissolution rate of carbides that increases in the sequence MC, M_6C, M_7C_3, $M_{23}C_6$ (Karagoz and Fischmeister, 1987). In contrast, the H21 tool steel contained high volume fraction of the W rich carbides (M_6C carbides). Higher dissolution rate of the Cr rich carbides meant that more of them were dissolved in the matrix compared with the M_6C carbides. Hence, it is suggested that the decrease in the volume fraction of carbide in the as quenched H23 tool steel was due to the dissolution of Cr rich carbides.

In this study, the correlation between mean size of carbides and the solutioning temperature cannot be conclusive, especially in the H23 tool steel since the mean size of carbides was measured individually and the carbide networks still existed at

the lower solutioning temperature. However, the qualitative analyses indicated that at the higher solutioning temperature the undissolved carbides tend to become coarser.

5.2.4 X-ray Diffraction of the As Quenched H21 and H23 Tool Steels

XRD was performed to confirm the phases that were present in the as quenched microstructures. Figure 5.11 shows XRD results of the as quenched H21 tool steel.

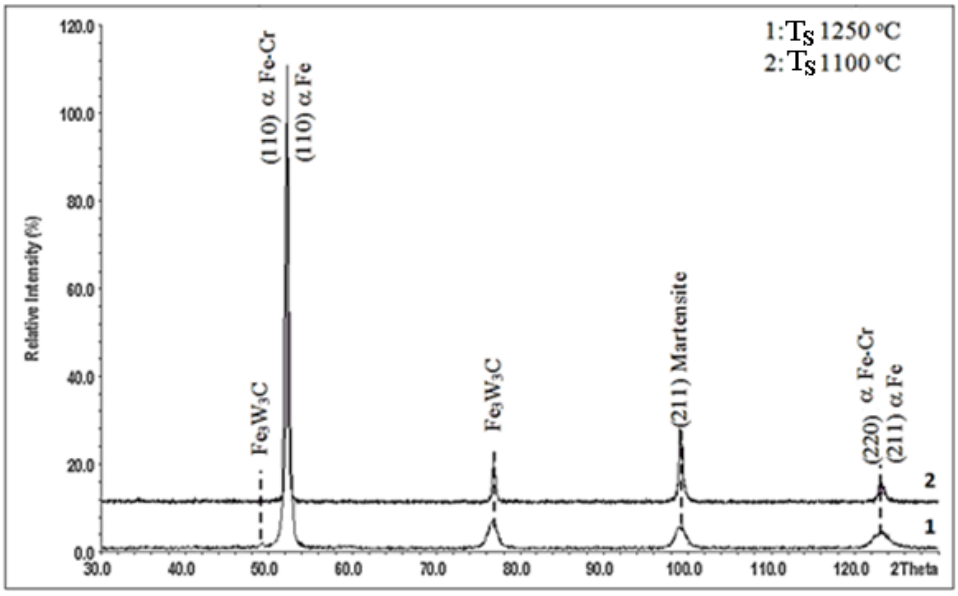

Figure 5.11 X-ray diffractograms of the as quenched H21 tool steel.

The XRD confirmed the presence of α Fe-Cr and α Fe (the super saturated solutioning), martensite and that the M_6C carbide was Fe_3W_3C. The ICDD cards used for phase identification are given in Table 5.5.

Table 5.5 The ICDD cards used for the identification of the diffraction peaks in the as quenched H21 tool steel.

Phase	ICDD card
α Fe	6-696
α Fe-Cr	34-396
M_6C (Fe_3W_3C)	41-1351
martensite	44-1289

The intensity of the Fe_3W_3C carbide peaks at the solutioning temperature of 1100 ^oC was higher than at the solutioning temperature of 1250 ^oC, which indicated that the volume fraction of this carbide was higher at the former solutioning temperature. This is in good agreement with the microstructure studies and the quantitative measurement of volume fraction of carbides, see Table 5.4. No peaks corresponded to the retained austenite and MC carbides due to their volume fraction being very low. No distinction can be made between ferrite and bainite phases due to the fact that theoretical X-ray diffraction intensities are nearly the same for the two phases.

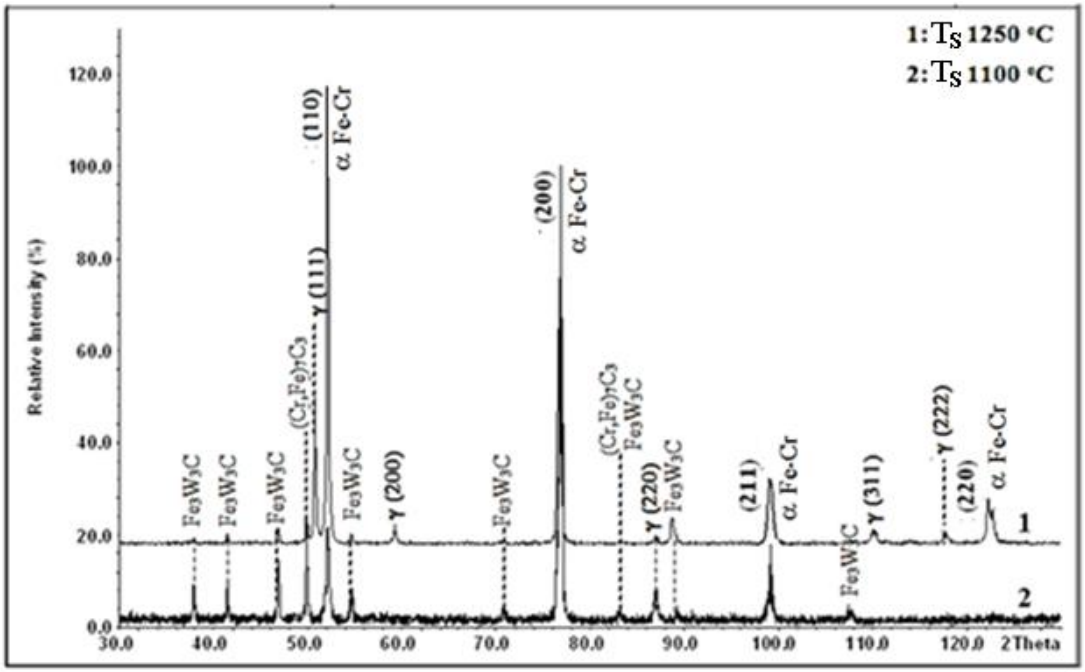

Figure 5.12 X-ray diffractograms of the as quenched H23 tool steel.

The XRD diffractogram of the as quenched H23 tool steel can be seen in Figure 5.12. The peaks corresponded to α Fe-Cr (the super saturated solutioning), austenite, and the M_6C and M_7C_3 carbides and were identified using the ICDD cards given in Table 5.6.

Table 5.6 The ICDD cards used for the identification of the diffraction peaks in the as quenched H23 tool steel.

Phase	ICDD card
α Fe-Cr	34-396
austenite (γ)	52-512
M_6C (Fe_3W_3C)	41-1351
M_7C_3 $(Cr,Fe)_7C_3$	5-720

The M_6C carbide was Fe_3W_3C, and the M_7C_3 carbide was $(Cr,Fe)_7C_3$. There were more peaks of the Fe_3W_3C and $(Cr,Fe)_7C_3$ carbides with higher intensity at solutioning temperature 1100 ^oC than at 1250 ^oC, which indicated that the volume fraction of these carbides was higher at the lower solutioning temperature. As mentioned before the dissolution rates of M_6C and M_7C_3 carbides are different and the higher the solutioning temperature the more carbides dissolve in the matrix. The XRD results were consistent with the microstructures of the as quenched H23 tool steel.

5.2.4.1 Calculation of the Retained Austenite and Carbon Concentration in the As Quenched H23 Tool Steel

The X-ray diffractograms of the as quenched H23 tool steel showed the presence of retained austenite in both solutioning temperatures. The volume fraction of retained austenite was quantitatively determined using the XRD data and equation 3.14. This data however must be interpreted with caution because the reflections of austenite and ferrite selected for analyses must be free of interference from the carbides and no peaks should be close to each other (He, 2009). After careful analyses of the XRD data, the retained austenite content was determined from the integrated intensities with two austenite peaks $(200)_\gamma$, $(220)_\gamma$, and two ferrite peaks $(200)_\alpha$ and $(211)_\alpha$. The $(111)_\gamma$ and $(110)_\alpha$ peaks were the strongest peaks for austenite and ferrite respectively, but were too close to each other to be resolved and therefore these lines were not used in the calculation. Other lines not included into the calculation were

the small split peaks $(311)_\gamma$, $(222)_\gamma$ and $(220)_\alpha$ (probably a K_β reflection). The 2θ peak position values of the austenite and ferrite phase lines for the as quenched H23 tool steel are given in Table 5.7. The integrated intensities of each phase were obtained by area integration over the defined regions for each peak using ImageJ software.

Table 5.7 XRD data used for the calculation of retained austenite volume fraction in the as quenched H23 tool steel[1].

Phase	(hkl)	2θ	R_γ and R_α [2]	T_S = 1250 °C				T_S = 1100 °C			
				I	$I/R_{\gamma,\alpha}$	Mean of $I/R_{\gamma,\alpha}$	V_c [3] (%)	I	$I/R_{\gamma,\alpha}$	Mean of $I/R_{\gamma,\alpha}$	V_c [3] (%)
γ	(200)	59.3	66.8	3814.3	57.1	37.2	13.9	-		26.3	15.3
	(220)	88.7	41.0	705.2	17.2			1078.3	26.3		
α	(200)	76.9	28.6	17920.8	626.6	342.1		17769.2	621.3	339.1	
	(211)	98.9	66.9	3846.8	57.5			3813.3	57.0		

[1] For symbols, see Section 3.4
[2] (ASTM E975-03, 2003)
[3] Volume fraction of carbide, see Table 5.4.
T_S = solutioning temperature

The volume fraction of retained austenite (V_γ) after water quenching from T_S = 1100 ^oC and T_S = 1250 ^oC were 6.1 % and 8.4 %, respectively. The volume fraction of retained austenite in the as quenched H23 tool steel increased with increasing solutioning temperature. This increase was attributed to more carbides being dissolved in the matrix that became rich in alloying elements and carbon. The higher the carbon concentration in austenite the larger the volume fraction of retained austenite (Matlock *et al.*, 2001).

Variation in austenite peak positions and shapes for the two solutioning temperatures reflected changes that took place due to carbon concentration. To estimate the stability of retained austenite, the carbon concentration in retained austenite, C_γ, was determined from the XRD data by calculating the austenite lattice parameter using the equation 5.1 (Ridley *et al.*, 1969, Ruhl and Cohen, 1969):

$$C_\gamma = \frac{(a_\gamma - 0.3572)}{0.0033} \quad (5.1)$$

where a_γ is the lattice constant of austenite (nm), and C_γ is the carbon concentration in austenite (wt%). The wavelength of the radiation used is λ_{Cr} = 0.179 nm. The results of the calculation of C_γ are given in Table 5.8.

Table 5.8 The calculation of a_γ and C_γ in retained austenite of the as quenched H23 tool steel.

T_s (°C)	hkl	2θ	d (nm)	a_γ (nm)	Mean of a_γ (nm)	C_γ (%)	Mean of C_γ (%)	M_s temp. of $\gamma_{retained}$ (°C)*
1100	220	88.7	0.127	0.360	0.360	0.989	0.99	- 32.8
1250	200	59.3	0.181	0.361	0.361	1.238	1.19	- 97.47
	220	88.7	0.128	0.361		1.149		

* Calculated using equation 2.6 and the alloying element content determined by SEM-EDS see Table 5.2.
T_s = solutioning temperature

The lattice parameter of austenite was 0.360464 nm at 1100 °C, and increased to 0.360914 nm when the solutioning temperature was 1250 °C. With increasing solutioning temperature, the dissolution rate of carbides increased and the C content in austenite increased. These C atoms occupied interstitial positions in the austenite lattice and the latter expanded. The high W content in the H23 tool steel probably contributed to increasing the lattice parameter of austenite due to the atomic radius of W being higher than that of Fe, see also Table 5.2.

Increasing the carbon concentration shifted the M_s temperature to lower value and the austenite became stable. Therefore, the stability of retained austenite increased with increasing solutioning temperature, which in agreement with previous work (Yaso *et al.*, 2009). Note that the actual values of the M_s temperature should be lower

than the data shown in Table 5.8 since these calculations did not consider the Mn and Ni elements.

5.3 Double Tempering of the H21 Tool Steel

5.3.1 The Effect of Double Tempering Temperature on Microstructure

It is strongly recommended to temper the quenched tool steels at least twice to improve the toughness and thermal stability of the microstructure, which would not be achieved by a single tempering process (Roberts *et al.*, 1998). The double tempering (DT) process also increases the secondary hardness by allowing the amount of retained austenite to transform to lower bainite and increases the volume fraction of carbides. Figure 5.13 shows the microstructures of the H21 tool steel after double temper at different temperatures.

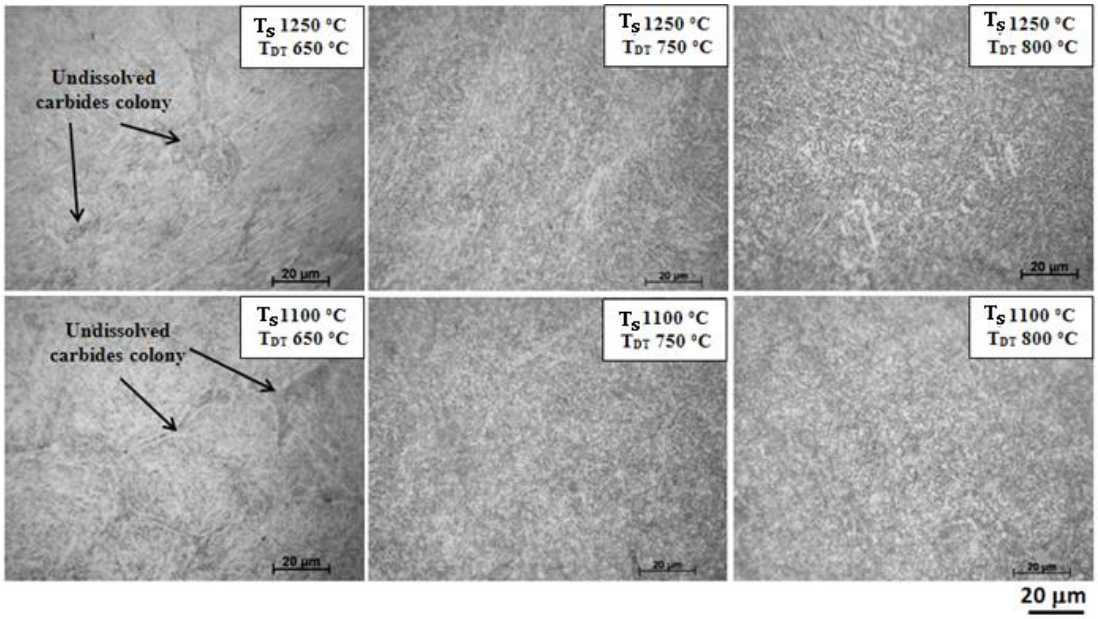

Figure 5.13 Optical images of the microstructure of the H21 tool steel after solutioning and double tempering at different temperatures.

Optical microscopy did not reveal any significant changes in the microstructure accompanying double tempering, even at 800 ^{o}C, Figure 5.13. The PAGBs were not revealed as they were covered by carbides. In order to study the effect of double tempered condition on the precipitating carbides and matrix, a TEM study was

carried out. In general, the bright field TEM images (Figures 5.14, 5.15 and 5.16) showed that the carbides precipitated along the lath martensite boundaries (interlath) and within laths (intralath). The nucleation of most carbides was heterogeneous and took place preferentially at lath boundaries and prior austenite grain boundaries, as these are energetically favorable sites. The carbides exhibited rod-like, spherical and irregular morphology.

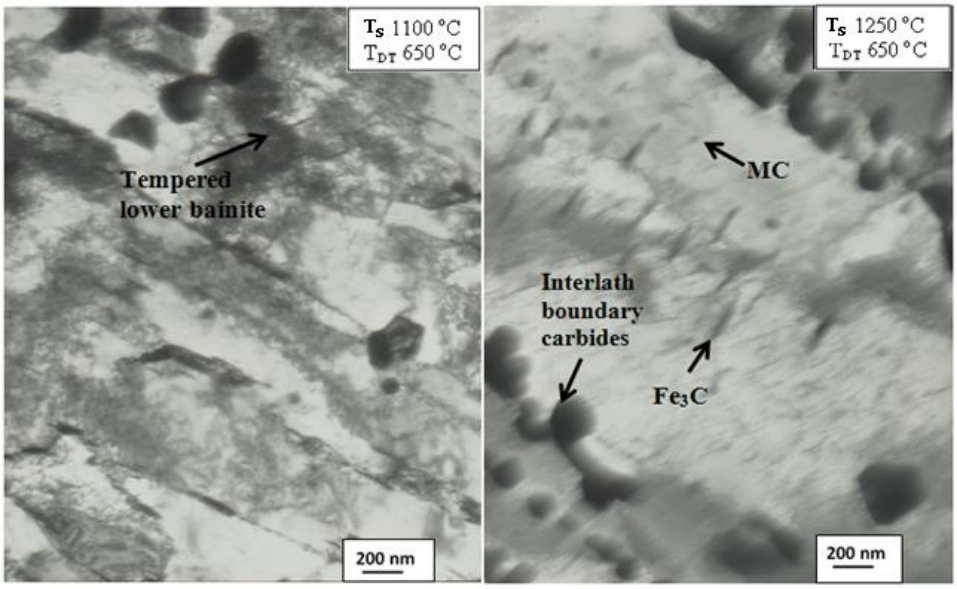

Figure 5.14 Bright field TEM images of the H21 tool steel after solutioning at different temperatures and double tempering at 650 ^{o}C.

It is apparent from Figure 5.14 that the double tempered microstructure at 650 ^{o}C from both solutioning temperatures of the H21 tool steel consisted of lath tempered martensite, and carbides. The lath martensite morphology was still present with low dislocation density in some areas and coarse needle or rod bar cementite carbides located in the interlath and intralath boundary. A tempered lower bainite was also observed after solutioning at 1100 ^{o}C and double temper at 650 ^{o}C, as indicated by the major axis of the cementite that forms parallel arrays at about 60^{o} to the axis of the bainitic lath (Bhadeshia, 2001). The thickness of cementite carbides was finer at the lower solutioning temperature. The double tempered microstructure at 650 ^{o}C showed that the dislocations formed networks through recovery process and this recovery seemed to be more effective at the higher solutioning temperature. The

microstructure in Figure 5.14 indicated that the recovery process occurred partially as the dislocation density was still high in some areas, especially after solutioning at 1100 ^{o}C and double tempering at 650 ^{o}C.

During tempering, the recovery process in the matrix was associated with migration of boundaries containing relatively low dislocation density (i.e., lath boundaries) and dislocation cells toward higher dislocation density boundaries (Caron and Krauss, 1972). The partial recovery of lath martensite during double temper at 650 ^{o}C was attributed to incomplete lath boundary migration owing to insufficient time for completing the recovery process. In addition, it seems that the presence of secondary carbides (M_2C carbides) within the matrix delayed the recovery process during tempering by impeding the dislocation movement through a pinning effect. Figure 5.14 also indicated that the recovery area at the lower solutioning temperature was less than at the higher solutioning temperature because the volume fraction of fine lath boundary carbides qualitatively was greater at the lower solutioning temperature than at the higher solutioning temperature and as a result the dislocation movement became more difficult at the lower solutioning temperature.

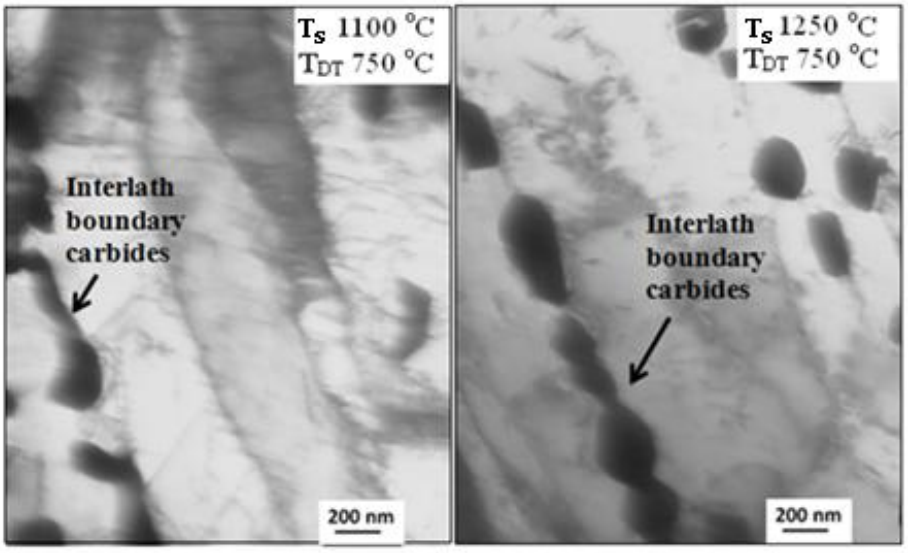

Figure 5.15 Bright field TEM images of the H21 tool steel after solutioning at different temperatures and double tempering at 750 ^{o}C.

Figure 5.15 shows TEM images after double temper at 750 ^{o}C. It can be seen that the morphology of interlath boundary carbides changed as the continuous rod-like tended to split in sphere or oval shape ones and the fine lath boundary carbides dissapeared. The lath martensite coarsened and tended to dissapear, especially at the higher solutioning temperature until the very late stages of tempering when equiaxed grains gradually developed. The martensite laths also showed extensive reduction in dislocation density, which was attributed to the dissolution of fine lath boundary carbides and as a result the dislocation movement accross the lath boundaries becomes easier. It is suggested that the carbides made a significant contribution in the recovery of the lath martensite matrix.

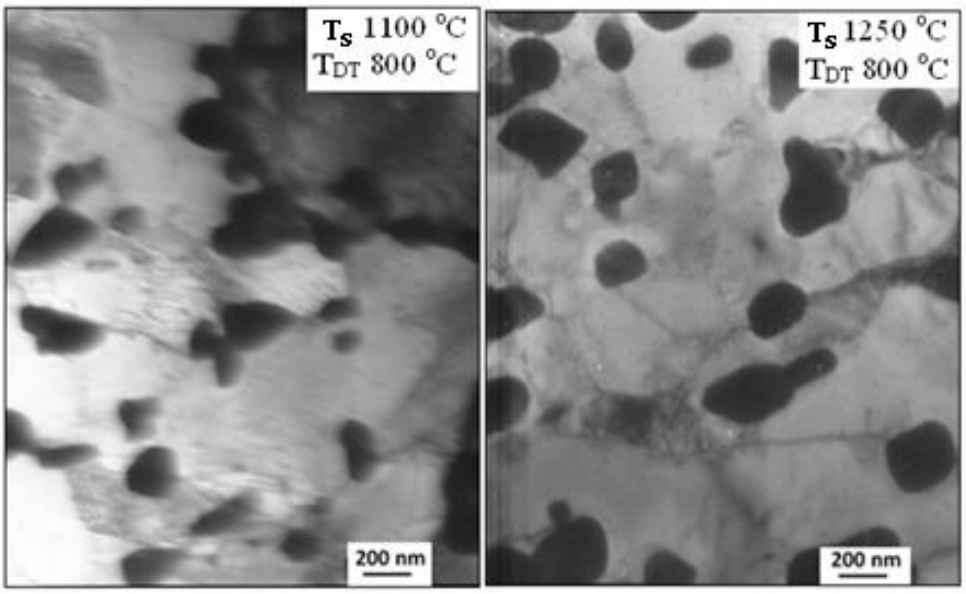

Figure 5.16 Bright field TEM images of the H21 tool steel after solutioning at different temperatures and double tempering at 800 ^{o}C.

The double tempered microstructure at 800 ^{o}C, Figure 5.16, showed that the lath morphology of the matrix had dissapeared and equiaxed grains were formed with clear boundaries. At the lower solutioning temperature of 1100 ^{o}C, the carbides coalesced on the grain boundaries. Spherical larger carbides were observed at prior austenite grain boundaries and inside the grains at both solutioning temperatures. The carbides that were located along the grain boundaries were larger than those within the grain interiors, which would suggest that the stable carbides nucleated first in the

grain boundaries and grew rapidly. The TEM study also indicated that the growth rate of the carbides was faster at the grain boundary (Speight, 1968). The formation of alloy carbides to replace cementite carbides occurred by nucleation at PAGBs that are energetically favorable nucleation sites (Durrand-Charre, 2004). It can be said that the size and morphology of lath boundary carbides and the morphology of the matrix were a function of the tempering temperature. The TEM investigations did not reveal the presence of retained austenite in the double tempered microstructures. The very low volume fraction of retained austenite that occurred after water quenching was attributed to the diffusion of alloying elements out of it to form carbides during the first temper and the retained austenite transformed to lower bainite on cooling to room temperature and later, when the second temper was performed, the lower bainite tranformed to tempered lower bainite or ferrite.

5.3.2. Identification of Carbides

It is important to identify the type of carbide formed during double temper as these could contribute to secondary hardening. The type of carbide in the double tempered H21 tool steel was identified by SEM-EDS and TEM.

a. M_6C carbide

The M_6C carbides observed in the double tempered H21 tool steel can be seen in Figure 5.17.

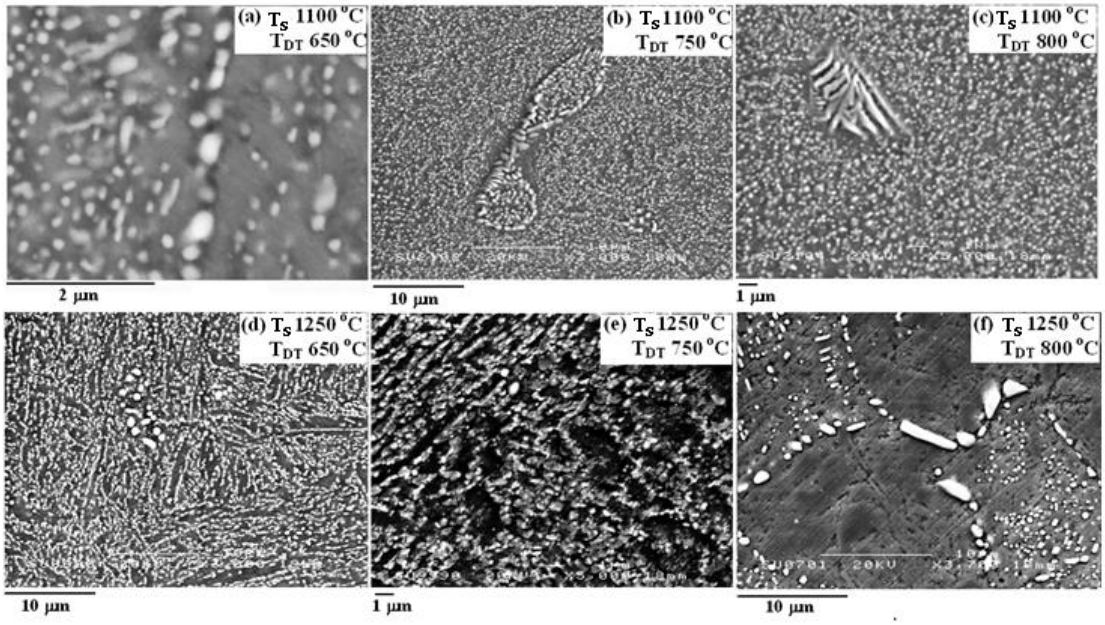

Figure 5.17 SEM secondary electron images of the double tempered H21 tool steel showing M_6C carbides.

The carbides in Figure 5.17 were identified by SEM-EDS as M_6C carbides. They exhibited spherical, irregular and rodlike morphologies with average carbide size 20 to 4000 nm. The fishbone morphology of M_6C carbide was also found (Figure 5.17c). Note that the fine M_6C carbides in the double tempered microstructure from solutioning at 1100 ^oC had formed before tempering was performed. It was difficult to establish whether the fine M_6C carbides formed before and or after double temper. Table 5.9 gives the SEM-EDS quantitative data for M_6C carbides in the double tempered condition.

Table 5.9 SEM-EDS analyses of the M_6C carbides in the H21 tool steel with different solutioning and double temper temperatures (wt%).

T_S (^oC)	T_{DT} (^oC)	Element				Phase*
		Fe	Cr	V	W	
1100	650	75.8 ± 4.4	3.9 ± 0.4	0.8 ± 0.2	19.5 ± 4.0	M_6C
	750	52.9 + 3.6	4.2 ± 0.6	1.2 ± 0.3	41.7 ± 2.7	M_6C
	800	41.6 ± 1.9	4.0 ± 0.4	1.7 ± 0.1	52.8 ± 2.3	M_6C
1250	650	46.9 ± 5.1	4.2 ±0.3	0.9 ± 0.2	48.9 ± 5.0	M_6C
	750	37.7 ± 3.1	3.6 ± 0.0	1.3 ± 0.1	57.4 ± 3.0	M_6C
	800	32.4 ± 3.3	3.4 ± 0.2	1.4 ± 0.1	62.8 ± 3.4	M_6C

It can be seen from the data in Table 5.9 that the M_6C carbides were rich in W and that their W content increased with increasing solutioning and tempering temperature, which was attributed to the growth and stability of the carbides. At the higher solutioning and tempering temperatures, the M_6C carbides became coarser and richer in W to enhance their stability. The lowest W content in the M_6C carbide was observed after solutioning at 1100 ^oC and double temper at 650 ^oC. At this condition the M_6C carbides were fine. Thus, the growth of the alloy carbides toward equilibrium involved considerable atom diffusion and was time and temperature dependent.

Concerning the size of carbides, there was interference of interaction volume with matrix in all double tempered conditions and the strongest interference occurred when the carbides were analysed for the condition T_S = 1100 ^oC and T_{DT} = 650 ^oC where the carbides' size was smaller than that at the higher solutioning and double tempering temperature. Therefore, the quantitative data should be considered with caution given the size of the carbides.

b. MC and $M_{23}C_6$ carbides

The fine carbides were identified by TEM-EDS, see Figure 5.18. Identification of carbides on thin samples by TEM-EDS gave better spatial resolution than SEM-EDS since the operating voltage was higher than SEM and as a result the interaction volume was smaller. The spatial resolution of TEM in the JEOL 2010F operated with accelerating volatage 200 kV was a few nanometers whereas the carbides' size was in the range 40 nm – 300 nm and as a result interference between the interaction volume of the MC carbides and matrix still occurred.

The presence of the MC carbide was identified by the highest peak of V in the TEM-EDS spectrum. The MC carbides had nearly spherical morphology and their size was around 35 nm to 45 nm. No significant difference in size compared with the as cast and as quenched condition was observed.

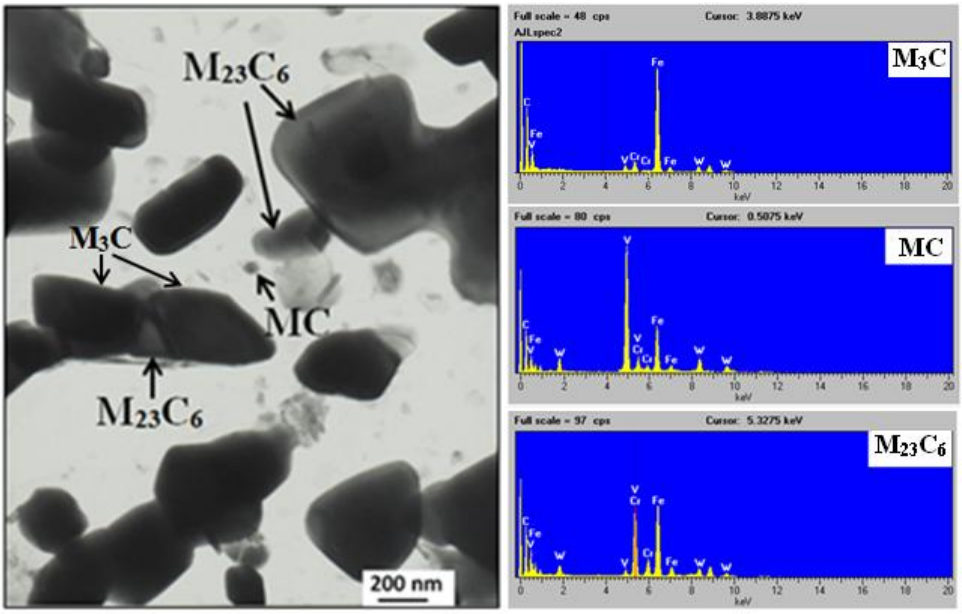

Figure 5.18 A bright field TEM image (JEOL 2010F) taken from thin foil showing carbides of different morphology in the H21 tool steel after solutioning at 1100 ^{o}C and double temper at 750 ^{o}C (left) and EDS spectra of the $M_{23}C_6$, MC and M_3C carbides (right).

The presence of the $M_{23}C_6$ carbides was confirmed by TEM-EDS, see Figure 5.18. The $M_{23}C_6$ carbides were secondary carbides and formed during double temper. The identification of carbides was based on qualitative analyses using EDS spectra. The spectrum of $M_{23}C_6$ carbides had similar height peaks of Fe and Cr or Fe/Cr count ratio of about 1. During tempering the formation of the $M_{23}C_6$ carbides, which had high Cr and W content occurred as the Cr replaced Fe gradually in M_3C and as the Cr content was getting higher, in order to become more stable, the M_3C carbide transformed to Cr based carbides (either M_7C_3 or $M_{23}C_6$ carbide). The diffusivity of W in ferrite is lower than that of other alloying elements and all elements (except C) have very low solubilities in M_3C. Kuo (1953) reported that the transformation of M_3C carbides to Cr rich carbides started by the increase of Cr concentration in the former until a saturation value was reached and then the M_3C transformed to Cr rich carbide (M_7C_3 or $M_{23}C_6$) and this transformation was accompanied by an abrupt

increase in the concentration of Cr. Secondary carbides usually do not form at tempering temperatures below 500 ºC because the alloying elements cannot diffuse rapidly enough to allow alloy carbides to nucleate (Totten, 2006). As described by Bhadeshia and Honeycombe (2006), in many alloy steels, the first alloy carbide to form is not the final equilibrium carbide. The presence of $M_{23}C_6$ carbide was also observed for a short tempering (1~2 h) of a steel containing 10 wt% W (Tunney and Ridley, 1979).

Figure 5.18 also shows *in-situ* transformation of carbides and is further discussed in Section 5.3.4.

c. M_3C and M_2C carbides

The M_3C carbide is rich in Fe, has orthorhombic crystal structure and as a consequence it is often referred to as Fe_3C or cementite. The Fe_3C carbides were identified based on their specific coarse needle or rod-shape morphology, as reported by Fujita and Bhadeshia (2002) and by electron diffraction. The cementite carbide was first formed in the early stages of tempering owing to the rapid diffusion of C in Fe and the low diffusivity of the substitutional alloying elements. This carbide can take into solution very considerable amounts of other alloying elements, in particular Cr can substitute for Fe gradually as the tempering temperature increases (Roberts *et al.*, 1998). The TEM image in Figure 5.19 shows different locations of cementite precipitation, which has been also reported by Furuhara *et al* (2004), and the presence of M_2C carbides.

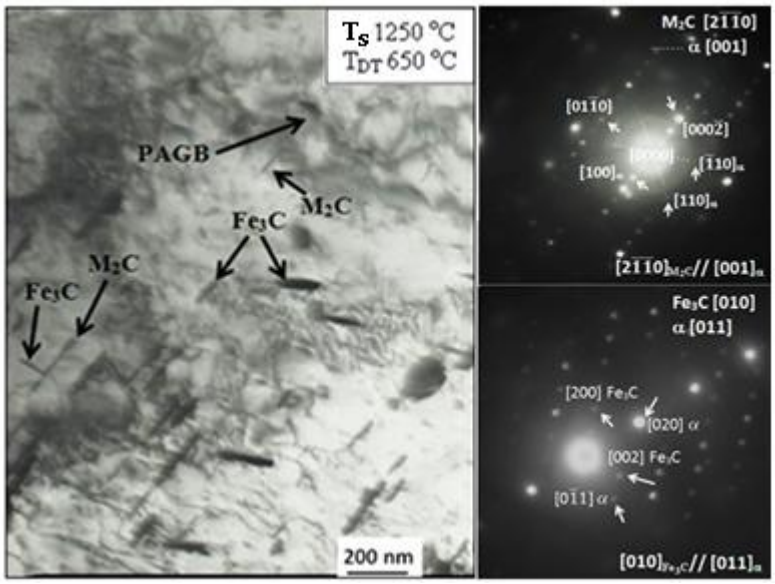

Figure 5.19 Bright field TEM image showing the presence of M_2C with the typical thin needle morphology and rod-like or bar shape Fe_3C carbides. The SADPs were taken at the interface between Fe_3C and matrix with $[010]_{Fe_3C}$ // $[011]_\alpha$ and between M_2C and matrix with $[2110]_{M_2C}$ // $[001]_\alpha$.

Figure 5.19 shows that the cementite and M_2C carbides precipitated from martensite during tempering with the Bagaryatsky orientation relationship with the matrix. The cementite carbides were observed to precipitate independently in the PAGB, the interlath and intralath boundaries. The presence of coarsened cementite within martensite laths as well as at lath boundaries indicated that the cementite carbides grew rapidly at double tempering temperature (T_{DT}) of 650 ^oC. The cementite carbide, which has a rod-like morphology, was slightly coarser at the interlath compared with that at the intralath boundaries. The thickness of cementite carbides in the interlath and within boundaries was in the range 10 to 15 nm, which is slightly finer than that reported by Furuhara *et al* (2004). This is probably due to the W content restricting the growth of cementite during temper. From the aforementioned locations, the appearance of bar shape cementite carbide indicated that cementite precipitation occurred in the early stages of tempering, and the precipitation of cementite was controlled by diffusion to interlath boundaries (fine interlath

cementite) and dislocations (finer intralath cementite) and the cementite grew with increasing tempering temperature (Caron and Krauss, 1972, Speich, 1969).

The M_2C carbides were identified by TEM (Figures 5.19) using electron diffraction and also based on their morphology, which was fine needle-like (Bhadeshia and Honeycombe, 2006, Fujita and Bhadeshia, 2002). The M_2C carbides had high aspect ratio, typically higher than 10 (Asadabad *et al.*, 2010). Figure 5.19 shows that the M_2C carbides nucleated at the Fe_3C/ferrite interface and ferrite lath boundaries. The M_2C carbides were rich in W and thus their formation was attributed to the high W content of the H21 tool steel. This type of carbide can also dissolve a considerable amount of Cr (Davis, 1995) and therefore their formation in the H21 tool steel was enhanced by the W and Cr content. In this study, the M_2C carbides were only observed after double temper at 650 ^oC. According to Cai *et al* (1998) the M_2C carbide in a steel containing 5 wt% Cr was not stable and rapidly transformed to stable $M_{23}C_6$ carbide. M_2C carbides were also observed by Asadabad *et al* (2010) in a 4.5Cr-2W-0. 25V-0. 1C steel (wt%) in the early stages of tempering at 600 ^oC for 0.5 hour.

5.3.3 X-ray Diffraction of the Double Tempered H21 Tool Steel

Figure 5.20 shows the XRD diffractograms after solutioning and double tempering of the H21 tool steel. The peaks were identified using the ICDD cards given in Table 5.10.

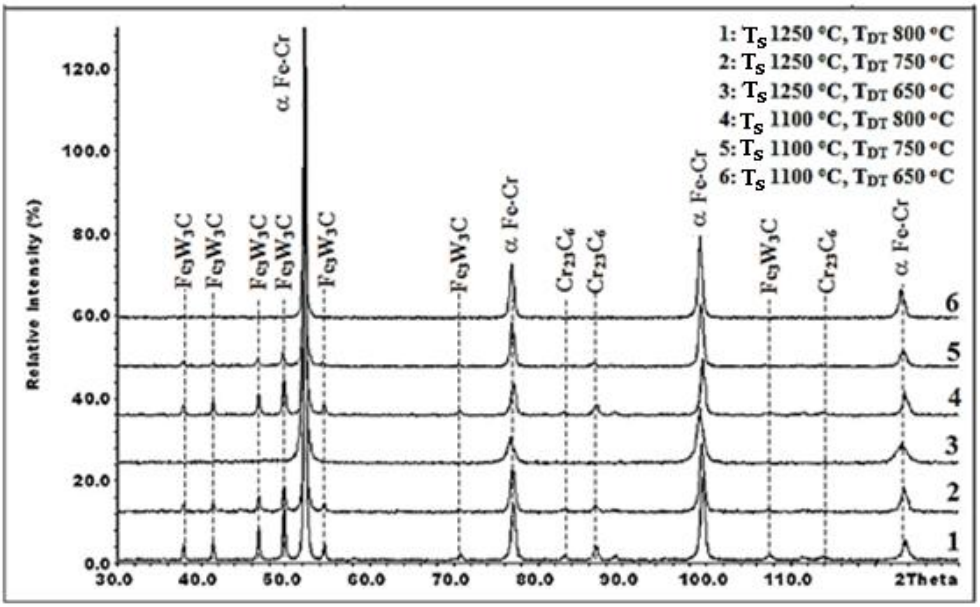

Figure 5.20 XRD diffractograms of the double tempered H21 tool steel.

Table 5.10 The ICDD cards used for the identification of phases in the H21 tool steel after double temper.

Phase	ICDD card
α Fe-Cr	34-396
M_6C (Fe_3W_3C)	41-1351
$M_{23}C_6$ ($Cr_{23}C_6$)	35-783

The diffractograms for the same double tempering temperature and different solutioning temperatures were different regarding number of peaks and intensities. The peak intensity of each carbide was higher at solutioning temperature 1250 ^oC than at 1100 ^oC. The XRD suggested that the main carbide formed in all double tempered conditions was the M_6C carbide. The number and intensity of the M_6C carbide peaks increased with increasing double tempering temperature, this was attributed to the formation of secondary M_6C carbides. Peaks of the $Cr_{23}C_6$ carbide were detected after double temper at 750 ^oC at both solutioning temperatures. Increasing the tempering temperature to 800 ^oC caused the intensity of the $Cr_{23}C_6$ carbide peak to increase further. Thus, the $Cr_{23}C_6$ carbides nucleated above 650 ^oC and grew with increasing tempering temperature. The MC, M_2C and M_3C carbides

were not clearly identified by XRD, probably owing to their volume fraction being very low.

5.3.4 Carbide Evolution

The evolution of carbides during heat treatment is strongly related to the chemical composition of tool steels, the diffusivities of alloying elements and the selected heat treatment. The carbides found after double temper at 650 ºC were the M_6C, M_2C and Fe_3C carbides. The carbides found after double temper at 750 ^oC were the Fe_3C, M_6C and $M_{23}C_6$ carbides. TEM investigation of the H21 tool steel after double temper at 800 ^oC confirmed the $M_{23}C_6$ and M_6C carbides but not the presence of cementite. The MC carbides were present in the as cast, as quenched and double tempered samples. Significant coalescence of the MC carbides was not observed. This would suggest that the MC carbide had high thermal stability and was an equilibrium phase once formed. Yongtao *et al* (2009) reported an increase of average size and dissolution of MC carbides in a steel containing 0.25 %wt V after tempering at 710 ^oC for 10 hours. In this study, the V content of the H21 tool steel was higher than that of Yongtao *et al*, which would suggest that the stability of MC was due to the presence of V in the tool steel.

In this study, the M_2C carbide was not the first carbide to precipitate and formed after the Fe_3C carbide. This conclusion was based on the size of the Fe_3C carbides that were coarser than the M_2C carbides, and indicated that the Fe_3C had formed earlier than the M_2C and grew by increasing tempering time. Bała and Pacyna (2008) studied the tempering behaviour of a steel containing 4.14 wt% Cr, and 6.55 wt% W and observed that the Fe_3C carbides strated to precipitate at ~ 280 ^oC, the M_2C carbides formed at ~ 600 ^oC and the former transformed to more stable Cr rich carbides when the Cr content of the Fe_3C increased with time.

The M_2C carbides, which were observed at tempering 650 ^oC, were not stable. With increasing tempering temperature, they went back into solution and the cubic M_6C

carbides formed predominantly at grain boundaries as massive carbides and grew quickly. Thus, the M_2C carbides were not observed after double tempering at 750 and 800 ^oC.

In alloyed steels the transformation of carbides can take place by in situ nucleation at pre-existing carbides or by separate nucleation within the matrix or at grain boundaries and sub grain boundaries (Bhadeshia and Honeycombe, 2006). Figure 5.21 shows bright field TEM images showing *in-situ* transformation of carbides in the H21 tool steel after solutioning at 1100 ^oC and double temper at 750 ^oC.

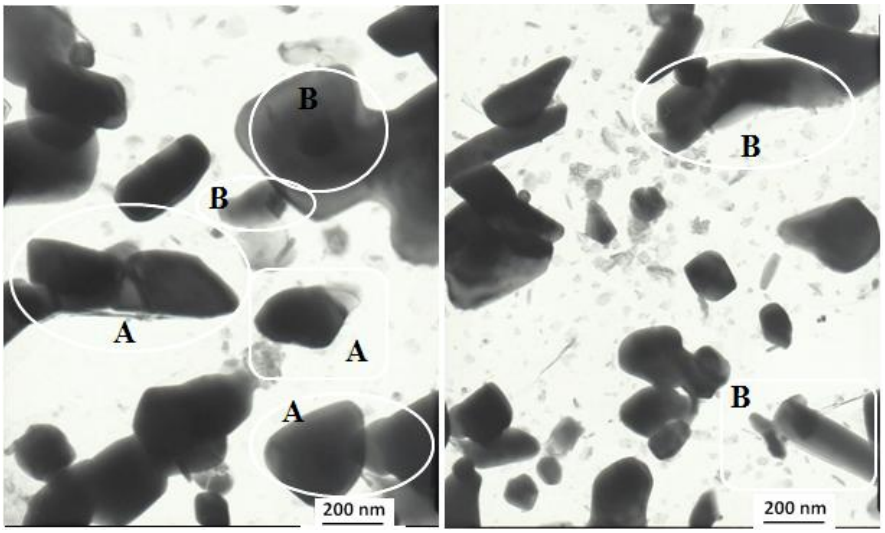

Figure 5.21 Bright field TEM images of the H21 tool steel after solutioning at 1100 ^oC and double temper at 750 ^oC showing *in situ* transformation of M_3C to $M_{23}C_6$ carbides. The letter A indicates that in situ nucleation had occurred and the letter B indicates grown $M_{23}C_6$ carbides.

Note that the carbide types in Figure 5.21 were identified by TEM-EDS qualitative analyses using JEOL 2010F and that the typical spectrum of $M_{23}C_6$ and M_3C carbides was shown in Figure 5.18. The letter A in Figure 5.21 indicates that had occurred and the letter B indicates. Detail of *in-situ* nucleation (A) and grown $M_{23}C_6$ carbides (B) can be seen in Figures 5.22 and 5.23.

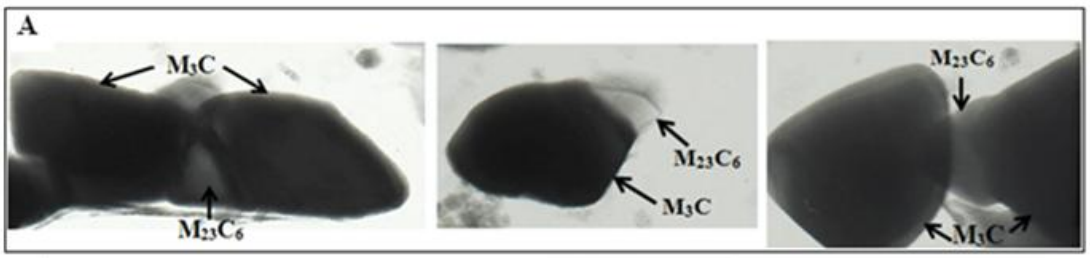

Figure 5.22 Bright field TEM images showing *in-situ* transformation of M_3C to $M_{23}C_6$ carbides indicated by A in Figure 5.21.

The Fe_3C carbide was present and identified by TEM-EDS spectrum, see Figure 5.18, which was indicated in the spectrum by a single high peak of Fe. The Figure 5.22 shows that there was a change of cementite morphology with increasing tempering temperature. At double temper at 650 ^{o}C, Figure 5.19, most cementite carbides maintained rod like morphology with aspect ratio around ~ 6.5 and with the tempering temperature increasing to 750 ^{o}C (Figure 5.22) the cementite began to change toward a spherical morphology. The Figure 5.22 also shows that the $M_{23}C_6$ carbides nucleated at the Fe_3C/ferrite interfaces. *In-situ* nucleation of alloy carbides at pre-existing cementite carbide is a common occurrence due to these cementite carbides being widely spaced at temperatures above 500 $^{\circ}$C (Bhadeshia and Honeycombe, 2006). The high W content in the H21 tool steel encouraged the formation of the $M_{23}C_6$ by enhancing it nucleation (Bhadeshia and Honeycombe, 2006). The Fe_3C carbide was completely replaced by Cr carbide when tempering was higher at 800 ^{o}C. The Figure 5.23 shows the $M_{23}C_6$ carbides.

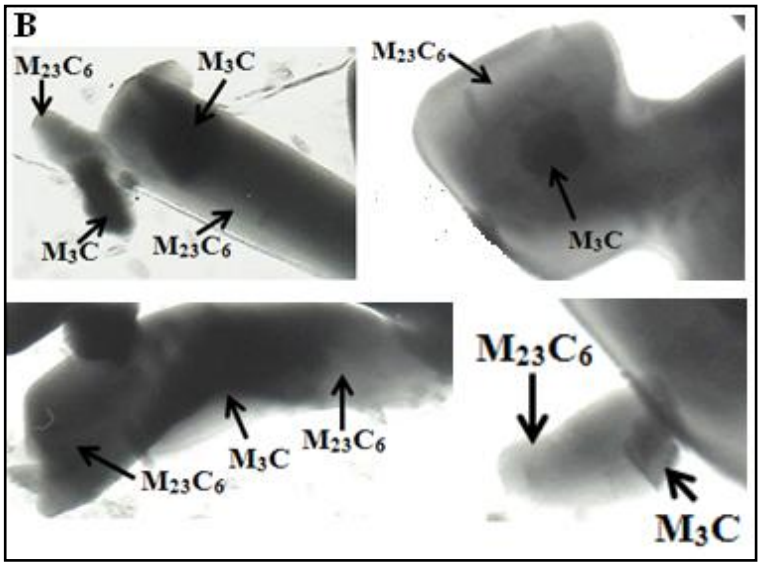

Figure 5.23 Bright field TEM images showing $M_{23}C_6$ carbide after *in- situ* nucleation indicated by B in Figure 5.21 (for the size of carbides see Figure 5.21).

Figure 5.23 shows that the $M_{23}C_6$ carbides grew toward the M_3C carbides to "consume" them and increase their size and volume fraction.

Even though the M_6C carbides can form at the expense of $M_{23}C_6$ carbides, in this study the double tempering time (one hour) was insufficient for the latter carbides to transform to the M_6C carbide, which occurred after prolonged tempering. Thus, the sequence of carbide evolution in the H21 tool steel of this study was as follows:

separate transformation: Matrix → Fe_3C → M_2C → M_6C
in-situ transformation : Matrix → Fe_3C → $M_{23}C_6$

It must be emphasized that the sequence of carbide evolution was time and temperature dependent and both carbide sequences occurred simultaneously. The formation of the secondary M_6C carbides within the matrix during double temper increased with increasing tempering temperature, as shown by the XRD where the M_6C carbide peaks increased in number and intensity at double temper at 800 ^oC.

5.4 Double Tempering of the H23 Tool Steel

5.4.1 The Effect of Double Tempering Temperature on the Microstructure

The microstructure evolution of tool steels is distinctly affected by the different tempering conditions. Figure 5.24 shows secondary electron SEM images of the double tempered microstructure of the H23 tool steel.

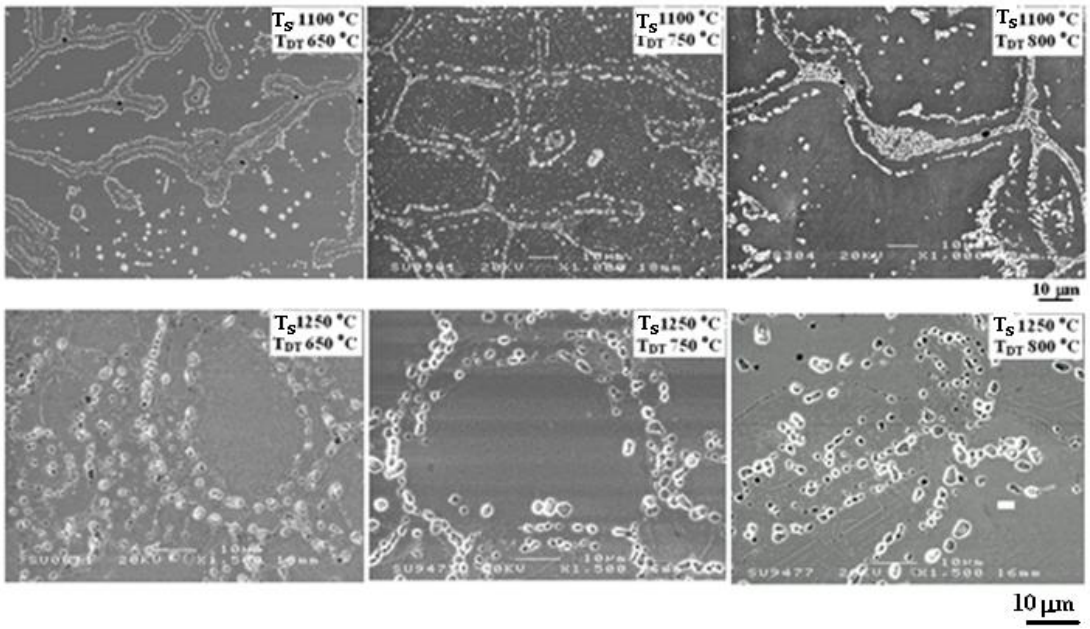

Figure 5.24 SEM secondary electron images of the H23 tool steel at different solutioning and double tempering temperatures.

The double tempered microstructures with different solutioning temperatures consisted of ferrite and carbides as can be seen in Figure 5.24. In general, at the higher solutioning temperatures the carbides were more separated in their prior network and at the lower solutioning temperature most carbides were still interconnected in their prior network and the undissolved delta ferrite was also observed. Figure 5.25 shows SEM back scatter electron images of secondary carbides after double temper.

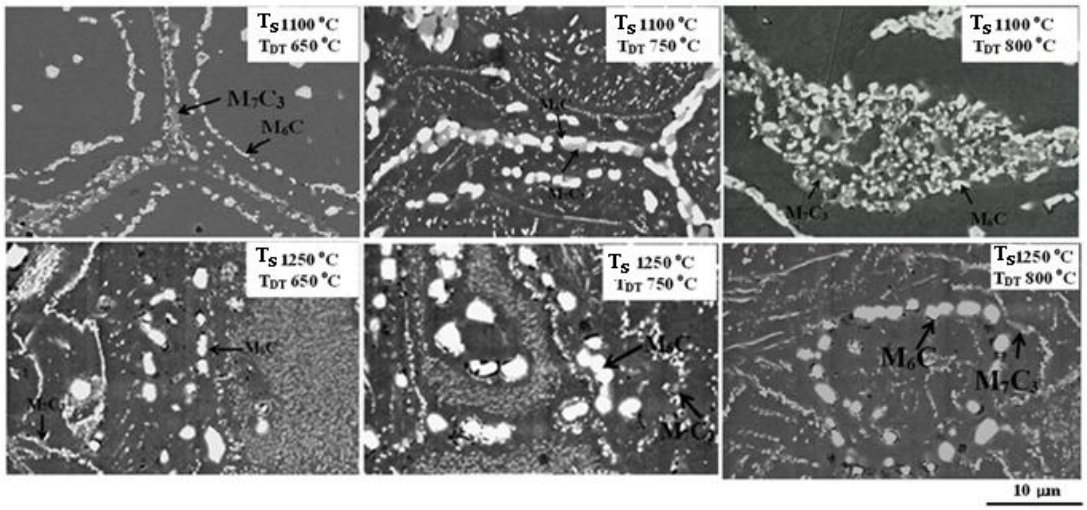

Figure 5.25 SEM back scatter electron images of the H23 tool steel at different solutioning and double tempering temperatures.

Figure 5.25 shows that at the higher solutioning temperature, fine secondary carbides were observed at double temper at 650 ^{o}C, whereas at the lower solutioning temperature fine secondary carbides were observed at double temper at 750 ^{o}C. The volume fraction of secondary carbides seemed to be higher at the higher solutioning temperature than at the lower solutioning temperature with the same double tempering temperature. This was due to the increased dissolution of carbides at the higher solutioning temperature causing more carbon to be dissolved in the matrix, which provided the driving force for precipitation during the double tempering process.

The presence of retained austenite after water quenching also affected the secondary carbide precipitation process during temper. The retained austenite phase continually transformed during the first and second temper. The retained austenite was decomposed by a diffusion mechanism accompanying more precipitation of carbides (Saha Podder and Bhadeshia, 2010) or precipitation of carbides from austenite, which reduced austenite stability, resulting in transformation from austenite to ferrite during the cooling process. As shown before (see Section 5.2.4.1), at the higher solutioning temperature the volume fraction of retained austenite and the carbon content in the matrix were higher than at the lower solutioning temperature, as a

result during tempering the transformation of retained austenite increased the volume fraction of secondary carbides. Figures 5.25 also shows that with increasing tempering temperature the fine carbides coalesced and as a result the fine carbides tended to disappear at tempering at 800 ^{o}C. As the process is controlled by diffusion, with increasing tempering temperature there was sufficient time for the carbides to grow.

5.4.2 Identification of Carbides

SEM back scatter electron images can be used to differentiate the type of carbide. Figure 5.26 shows a SEM back scatter electron image and EDS spectra of matrix and carbides in the H23 tool steel after double temper.

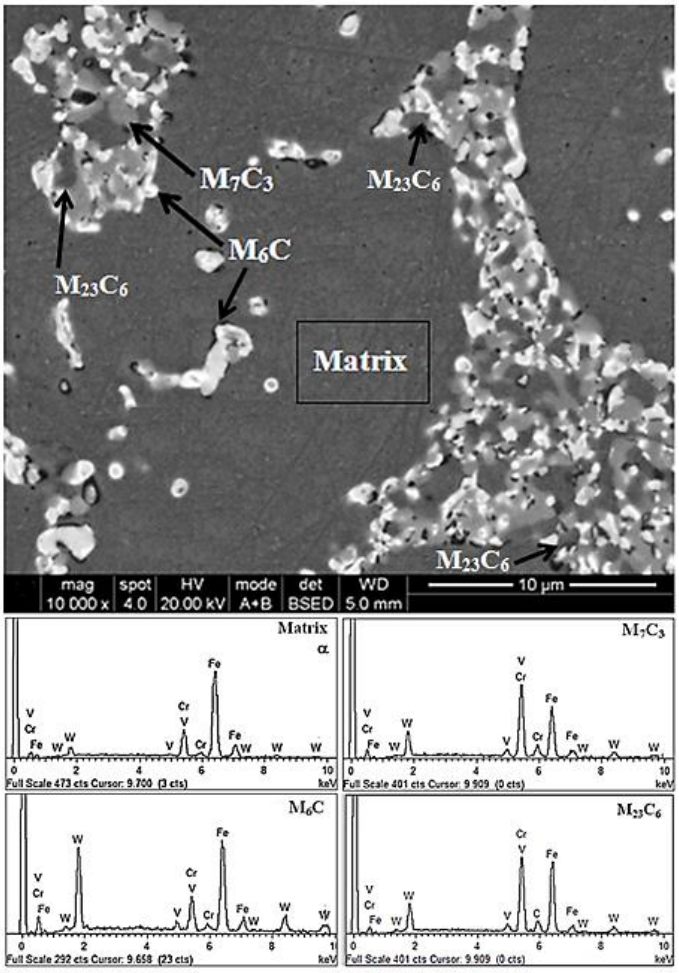

Figure 5.26 SEM back scatter electron image and EDS spectra of matrix and carbides in the H23 tool steel after solutioning at 1100^{o}C and double temper at 650 ^{o}C**.**

Figure 5.26 shows that precipitates exhibiting three different contrasts were present in the microstructure. The carbides with higher atomic number than the matrix appeared as white areas (M_6C), and there were also grey ($M_{23}C_6$) and lighter grey (M_7C_3) areas of carbides. The main metallic elements in the carbides were Cr, Fe, V and W. The SEM-EDS data is given in Table 5.11. Due to the volume fraction of the $M_{23}C_6$ carbides being very small, the Table 5.11 has data only for the dominant carbides M_6C and M_7C_3. It must be noted that with a spatial resolution ~ 1 μm, when analysing the M_7C_3 and $M_{23}C_6$ carbides, the interference occurred not only with the matrix but also with other carbide types. Quantitative EDS data for the $M_{23}C_6$ carbides showed that their average composition was 3.2V-40.9Cr-40.4Fe-15.5W (wt%) with Fe/Cr ratio ~ 1. The EDS data showed that the $M_{23}C_6$ and M_7C_3 carbides were rich in Cr, with the Cr and W contents in the $M_{23}C_6$ carbides being respectively higher and lower than in the M_7C_3 carbide. Thus, the M_7C_3 carbides exhibited a lighter grey contrast than the $M_{23}C_6$ carbides.

The M_6C carbides were rich in W, which was indicated by high W and Fe peaks and the M_7C_3 carbides were rich in Cr and W, as indicated by the presence of Cr peak higher than the Fe peak. The $M_{23}C_6$ carbides had spectra with peaks of Fe and Cr of similar height or the Fe/Cr count ratio was about 1. The dominant carbide that existed in all double tempered conditions was the M_6C carbide, followed by the M_7C_3 carbide. The volume fraction of the $M_{23}C_6$ carbides was smaller than the M_7C_3 carbides. It should be emphasized that M_6C and M_7C_3 carbides were present in the as quenched microstructures, therefore the M_6C and M_7C_3 carbides in the double tempered condition were undissolved and secondary carbides. The primary $M_{23}C_6$ carbides had dissolved during austenisation and formed as secondary $M_{23}C_6$ carbides during temper.

Two different sites of the M_7C_3 carbides were observed, first they coexisted with others carbide types, which indicated that they had formed via *in-situ* transformation and second, they were not joined with other carbide types, which indicated that they had formed individually in the matrix (Cai *et al.*, 1998). The M_6C carbides were

present everywhere. The $M_{23}C_6$ carbides coexisted with the M_7C_3 and M_6C carbides. These three carbide types had spherical and irregular morphology.

Table 5.11 SEM-EDS data of carbides in the double tempered H23 tool steel (wt%).

T_S (^oC)	T_{DT} (^oC)	Element				Comment*
		Fe	Cr	V	W	
1100	650	54.6 + 3.1	11.8 ± 0.3	0.9 ± 0.1	32.7 ± 3.2	M_6C
	750	48.7 ± 3.3	11.9 ± 2.6	2.6 ± 0.1	36.5 ± 2.0	
	800	39.5 ± 5.2	11.8 ± 1.6	1.9 ± 0.1	46.9 ± 2.6	
	650	44.8 ± 3.6	35.2 ± 4.0	3.1 ± 0.1	16.9 ± 0.4	M_7C_3
	750	34.5 ± 0.1	38.8 ± 0.1	3.7 ± 0.1	23.0± 0.2	
	800	60.7 ± 6.4	13.2 ± 1.1	1.3 ± 0.6	24.8 ± 4.7	
1250	650	37.1 + 5.3	11.8 ± 1.2	2.4 ± 0.2	48.7 ± 5.9	M_6C
	750	28.1 ± 2.2	8.3 ± 0.1	2.6 ± 0.2	61.0 ± 2.1	
	800	25.6 ± 2.4	8.7 ± 0.4	2.5 ± 0.2	63.1 ± 2.8	
	650	46.4 ± 1.8	19.6 ± 0.8	2.2 ± 0.1	31.7 ± 1.0	M_7C_3
	750	70.5 ± 2.5	16.3 ± 2.6	1.4 ± 0.2	11.9 ± 0.5	
	800	77.2 ± 2.1	12.3 ± 1.3	1.0 ± 0.1	9.5 ± 0.3	

* The quantitative data should be considered with caution given the size of the carbides.

The data in Table 5.11 would suggest that at the solutioning temperature of 1100 ^oC, the Cr content in the M_7C_3 carbide increased up to the tempering temperature of 750 °C and then decreased significantly after tempering at 800 ^oC, whereas the W content in the M_7C_3 carbides increased with increasing tempering temperature. When tempering at 650°C, the M_7C_3 carbides were very fine (Figure 5.25) and as the tempering temperature increased to 750 ^oC, these carbides grew and their composition moved closer to the equilibrium value. As the tempering temperature increased further to 800 ^oC, the M_7C_3 carbides began to lose their stability and their Cr contents decreased. Note that the M_7C_3 carbide is rich in Cr and the diffusivity of Cr is higher than that of W and V. Thus, it is suggested that after solutioning at 1100

^{o}C, the M_7C_3 carbides became unstable when tempering above 750 ^{o}C. At the solutioning temperature of 1250 ^{o}C, the Cr content in the M_7C_3 carbides was lower than at the solutioning temperature of 1100 ^{o}C compared with the same tempering temperature, which indicated that at the higher solutioning temperature the M_7C_3 carbides were not stable at tempering temperature of 650 ^{o}C. This finding would suggest that the higher solutioning temperature had accelerated the approach of carbides to equilibrium.

The evolution of the chemical composition of the M_6C carbides was different than that of the M_7C_3 carbides. The W content of the M_6C carbides was higher at the solutioning temperature of 1250 ^{o}C than at 1100 ^{o}C with the same tempering temperature. This is because at the higher solutioning temperature the matrix became more rich in W owing to the fact that more carbides had dissolved in it. The W content in the M_6C carbides in the double tempered condition also increased with increasing tempering temperature. When precipitated at 650°C, the secondary M_6C carbides were fine and their composition was far from the equilibrium value. With increasing tempering temperature, the carbides grew by consuming more W to get closer to equilibrium. However, there was no indication that their W content decreased after tempering at 800 ^{o}C, which indicated that these carbides still grew and did not reach equilibrium. Since the growth of carbides is controlled by diffusion and is time and temperature dependent, and the diffusivity of W is lower than that of the other alloying elements, more time and or higher temperature will be required for the M_6C carbides to become unstable.

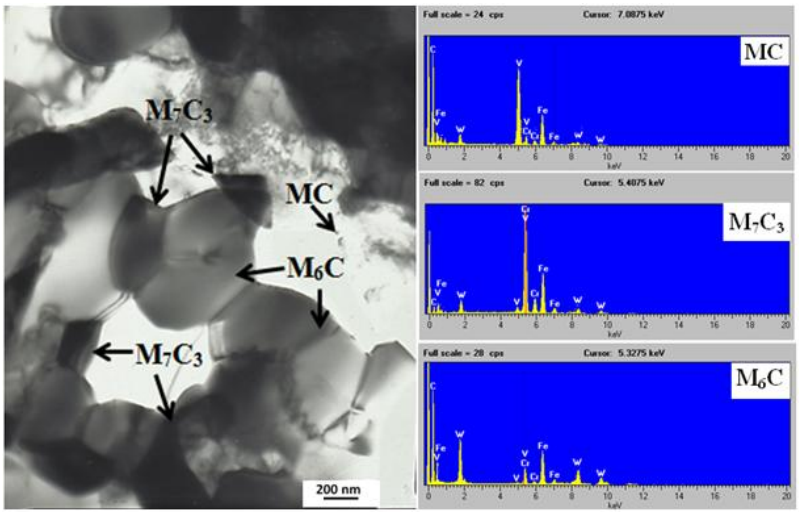

Figure 5.27 A bright field TEM image of the H23 tool steel after water quenching from 1100 ^{o}C and double tempered at 750 ^{o}C and EDS spectra of carbides.

Figure 5.27 shows a bright field TEM image of carbides formed in the double tempered H23 tool steel. As the M_7C_3 carbides coexisted with the M_6C carbides and the former were smaller than the latter, when the M_7C_3 carbides were analysed, there was interference between the interaction volume and the matrix and the M_6C carbides. Interference also occurred when the MC carbides were analysed.

Figure 5.27 does not show Fe_3C and M_2C carbides after double temper at 750 ^{o}C. These carbides might have been produced in the early stages of transformation and dissolved quickly with increasing tempering temperature. Baker and Nutting (1959) also studied the precipitation sequence in a 2.25Cr-1Mo (wt%) steel in ferritic microstructures. The ferrite contained M_2C carbides. Subsequent tempering led to the dissolution of the M_2C and its replacement by the more stable M_6C carbides. The M_6C and M_7C_3 carbides can be clearly seen compared with the as quenched microstructure (Figure 5.6). The M_7C_3 carbides nucleated between pre-existing M_6C carbides. It suggests that the M_6C carbides acted as nucleation sites for M_7C_3 secondary carbides. Fine MC carbides were observed in the matrix but there was no evidence of the $M_{23}C_6$ carbides.

5.4.3 Carbide Evolution

Four carbide types were found in the H23 tool steel after double tempering, namely the MC, M_6C, M_7C_3 and $M_{23}C_6$ carbides. The dominant carbides in the double tempered conditions were the M_6C and M_7C_3 carbides. The formation of the M_6C carbide at the expense of the $M_{23}C_6$ carbide was not observed. Secondary M_6C carbides formed within the W rich matrix due to the dissolution of the M_2C carbides.

Although the Fe_3C carbides were not observed in all double tempered microstructures, it is believed that this type of carbide had precipitated below the tempering temperature of 650 ^oC and transformed quickly to the Cr rich carbides M_7C_3 and $M_{23}C_6$. The $M_{23}C_6$ carbides grew with increasing tempering temperature and gradually disappeared from the microstructure after tempering at 800 ^oC. The M_7C_3 carbides formed either via the reaction $M_3C \rightarrow M_7C_3 + M_{23}C_6$ or nucleated directly from ferrite (separate or individual nucleation). In the former case, the reaction started by the increase of the Cr content in the M_3C carbide and the M_7C_3 grew. The M_7C_3 carbides rather than the $M_{23}C_6$ carbides were the dominant ones in the double tempered H23 tool steel because of the presence of V in the steel that tends to stabilise the M_7C_3 (Bhadeshia and Honeycombe, 2006). Bjarbo *et al* (2001) reported that there is a competition between the nucleation and growth processes of the M_7C_3 and $M_{23}C_6$ carbides and that in high Cr content tool steel, the $M_{23}C_6$ carbide would nucleate at the same time as the M_7C_3 carbide. It can be said that the Fe_3C transformed to M_7C_3 carbide and probably a small volume fraction of M_3C transformed to the $M_{23}C_6$ carbide. Therefore, the carbide evolution in the H23 tool steel occurred as follows:

in-situ transformation : Matrix $\rightarrow M_3C \rightarrow M_7C_3 + M_{23}C_6$

separate transformation : Matrix $\rightarrow M_3C \rightarrow M_2C \rightarrow M_6C$

Matrix $\rightarrow M_7C_3$

These evolution paths were followed simultaneously and were time and temperature dependent.

5.4.4 X-ray Diffraction of the Double Tempered H23 Tool steel

Figure 5.28 shows the XRD diffractograms after solutioning and double tempering of the H23 tool steel and Table 5.12 gives the ICDD cards used for the identification of phases.

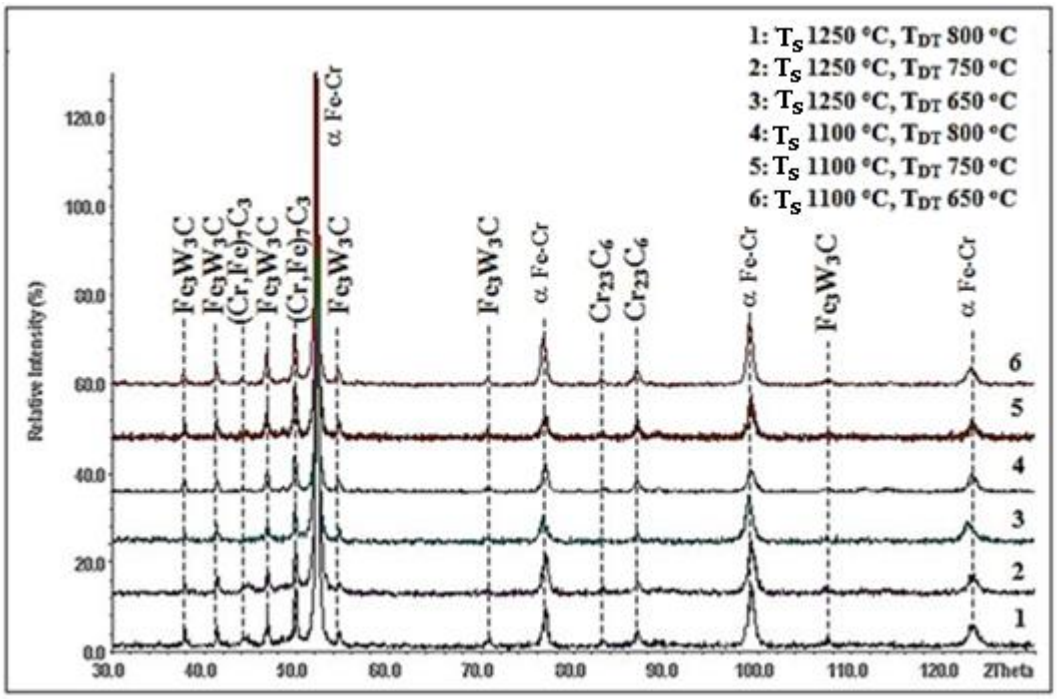

Figure 5.28 XRD diffractograms in the H23 tool steel with varying solutioning and double tempering temperatures.

Table 5.12 The ICDD cards used for the identification of phases in the H23 tool steel after solutioning and double tempering.

Phase	ICDD card
α Fe-Cr	34-396
M_6C (Fe_3W_3C)	41-1351
$M_{23}C_6$ ($Cr_{23}C_6$)	35-783
M_7C_3 ($(Cr,Fe)_7C_3$)	5-720

The XRD determined the presence of solutioning ferrite (αFe-Cr) and M_6C, $M_{23}C_6$ and M_7C_3 carbides. The MC carbide was not identified by XRD, but its presence was confirmed by TEM. The low volume fraction of the MC carbide and the overlap

of its peaks with those of the M_7C_3 and $M_{23}C_6$ carbides (Asakura *et al.*, 1990) made the detection of the MC carbide by XRD not possible.

Figure 5.28 shows that the peaks of the M_6C carbide were dominant and that the intensity of the peaks of the M_7C_3 carbide was higher than the $M_{23}C_6$ carbide in all double tempered conditions. These results are in good agreement with the microstructure studies regarding the high volume fraction of the M_6C carbides and the dominance of the M_7C_3 over the $M_{23}C_6$ carbides.

5.5 The Effect of Double Tempering Temperature on Hardness of the H21 and H23 Tool Steels

The tempering hardness is linked with precipitation strengthening of carbides, and the decomposing of martensite and austenite. Tempering curves of hardness as a function of tempering temperature for solutioning temperatures of 1100 and 1250 ^{o}C are shown in Figures 5.29 and 5.30.

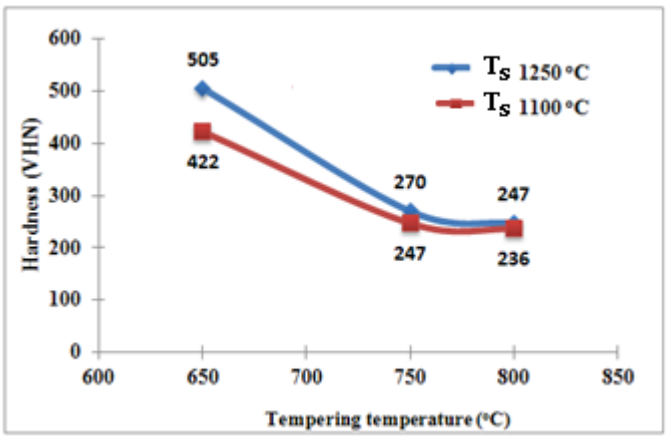

Figure 5.29 The effect of solutioning and double tempering temperatures on the hardness of the H21 tool steel.

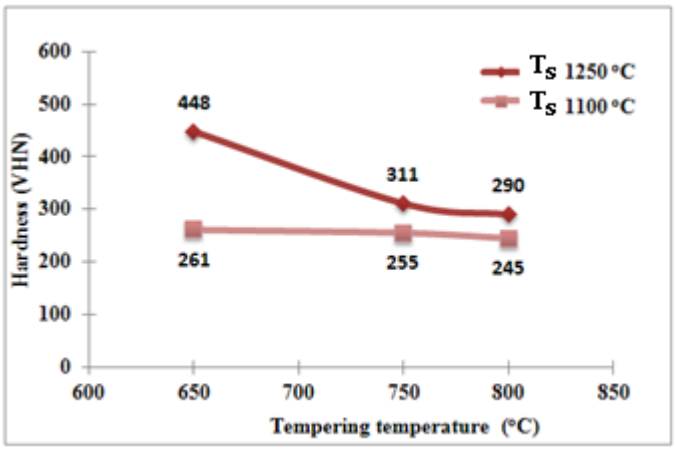

Figure 5.30 The effect of solutioning and double tempering temperatures on the hardness of the H23 tool steel.

Figures 5.29 and 5.30 show that the hardness after double tempering increased with increasing solutioning temperature and decreased with decreasing double tempering temperature. In both tool steels the highest hardness was achieved after solutioning at 1250 ^{o}C and double tempering at 650 ^{o}C. This is because at the higher solutioning temperature, the more the carbides were dissolved in the matrix, giving a higher supersaturation and driving force for precipitation, which provided more nucleation sites for carbide precipitation during the double tempering.

Tempering in the range 650 ^{o}C to 800 ^{o}C did not show a secondary hardening peak for both tool steels. The secondary hardening peak has been attributed to the precipitation of fine M_2C carbides (Roberts *et al.*, 1998). TEM investigations of the H21 tool steel after double temper at 650 ^{o}C, see Figures 5.14 and 5.19, indicated that the Fe_3C precipitated at interlath and intralath boundaries and that some M_2C carbides were still present. As mentioned before, the M_2C carbide was not stable and rapidly transformed to stable carbide and double temper at 650 ^{o}C for 1 hour promoted the dissolution of the M_2C carbides and favoured the coarsening of the F_3C carbides. The precipitation of cementite was accompanied by a decrease in hardness. Meanwhile, in the microstructure of the double tempered H23 tool steel the unstable M_2C or M_3C carbides were not observed. The higher Cr content in the H23 tool steel

compared with the H21 tool steel caused those unstable carbides to dissolve below 650 ^{o}C. Quantitative data of carbide size and volume fraction for the three double tempering temperatures is given in Table 5.13.

Table 5.13 Volume fraction (V_c) and average size (μm) of carbides in the H21 and H23 tool steels at different solutioning and double tempering temperatures.

Tool steel	T_S (^{o}C)	Double tempering temperature (^{o}C)					
		650		750		800	
		V_c (%)	Mean size (μm)	V_c (%)	Mean size (μm)	V_c (%)	Mean size (μm)
H21	1100	14.5 ± 0.5	0.2 ± 0.1	17.3 ± 0.9	0.3 ± 0.1	18.6 ± 0.7	0.3 ± 0.2
	1250	15.2 ± 0.6	0.2 ± 0.01	17.9 ± 0.3	0.3 ± 0.2	18.9 ± 0.4	0.5 ± 0.1
H23	1100	16.0 ± 0.2	0.3 ± 0.1	17.7 ± 0.5	0.2 ± 0.2	18.2 ± 0.3	0.3 ± 0.2
	1250	16.9 ± 0.3	0.3 ± 0.1	18.3 ± 0.6	0.3 ± 0.1	18.5 ± 0.4	0.3 ± 0.2

It can be seen from Table 5.13 that the volume fraction of carbides slightly increased with increasing tempering temperature. This was attributed to the precipitation of secondary carbides that was higher at the higher tempering temperature owing to the higher diffusivity of alloying elements.

Table 5.13 would suggest that the volume fraction of carbides was slightly higher in the double tempered H21 tool steel than that in the H23 tool steel, especially after tempering at 800 ^{o}C. This is attributed to the carbides formed during double temper. The secondary carbides formed during the double temper of the H23 tool steel were the M_6C, and Cr rich carbides (M_7C_3 and $M_{23}C_6$). The Cr rich carbides reached their equilibrium and dissolved at lower temperature than the M_6C carbide, and the higher solutioning temperature had accelerated the approach of the Cr rich carbides to equilibrium at tempering at 650 ^{o}C, as described in Section 5.4.1. Hence, there was no significant difference in the volume fraction of carbides when tempered at 750 and 800 ^{o}C.

There was no correlation between the average size of carbides with increasing tempering temperature, probably due to coalesced carbides forming networks that

made the measurement of carbide size less accurate. The average carbide size in the double tempered H23 tool steel increased with increasing tempering temperature when austenised at 1250 ^{o}C owing to a reduction in the total area of the ferrite/carbide interphase boundary. The overall impression from the microstructure studies was that there was a slight coarsening of carbides with increasing tempering temperature. It is concluded that the decrease of hardness with increasing tempering temperatures was due to the coarsening of carbides, the recovery of lath structure and ferrite grain growth. This implies that the double tempering of the H21 tool steel should be carried out below 650 ^{o}C.

5.6 The Tempering Parameter of the H21 and H23 Tool Steels

It is common in tempering studies to use a tempering parameter as a single variable to encompass the effects of time and temperature. In this study, the Larson-Miller parameter (LMP) was used to correlate microstructural change with thermal cycle. The LMP was calculated using equation 2.4 to give a typical curve for the H21 and H23 tool steels, see Figure 5.31.

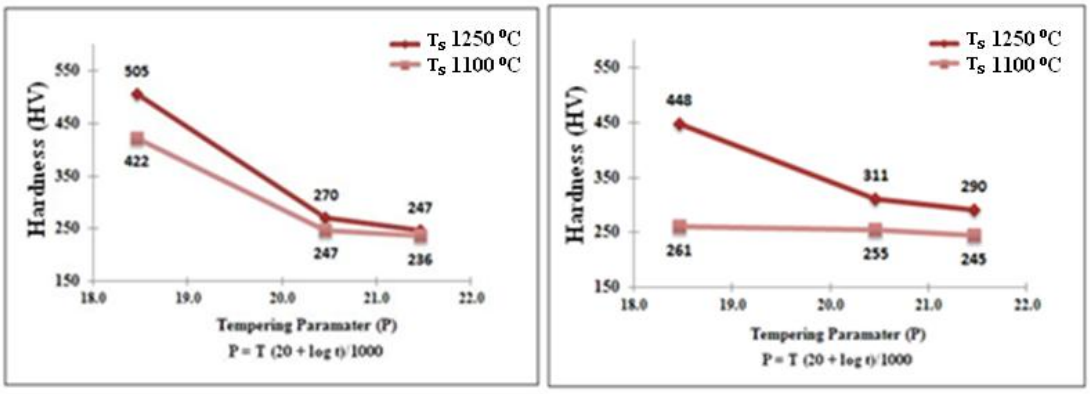

a.H21 tool steel b. H23 tool steel

Figure 5.31 Relationship between hardness (HV) and the LMP of the H21 and H23 tool steels after double temper at different tempering temperatures.

The value for the constant C was chosen to be 20 as for alloy steels (Bhadeshia and Honeycombe, 2006). The tempering treatments of this study represented a variation in P between 18.5 and 21.5, which covers a tempering temperature range of 650 to

800 ^{o}C and tempering time of 1 hour. For both tool steels, with the tempering parameter, P, increasing the hardness decreased rapidly, which was attributed to the formation of coarse ferrite grains, the evolution of carbides and the recovery process, as mentioned in Section 5.5.

5.7 Comparison the Experimental Results with Theoretical Prediction

Calculation of phase diagrams using ThermoCalc software was performed to identify the phases in the tool steels. Figure 5.32 shows the calculated phase diagrams of the tool steels.

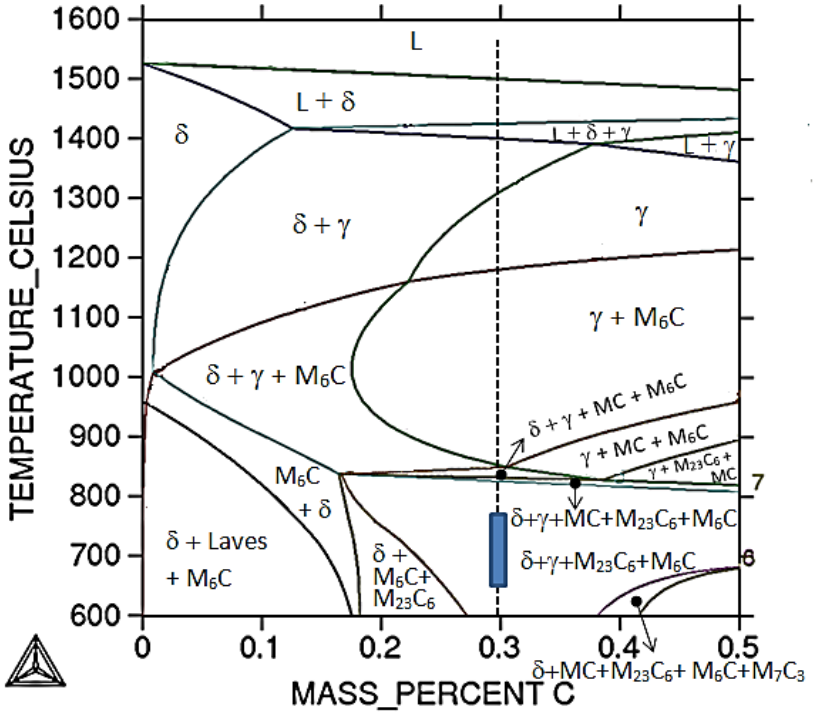

a.H21 tool steel

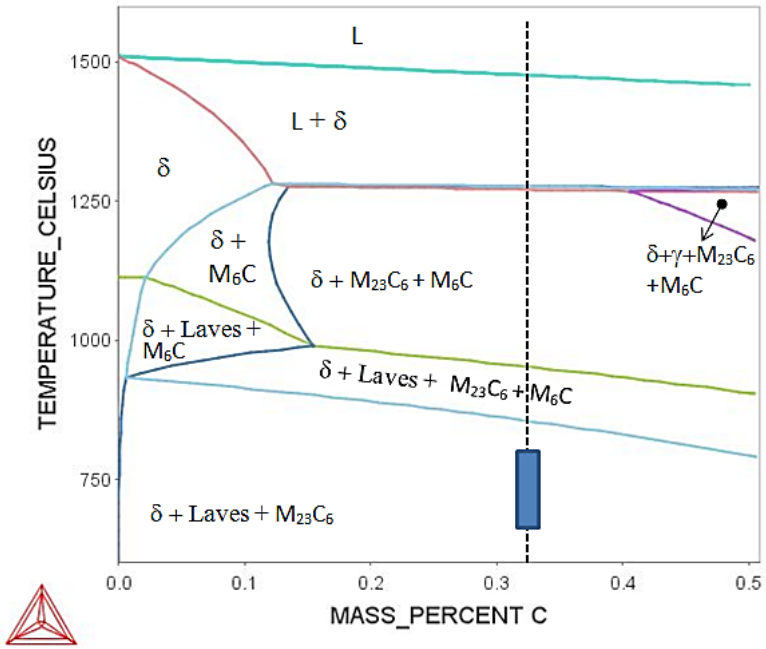

b. H23 tool steel

Figure 5.32 Isopleths of the phase diagrams of the H21 and H23 tool steels. The dotted lines indicate the chemical composition of the investigated tool steels and the tempering temperature range is shown by the dashed area.

The ThermoCalc calculation predicted that in the tempering temperature range 650 - 800 ^{o}C (Figure 5.32a), the most stable phases in the H21 tool steel should be δ, $M_{23}C_{6,}$ and M_6C. Thus, the thermodynamic prediction for the H21 tool steel was not in agreement with the experimental results that showed that the stable phases in the double tempered condition were α, $M_{23}C_{6,}$ MC, and M_6C.

The ThermoCalc calculation of the H23 tool steel predicted that in the tempering temperature range 650 – 800 ^{o}C (Figure 5.32b) the stable phases should be α, Laves, and $M_{23}C_6$ carbide. Thus, the thermodynamic calculations did not agree with the experimental results, which show that the phases found in the double tempered condition were α, MC, M_6C, M_7C_3, and $M_{23}C_6$.

5.8 CONCLUSIONS

In the first part of this chapter the effect of solutioning temperature on the microstructure evolution and hardness of the H21 and H23 tool steels was studied. The following conclusions can be drawn from this study:

1. The as quenched microstructure of the H21 tool steel consisted of lath martensite, lower bainite and carbides. The width of martensite laths varied between 0.1 to 0.6 μm. The as quenched microstructure of the H23 tool steel consisted of ferrite, retained austenite and carbides and there was no evidence of martensite formation.
2. The presence of retained austenite in the H21 tool steel was not confirmed by XRD but was observed by TEM using the dark field technique.
3. The XRD confirmed the presence of retained austenite in the H23 tool steel. The volume fraction of retained austenite in the H23 tool steel increased from 6.1 % at T_S = 1100 ^oC to 8.4 % at T_S = 1250 ^oC, and the austenite lattice parameter increased from 0.360 nm at T_S = 1100 ^oC to 0.361 nm at T_S = 1250 ^oC.
4. The XRD identified the M_6C carbide as Fe_3W_3C in both tool steels. The XRD also identified the M_7C_3 carbide as $(Cr, Fe)_7C_3$ in the H23 tool steel.
5. The highest as quenched hardness values of the H21 and H23 tool steels were 574 HV and 302 HV, respectively, and were obtained after solutioning at 1250 ^oC.

In the second part of this chapter, the effect of double tempering temperature on the microstructure and hardness evolution of the H21 and H23 tool steels was studied. The following conclusions can be made:

1. The double tempered microstructure of the H21 tool steel consisted of tempered martensite, lower tempered bainite and carbides. The double tempered microstructure of the H23 tool steel consisted of ferrite and carbides.

2. The double tempered matrix of the H21 tool steel at 650 ^{o}C showed that the lath morphology of martensite still existed and with increasing tempering temperature, the matrix had recovered and an equiaxed ferrite grain structure gradually developed.
3. The M_3C (or cementite) and M_2C carbides were only observed in the H21 tool steel at the tempering temperature of 650 ^{o}C and disappeared with increasing tempering temperature.
4. The present study confirmed previous findings and contributed additional evidence to support the suggestion that carbides make a great contribution in retarding the recovery of the lath martensite matrix.
5. The XRD confirmed that the M_6C carbide was Fe_3W_3C and the $M_{23}C_6$ carbide was $Cr_{23}C_6$ in both tool steels. The XRD also identified the M_7C_3 as $(Cr, Fe)_7C_3$.
6. The Cr content of the M_7C_3 carbide in the H23 tool steel tended to decrease at higher solutioning and tempering temperatures and the W content in the M_6C carbides increased with increasing solutioning and tempering temperature in both tool steels.
7. Higher solutioning temperature had accelerated the approach of carbides to their stability during tempering.
8. This study found that the MC and M_6C carbides in both tool steels were stable over the whole double tempering temperature range.
9. In this study secondary hardening as a consequence of secondary precipitation of fine carbide particles did not occur in both tool steels.
10. The highest double tempered hardness of the H21 and H23 tool steels was 505 HV and 448 HV, respectively, and was obtained after solutioning at 1250 ^{o}C and double tempering at 650 ^{o}C.
11. The carbide evolution sequence in the H21 and H23 tool steels respectively were:

in-situ transformation : Matrix → Fe_3C → $M_{23}C_6$

separate transformation : Matrix → Fe_3C → M_2C → M_6C

and

in-situ transformation : Matrix → M_3C → M_7C_3 + $M_{23}C_6$

separate transformation : Matrix → M_3C → M_2C → M_6C

Matrix → M_7C_3

12. Experimental results and thermodynamic predictions using the ThermoCalc software were not in agreement for the double tempered H21 and H23 tool steels.

Chapter 6
The Controlled Thermomechanical Processing and Double Temper of The Tool Steels

6.1 Introduction

Controlled thermomechanical processing (TMP) has been developed in recent years and has been considered in various industries. Applying TMP on tool steels, as well as heat treatment, affects their mechanical properties. The TMP of highly alloyed tool steels is of great interest from both fundamental and industrial viewpoints due to the formation of carbides' network in the ingot that remain throughout processing. This has a detrimental effect on mechanical properties.

In this study, the effects of TMP parameters, namely solutioning and deformation temperatures on the flow stress, microstructure and hardness of the H21 and H23 tool steels were studied using high axisymmetric compression test. Special attention was paid to establish the deformation conditions that lead to break down of the carbide network and to improve the hardness. The primary focus was on the H21 tool steel owing to its hardness after hot deformation (TMP) showing promising results. The deformed H21 tool steel proceeded to double temper with the same parameters as in the conventional heat treatment. The study would benefit our understanding on microstructure evolution and hardness behaviour of the tool steels.

6.2 Controlled Thermomechanical Processing

6.2.1 Validity of Axisymmetric Compression Test

From the total number of valid axisymmetric compression samples of the H21 and H23 tool steels (10 for each steel) showed the deformed samples did not crack. There were six deformed samples with different experimental conditions for each of the H21 and H23 tool steels that did not stick to the tool during the compression test. The other samples failed during hot axisymmetric compression test because the use of low strain rate during compression made some samples stick on the surface of the tools and as a consequence these samples were delayed for more than 1 minute prior to water quench. The twelve deformed samples are shown in Figure 6.1.

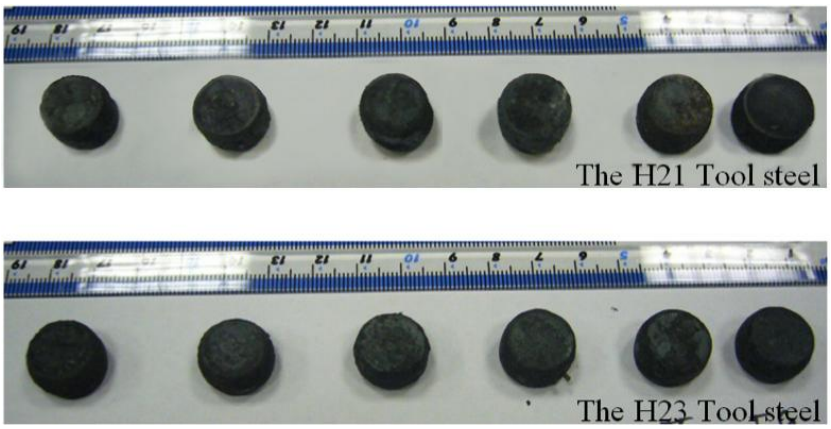

Figure 6.1 The 12 deformed samples of the H21 and H23 tool steels before removing the oxide scales.

The dimensions of the samples before and after deformation are summarised in Table 6.1. These dimensions were used to judge the validity of the tests, based on the method discussed in Section 3.2.1.3. All tests were valid because the aspect ratio (D_R) was in the range 1 to 2, the barrelling coefficient (B) was not larger than 1.1 and the height coefficient (H) was below 0.04. The results of the validity tests are given in Table 6.1.

Table 6.1 Dimensions of samples before and after hot deformation and validity test results.

Tool steel	T_S[1] (^oC)	T_D[2] (^oC)	d_o (mm)	d_f (mm)	h_c (mm)	h_f (mm)	Validity tests		
							D_R	B	H
H23	1250	1100	11.96	15.83	14.87	8.70	1.24	1.02	0.015
	1250	1050	11.94	15.89	14.70	8.82	1.23	1.06	0.013
	1250	1000	11.94	15.74	14.93	8.53	1.25	0.99	0.014
	1100	1100	12.04	15.87	14.98	9.07	1.24	1.05	0.004
	1100	1050	11.98	15.66	14.96	9.43	1.25	1.08	0.019
	1100	1000	12.08	16.11	15.06	9.21	1.25	1.09	0.002
H21	1250	1100	11.97	15.21	14.93	9.42	1.25	1.02	0.003
	1250	1050	11.89	15.23	14.89	9.52	1.25	1.05	0.006
	1250	1000	12.01	15.12	14.85	10.28	1.24	1.10	0.008
	1100	1100	12.01	15.68	14.85	9.27	1.24	1.06	0.013
	1100	1050	11.98	15.47	14.85	8.78	1.24	0.99	0.005
	1100	1000	11.98	15.89	14.95	8.81	1.24	1.03	0.011

[1]T_S = solutioning temperature
[2]T_D = deformation temperature

6.2.2 Flow Stress Behaviour

The recorded raw data from the hot deformation tests were converted to flow stress-strain data based on the method given in Section 3.2.1.4. Figures 6.2 and 6.3 show the flow curves of the H21 and H23 tool steels after hot deformation with different solutioning temperature.

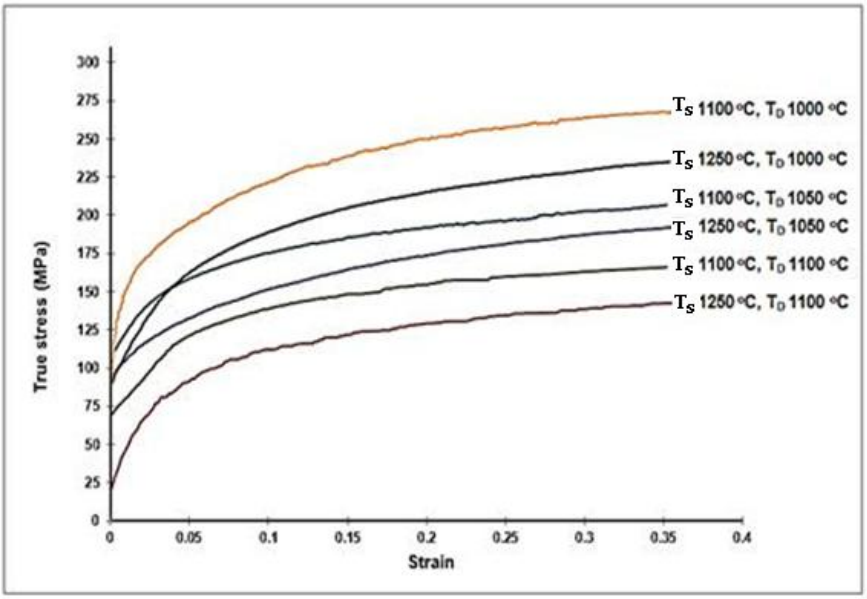

Figure 6.2 Flow curves of the H21 tool steel after deformation at 1000, 1050 and 1100 ^{o}C with different solutioning temperature.

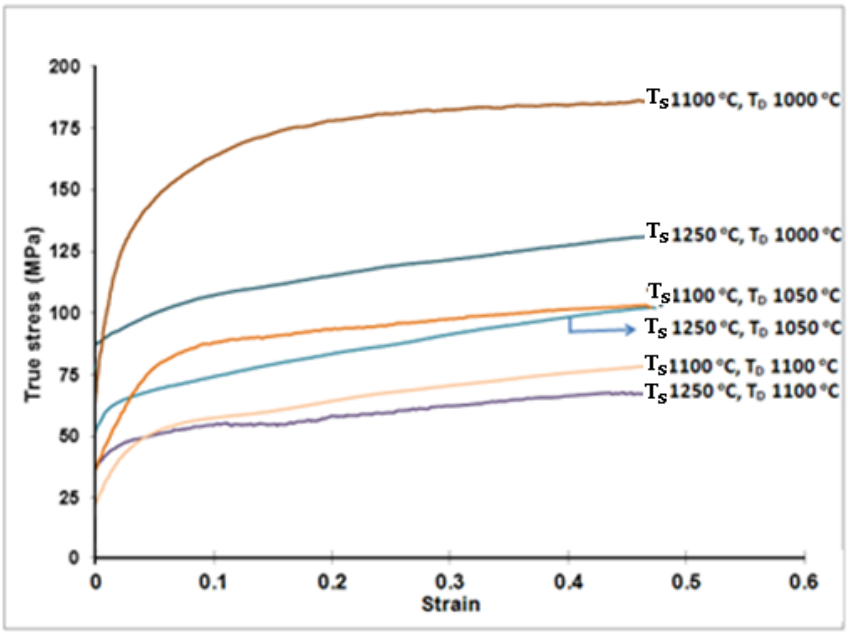

Figure 6.3 Flow curves of the H23 tool steel after deformation at 1000, 1050 and 1100 ^{o}C with different solutioning temperature.

As mentioned in Section 3.2.1.4.e, the Q_{def} value was not calculated because this study only focused on one strain rate (0.01 s^{-1}). To get an overview of the flow curve

behaviour, and to correct for the effects of deformational heating, the flow stress was calculated using Q_{def} = 607 kJ/mol that was taken from the literature (Fajfar *et al.*, 2010). The shapes of all flow curves in Figures 6.2 and 6.3 were almost identical, i.e., fluctuation features and no peak in flow curves that are indicative of no dynamic recrystallisation having occurred. Figure 6.4 shows variation of the peak stress as a function of temperature for both tool steels.

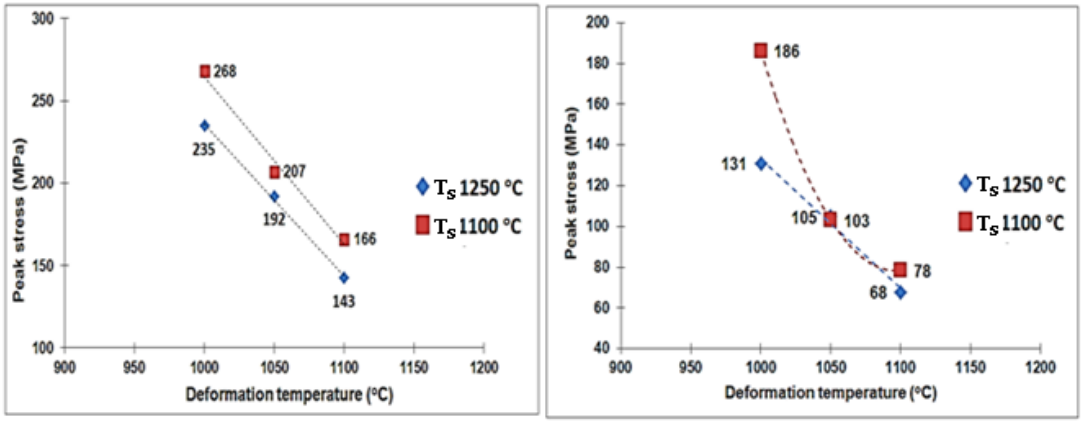

a. The H21 tool steel b. The H23 tool steel

Figure 6.4 Relationship between the peak stress and deformation temperature.

Figure 6.4 shows that the curves of the H21 tool steel for the two solutioning temperatures were almost parallel and that the peak stress was higher at the lower solutioning temperature. The curves of the H23 tool steel displayed a decrease of slope with increasing deformation temperature.

It can be seen from Figures 6.2, 6.3 and 6.4 that the flow stress increased with decreasing solutioning and deformation temperatures. This indicated that the temperature had a significant effect on the flow stress, which has been attributed to dislocation movement (Lee and Liu, 2006, Conrad and Frederick, 1962). The movement of dislocations became easier with increasing the solutioning and deformation temperatures and hence the resistance of the material to deformation decreased, which was indicated by decrease of the flow stress. Meanwhile, at the lower solutioning and deformation temperatures the mobility of the dislocations

decreased owing to the increased dislocation density and degree of dislocation tangling, which enhanced the resistance to plastic deformation.

6.2.3 The Effect of Solutioning and Hot Deformation Temperatures on Microstructure

6.2.3.1 The H21 Tool Steel

It is well known that the microstructure of a material strongly affects its flow behaviour during deformation. Figure 6.5 shows optical images of the deformed H21 tool steel.

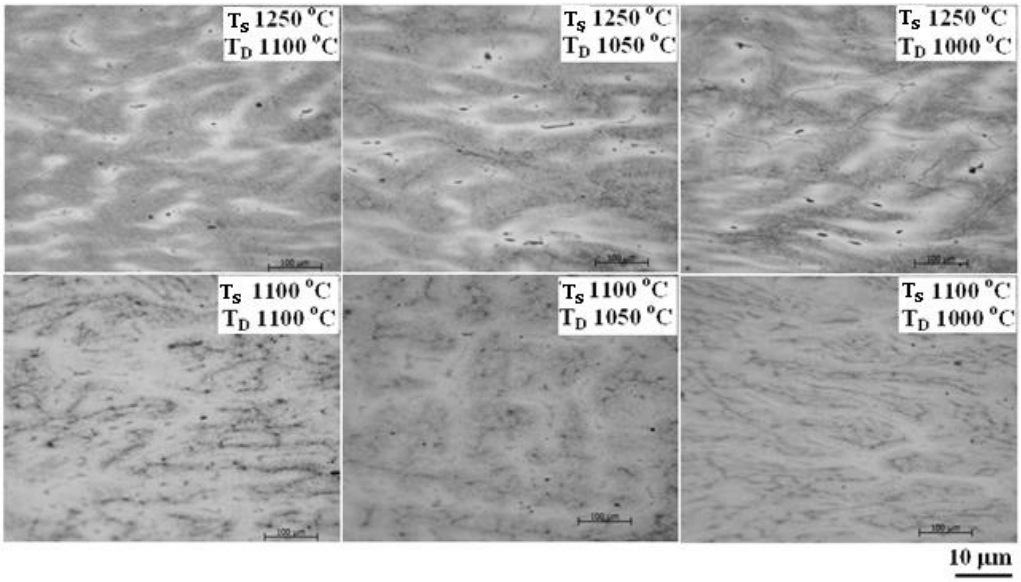

Figure 6.5 Optical microscope images of the microstructure of the H21 tool steel after hot deformation.

There was no evidence of dynamic or static recrystallisation after hot deformation. The microstructures showed elongated regions of martensite and carbides. The PAGBs were not revealed clearly in all conditions because of the presence of thick martensite layer and the precipitation of carbides that covered the prior-austenite grain boundaries, except after solutioning at 1250 ^{o}C and deformation at 1000 ^{o}C where they were not observed uniformly. The packet size martensite could not be measured precisely due to the poor resolution. Higher deformation temperature resulted to slightly coarser structure with thicker martensite layers.

The applied low strain rate and hot deformation would provide longer time for energy accumulation and higher mobility of boundaries for the nucleation and growth of dynamically recrystallised grains and dislocation annihilation. However, the microstructure and behaviour of the flow curves showed no evidence that dynamic recrystallisation (DRX) had occurred. In this study, there were two dominant factors affecting the absence of DRX in the H21 tool steel, which had high content of carbide forming elements that produced a significant volume fraction of carbides in the as cast condition. First, the type and volume fraction of carbides present and second, the presence of dispersed carbides after hot deformation. Karagoz and Fischmeister (1987) reported that the lowest dissolution rate of carbide during austenisation is exhibited by the MC carbide and then by the M_6C carbide. Both types of carbide are thermodynamically stable and do not completely dissolve even at high solutioning temperature (Totten, 2006). Thus, after solutioning for 10 minutes, the undissolved MC and M_6C carbides still existed in the material subjected to hot deformation. The undissolved carbides shown in Figure 6.6 were M_6C and were confirmed by back scatter imaging. The fine MC carbides were observed by TEM (see Figure 6.8).

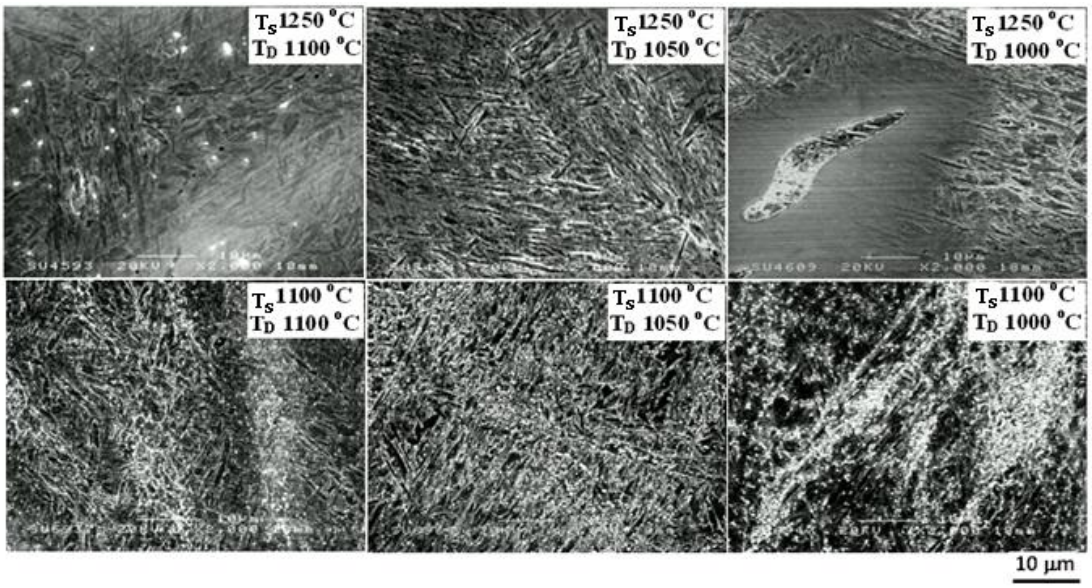

Figure 6.6 SEM secondary electron images of the H21 tool steel after hot deformation and water quenching.

Figure 6.6 shows that the H21 tool steel after hot deformation and water quenching consisted of martensite and carbides. At the lower solutioning temperature, the martensite structure was not clear, as there was a high volume fraction of dispersed carbides. It can be seen that the consequence of hot deformation was banding of the primary carbide colonies. The banding of carbides consisted of disintegrated undissolved carbides formed by mechanical fragmentation during hot deformation, and these bands were more pronounced at the lower solutioning temperature. The banding of carbides is linked with the segregation of substitutional alloying elements during solidification and this chemical inhomogeneity persists in the wrought product despite homogenisation because the diffusion coefficients of substitutional alloying elements in austenite are low (Krauss, 2003). In addition bands of carbides formed due to the greater deformability of the matrix compared with that of the carbides (Ghomashchi and Sellars, 1993). Besides the formation of bands of carbides, Figure 6.6 also shows that the broken carbides were distributed everywhere, not only along the grain boundaries but also in the grain interiors. The deformation temperature influenced the carbide network in the direction perpendicular to the compression axis and reduced the carbide size effectively.

Figure 6.6 also indicated that the lower solutioning temperature, the higher volume fraction of carbides, which was attributed to the formation of secondary M_6C carbides. These secondary M_6C carbides dissolved into the matrix when the solutioning temperature was increased to 1250 ^oC. Therefore, the higher solutioning temperature, the more carbides dissolved into the matrix. However, due to the high thermal stability of the M_6C carbides, the coarse M_6C carbides still remained at a considerable volume fraction as undissolved carbides and when deformation was performed, these carbides was broken down by mechanical fragmentation as dispersed carbides. The carbides in Figure 6.6 were identified by SEM-EDS as M_6C carbides and their EDS data is given in Table 6.2. Note that there were interference between the interaction volume of the carbides and the matrix in all conditions due to the spatial resolution being ~ 1 μm. The strongest interference was at T_S = 1100 ^oC and T_D = 1000 ^oC owing to having the finest carbides.

Table 6.2 SEM-EDS data of the deformed H21 tool steel (wt%).

T_S (^oC)	T_D (^oC)	Element				Comment*
		Fe	Cr	V	W	
1250	1100	52.5 ± 0.5	3.3 ± 0.1	1.4 ± 0.3	42.8 ± 0.3	M_6C
1250	1050	63.4 ± 0.4	4.0 ± 0.4	1.0 ± 0.1	31.6 ± 0.3	M_6C
1250	1000	70.1 ± 0.3	3.8 ± 0.2	0.8 ± 0.2	25.3 ± 0.2	M_6C
1100	1100	66.1 ± 0.5	3.4 ± 0.2	0.9 ± 0.2	29.6 ± 0.4	M_6C
1100	1050	69.2 ± 0.5	2.9 ± 0.1	0.7 ± 0.1	27.2 ± 0.3	M_6C
1100	1000	71.1 ± 0.4	3.8 ± 0.1	0.9 ± 0.1	24.2 ± 0.2	M_6C

* The quantitative data should be considered with caution given the size of the carbides

Table 6.2 shows that the chemical composition of the M_6C carbides depended on temperature as was the case in the conventional heat treatment. At the lower solutioning and deformation temperatures, the concentration of W in the M_6C carbides was lower compared with the higher temperature. These data corresponded to the microstructures shown in Figure 6.6. The latter shows that the volume fraction of carbides was larger and their size was finer at the lower solutioning and deformation temperatures. The growth kinetics of carbides is strongly dependent on the diffusivity of elements, stability of carbides and the process applied to the tool steel.

Compared with the M_6C carbides observed in the as quenched H21 tool steel without deformation (Table 5.1), the undissolved M_6C carbides without deformation were richer in W for the same solutioning temperature for all deformation temperatures. The M_6C carbides in the as quenched condition without deformation were bigger than in the deformed condition, with the same solutioning temperature for all deformation temperature. This is because the deformation had broken down the carbides in the deformed samples while, during austenisation in the conventional heat treatment (without deformation), there was more time (1 hour) for the carbides to grow and become richer in W. Figure 6.7 shows the morphology of the M_6C carbides.

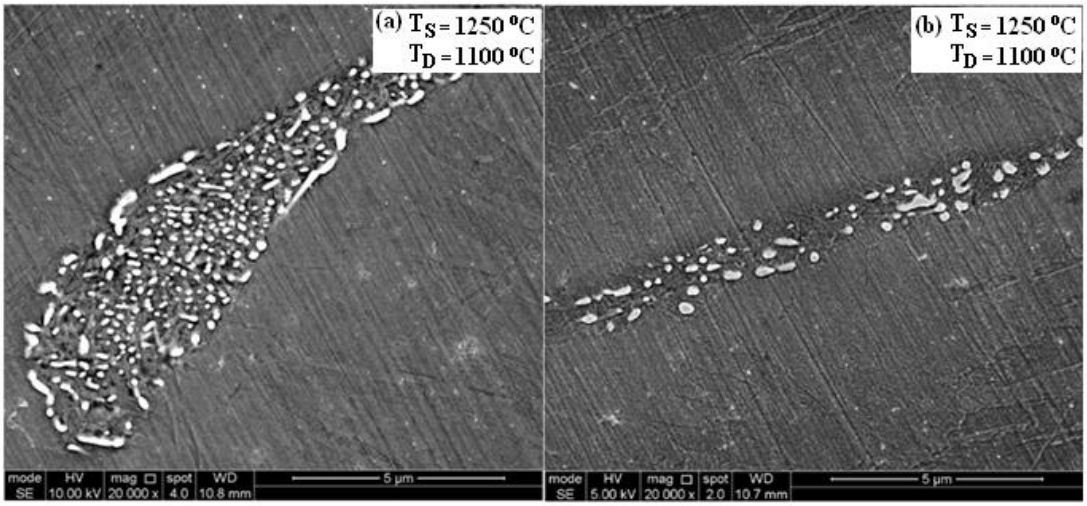

Figure 6.7 SEM secondary electron images of the H21 tool steel (a) solutioning at 1100 ^{o}C and deformation at 1000 ^{o}C, (b) solutioning at 1250 ^{o}C and deformation at 1100**.**

The morphology of the M_6C carbides in all deformation conditions was almost the same as in the as cast microstructure. As shown in Figure 6.7, the carbides existed in the matrix and on grain boundaries. In general, after hot deformation the average carbide size was less than 1 μm. The dispersed carbides in the matrix were finer than on the grain boundaries. In this study, at the lower solutioning and deformation temperatures, the carbides were more refined and uniformly dispersed and closely spaced and the volume fraction of carbides was higher than at the higher solutioning and deformation temperatures. The most dispersed of M_6C carbides with average size of ~ 0.2 μm were observed after solutioning at 1100 ^{o}C and followed by hot deformation at 1000 ^{o}C. The dispersed and fine undissolved carbides are believed to play an important role in retarding the recrystallisation owing to their presence before any recrystallisation could occur (Humphreys and Hatherly, 2004), and existed throughout the hot working temperature range and caused a Zener pinning effect (Imbert and McQueen, 2007). The grain boundaries were pinned by the carbides, subsequently suppressing any dynamic recrystallisation and stabilised the deformed or recovered microstructure. Carbides have an important role as pinning agents keeping grain boundaries in place (Momeni *et al.*, 2010, Kostka *et al.*, 2007).

Milovic *et al* (1992) reported that carbide precipitation retarded the dislocation movement and also the movement of subgrains and grain boundaries, thus suppressing dynamic recrystallisation. The Zener pinning effect became stronger when the volume fraction of carbides was higher. With a sufficiently small spacing of thermally stable precipitates, it is possible to keep the deformed or recovered microstructure up to high temperature and as a consequence increase the retention of the dislocation substructure at high deformation temperatures, thus providing a strengthening mechanism in addition to that of the precipitates (Humphreys and Hatherly, 2004). This is consistent with the flow curves showing that the highest flow stress was obtained after solutioning at 1100 ^{o}C and deformation at 1000 ^{o}C. The higher the solutioning and deformation temperatures, the more the carbides were dissolved into the matrix and as a result the Zener pinning effect was decreased, as demonstrated by the decreasing flow stress in Figure 6.2. The presence of MC carbides was confirmed using bright field TEM, see Figure 6.8.

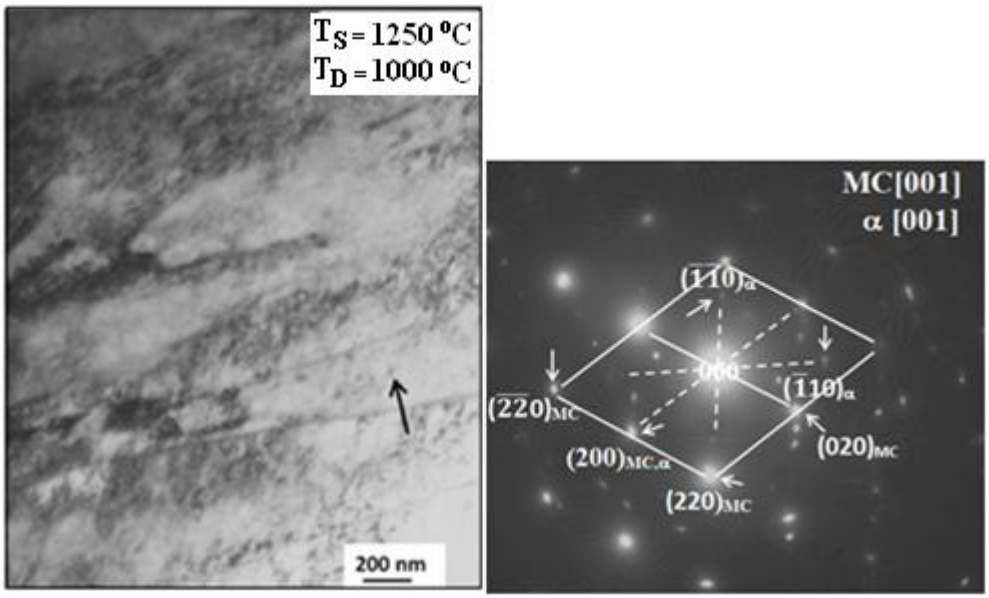

Figure 6.8 A bright field TEM image of a martensitic lath showing the MC carbides in the deformed H21 tool steel (left) and diffraction pattern of the MC carbide indicated by arrow (right).

The fine spherical MC carbides with size 5-10 nm were observed in the lath martensite. The lattice parameter of the MC carbide was ~ 0.422 nm. The

morphology and size of the MC carbides remained unchanged compared with the as cast condition. The MC carbide was not sensitive to deformation and had high thermal stability. This was different from the M_6C carbides that were very sensitive to deformation regarding both their size and morphology, as the M_6C carbides were coarser than the MC carbides. The typical dynamic recovery of elongated subgrains was observed using TEM, this provided further evidence for the absence of dynamic recrystallisation in the H21 tool steel, see Figure 6.9.

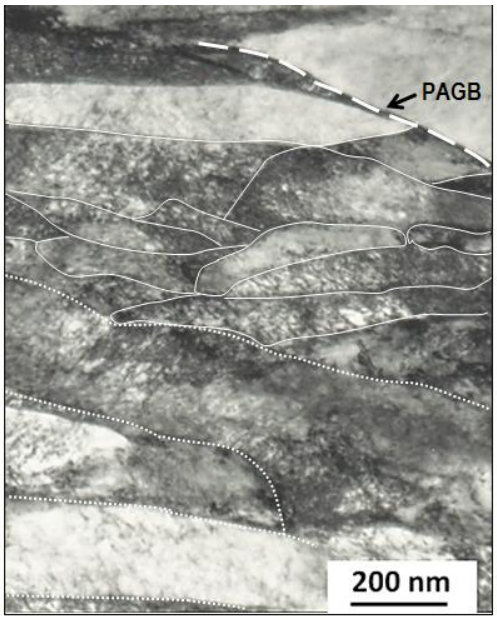

Figure 6.9 A bright field TEM image after solutioning at 1100 ^{o}C and deformation at 1100 ^{o}C showing elongated subgrains in the martensite lath. A prior austenite grain boundary (PAGB) is indicated by dashed line, prior martensite laths are indicated by dotted lines and sub-grain boundaries are indicated by full lines.

The formation of elongated subgrains during hot deformation, dislocation annihilation and rearrangement decreased rapidly the energy stored in the steel (Humphreys and Hatherly, 2004). Further TEM investigation was carried out to confirm the martensite structure on some deformed samples, see Figure 6.10.

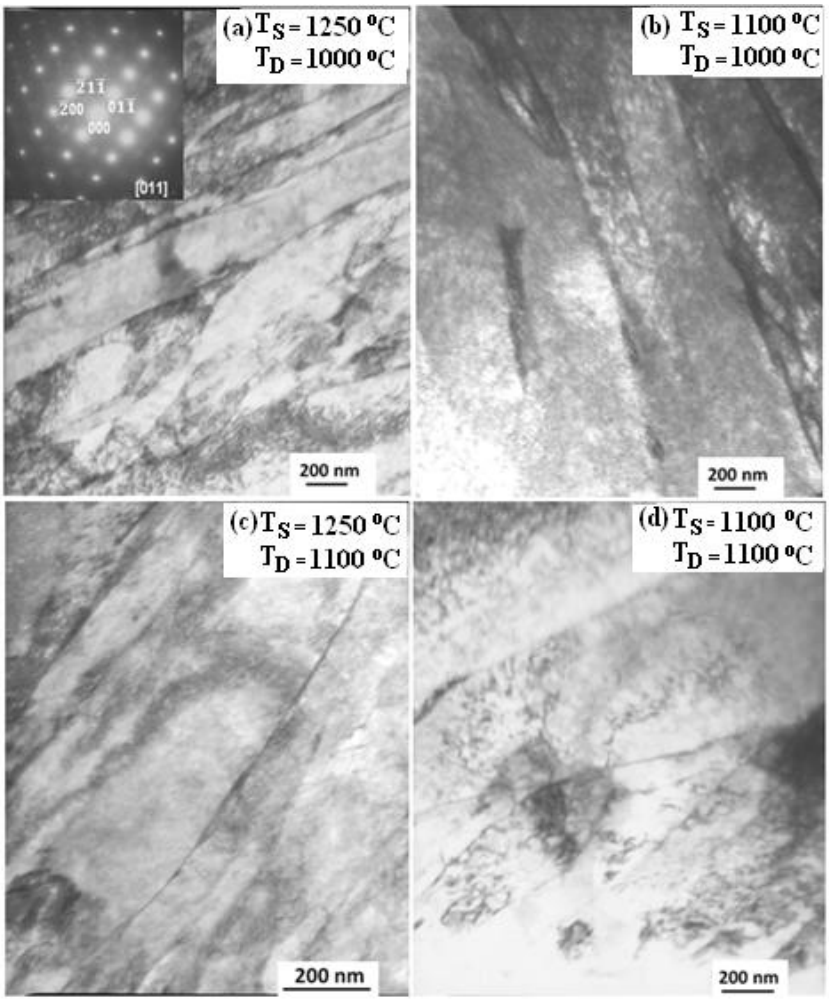

Figure 6.10 Bright field TEM images after solutioning and deformation. The inset of (a) shows selected area diffraction pattern of martensite region.

Figure 6.10 shows that the microstructure of the H21 tool steel following hot deformation and water quenching consisted of martensite and carbides. The morphology of the martensite was of lath type, and the martensite was heavily dislocated. The width of martensite laths varied between 0.1 to 0.4 μm, and they were slightly parallel to each other. The morphology of martensite did not change significantly at all the deformation and solutioning temperatures. However, the width of laths was slightly smaller at the higher solutioning temperature due to the larger driving force producing finer martensite laths. Figure 6.10 also shows qualitatively

that the higher the solutioning and deformation temperatures, the more the free dislocation areas, which indicated lower dislocation density.

Hot deformation of the H21 tool steel had an effect on the formation of fine lath martensite, which was primarily to increase the internal strains and M_s temperature, and as a result make the nucleation of martensite easier (Bhadeshia and Honeycombe, 2006). The formation of fine lath martensite structure in the deformed sample was attributed to the higher dislocation density in the course of deformation. The dislocation density was higher in the course of deformation so that within the martensite structure after hot deformation, a higher dislocation density still remained. TEM study also observed the formation of micro-twins appearing in the lath martensite with an average spacing of around 20 nm, see Figure 6.11.

Figure 6.11 A bright field TEM image after solutioning at 1250 ^{o}C and deformation at 1000 ^{o}C showing micro-twins.

The formation of micro-twins, as explained in Section 5.2.1, was attributed to dissolution of carbides producing a local area of austenite enriched with C. As micro-twins were also observed on the as quenched H21 tool steel without deformation, Figure 5.3, this formation of micro-twins was more affected by rapid cooling rather than by the deformation process itself.

TEM study also confirmed that lower bainite was present after deformation at 1000 ^{o}C and water quenching. A bainite plate with a curved surface can be seen in Figure 6.12, due to deformation-induced lattice curvature present in the former austenite grains prior to transformation (Bhadeshia, 2001).

Figure 6.12 A bright field TEM image after solutioning at 1250 ^{o}C and deformation at 1000 ^{o}C showing the presence of lower bainite (arrow indicates curved surface).

The presence of carbides can affect the bainite transformation (Xiao *et al.*, 2006). Undissolved carbides enable the composition of the austenite to be inhomogeneous during deformation and retard dislocation movement, producing a higher density of dislocations near the carbide. As a consequence of the increased dislocation density and high diffusivity paths, the carbides can dissolve, and the carbon concentration becomes higher, producing localised carbon segregation in the hot deformed austenite that subsequently promotes cementite carbide precipitation during the bainite transformation, producing the area with decreasing carbon concentration, which stimulates the nucleation of bainite. A secondary electron image and EDS data, Figure 6.13, show the C content near the carbides and the matrix.

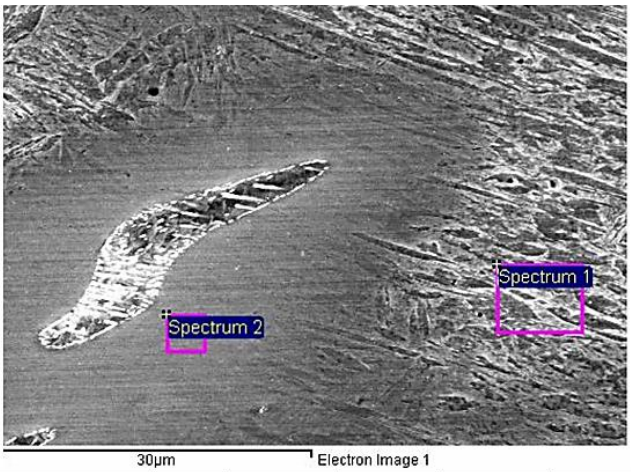

Element (wt%)	C	V	Cr	Fe	W
Spectrum 1	1.76	0.59	3.09	90.18	4.38
Spectrum 2	1.89	0.55	3.23	87.73	6.48

Figure 6.13 A SEM secondary electron image and EDS data of the H21 tool steel after solutioning at 1250 ^{o}C and deformation at 1000 ^{o}C.

In this study, (i) as the deformation temperature decreased, the volume fraction of undissolved carbides increased and the bainite transformation was more pronounced and (ii) the SEM-EDS data shown in Figure 6 13 would suggest that the C content near the undissolved carbide was slightly higher than that of the martensite area far away from the carbides. These observations could explain why the undissolved carbides influenced the bainitic transformation. However, internal stresses during the transformation from austenite to martensite can also accelerate the formation of bainite (Radcliffe and Rollason, 1959) as well as the stress applied during hot deformation produces a high density of dislocations that can affect the bainite transformation by increasing the driving force and transformation kinetics, and reducing the incubation period (Hase *et al.*, 2004, Shipway and Bhadeshia, 1995).

Figure 6.13 shows that the W content of the bulk matrix (spectrum 1) was lower than that of the matrix near the carbide (spectrum 2), which indicates the chemical heterogeneity between the matrix near the carbides and the martensitic matrix away from them. This heterogeneity led to different etching response, as shown in Figure 6.5 where the light areas are W rich. The light contrast area at higher magnification in Figure 6.7, shows that the martensite layer became thinner near the carbides. It is

well-known that the diffusion rate of interstitial solutes is greater than that of substitutional ones. In this tool steel the dissolution of the W rich M_6C carbides required longer time because the W diffused more slowly than C. As a consequence, when the carbides dissolved, the adjacent austenite became rich in W while the C diffused away. In addition, it is important to note that the M_s temperature varies with local alloying composition, which could cause the transformation of austenite to martensite to occur with different transformation kinetics from the grains to the prior austenite grain boundaries.

The microstructure produced by any of the heat treatments can be deduced using continuous cooling transformation (CCT) diagrams. This type of diagram gives the microstructures that should develop if equilibrium conditions are attained. To support the microstructure analyses, the CCT diagram of the H21 tool steel was used, as shown in Figure 6.14.

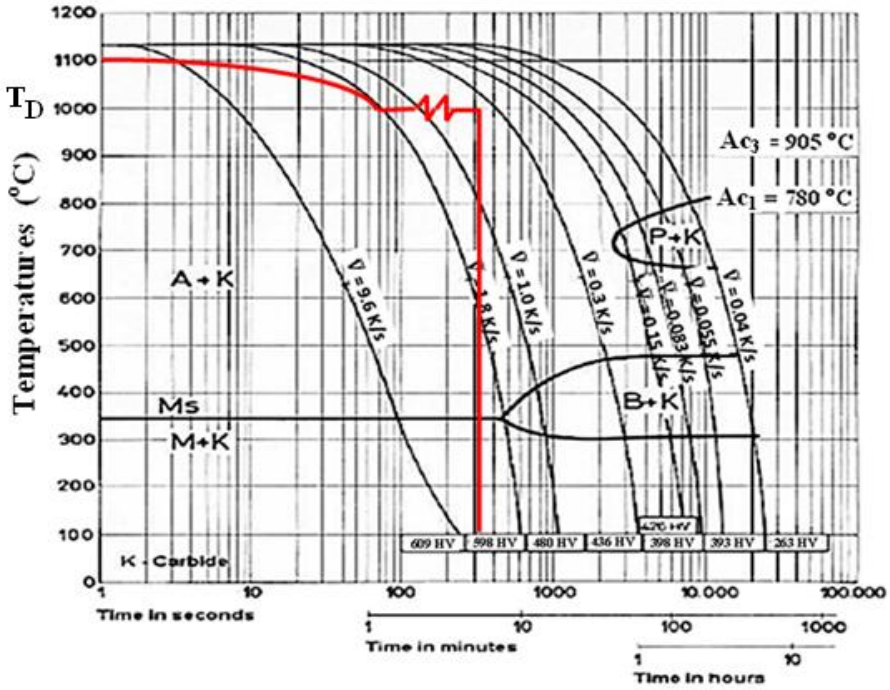

Figure 6.14 A CCT diagram for the H21 tool steel (Kaker, 2011) with one parameter of thermomechanical path superimposed (red line indicates the continuous cooling prior to deformation from T_S = 1100 ^oC to T_D = 1000 ^oC and then deformed at 1000 ^oC and water quenched).

Figure 6.14 presents the CCT diagram for the H21 tool steel (Kaker, 2011) together with the imposed cooling curve for solutioning at 1100 ^{o}C and deformation at 1000 ^{o}C. It is worthy to note that the position of different phases in the given CCT diagram can change depending on the deformation parameters. The M_s, Ac_1 (austenite formation start temperature on heating), Ac_3 (austenite formation complete on heating) temperatures as well as the critical cooling rate are the important findings of the obtained CCT diagram. The mechanical driving force supplied during deformation increased the M_s temperature (Guimarães, 2008) and B_s temperature (Bhadeshia, 2001). The CCT diagram in Figure 6.14 shows the temperature ranges of the precipitation of carbide, transformations of austenite to martensite, bainite, and pearlite. This diagram also indicated the hardness that could be achieved with various cooling rates. From Figure 6.14, it can be seen that the formation of bainite was highly possible, especially when the solutioning temperature was decreased. The deformation also affected the formation of bainite. Under applied low strain rate, which means longer time of deformation and increase of the B_s temperature, the formation of bainite was more pronounced in the deformed samples than in the undeformed samples and in addition the dislocation and other defects produced during deformation affected the progress of the bainite transformation (Shipway and Bhadeshia, 1995). In conventional heat treatment of the H21 tool steel, the formation of lower bainite was observed, Figure 5.2. The formation of lower bainite after deformation at 1000 ^{o}C can be seen in Figure 6.12.

TEM investigation also found the presence of retained austenite using the dark field imaging technique. Figure 6.15 shows the banded morphology of retained austenite in the H21 tool steel after hot deformation and water quenching.

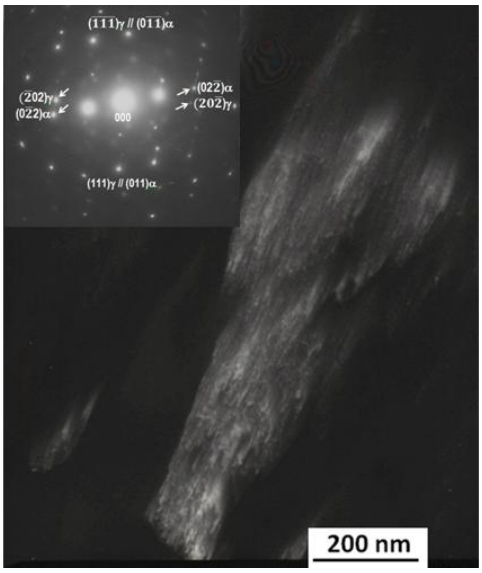

Figure 6.15 A dark field TEM image showing retained austenite (T_S = 1100 ^oC, T_D = 1000 ^oC). The insert shows the selected area diffraction pattern taken at the interface between retained austenite and martensite with $[011]_\gamma // [111]_\alpha$.

The banded morphology of the retained austenite further indicated that no recrystallisation had occurred during the time interval following deformation to the start of transformation. The electron diffraction pattern in Figure 6.15 shows that the orientation of the phases between martensite and austenite was in good agreement with a Kurdjumov-Sachs relation. Retained austenite was observed in the as quenched H21 tool steel without deformation, see Figure 5.4. In both cases quantitative measurements of the volume fraction of retained austenite were not made, however the impression from the microstructure studies was that the hot deformation decreased the volume fraction of the retained austenite compared with the as quenched H21 tool steel without deformation.

6.2.3.2 The H23 Tool Steel

As shown in Figure 6.3, the flow stress of the H23 tool steel exhibited the same behavior as the H21 tool steel, and indicated that dynamic recovery had occurred

during the hot deformation. Microstructure investigation was carried out to confirm the absence of DRX. Figure 6.16 shows the optical images of the deformed H23 tool steel.

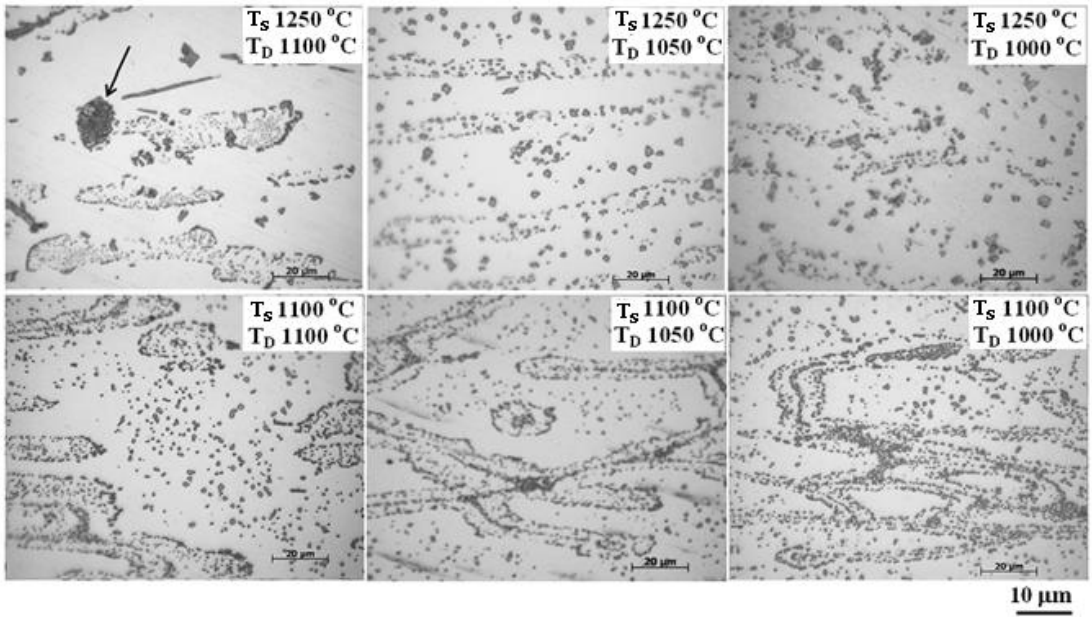

Figure 6.16 Optical images of the H23 tool steel after hot deformation and water quenching (arrow indicates the fishbone morphology of the M_6C carbide).

Attempts were made to reveal the PAGBs by using various etchants, see Section 3.3.1. Unfortunately, the PAGBs could not be revealed in the deformed microstructures for all deformation conditions, as can be seen in Figure 6.16. The structure of the deformed H23 tool steel consisted of ferrite and carbides, which was the same as in the as quenched condition without deformation. As mentioned before, the martensite was absent due to the M_s temperature of the H23 tool steel being far below room temperature (- 46 ^oC). This also contributed to the lower peak stress of the H23 tool steel, see Figure 6.4b. The formation of bands was also observed in the microstructure of the deformed H23 tool steel. Banding occurred primarily because of the segregation of solutes in the last regions of the liquid to solidify during the cooling of steel from the molten state. Hot deformation caused these regions to spread out as bands (Bhadeshia, 2010). The formation of banding was more pronounced in the H23 than the H21 tool steel owing to the greater difference in deformability between the matrix and the carbides. The ferrite matrix of the H23 tool

steel, which has higher deformability than the austenitic matrix of the H21 tool steel, gave better contrast between the matrix and the carbides in the former steel. As was the case in the H21 tool steel, the deformation influenced the carbide network in the direction perpendicular to the compression axis for all deformation temperatures. The carbides formed everywhere, not only on the grain boundaries but also in the grain interiors and at the lower solutioning temperature, the carbides network still existed as well as delta eutectoid carbides. Figure 6.16 shows that the higher deformation temperature, the lower volume fraction of carbides. As the deformation temperature increased the more carbides dissolved into the matrix.

The same mechanism as occurred in the H21 tool steel is thought to be responsible for the absence of dynamic recrystallisation. As shown in Figure 6.16, carbides in all deformation conditions existed throughout the hot deformation temperature range and their volume fraction seemed to be sufficient to prevent recrystallisation through a Zener pinning effect. The volume fraction of carbides was much higher at the lower deformation temperature and as a result the Zener pinning effect was increased. This is consistent with the flow curves that show the increase of the flow stress as the deformation temperature was decreased, Figure 6.3. Dispersed carbides in the H23 tool steel can be seen in Figure 6.17.

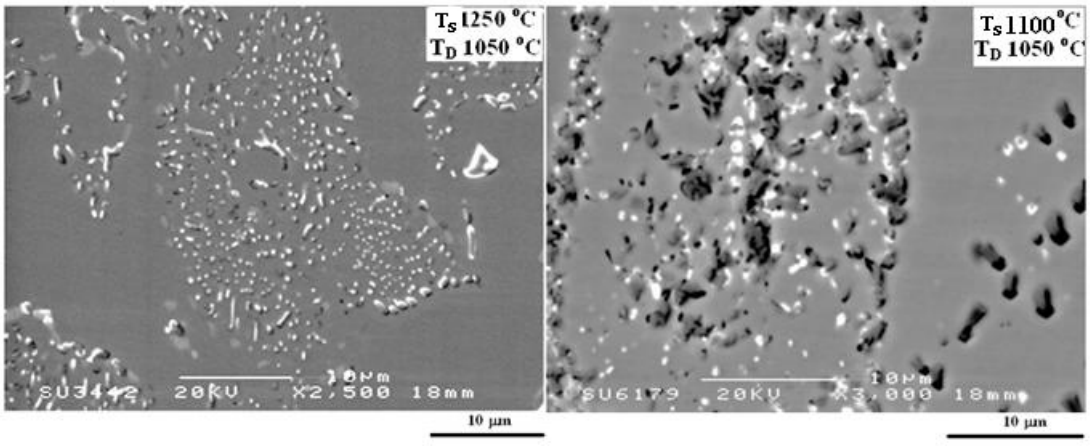

Figure 6.17 SEM back scatter electron images of the H23 tool steel after hot deformation with different solutioning temperatures.

Compared with the as quenched microstructure without deformation (Figures 5.9 and 5.10), the carbides after hot deformation, Figure 6.17, were finer and more dispersed. Back scatter electron imaging in the SEM can be used to identify the types of carbide using the different contrast of carbides. Figure 6.17 shows that there were two different contrasts of carbides, namely the white carbides that were M_6C carbides and the light grey carbides that were the M_7C_3 carbides. The total volume fraction of carbides was higher at the lower solutioning temperature. At the higher solutioning temperature, the M_6C carbides were finer and dominant and a smaller volume fraction of the M_7C_3 carbides was found in some areas. At the lower solutioning temperature, the volume fraction of the M_6C carbides was nearly the same with the M_7C_3 carbides and the latter clearly were coarser and had coalesced with the M_6C carbides. There was no indication of the existence of the $M_{23}C_6$ carbides owing to the high Cr content of the $M_{23}C_6$ carbides and their low dissolution temperature that caused the $M_{23}C_6$ carbides to dissolve completely before reaching the solutioning temperature.

It is well known that the stability of carbides depends on time, temperature and their chemical composition. Increasing the solutioning temperature caused the more carbides to dissolve into the matrix and as a result decreased the volume fraction of carbides. As the M_7C_3 carbides were rich in Cr and the M_6C carbides rich in W, and the diffusivity of Cr is higher than W, the M_7C_3 carbides grew and dissolved faster than the M_6C carbides. The M_7C_3 carbides were more stable at the solutioning temperature of 1100 ^oC compared with T_S = 1250 ^oC as they were coarser at the former temperature. With increasing the solutioning temperature, the M_7C_3 carbides lost their stability and dissolved into the matrix and as a result the M_6C carbides became the dominant ones. TEM investigation was carried out on one deformation condition to confirm the absence of dynamic recrystallisation, see Figure 6.18.

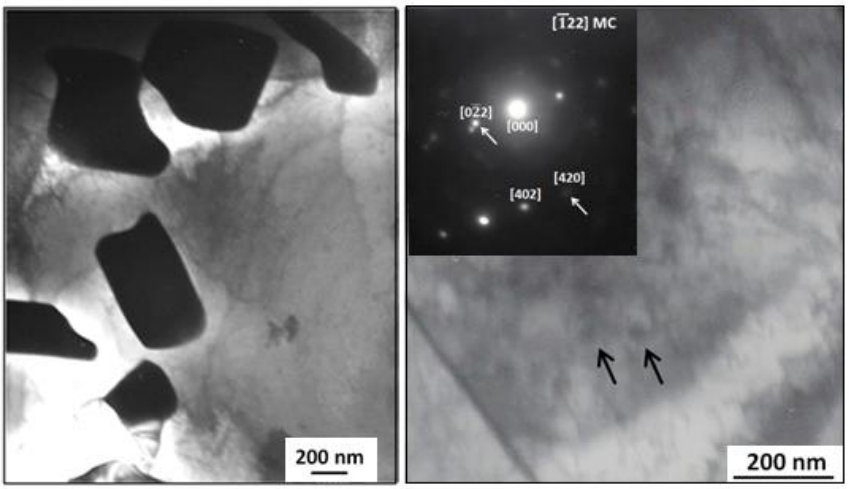

(a) (b)

Figure 6.18 Bright field TEM images of the H23 tool steel after solutioning at 1250 ^{o}C and deformation at 1000 ^{o}C showing (a) coarse M_6C carbides, and (b) the presence of dispersed fine MC carbides (indicated by arrows) and diffraction pattern of MC carbide.

Figure 6.18(a), shows the microstructure of the H23 tool steel after hot deformation. The grain structure was not clear enough but elongated grains, which are typical of dynamic recovery, were seen and there was no indication that recrystallisation had occurred. Figure 6.18(b) shows the presence of fine MC carbides and the diffraction pattern of a MC carbide. The morphology of MC carbides was the same as observed in the as quenched condition without deformation, Figure 5.6, i.e., spherical with size in the range 20-50 nm. This indicated that the MC carbides were not sensitive to deformation. The fine MC carbides also played an important role to pin the grain boundaries movement.

Based on the aforementioned results and discussion, it is suggested that the fine and dispersed MC and M_6C carbides played an important role in the H23 tool steel to inhibit the dynamic recrystallisation through a Zener pinning effect.

6.2.4 X-ray Diffraction of the H21 and H23 Tool Steels after Hot Deformation

XRD was performed to identify the phases after hot deformation. Figure 6.19 shows the XRD diffractograms of the H21 tool steel after hot deformation.

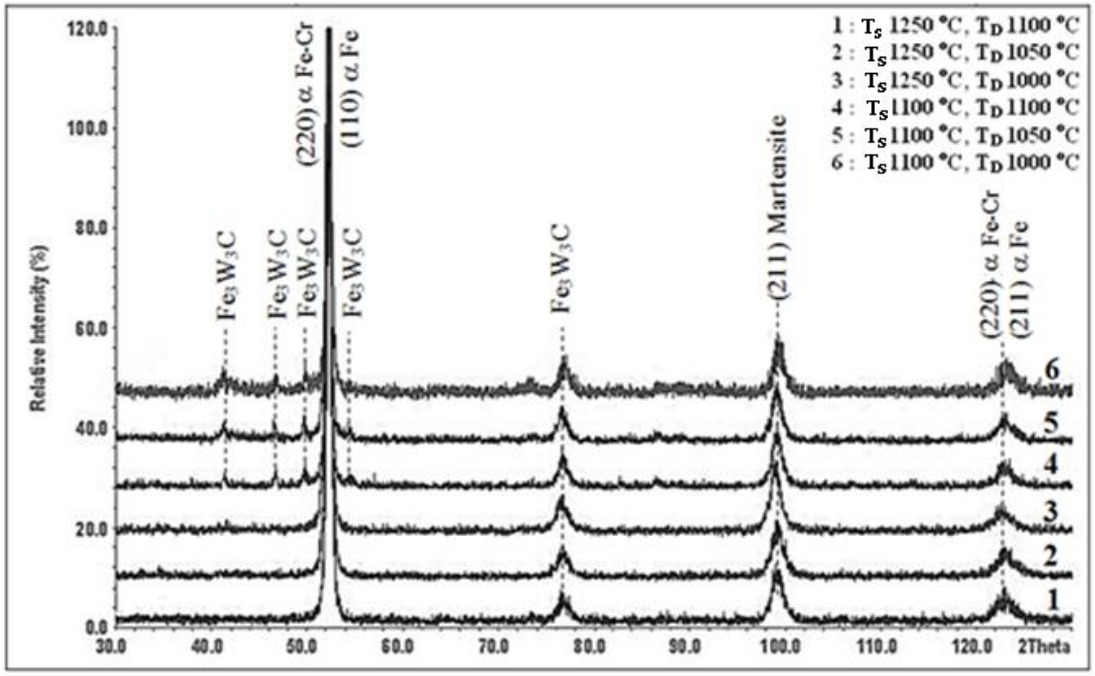

Figure 6.19 XRD diffractograms of the H21 tool steel after hot deformation.

The XRD diffractograms in Figure 6.19 confirmed the presence of αFe-Cr (ferrite) and α Fe (the super saturated solution or bainite), in good agreement with the ICDD cards 34-396 and 6-696, respectively, of martensite (ICDD card 44-1289) and of the M_6C carbides that were identified as Fe_3W_3C (ICDD card 41-1351). The number and intensity of peaks of the Fe_3W_3C carbides at the lower solutioning temperature was higher than that at the higher solutioning temperature, which indicated that the volume fraction of this carbide was higher at the solutioning temperature of 1100 ^oC. This is in good agreement with the microstructure analyses. Compared with the XRD results of the as quenched H21 tool steel without deformation, Figure 5.11, at the lower solutioning temperature with all deformation temperatures, the number and the intensity of peaks of the M_6C carbides was higher in the deformed samples than in the as quenched without deformation condition, which would suggest that the volume fraction of carbide precipitation had increased after hot deformation. No

peaks corresponding to retained austenite and MC carbides were observed owing to their volume fractions being very low to be detected by XRD.

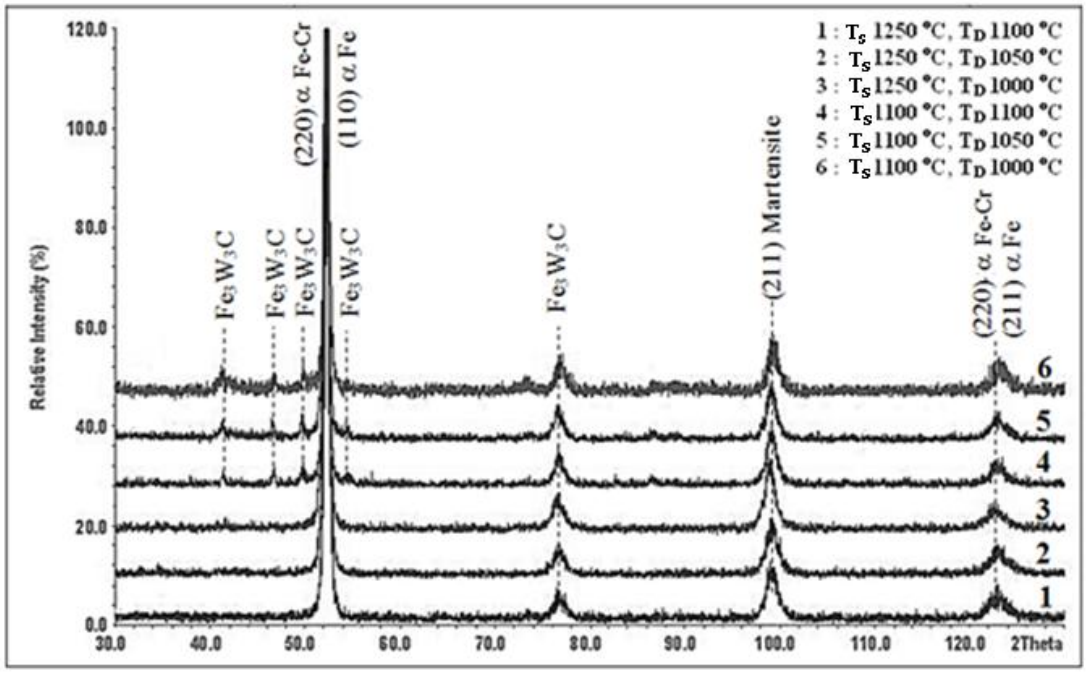

Figure 6.20 XRD diffractograms of the H23 tool steel after hot deformation.

Figure 6.20 shows the XRD data of the H23 tool steel after hot deformation. The XRD confirmed the presence of αFe-Cr (ferrite) in good agreement with ICDD card 34-396, and of the M_6C and M_7C_3 carbides that were identified as Fe_3W_3C and $(Cr,Fe)_7C_3$ (ICDD cards 41-1351 and 5-720, respectively). At all deformation conditions, there are more peaks of the Fe_3W_3C carbides than the $(Cr,Fe)_7C_3$ carbides. The MC carbides were not detected by XRD owing to their very small volume fraction. The presence of austenite was indicated by only one small peak (ICDD card 52-512). The XRD data in Figure 6.20 was compared with that of the as quenched H23 tool steel without deformation, Figure 5.12, to show that there was a decrease in the number and intensity of austenite peaks in all deformed samples. Therefore, the hot deformation had decreased the volume fraction of retained austenite. Hot deformation enhanced ferrite transformation kinetics by creating highly strained regions in the austenite lattice (Kozasu, 1972). Grain boundaries, slip bands, and other dislocation structures can act as nucleation sites to promote ferrite

transformation. The retained austenite and C concentration were not calculated due to the peak intensity of retained austenite in all deformation conditions being very low and showing a small split peak.

6.2.5 The Effect of Hot Deformation on Hardness

The hardness of the tool steels was affected by solutioning and deformation temperatures. The hardness of the tool steels after hot deformation is given in Table 6.3.

Table 6.3 The effect of hot deformation on hardness.

Tool Steel	Solutioning temperature (^{o}C)	Hardness (HV)			
		Deformation temperature (^{o}C)			Without deformation*
		1000	1050	1100	
H21	1250	617 ± 4	589 ± 1	569 ± 1	574 ± 1
	1100	570 ± 4	535 ± 3	524 ±5	536 ± 7
H23	1250	274 ± 2	236 ± 2	220 ± 1	302 ± 7
	1100	264 ± 3	235 ± 1	210 ± 2	279 ± 1

*See Table 5.3.

It can be seen that the higher solutioning temperature resulted to a higher hardness than the lower solutioning temperature. The hardness value of the deformed H21 tool steel was higher than that of the undeformed samples for the same solutioning temperature. The highest hardness with deformation (617 HV) of the H21 tool steel occurred after solutioning at 1250 ^{o}C, followed by deformation at 1000 ^{o}C. The highest hardness without deformation (574 HV) occurred after solutioning at 1250 ^{o}C. This confirmed the hardening effect of hot deformation on the H21 tool steel in all deformation temperatures. The volume fraction of carbides was measured for all deformation conditions, see Table 6.4.

Table 6.4 The volume fraction of carbides in the H21 and H23 tool steels after hot deformation.

Tool Steel	T_S (^oC)	Volume fraction of carbides (V_c)			
		With deformation			Without deformation*
		T_D = 1000 ^oC	T_D =1050 ^oC	T_D =1100 ^oC	
H21	1250	14.2 ± 1.1	14.0 ± 0.8	13.6 ± 0.3	14.7 ± 0.4
	1100	14.7 ± 0.9	14.3 ± 0.5	13.9 ± 0.4	15.1 ± 0.7
H23	1250	13.8 ± 0.4	13.7 ± 0.3	13.5 ± 0.3	13.9 ± 0.6
	1100	15.3 ± 0.6	15.0 ± 0.2	14.8 ± 0.2	15.3 ± 1.0

* See Table 5.4 .

It can be seen from Table 6.4 that the volume fraction of carbides after deformation was slightly lower than without deformation at both solutioning temperatures. This result suggested that the hot deformation increased the dissolution of the primary carbides into the matrix thus enriching the matrix with more alloying elements compared with the undeformed samples. In addition, the hardness of the deformed H21 tool steel was also affected by the martensite structure, owing to the lath martensite structure being finer in the deformed samples than in the undeformed samples.

The effect of deformation temperature on the hardness of the H21 tool steel, as shown in Table 6.3, was to increase the hardness with decreasing deformation temperatures at both solutioning temperatures owing to the higher volume fraction of dispersed M_6C carbides that existed at the lower deformation temperatures, see Table 6.4. The bainite formation, which was dominant at the lower solutioning and deformation temperatures, did not seem to contribute significantly to the hardness. Therefore, the dispersed carbides had a major role in defining the hardness after hot deformation.

There was a significant difference in hardness behaviour between the H23 and the H21 tool steels. The data in Table 6.3 shows that the hardness value of the deformed H23 tool steel was always lower than that of the non-deformed samples for the same

solutioning temperature. Note that there were two type of coarse carbides formed in the H23 tool steel during austenisation (with and without deformation), namely the M_6C and M_7C_3 carbides. The hot deformation accelerated the dissolution of carbides, and the M_7C_3 carbides dissolved into the matrix due to their high Cr content and lower thermal stability than the M_6C carbides. Compared with other alloying elements, Cr gives the smallest increase to the hardness of ferrite (Roberts *et al.*, 1998). Thus, the dissolution of the Cr rich M_7C_3 carbides during hot deformation did not make a strong contribution to hardness. For the samples without deformation the holding time (1 hour) during austenisation allowed not only M_7C_3 carbides but also the finer M_6C carbides to dissolve, thus enriching the ferrite matrix with more alloying elements. Therefore, it can be said that, in the as quenched H23 tool steel without deformation, the matrix was enriched not only in Cr but also in W, which significantly increased the hardness of ferrite.

The data for the H23 tool steel in Table 6.3 shows that the lower deformation temperature the higher the hardness value. This may be attributed to the higher volume fraction of dispersed M_6C carbides at the lower deformation temperature. However, the absence of martensite in the H23 tool steel was the main reason for the great difference in hardness values between the H21 and H23 tool steels.

Based on the hardness data after hot deformation in Table 6.3, the H21 tool steel, which reached higher hardness than the H23 tool steel, was selected for double temper.

6.3 The Effect of Double Temper in the H21 Tool Steel after Hot Deformation

6.3.1 The Effect of Double Tempering Temperature on Microstructure

The double tempering process was necessary to stabilise the microstructure of the H21 tool steel after hot deformation. Double tempering can increase the secondary

hardness, and the volume fraction of carbides (Fares *et al.*, 2012, Hufenbach *et al.*, 2012). A TEM investigation was carried out to support the microstructure analyses on some double tempered samples. The double temper samples for thin foil sample preparation were selected from the highest and lowest deformation and double tempering temperatures by considering significant differences of microstructure. The resulting microstructures consisted of tempered lower bainite, tempered martensite, with precipitates located along the grain boundaries and within the lath boundaries, see Figure 6.21.

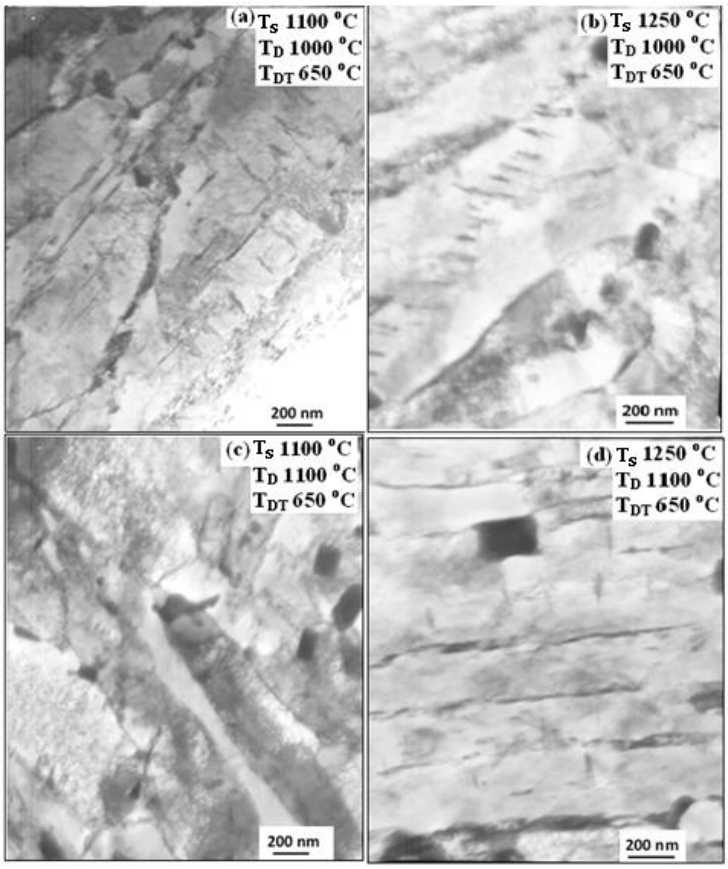

Figure 6.21 Bright field TEM images after solutioning, hot deformation and double tempering at 650 ^{o}C, showing the formation of tempered lath martensite (a, c and d) and tempered lower bainite (b).

TEM images of the H21 tool steel after double tempering for 1 hour at 650 ^{o}C with air cooling in between the first and the second stages in Figure 6.21 show cementite

precipitates and that the lath morphology was still present. Needle shape coarse cementite precipitates were located within laths and lath boundaries. The appearance of the cementite precipitates within laths and lath boundaries indicated that cementite precipitation occurred in the early stages of tempering. The cementite grew as the tempering temperature increased. The mean thickness of cementite carbides was in the range 9-15 nm, which was not significantly different than that measured in the as quenched condition without deformation, Figure 5.19. The microstructures in Figure 6.21 also show that dislocations formed networks through recovery process. However, as was the case in the double tempered H21 tool steel without deformation, the recovery was not completed as indicated by the presence of high dislocation density in some areas in martensite lath. The partial recovery was probably due to insufficient time being available for completing the recovery process and the presence of fine carbides within the matrix delayed the recovery process during tempering by impeding the dislocations movement through a pinning effect. The recovery seemed to be more effective at the higher solutioning temperature (Figure 6.21b,d) and the higher deformation temperature (Figure 6.21c,d). This was attributed to the lower dislocation density at higher solutioning and deformation temperature.

Figure 6.21b shows the formation of tempered lower bainite. The major difference between tempered martensite and tempered lower bainite is that the cementite precipitates in lower bainite occur frequently on one crystallographic variant of the orientation relationship. The major axis of the cementite forms parallel arrays at about 60^{o} to the axis of the bainitic lath whereas, in tempered martensite, the carbides tend to precipitate in Widmanstätten arrays. The occurrence of single variants of cementite in lower bainite illustrated in Figure 6.21b because the cementite precipitation was influenced by the self-stress of the bainite plate (Chang and Bhadeshia, 1996).

There were two significant differences regarding carbide (Figure 6.21) and equiaxed grain (Figure 6.22) formation between the two double tempered conditions with

deformation and without deformation (Figure 5.19) at the tempering temperature of 650 ^{o}C. The double tempered microstructure with deformation in Figure 6.21 shows that the M_2C carbides were not clearly observed. It seems that hot deformation caused the unstable M_2C carbides to dissolve below 650 ^{o}C (or lower temperature than in the double temper without deformation) and resulted to the formation of secondary M_6C carbides. This finding suggests that hot deformation had accelerated the dissolution of M_2C carbides and promoted the formation and growth of the stable M_6C carbides. Further TEM study was carried out on thin foil of the H21 tool steel after solutioning at 1100 ^{o}C, deformation at 1100 ^{o}C and double temper at 650 ^{o}C, see Figure 6.22.

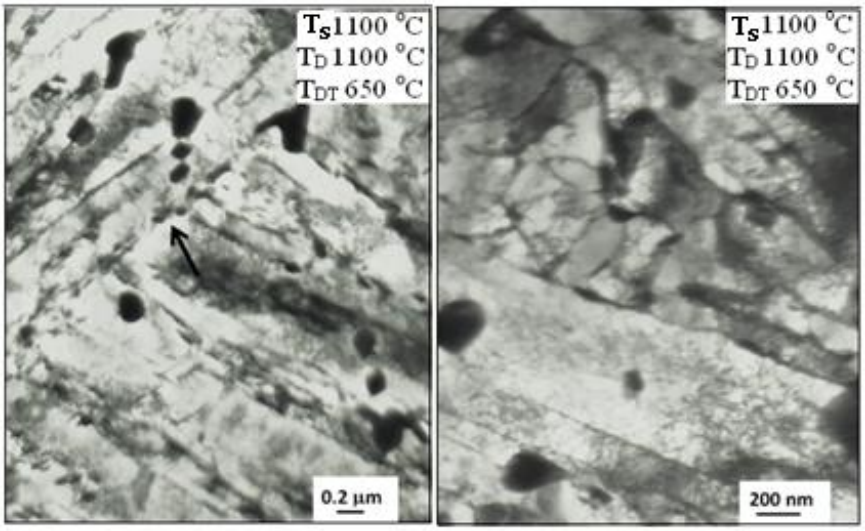

Figure 6.22 Bright field TEM images showing the prior austenite grain boundary, PAGBs, indicated by arrows (left) and the formation of equiaxed grain within lath (right).

It can be seen from Figure 6.22 that the PAGBs and dislocations within the lath were revealed. At higher magnification (Figure 6.22, right), TEM found that the equiaxed grains had gradually developed within the lath indicating that the recrystallisation had started at 650 ^{o}C. This finding would suggest that the effect of hot deformation on double temper not only accelerated the dissolution of the M_2C carbides and the formation of the secondary M_6C carbides but also accelerated the formation of equiaxed grains at double temper at 650 ^{o}C.

It is well known that the lath morphology formed in as quenched steel (without deformation) is quite stable and does not change after tempering, although equiaxed ferrite grains are sometimes formed after long time holding at higher tempering temperatures (Speich, 1969). In this study, recrystallisation was not observed in the as quenched martensite (without deformation) on double tempering even at 750 ^{o}C (Figure 5.15). With increasing tempering temperature to 800 ^{o}C, the carbides tended to become spheroidised and coalesced, and equiaxed ferrite grains formed partially (Figure 5.16). The high resistance to recrystallisation of the undeformed quenched H21 tool steel during double tempering below 750 ^{o}C, despite the fact that the lath martensite contains a high density of dislocations formed during quenching, was due to the inhibiting effect of precipitated fine carbides, which suppressed the boundary migration and retarded the recrystallisation (Caron and Krauss, 1972).

Some authors (Tokizane *et al.*, 1982, Babich *et al.*, 1977) reported that the lath martensite recrystallised easily on tempering when martensite was deformed. In this study, the recrystallisation was observed in deformed lath martensite at double temper 650 ^{o}C, see Figure 6.22. According to Tokizane *et.al* (1982) the phase transformation from austenite to martensite (without deformation) resulted in a fairly uniform distribution of dislocations. On the contrary, the plastic deformation prior to tempering produced deformation bands and cell structure of dislocations resulting in heterogeneous dislocation arrangement in the deformed regions even with the same dislocation density. This heterogeneity caused the driving force for recrystallisation in deformed ferrite to be higher than without deformation, and provided effective nucleation sites for recrystallisation. Therefore, it can be said that, the heterogeneity of deformed regions was favorable for the nucleation of recrystallisation during temper.

It is believed that no retained austenite remained in all double tempered conditions. The double tempered microstructure in Figure 6.21 did not indicate the presence of retained austenite. During the first tempering, retained austenite had decomposed

into lower bainite in the temperature range 230 - 300 ^{o}C, which was indicated by the formation of the coarse and elongated cementite at the lath boundaries. Kwon and Kim (1983) reported that the coarse and elongated interlath cementite is the typical characteristic of the decomposition of retained austenite. The stability of retained austenite decreased with increasing tempering temperature. Let us now consider the results of the TEM study of the H21 tool steel double tempered at 800 ^{o}C, see Figure 6.23.

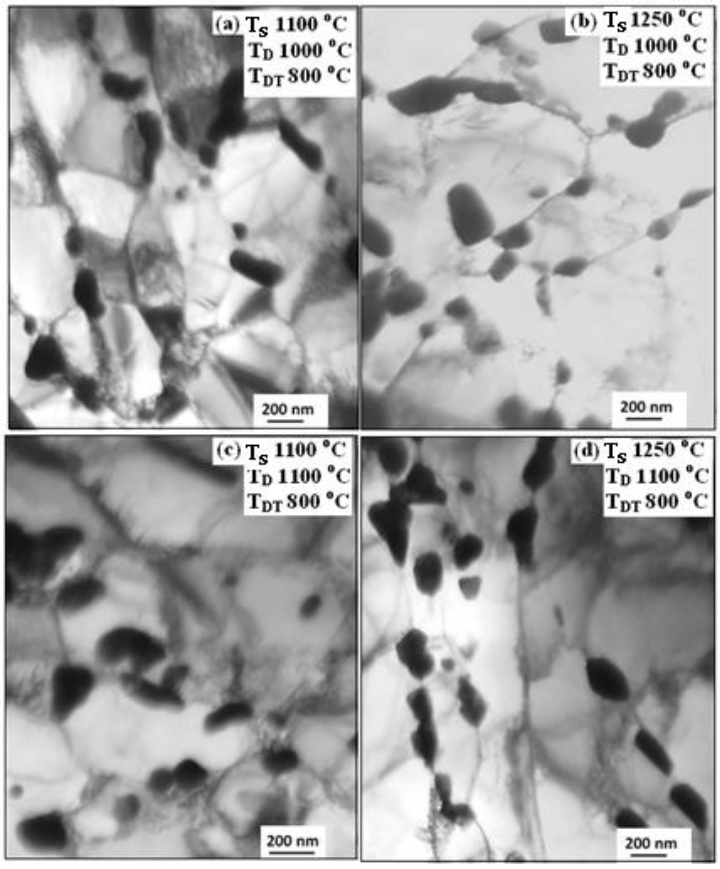

Figure 6.23 Bright field TEM images after solutioning, hot deformation and double tempering at 800 ^{o}C.

The TEM images in Figure 6.23 show that the lath morphology had disappeared and equiaxed grains tended to form with clear boundaries and larger carbides. The ferrite grains in Figure 6.23 are finer and the carbides smaller and separated compared with the double tempered without deformation condition, Figure 5.16. Figure 6.23 also shows clearly that the carbides located along the grain boundaries were larger than

those within the grain interiors, which would suggest that the stable carbides nucleated first in the grain boundaries and grew rapidly and replaced non-stable carbides within the grains. In summary, the growth rate of the carbides was faster at the grain boundaries. This phenomenon was the same as in the double tempered H21 tool steel without deformation.

In Figure 6.23 there is no indication of the presence of M_3C carbides. Increasing the tempering temperature from 650 to 800 ^oC caused the increase of the mean size of cementite carbides in order to reduce the total area of the ferrite/carbide interphase boundary. This process caused decrease of the volume fraction of cementite carbides and increased the spacing between the carbides. The increase of the spacing between the carbides decreased the effectiveness of these carbides in hindering the dislocation movement and as a result the hardness of the steel decreased. Since the cementite carbides were not observed, it seems that the precipitation of cementite was complete before reaching the tempering temperature of 800 ^oC and these cementite carbides were replaced by secondary carbides. The formation of the secondary $M_{23}C_6$ carbides was also found by TEM-EDS, as can be seen in Figure 6.24. Note that, during the EDS analysing of the $M_{23}C_6$ carbides, there was interference between the interaction volume and matrix owing to the carbide size.

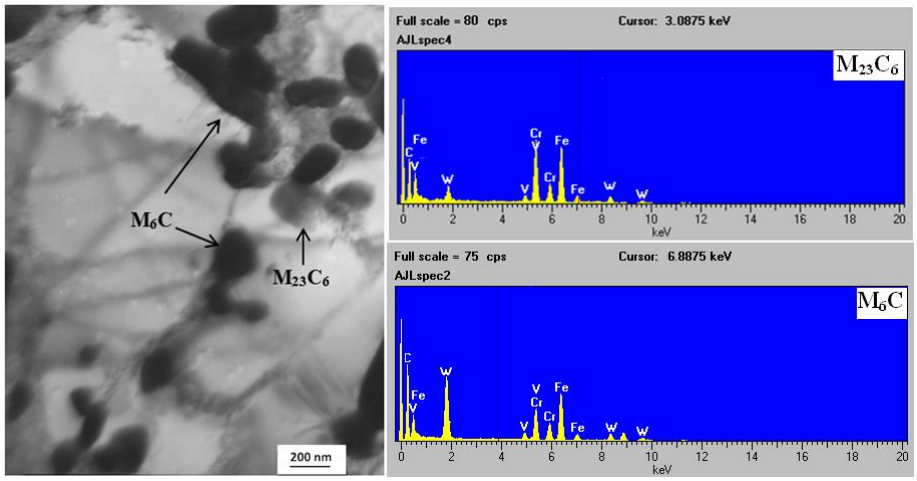

Figure 6.24 A bright field TEM image of the deformed H21 tool steel (T_S = 1250 ^oC, T_D = 1000 ^oC, T_{DT} = 800 ^oC) and EDS spectra of the M_6C and $M_{23}C_6$ carbides.

Figure 6.24 shows that the $M_{23}C_6$ carbides were present and had a nearly spherical morphology. This Cr-rich type of carbide that formed during double temper was the result of the transformation from Fe_3C, as discussed in Section 5.3. The formation of alloy carbides to replace cementite carbides occurred by nucleation at prior austenite grain boundaries that are energetically favourable nucleation sites (Durrand-Charre, 2004). The massive carbides were identified as the M_6C carbides. It is believed that the secondary M_6C carbides formed from the M_2C carbide transformation within the matrix and nucleated predominantly on the grain boundary. There was no indication that the Fe_3C carbides still existed after tempering at 800 ^oC.

In-situ nucleation was not observed in the TEM studies. The carbides had nucleated heterogeneously. It can be concluded that the deformation did not affect the carbide transformation sequence and could only cause a change in the rate of formation, dissolution and coarsening of the carbides. The acceleration of carbide precipitation was due to increased vacancy concentration by the deformation and the local residual strain, which created more opportunities for carbide nucleation and greater mobility of carbide forming elements (Bain and Paxton, 1966).

6.3.2 X-ray Diffraction of the Double Tempered H21 Tool Steel

The XRD diffractograms for two tempering temperatures of the deformed H21 tool steel are shown in Figures 6.25 and 6.26.

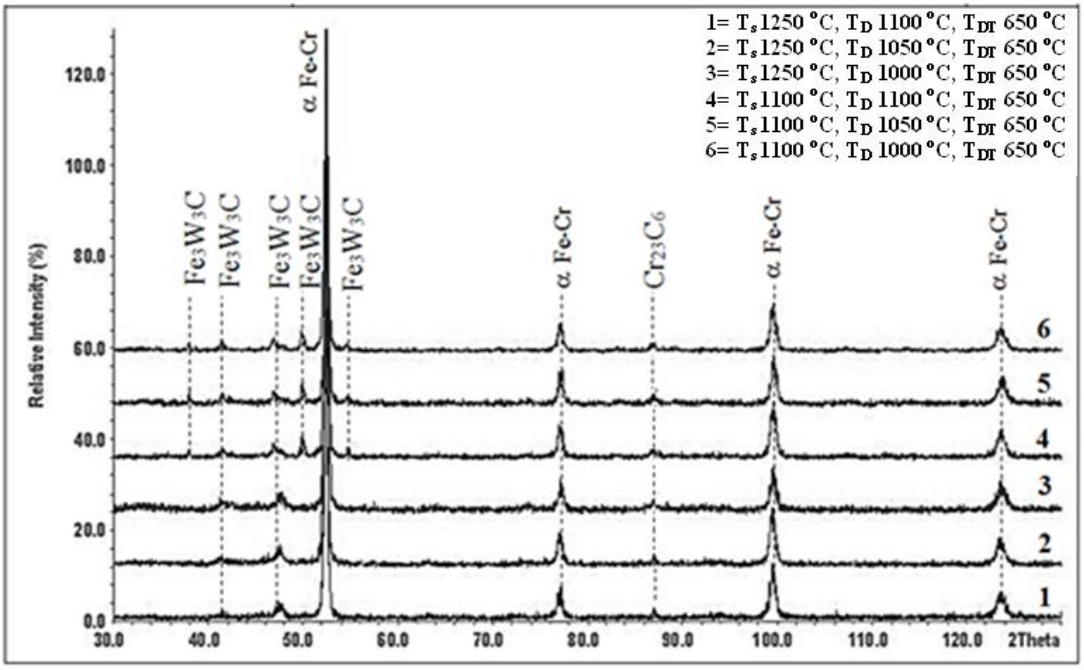

Figure 6.25 XRD diffractograms of the deformed H21 tool steel after double temper at 650 ^{o}C.

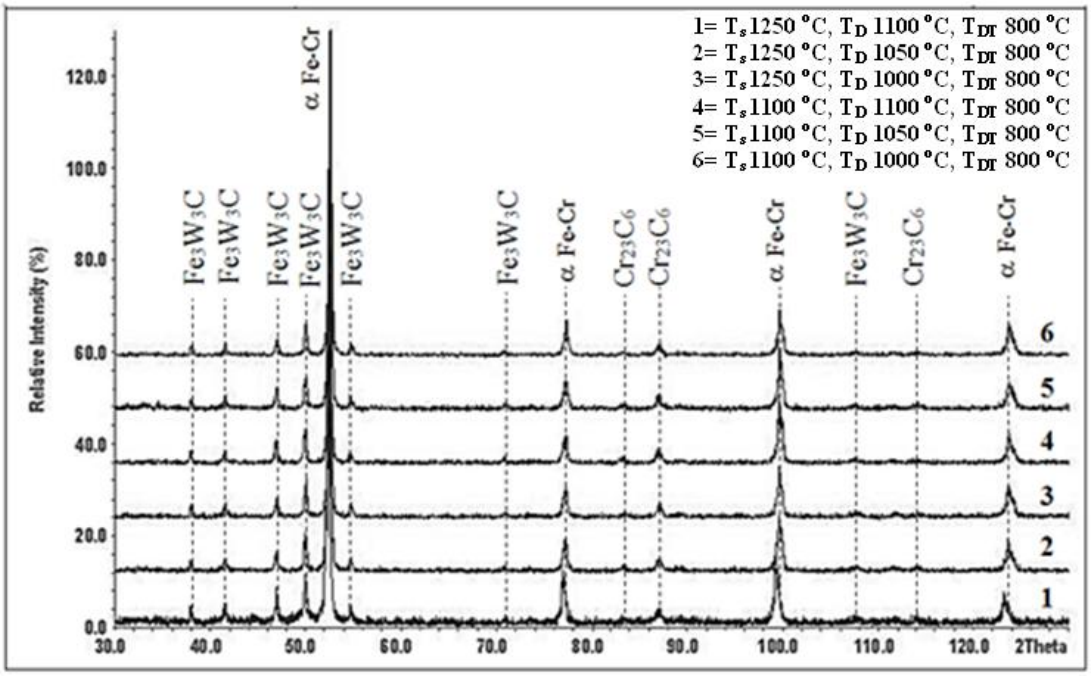

Figure 6.26 XRD diffractograms of the deformed H21 tool steel after double temper at 800 ^{o}C.

Figures 6.25 and 6.26 show that the phases present in the double tempered H21 tool steel with deformation were the same as those in the double tempered condition without deformation, see Figure 5.20. The αFe-Cr phase was in good agreement with ICDD 34-396, and the M_6C and $M_{23}C_6$ carbides were identified as the Fe_3W_3C and $Cr_{23}C_6$ carbides (ICDD cards 41-1351 and 35-783, respectively).

There was a significant difference in the XRD data regarding the $Cr_{23}C_6$ carbides at double temper at 650 ^oC and 800 ^oC. The number of peaks of the $Cr_{23}C_6$ carbides at double temper at 650 ^oC, Figure 6.25, was less than at double temper at 800 ^oC, Figure 6.26. This indicated that the $Cr_{23}C_6$ carbides had formed at the double tempering temperature of 650 ^oC and the volume fraction of this carbide was higher at the double tempering temperature of 800 ^oC. In the double tempered at 650 ^oC without deformation condition, Figure 5.20, no peak corresponded to the $Cr_{23}C_6$. This finding would suggest that the hot deformation had accelerated the formation of the $Cr_{23}C_6$ carbides, which started to nucleate below the tempering temperature of 650 ^oC. The number of peaks of the $Cr_{23}C_6$ carbides at double temper at 800 ^oC with deformation was higher than that without deformation. This was attributed to hot deformation providing more nucleation sites for carbide precipitation and as a result increasing the volume fraction of this carbide.

Figure 6.25 shows that the number of peaks of the M_6C carbides at the higher solutioning temperature was less than at the lower solutioning temperature owing to higher volume fraction of carbides dissolved into the matrix. The number of peaks of the M_6C carbide was increased with increasing double tempering temperature, Figure 6.26. This was attributed to the formation of secondary M_6C carbides. The hot deformation also affected the formation of Fe_3W_3C carbides. More peaks of the Fe_3W_3C carbide were detected in the deformed H21 tool steel after double temper at 650 ^oC, at solutioning temperature of 1100 or 1250 ^oC, than without deformation. It is suggested that the formation of secondary M_6C carbides occurred below double temper 650 ^oC.

6.3.3 The Effect of Double Tempering Temperature on Hardness

Tempering of tool steels after hot deformation and water quench can bring about secondary hardening by the precipitation of alloy carbides in the material, which moderately improves the mechanical properties. The double tempering temperature also affected the hardness of the tool steel. Table 6.5 shows the hardness variation as a function of tempering temperature.

Table 6.5 The effect of double tempering temperatures on hardness.

With deformation				Without deformation*		
T_S (^oC)	T_D (^oC)	T_{DT} (^oC)	Hardness (HV)	T_S (^oC)	T_{DT} (^oC)	Hardness (HV)
1100	1000	650	311 ± 2.4	1100	650	422 ± 1.8
		750	244 ± 2.2			
		800	237 ± 2.1			
	1050	650	306 ± 2.0		750	247 ± 1.2
		750	235 ± 1.2			
		800	232 ±0.7			
	1100	650	303 ± 1.2		800	236 ± 0.8
		750	234 ± 1.4			
		800	231 ± 1.6			
1250	1000	650	354 ± 2.4	1250	650	505 ± 1.0
		750	264 ± 2.0			
		800	237 ± 3.3			
	1050	650	347 ± 2.3		750	270 ± 1.1
		750	260 ± 0.8			
		800	234 ± 2.0			
	1100	650	336 ± 2.1		800	247 ± 1.1
		750	256 ± 2.2			
		800	233 ± 1.7			

*See Figure 5.29.

The double tempered hardness after hot deformation decreased significantly and was lower than the hardness after double tempering without deformation (505 HV) and the double tempered hardness decreased continuously with increasing tempering temperature at both solutioning temperatures. However, the double tempered

hardness after solutioning at 1250 ^{o}C was higher than that at 1100 ^{o}C. As explained before, this is because at the higher solutioning temperatures, more carbides were dissolved into the matrix, giving a higher supersaturation and driving force for precipitation, which in turn provided more nucleation sites for carbide precipitation during the double tempering process.

The highest double tempered hardness (354 HV) occurred after double temper at 650 ^{o}C with solutioning at 1250 ^{o}C and deformation at 1000 ^{o}C. The values are lower and far from the desired hardness, which is 450-550 HV (Roberts *et al.*, 1998). This implies that the operating temperature for the H21 tool steel after experiencing hot deformation should be less than 650 ^{o}C. Softening of hot work tool steels during tempering has been strongly connected with the evolution of carbide precipitation and martensite decomposition. Deformation affected the tempering resistance of the tool steel resulting to rapid softening as the deformation temperature increased. The deformation accelerated the sequence of carbide precipitation in which the fine carbides (M_2C) that are responsible for secondary hardening were gradually replaced by coarse cementite carbides during temper at 650 ^{o}C (Lee and Chun, 1981). The acceleration of carbide precipitation was due to an increased vacancy concentration by the deformation and the local residual strain, which created more opportunities for carbide nucleation and greater mobility of carbide forming elements (Bain and Paxton, 1966). Higher tempering temperatures resulted in a decrease in hardness due to coarsening of carbide precipitates, the recovery of the dislocation-rich martensitic structure and ferrite grain growth. No secondary hardening occurred. This implies that in the tool steel of this study the secondary hardening during double tempering after hot deformation occurs below 650 ^{o}C.

6.4 Conclusions

In the first part of this chapter, the effects of solutioning and deformation temperature on the flow stress behaviour, microstructure evolution and hardness of the H21 and H23 tool steels were studied. The following concluding remarks can be made:

1 In all experimental conditions, the flow curves of the H21 and H23 tool steels showed that no dynamic recrystallisation occurred and the peak stress of the H23 tool steel was lower than the H21 tool steel.

2 The dispersed M_6C and MC carbides played an important role in hindering the grain boundary movement through a Zener pinning effect that caused dynamic recovery in the H21 and H23 tool steels.

3 The deformation temperature influenced the carbide network in the direction perpendicular to the compression axis and reduced the carbide size effectively. At higher solutioning and deformation temperatures the carbide networks had broken down.

4 The most dispersed of M_6C carbides with mean size of ~ 0.2 μm were observed after solutioning at 1100 ^oC and followed by hot deformation at 1000 ^oC in the H21 tool steel.

5 The as quenched microstructure of the H21 tool steel after hot deformation consisted of lath martensite, lower bainite, retained austenite and carbides and lower deformation temperatures tended to stabilise the bainite transformation. The as quenched microstructure of the H23 tool steel after hot deformation consisted of ferrite, retained austenite and carbide.

6 The relationship between the product martensite and parent austenite was in good agreement with a Kurdjumov-Sachs orientation.

7 The improvement of the hardness of the H21 tool steel by high temperature axisymmetric compression test was due to the distribution of fine carbide precipitates and the refinement of the martensite structure.

8 The hot deformation had increased the hardness of the H21 tool steel, the highest hardness with deformation (617 HV) occurred after solutioning at 1250 ^oC, followed by deformation at 1000 ^oC. On the contrary, the hot deformation had decreased the hardness of the H23 tool steel, the highest hardness (274 HV) was achieved after solutioning at 1250 ^oC, followed by deformation at 1000 ^oC.

9 The peak stress, microstructure and hardness data indicated that the optimum hot deformation condition was solutioning at 1250 ^{o}C and deformation at 1100 ^{o}C.

The second part of this chapter focused on the effect of double tempering temperature of the H21 tool steel on the microstructure evolution, and hardness. The conclusions of this study are as follows:

1 After hot deformation and double tempering, the microstructure of the H21 tool steel consisted of tempered martensite, tempered lower bainite and carbides.

2 No secondary hardening phenomena occurred after double tempering at 650, 750 and 800 ^{o}C for the H21 tool steel samples that were first subjected to hot deformation. The highest double tempered hardness (354 HV) occurred after a double temper at 650 ^{o}C following solutioning at 1250 ^{o}C and subsequent deformation at temperature 1000 ^{o}C. The evidence from this study suggested that the operating temperature for the H21 tool steel after experiencing hot deformation with the conditions used in this study should be less than 650 ^{o}C.

3 The softening of the H21 tool steel when double tempered at high tempering temperatures was due to coarsening of carbide precipitates, the recovery of the dislocation-rich martensitic structure and ferrite grain growth.

4 The present study found that deformation did not affect the carbide transformation sequence and could only cause a change in the rate of carbide formation, dissolution and coarsening.

Chapter 7
Conclusions and Future Work

7.1 Conclusions

The present study was designed to determine (a) the process parameter (deformation temperature) of controlled thermomechanical processing that makes possible the break-down of the carbide network and (b) the double tempering parameter (temperature), which could achieve satisfactory balance in hardness and toughness of two tungsten hot working tool steels. The study of the microstructures of the as cast H21 and H23 tool steels was given in Chapter 4. The effects of conventional heat treatment on microstructures and hardness of the two tool steels were presented in Chapter 5. The main focus of the study was the effect of controlled thermomechanical processing and double temper on microstructure and hardness as described in Chapter 6. The following were the conclusions of the whole study.

7.1.1 The As Cast H21 and H23 Tool Steels

1. The morphology of the M_6C carbides in the as cast H21 tool steel was lamellar with very little or no interconections between individual carbide platelets; there was neither a backbone at the center or carbide wall around the eutectic carbide-matrix interfaces.
2. In the H23 tool steel, there were two different carbide morphologies, namely a rod like morphology for the M_6C carbides located inside the grains and forming thick layer carbides (skeleton) at the centre and a “discontinuous wall” of carbides around the outer edge of the eutectic colony of M_6C carbides located along the

grain boundaries. The eutectoid M_6C carbides formed inside the grains in some areas and their features were nearly the same as those of the eutectic carbides.

3. The fine carbides were MC carbide in the H21 tool steel and MC and $M_{23}C_6$ carbides in the H23 tool steel.
4. The H21 and H23 tool steels basically had the same solidification path starting with the formation of delta ferrite from the melt and followed by the formation of austenite through peritectic reaction and then eutectic transformation.

7.1.2 Conventional Heat Treatment

1. The as quenched microstructure of the H21 tool steel consisted of lath martensite, lower bainite and carbides and the as quenched microstructure of the H23 tool steel consisted of ferrite, retained austenite and carbides and no evidence of martensite formation.
2. XRD detected the presence of retained austenite in the H23 tool steel. The content of retained austenite in the H23 tool steel increased from 6.1 % at T_S = 1100 ^oC to 8.4 % at T_S = 1250 ^oC. The austenite lattice parameter increased from 0.360 at T_S = 1100 ^oC nm to 0.361 nm at T_S = 1250 ^oC .
3. The highest as-quenched hardness values of the H21 and H23 tool steels were 574 HV and 302 HV, respectively, and were obtained after solutioning at 1250 ^oC. The martensitic transformation contributed significantly in the hardening of the H21 tool steel.
4. The double tempered microstructure of the H21 tool steel consisted of lower tempered martensite, lower tempered bainite and carbides and the double tempered microstructure of the H23 tool steel consisted of ferrite and carbides.
5. The MC and M_6C carbides in both tool steels were stable over the whole temperature range.
6. The highest double tempered hardness of the H21 and H23 tool steels was 505 HV and 448 HV, respectively and was obtained after solutioning at 1250 ^oC and

double temper at 650 ^{o}C. Secondary hardening due to secondary precipitation of fine carbides was not observed.

7. The carbide evolution sequence in the H21 and H23 tool steels was as follows:

   in the H21 tool steel:

   in-situ transformation : Matrix → Fe_3C → $M_{23}C_6$

   separate transformation : Matrix → Fe_3C → M_2C → M_6C

   in the H23 tool steel:

   in-situ transformation : Matrix → M_3C → M_7C_3 + $M_{23}C_6$

   separate transformation : Matrix → M_3C → M_2C → M_6C

   Matrix → M_7C_3

7.1.3 Controlled Thermomechanical Processing

1 In all experimental conditions, the flow curves of the H21 and H23 tool steels showed that no dynamic recrystallisation had occurred. The peak stress of the H23 tool steel was lower than the H21 tool steel.

2 The deformation temperature influenced the carbide network in the direction perpendicular to the compression axis and reduced the carbide size effectively. At the higher solutioning and deformation temperatures the carbide networks had broken down.

3 The most dispersed of M_6C carbides with mean size of ~ 0.2 μm were observed after solutioning at 1100 ^{o}C, followed by hot deformation at 1000 ^{o}C in the H21 tool steel.

4 The hot deformation had increased the hardness of the H21 tool steel, and the highest hardness with deformation (617 HV) occurred after solutioning at 1250 ^{o}C, followed by deformation at 1000 ^{o}C. On the contrary, the hot deformation had decreased the hardness of the H23 tool steel, which achieved the highest

hardness (274 HV) after solutioning at 1250 ^{o}C, followed by deformation at 1000 ^{o}C.

5 The peak stress, microstructure and hardness data indicated that the optimum hot deformation condition was solutioning at 1250 ^{o}C and deformation at 1100 ^{o}C.

6 The H21 tool steel showed a promising result based on the hardness value after hot deformation.

7 No secondary hardening phenomenon occurred in the H21 tool steel after double tempering at 650, 750 and 800 ^{o}C for samples that were first subjected to hot deformation. The highest double tempered hardness (354 HV) occurred after double temper at 650 ^{o}C with solutioning temperature at 1250 ^{o}C and deformation temperature 1000 ^{o}C.

8 Hot deformation did not affect the sequence of the evolution of carbides during double temper. The hot deformation caused a change in the rate of the formation, dissolution and coarsening of the carbides.

7.2 Industrial implications

The implications of this study for industrial practices are as follows:

1 It is possible to use high axisymmetric compression with strain rate 0.01/s, solutioning at 1100 and 1250 ^{o}C, and deformation at 1000-1100 ^{o}C for the H21 tool steel to improve its hardness.

2 The operating temperature for the H21 tool steel either after conventional heat treatment or hot deformation with the conditions used in this study should be less than 650 ^{o}C.

7.3 Limitation of the Study

The study of the H21 and H23 tool steels was affected (1) by the limited availability of useful samples due to casting defects in the ingots, which forced the compression tests to be done using only one strain rate and the toughness to be estimated by calculating the reduction in area from hardness data, (2) by brittleness of the steels, which made difficult thin foil selection and preparation from the centre of the deformed samples and (3) by the inability to measure the volume fraction of each type of carbide separately owing to the size of carbides and them coexisting in networks.

7.4 Future Work

It is recommended that further research could be undertaken in the following areas:

1 Using the solutioning and deformation condition of this study, double tempering should be studied below 650 ^{o}C to establish secondary hardening.

2 The effect of different strain rates with controlled thermomechanical processing of the H21 tool steel should be studied.

Publications

1. Nurbanasari, M., Tsakiropoulos, P. and Palmiere, E.J., 2012. Microstructural Investigation of a Hot Work Tungsten Tool Steel during High Temperature Axisymmetric Compression, *1st International Conference on Ingot Casting, Rolling and Forging (ICRF)*, 3-7 June, Aachen, Germany.

2. Nurbanasari, M., Tsakiropoulos, P. and Palmiere, E. J. 2013. Influence of High Temperature Deformation and Double Tempering on the Microstructure of a H21 Tool Steel. *Materials Science and Engineering A*, 570**,** 92-101. (Nurbanasari *et al.*, 2013).

References

Abe, F., Araki, H. and Noda, T. 1991. The Effect of Tungsten on Dislocation Recovery and Precipitation Behavior of Low Activation Martensitic 9Cr Steels. *Metallurgical and Materials Transactions A,* 22**,** 2225-2235.

Abe, F. and Nakazawa, S. 1992. Microstructural Evolution and Creep Behaviour of Bainitic, Martensitic, and Martensite-Ferrite Dual Phase Cr-2W Steels. *Materials Science and Technology,* 8**,** 1063-1069.

Alvarado-Meza, M., García-Sanchez, E., Covarrubias-Alvarado, O., Salinas-Rodriguez, A., Guerrero-Mata, M. and Colás, R. 2012. Effect of the High-Temperature Deformation on the M_s Temperature in a Low C Martensitic Stainless Steel. *Materials Engineering and Performance,* Online First, 31 May 2012**,** 1-6.

Andrade, H., Akben, M. and Jonas, J. 1983. Effect of Molybdenum, Niobium, and Vanadium on Static Recovery and Recrystallization and on Solute Strengthening in Microalloyed Steels. *Metallurgical and Materials Transactions A,* 14**,** 1967-1977.

Andrews, K. W. 1965. Empirical Formulae for the Calculation of Some Transformation Temperatures. *Journal of the Iron and Steel Institute,* 203**,** 721-727.

Asadabad, M. A., Kheirandish, S. and Novinrooz, A. J. 2010. Tempering Behavior of 4.5Cr-2W-0.25V Steel. *Journal of the Iron and Steel Research, International,* 17**,** 57-62.

Asakura, K., Kohyama, A. and Yamada, T. 1990. Mechanical Properties and Microstructure Changes of Low-Activation 3Cr-2W-V-Ti Ferritic Steels Developed for Nuclear Applications. *ISIJ International,* 30**,** 947-954.

ASTM E975-03 2003. *Standard Practice for X-Ray Determination of Retained Austenite in Steel with Near Random Crystallographic Orientation*. Pensilvania, American Society for Testing and Materials.

Babich, V. K., Drozdov, B. Y., Pirogov, V. A. and Plevako, P. S. 1977. Structure and Properties of Quenched Low Carbon Steel after Plastic Deformation and Tempering. *Metal Science and Heat Treatment,* 19**,** 98-101.

Bain, E. C. and Paxton, H. W. 1966. *Alloying Elements in Steels*. 2nd edition. Ohio, ASM International, Metals Park.

Baker, R. G. and Nutting, J. 1959. The Tempering of 2.25Cr-1Mo Steels after Quenching and Normalizing. *Journal Iron and Steel Inst,* 193**,** 257-268.

Bakhsheshi-Rad, H. R., Monshi, A., Monajatizadeh, H., Idris, M. H., Abdul Kadir, M. R. and Jafari, H. 2011. Effect of Multi-Step Tempering on Retained Austenite

and Mechanical Properties of Low Alloy Steel. *Journal of the Iron and Steel Research, International,* 18**,** 49-56.

Bała, P. and Pacyna, J. 2008. The Influence of Kinetics Phase Transformation during Tempering on the Mechanical Properties of HS6-5-2 Steel. *Journal of Achievements in Materials and Manufacturing Engineering,* 28**,** 123-130.

Barkalow, R. H., Kraft, R. W. and Goldstein, J. I. 1972. Solidification of M2 High Speed Steel. *Metallurgical and Materials Transactions B,* 3**,** 919-926.

Barraclough, D. R. and Sellars, C. M. 1979. Static Recrystallization and Restoration after Hot Deformation of Type 304 Stainless Steel. *Metal Science,* 13**,** 257-268.

Beladi, H. and Hodgson, P. D. 2007. Effect of Carbon on the Hot Deformation Behaviour in Nb-Steels. *Materials Forum,* 31**,** 11-15.

Bhadeshia, H. K. D. H. 2001. *Bainite in Steels: Transformation, Microstructures and Properties*. 2nd edition. London, The Institute of Materials Communication Ltd.

Bhadeshia, H. K. D. H. 2002. *Martensite in Steels* [Online]. Available from: www.msm.cam.ac.uk/phase-trans/2000/C9/lectures45.pdf [Accessed 09 January 2011].

Bhadeshia, H. K. D. H. 2010. Phase Transformations Contributing to the Properties of Modern Steels. *Bulletin of the Polish Academy of Science* 58.

Bhadeshia, H. K. D. H. and Edmonds, D. V. 1979. The Bainite Transformation in a Silicon Steel. *Metallurgical Transactions A,* 10**,** 895-907.

Bhadeshia, H. K. D. H. and Edmons, D. V. 1980. The Mechanism of Bainite Formation in Steels. *Acta Metallurgica,* 28**,** 1265-1273.

Bhadeshia, H. K. D. H. and Honeycombe, R. W. K. 2006. *Steels Microstructure and Properties*. 3rd edition. Oxford, Elsevier Ltd.

Bjärbo, A. and Hättestrand, M. 2001. Complex Carbide Growth, Dissolution and Coarsening in a Modified 12 pct Chromium Steel-an Experimental and Theoretical Study. *Metallurgical and Materials Transactions A,* 32A**,** 19-27.

Boccalini, M. and Goldenstein, H. 2001. Solidification of High Speed Steels. *International Materials review,* 46**,** 92-115.

Brick, R. M., Pense, A. W. and Gordon, R. B. 1977. *Structure and Properties of Engineering Materials*. 4th edition. New York, Mc-Graw-Hill Book Company.

Cahn, J. W. 1956. The Kinetics of Grain Boundary Nucleated Reactions. *Acta Metallurgica,* 4**,** 449-459.

Cahn, R. W. and Haasen, P. (eds.) 1996. Physical Metallurgy, Amsterdam, North Holland Publishing Company.

Cai, G. J., Andren, H. O. and Svensson, L. E. 1998. Microstructural Change of a 5% Cr Steel Weld Metal during Tempering. *Materials Science and Engineering: A,* 242**,** 202-209.

Campbell, F. C. 2008. *Elements of Metallurgy and Engineering Alloys*. Ohio, ASM International, Materials Park.

Campbell, F. C. 2012. Peritectic Alloy Systems. *Phase Diagrams: Understanding the Basics.* Ohio: ASM International.

Canale, L. C. F., Yao, X., Gu, J. and Totten, G. E. 2008. A Historical Overview of Steel Tempering Parameters. *International Journal of Microstructure and Materials Properties,* 3**,** 474-525.

Cao, Y. B., Xiao, F. R., Qiao, G. Y., Huang, C. J., Zhang, X. B., Wu, Z. X. and Liao, B. 2012. Strain-induced Precipitation and Softening Behaviors of High Nb Microalloyed Steels. *Materials Science and Engineering A,* 552**,** 502–513.

Caron, R. N. and Krauss, G. 1972. The Tempering of Fe-C Lath Martensite. *Metallurgical Transactions,* 3**,** 2381–2389.

Chang, L. C. and Bhadeshia, H. K. D. H. 1996. Stress-Affected Transformation to Lower Bainite. *Journal of Materials Science,* 31**,** 2145-2148.

Conrad, H. and Frederick, S. 1962. The Effect of Temperature and Strain Rate on the Flow Stress of Iron. *Acta Metallurgica,* 10**,** 1013-1020.

Davenport, S. B., Silk, N. J., Sparks, C. N. and Sellars, C. M. 2000. Development of Constitutive Equations for Modelling of Hot Rolling. *Materials Science and Technology,* 16**,** 539-546.

Davis, J. R. 1995. *Tool Materials*. Illustrated edition. Ohio, ASM International, Materials Park.

DeArdo, A. J., Garcia, C. I. and Palmiere, E. J. 1991. Thermomechanical Processing of Steels. *ASM Handbook.* 10th edition. Ohio: ASM International, Materials Park, p.237-255.

DeColnet, L., Pirard, E., Tchuindjang, J. T., Lecomite-Beckers, J., Gfhiri, R., Boeraeve, P. and Cescotto, S. 2001. *Quantitative Description of MC, M_2C, M_6C and M_7C_3 Carbides in High Speed steel Rolls*. *In:* Sandera, P., ed. *MSMF-3 International Conference Held in Brno, Krakowic, Pologne*. p.710-717.

Dieter, G. E., Kuhn, H. S. and Semiatin, S. L. 2003. *Handbook of Workability and Process Design*. Ohio, ASM International, Materials Park.

Djaic, R. A. P. and Jonas, J. J. 1972. Static Recrystallization of Austenite between Intervals of Hot Working. *Journal Iron and Steel Institute,* 210**,** 256-261.

Djaic, R. A. P. and Jonas, J. J. 1973. Recrystallization of High-Carbon Steel between Intervals of High Temperature Deformation. *Metallurgical Transactions,* 4**,** 621-624.

Dobrzański, L. A. 1993. High Temperature Thermo-mechanical Treatment of 12-0-2+C Type High Speed Steel. *Materials Processing Technology,* 38**,** 123-134.

Dobrzanski, L. A., Kasprzak, W., Adamiak, M., Sokovic, M., Kopac, J. and Derrico, G. 2003. The Influence of Chemical Composition of High-Speed Steels on the Wear during Cutting and Erosion Tests. *Brazilian Society of Mechanical Sciences and Engineering,* 25**,** 194-200.

Doherty, R. D., Hughes, D. A., Humphreys, F. J., Jonas, J. J., Jensen, D. J., Kassner, M. E., King, W. E., McNelley, T. R., McQueen, H. J., Rollett, A. D., Cruz-Jr, J. A., Rodrigues, T. F. M., Viana, V. D. C., Abreu, H. and Santos, D. B. 1997. Current Issues in Recrystallization: A Review. *Materials Science and Engineering A,* 238 219-274.

Dudova, N. and Kaibyshev, R. 2011. On the Precipitation Sequences in a 10 % Cr Steel under Tempering. *ISIJ International,* 51**,** 826-831.

Durrand-Charre, M. 2004. *Microstructure of Steels and Cast Irons*. Berlin, Springer-Verlag

Dyson, D. J. and Andrews, K. W. 1969. Carbide M_7C_3 and Its Formation in Alloy Steels. *Journal of the Iron and Steel Institute***,** 208 - 219.

Elrakayby, A. M. and Mills, B. 1986. Identification of Carbides in High Speed Steel. *Materials Science Letters,* 5**,** 332-334.

Fajfar, P., Bombač, D. and Markoli, B. 2010. Flow Stress and Activation Energy of BRCMO Tool Steel. *RMZ-Materials and Geoenvironment,* 57**,** 159-164.

Fan, D. W., Kim, H. S. and Cooman, B. C. D. 2009. Review of the Physical Metallurgy Related to Hot Press Forming of Advanced High Strength Steel. *Steel Research International,* 80**,** 241-248.

Fares, M. L., Athmani, M., Khelfaoui, Y. and Khettache, A. 2012. An Investigation into the Effects of Conventional Heat Treatments on Mechanical Characteristics of New Hot Working Tool Steel. *Materials Science and Engineering* 28**,** 1-10.

Fischmeister, H. F., Karagöz, S. and Andrén, H. O. 1988. An Atome Probe Study of Secondary Hardening in High Speed Steels. *Acta Metallurgica,* 36**,** 817-825.

Fischmeister, H. F., Riedl, R. and Karagöz, S. 1989. Solidification of High Speed Tool Steels. *Metallurgical Transactions A,* 20A**,** 2133-2148.

France, C., Klocker, H., Coze, J. L. and Fraczkiewicz 1997. Nitrogen Strengthening of a Martensitic Steel: Relation between Microstructure and Mechanical Behaviour. *Acta Materiala,* 45**,** 2789-2799.

Fredriksson, H. and Brising, S. 1976. The Formation of Carbides during Solidification of High- Speed Steels. *Scandinavian Journal of Metallurgy,* 5**,** 268-275.

Fredriksson, H. and Nica, M. 1979. The Influence of Vanadium, Silicon and Carbon on the Eutectic Reaction in M2 High Speed Steels. *Scandinavian Journal of Metallurgy,* 8**,** 243-253.

Fujita, N. and Bhadeshia, H. K. D. H. 2002. Modelling Silmutaneous Alloy Carbide Sequence in Power Plant Steels. *ISIJ International,* 42**,** 760-769.

Fukino, T. and Tsurekawa, S. 2008. In-Situ SEM/EBSD Observation of α/γ Phase Transformation in Fe-Ni Alloy. *Materials Transactions,* 49**,** 2770-2775.

Furuhara, T., Kobayashi, K. and Maki, T. 2004. Control of Cementite Precipitation in Lath Martensite by Rapid Heating and Tempering. *ISIJ International,* 44**,** 1937-1944.

Galda, E. and Kraft, R. 1974. The Effects of Mo and W on Solidification of High Speed Steels. *Metallurgical and Materials Transactions B,* 5**,** 1727-1733.

Gao, Q., Di, X., Liu, Y. and Yan, Z. 2012. Recovery and Recrystallization in Modified 9Cr-1Mo Steel Weldments after Post-weld Heat Treatment. *International Journal of Pressure Vessels and Piping,* 93–94**,** 69-74.

Gauvin, R., Robertson, K., Horny, P., Elwazri, A. M. and Yue, S. 2006. Materials Characterization Using High Resolution Scanning Electron Microscopy and X-ray Microanalysis. *JOM*.

Gharehbaghi, A. 2012. *Precipitation Study in a High Temperature Austenitic Stainless Steel using Low Voltage Energy Dispersive X-ray Spectroscopy.* Master, Royal Institute of Technology (KTH).

Ghomashchi, M. R. and Sellars, C. M. 1993. Microstructural Changes in As-Cast M2 Grade High Speed Steel during Hot Forging. *Metallurgical Transactions A,* 24A**,** 2171-2180.

Guimarães, J. R. C. 2008. Stress Assisted Martensite: Pre-strain, Grain-size and Strain-rate Effects. *Material Science and Engineering A,* 475.

Guimaraes, J. R. C., Branco, J. R. T. and Kajita, T. 1986. Partial Substitution of Niobium for Vanadium in H13 Hot Work Tool Steel. *Materials Science and Technology,* 2**,** 1074-1076.

Halfa, H., Eissa, M., El-Fawakhry, K. and Mattar, T. 2012. Effect of Nitrogen and Niobium on the Structure and Secondary Hardening of Super Hard High Speed Tool Steel. *Steel Research International,* 83**,** 32-42.

Hanlon, D. N., Sietsma, J. and Zwaag, S. v. d. 2001. The Effect of Plastic Deformation of Austenite on the Kinetics of Subsequent Ferrite Formation. *ISIJ International,* 41**,** 1028-1036.

Hase, K., Garcia-Mateo, C. and Bhadeshia, H. K. D. H. 2004. Bainite Formation Influenced by Large Stress. *Materials Science and Technology,* 20**,** 1499-1505.

Hashimoto, M., Kubo, O. and Matsubara, Y. 2004. Analysis of Carbides in Multi Component White Cast Iron for Hot Rolling Mill Rolls. *ISIJ International,* 44**,** 372-380.

He, B. B. 2009. *Two-Dimensional X-Ray Diffraction*. New Jersey, A John Wiley and Sons, Inc.

Higginson, R. L. and Sellars, C. M. 2003. *Worked Examples in Quantitative Metallography*. London, Maney.

Hinton, J. S. 2006. *Laboratory Simulation of Microstructural Evolution in AISI 430 Ferritic Stainless Steel during the Steckel Mill Process.* Unpublished Ph.D. Thesis, University of Sheffield.

Hollomon, J. H. and Jaffe, L. D. 1945. Time-Temperature Relations in Tempering Steels. *Transactions of the Metallurgical Society of AIME,* 162.

Howard, R. T. and Cohen, M. 1948. Austenite Transformation above and within the Martensite Range. *Transactions of the Metallurgical Society of AIME,* 176**,** 384-400.

Hufenbach, J., Giebeler, L., Hoffmann, M., Kohlar, S., Kühn, U., Gemming, T., Oswald, S., Eigenmann, B. and Eckert, J. 2012. Effect of Short-term Tempering on Microstructure and Mechanical Properties of High-strength FeCrMoVC. *Acta Materialia,* 60**,** 4468-4476.

Humphreys, F. J. and Hatherly, M. 2004. *Recrystallization and Related Annealing Phenomena*. 1st edition. Oxford Elsevier Science Ltd.

Imbert, C. A. C. and McQueen, H. J. 2000. Flow Curves up to Peak Strength of Hot Deformed D2 and W1 Tool Steels. *Materials Science and Technology,* 16**,** 524-531.

Imbert, C. A. C. and McQueen, H. J. 2001. Peak Strength, Strain Hardening and Dynamic Restoration of A2 and M2 Tool Steels in Hot Deformation. *Materials Science and Engineering A,* 313**,** 88-103.

Imbert, C. A. C. and McQueen, H. J. 2007. Static Recyrstallization of Tool Steels. *Materials Science Forum,* 539-543**,** 4458-4463.

Imbert, C. A. C., Ryan, N. D. and McQueen, H. J. 1984. Hot Workability of Three Grades of Tool Steel. *Metallurgical Transactions A,* 15A**,** 1855-1864.

Isasti, N., Jorge-Badiola, D., Taheri, M. L., López, B. and Uranga, P. 2011. Effect of Composition and Deformation on Coarse-Grained Austenite Transformation in Nb-Mo Microalloyed Steels. *Metallurgical and Materials Transactions A,* 42**,** 3729-3742.

Jandova, D., Rehor, J. and Novy, Z. 2004. Microstructural Changes Taking Place during the Thermo-mechanical Processing and Cold Working of Steel 18Cr18Mn0.5N. *Materials Process and Technology,* 157-158**,** 523-530.

Janjušević, Z., Gulišija, Z., Mihalović, M. and Patarić, A. 2009. The Investigation of Applicability of the Hollomon-Jaffe Equation on Tempering the HSLA Steel. *Chemical Industry and Chemical Engineering Quarterly,* 15**,** 131-136.

Janovec, J., Výrostková, A. and Holý, A. 1992. Effect of Tempering on Development of Carbide Particles in 2.7Cr-0.6Mo-0.3V Steel. *Materials Science,* 27**,** 6564-6572.

Jonas, J. J. and Weiss, I. 1979. Effect of Precipitation on Recrystallization in Microalloyed Steels. *Metals Science and Heat Treatment,* 13**,** 238-245.

Kagawa, A. and Okamoto, T. 1986. Influence of Alloying Elements on Temperature and Composition for Peritectic Reaction in Plain Carbon Steels. *Materials Science and Technology,* 2**,** 997-1008.

Kaker, H. 2011. Slovenia: Metal Ravne Steel Selector. Available: http://www.metalravne.com/selector/steels/utop2.html [Accessed 31st October 2012].

Karagoz, S. and Fischmeister, H. 1987. Microstructure and Toughness in High Speed Tool Steels: the Influence of Hot Reduction and Austenitization Temperature *Steel Research* 58**,** 353-361.

Kesri, R. and Durand-Charre, M. 1987. Phase Equilibria, Solidification and Solid-state Transformations of White Cast Irons Containing Niobium. *Materials Science,* 22**,** 2959-2964.

Kheirandish, S., Kharrazi, Y. H. K. and Mirdamadi, S. 1997. Mechanical Properties of M7 High Speed Cast Steel Modified with Niobium. *ISIJ International,* 37**,** 721-725.

Kheirandish, S. and Noorian, A. 2008. Effect of Niobium on Microstructure of Cast AISI H13 Hot Work Tool Steel. *Iron and Steel Research, International,* 15**,** 61-66.

Khlestov, V. M., Konopleva, E. V. and McQueen, H. J. 2002. Effects of Deformation and Heating Temperature on the Austenite Transformation to Pearlite in High Alloy Tool Steels. *Materials Science and Technology,* 18**,** 54-60.

Kim, C., Kim, Y., Park, J., Lee, S., Kim, N. and Yang, J. 2005. Effects of Alloying Elements on Microstructure, Hardness, and Fracture Toughness of Centrifugally Cast High Speed Steel Rolls. *Metallurgical and Materials Transactions A,* 36**,** 87-97.

Kishore, Sampathkumaran, P. and Seetharamu, S. 2005. Erosion and Abrasion Characteristics of High Manganese Chromium Irons. *Wear,* 259**,** 70-77.

Koistinen, D. P. and Marburger, R. E. 1959. A General Equation Prescribing Extent of Austenite-Martensite Transformation in Pure Iron-Carbon Alloys and Carbon Steels. *Acta Metallurgica,* 7**,** 59-68.

Kostka, A., Tak, K. G., Hellmig, R. J., Estrin, Y. and Eggeler, G. 2007. on the Contribution of Carbides and Micrograin Boundaries to the Creep Strength of Tempered Martensite Ferritic Steels. *Acta Materiala,* 55**,** 539-590.

Kozasu, I. 1972. The Effect of Factors in Hot Rolling on the Properties of C-Si-Mn Structural Steel *Transactions of the Iron and Steel Institute of Japan,* 12**,** 241-250.

Krauss, G. 1984. Tempering and Structural Change in Ferrous Martensitic Structures *In:* Marder, A. R. and Goldstein, J. I. (eds.) *Phase Instrumentations in Ferrous Alloys.* Ohio: AIME, p.101-123.

Krauss, G. 1999. Martensite in Steel: Strength and Structure. *Material Science and Engineering A,* 273-275**,** 40-57.

Krauss, G. 2003. Solidification, Segregation, and Banding in Carbon and Alloy Steels. *Metallurgical and Materials Transactions B,* 34**,** 781-792.

Krauss, G. 2005. *Steels: Processing, Structure, and Performance*. Ohio, ASM International, Materials Park.

Kunitake, T. and Okada, Y. 1998. The Estimation of Bainite Transformation Temperatures in Steels by The Empirical Formulas. *Journal of the Iron and Steel Institute of Japan,* 84**,** 53-57.

Kuo, K. 1953. Carbides in Chromium, Molybdenum and Tungsten Steels. *Journal of Iron and Steel Institute,* 173**,** 363.

Kuo, K. 1957. Investigations on Carbides in Alloyed Steel. *Jernkontorets Ann,* 141**,** 206.

Kwon, H. and Kim, C. 1983. Tempered Martensite Embrittlement in Fe-Mo-C and Fe-W-C Steel. *Metallurgical and Materials Transactions A,* 14**,** 1389-1394.

Larson, F. R. and Miller, J. A. 1952. A Time-Temperature Relationship for Rupture and Creep Stresses. *Transactions of ASME,* 74**,** 765-775.

Launeau, P. and Robin, P. Y. F. 1996. Fabric Analysis using the Intercept Method. *Tectonophysics,* 267**,** 91-119.

Lee, J. S. and Chun, J. S. 1981. Effect of High Temperature Thermomechanical Treatment on the Mechanical Properties of Vanadium AISI 4330 Steel. *Materials Science,* 16**,** 1557-1566.

Lee, S. J. and Lee, Y. K. 2005. Effect of Austenite Grain Size on Martensitic Transformation of a Low Alloy Steel. *Materials Science Forum* 475-479**,** 3169-3172.

Lee, S. J., Park, J. S. and Lee, Y. K. 2008. Efect of Austenite Grain Size on the Transformation Kinetics of Upper and Lower Bainite in a Low-Alloy Steel. *Scripta Materiala,* 59**,** 87-90.

Lee, W. S. and Liu, C. Y. 2006. The Effects of Temperature and Strain Rate on the Dynamic Flow Behaviour of Different Steels. *Materials Science and Engineering: A,* 426**,** 101-113.

Lee, Y. K. 2002. Empirical Formula of Isothermal Bainite Start Temperature of Steels. *Materials Science Letters,* 21**,** 1253-1255.

Li, C. 1996. *Effect of Heat Treatment on the Microstructure of a 2CrMoNiWV Rotor Steel.* Published PhD Thesis, Sheffield Hallam University.

Li, J.-y., Zhao, P., Yanagimoto, J., Sugiyama, S. and Chen, Y.-l. 2012. Effects of Heat Treatment on the Microstructures and Mechanical Properties of a New Type of Nitrogen-Containing Die Steel. *International Journal of Minerals, Metallurgy, and Materials,* 19**,** 511-517.

Li, Q. 2006. Precipitation of Fe_2W Laves Phase and Modelling of Its Direct Influence on the Strength of a 12Cr-2W Steel. *Metallurgical and Materials Transactions A,* 37A**,** 89-97.

Lillywhite, S. J., Prangnell, P. B. and Humpreys, F. J. 2000. Interactions between Precipitation and Recrystallisation in an Al-Mg-Si Alloy. *Materials Science and Technology,* 16**,** 1112-1120.

Lin-xiu, D., Hai-long, Y., Hua, D., Xiang-hua, L. and Guo-dong, W. 2006. Effects of Deformation on Bainite Transformation During Continuous Cooling of Low Carbon Steels *Iron and Steel Research, International,* 13**,** 37-39.

Liu, J., H, H. C., Wu, R., Hsu, T. Y. and Ruan, X. 2000. Investigation on Hot Deformation Behavior of AISI T1 High-Speed Steel. *Materials Characterization,* 45**,** 175-186.

Liujie, X., Jiandong, X., Shizhong, W., Yongzhen, Z. and Rui, L. 2006. Investigation on Wear Behaviors of High-Vanadium High-Speed Steel Compared with High-Chromium Cast Iron under Rolling Contact Condition. *Materials Science and Engineering A,* 434**,** 63-70.

Longfei, L., Wangyue, Y. and Zuqing, S. 2012. Dynamic Recrystallization of Ferrite in a Low Carbon Steel with the (α+θ) Duplex Microstructure. *Materials Science Forum,* 715-716**,** 902-906.

Lord, J. D. and Loveday, M. S. 2001. Tools and Lubricants for High Temperature Metal Working Laboratory-Scale Tests. *NPL Measurement Note MN,* 50**,** 1-8.

Luton, M. J. and Sellars, C. M. 1969. Dynamic Recrystallization in Nickel and Nickel-iron Alloys during High Temperature Deformation. *Acta Metallurgica,* 17**,** 1033-1043.

Ma, L.-q., Liu, Z.-y., Jiao, S.-h., Yuan, X.-q. and Wu, D. 2008. Effect of Niobium and Titanium on Dynamic Recrystallization Behavior of Low Carbon Steels. *Iron and Steel Research, International,* 15**,** 31-36.

Ma, Y., Gao, H., Liang, Y. and Zhang, X. 2012. Secondary Hardening during Tempering of Cr-W-Mo-V High Alloy Medium-upper Carbon Steel and Its Hardness Forecast. *Advance Materials Research,* 415-417**,** 813-818.

Mahieu, J., Cooman, B. C. D. and Maki, J. 2002. Phase Transformation and Mechanical Properties of Si-free CMnAl Transformation-Induced Plasticity-Aided Steel. *Metallurgical and Materials Transactions A,* 33A**,** 2573-2580.

Matlock, D. K., Krauss, G. and Speer, J. G. 2001. Microstructure and Properties of Direct- Cooled Microalloy Forging Steels. *Journal of Materials Processing Technology* 117**,** 324-327.

McQueen, H. J. and Bergerson, S. 1972. Dynamic Recrystalization of Copper during Hot Torsion. *Metal Science Journal,* 6**,** 25-29.

McQueen, H. J. and Jonas, J. J. 1984. Recent Advances in Hot Working: Fundamental Dynamic Softening Mechanisms. *Applied Metal Working,* 3**,** 233-241.

McQueen, H. J. and Jonas, J. J. 1985. Role of the Dynamic and Static Softening Mechanisms in Multistage Hot Working. *Journal of Applied Metal Working,* 3**,** 410-421.

McQueen, H. J. and Ryan, N. D. 2002. Constitutive Analysis in Hot Working. *Materials Science and Engineering A,* 322**,** 43-63.

Mébarki, N., Delagnes, D., Lamesle, P., Delmas, F. and Levaillant, C. 2004. Relationship between Microstructure and Mechanical Properties of a 5% Cr Tempered Martensitic Tool Steel. *Materials Science and Engineering A,* 387-389**,** 171-175.

Medvedeva, A., Bergström, J., Gunnarsson, S., Krakhmalev, P. and Nordh, L. G. 2011. Influence of Nickel Content on Machinability of a Hot-Work Tool Steel in Prehardened Condition. *Materials and Design* 32**,** 706-715.

Mehl, R. F. 1939. *Hardenability of Alloy Steels*. Ohio, American Society for Metals.

Mesquita, R. A. and Kestenbach, H. J. 2011. On the Effect of Silicon on Toughness in Recent High Quality Hot Work Steels. *Materials Science and Engineering A,* 528**,** 4856-4859.

Miao, C. L., Shang, C. J., Zurob, H. S., Zhang, G. D. and Subramanian, S. V. 2012. Recrystallization, Precipitation Behaviors, and Refinement of Austenite Grains in High Mn, High Nb Steel. *Metallurgical and Materials Transactions A,* 43A**,** 665-676.

Miller, P. 2010. *New Developments in P/M Steels for Moldmaking* [Online]. USA: Gardnes Publications, Inc. Available from: http://www.moldmakingtechnology.com/articles/new-developments-in-pm-steels-for-moldmaking [Accessed 09th March 2012].

Milovic, R., Manojlovic, D., Andjelic, M. and Drobnjak, D. 1992. Hot Workability of M2 Type High Speed Steel. *Steel Research,* 63**,** 78-84.

Momeni, A., Dehghani, K., Keshmiri, H. and Ebrahimi, G. R. 2010. Hot Deformation Behavior and Microstructural Evolution of a Superasutenitic Stainless Steel. *Materials Science and Engineering A,* 527**,** 1605-1611.

Morgridge, A. R. 2002. Metadynamic Recrystallization in C Steels. *Bulletin Materials Science,* 25**,** 291-299.

Nishiyama, Z., Fine, M. E., Meshii, M. and Wayman, C. M. 1978. *Martensitic Transformation*. New York, Academic Press.

Nizhnikovskaya, P. F., Kalinushkin, E. P., Snagovskii, L. M. and Demchenko, G. F. 1982. Structural formation of high-speed steels during crystallization. *Metal Science and Heat Treatment,* 24**,** 777-784.

Nurbanasari, M., Tsakiropoulos, P. and Palmiere, E. J. 2013. Influence of High Temperature Deformation and Double Tempering on the Microstructure of a H21 Tool Steel. *Materials Science and Engineering: A,* 570**,** 92-101.

Oliver, W. C. and Pharr, G. M. 1992. An improved Technique for Determining Hardness and Elastic Modulus using Load and Displacement Sensing Indentation Measurements. *Materials Research,* 7**,** 1564-1583

Opal'chuk, A. S., Semenovskii, A. E. and Khrunik, R. A. 1995. Effect of Alloying on the Wear Resistance of Cast Steel. *Materials Science,* 31**,** 386-390.

Palmiere, E. J., Garcia, C. I. and DeArdo, A. J. 1993. The Influence of Niobium Supersaturation in Austenite on the Static Recrystallization Behavior of Low Carbon Microalloyed Steels. *Metallurgy and Materials Transactions A,* 27A**,** 951-960.

Peidao, D., Gongqi, S. and Shouze, Z. 1992. A Scanning Electron Microscopy Study of Carbides in High-Speed Steels. *Materials Characterization,* 29**,** 15-24.

Pickering, F. B. 1978. *Physical Metallurgy and Design of Steels*. London, Applied Science Publisher, Ltd.

Pickering, F. B. 1987. *The Properties of Tool Steels for Mould and Die Applications*. *In:* Krauss, G. and Nordberg, H., eds. *Tool Materials for Molds and Dies*. CSM Press, Golden, p.3-32.

Pirtovšek, T. V., Kugler, G., Godec, M. and Terčelj, M. 2011. Microstructural Characterization during the Hot Deformation of 1.17C-11.3Cr-1.48V-2.24W-1.35Mo Ledeburitic Tool Steel. *Materials Characterization,* 62**,** 1-9.

Pirtovšek, T. V., Peruš, I., Kugler, G., Turk, R. and Terčelj, M. 2008. Hot Forming of AISI A2 Tool Steel. *Metalurgija* 47**,** 307-311.

Porter, D. A. and Easterling, K. E. 2004. *Phase Transformations in Metals and Alloys*. Finland, CRC Press, Taylor & Francis Group.

Queen, H. J. M. and Vazquez, L. 1986. Static Recovery of Copper during Annealing and Stress Relaxation following Hot Deformation. *Material Science and Engineering* 81**,** 355-369.

Radcliffe, S. V. and Rollason, E. C. 1959. The Kinetics of the Formation of Bainite in High-Purity Iron-Carbon Alloys. *Journal of Iron and Steel Institute,* 191**,** 56-65.

Ridley, N., Stuart, H. and Zwell, L. 1969. Lattice Parameter of Fe - C Austenite at Room Temperature *Transactions of the Metallurgical Society of AIME,* 245**,** 1834 – 1836.

Rios, P. R. 1987. A Theory for Grain Boundary Pinning by Particles. *Acta Metallurgica,* 35**,** 2805–2814.

Roberts, G. A., Krauss, G. and Kennedy, R. L. 1998. *Tool Steels*. 5th edition. Ohio, ASM International, Metals Park.

Roberts, W. 1982. Deformation. *In:* Krauss, A. G. (ed.) *Processing and Structure.* Ohio: ASM International, Metals Park, p.109-184.

Roberts, W. 1984. Dynamic Changes that Occur during Hot Working and Their Significance regarding Microstructure Development and Hotworkability. *in :G. Krauss, editor. Deformation, processing and Structure, Metals Park, OH: American Society for Metals***,** 109-184.

Rodenburg, C., Krzyzanowski, M., Beynon, J. H. and Rainforth, W. M. 2004. Hot Workability of Spray Formed AISI M3:2 High Speed Steel. *Materials Science and Engineering A,* 386**,** 420-427.

Roebuck, B., Lord, J. D., Brooks, M., Loveday, M. S., Sellars, C. M. and Evans, R. W. 2006. Measurement of Flow Stress in Hot Axisymmetric Compression Tests. *Materials at High Temperatures,* 23**,** 59-83.

Rosso, M., Ugues, D. and Actis-Grande, M. 2006. The Challenge of PM Tool Steels for the Innovation. *Achievements in Materials and Manufacturing Engineering,* 18.

Ruhl, R. and Cohen, M. 1969. Splat Quenching of Iron - Carbon Alloys. *Transactions of the Metallurgical Society of AIME,* 245**,** 241-251.

Ryan, N. D. and McQueen, H. J. 1986a. Effects of Alloying upon the Hot Workability of Carbon, Microalloyed, Tool, and Austenitic Stainless Steels. *Mechanical Working Technology,* 12**,** 279-296.

Ryan, N. D. and McQueen, H. J. 1986b. Mean Pass Flow Stresses and Interpass Softening in Multistage Processing of carbon, HSLA, Tool and Stainless Steels. *Journal of Mechanical Working Technology,* 12**,** 323-349.

Ryan, N. D., McQueen, H. J. and Jonas, J. J. 1983. The Deformation Behaviour of Type 304, 316, 317 Austenitic Stainless Steels during Hot Torsion. *Canadian Metalurgical Quarterly,* 22**,** 369-378.

Saha Podder, A. and Bhadeshia, H. K. D. H. 2010. Thermal Stability of Austenite Retained in Bainitic Steels. *Materials Science and Engineering: A,* 527**,** 2121-2128.

Sawamoto, A., Ogi, K. and Matsuda, K. 1986. Solidification Structures of Fe-C-Cr-(V-Nb-W) Alloys. *Transaction of AFS***,** 403-416.

Sellars, C. M. 1980. Hot Working and Forming Processes. *In:* Sellars, C. M. and Davies, G. J. (eds.) *The Physical Metallurgy of Hot Working.* London: Metals Society, p.3-15.

Sellars, C. M. 1990. Modelling Microstructural Development during Hot Rolling. *Materials Science and Technology,* 6**,** 1072-1081.

Sellars, C. M. and Tegart, W. J. M. 1966. On the Mechanism of Hot Deformation. *Acta Metallurgica,* 14**,** 1136-1138.

Sellars, C. M. and Tegart, W. J. M. 1972. Hot Workability. *International Metallurgical Reviews,* 17**,** 1-24.

Serajzadeh, S. and Karimi Taheri, A. 2002. An Investigation on the Effect of Carbon and Silicon on Flow Behavior of Steel. *Materials and Design,* 23**,** 271-276.

Šesták, B. and Seeger, A. 1971. The Relationship between the Work-Hardening of B.C.C. and F.C.C. Metals. *Physica Status Solidi (b),* 43**,** 433-444.

Shin, E. J., Seong, B. S., Han, Y. S., Hong, K. P., Lee, C. H. and Kang, H. J. 2003. Effect of Precipitate Size and Dispersion on Recrystallization Behavior in Ti-added Ultra Low Carbon Steels. *Applied Crystallography,* 36**,** 624-628.

Shipway, P. H. and Bhadeshia, H. K. D. H. 1995. The Effect of Small Stresses on the Kinetics of the Bainite Transformation. *Materials Science and Engineering A,* 201**,** 143-149.

Shtansky, D. V. and Inden, G. 1997. Phase Transformation in Fe-Mo-C and Fe-W-C Steels. The Structural Evolution during Tempering at 700 ^{o}C. *Acta Materiala,* 7**,** 2861-2878.

Shu-qi, W., Kang-min, C., Xiang-hong, C., Qi-chuan, J. and Bian, H. 2006. Effect of Alloying Elements on Thermal Wear of Cast Hot-Forging Die Steels. *Iron and Steel Research, International,* 13**,** 53-59.

Sohar, C. R. 2011. *Lifetime Controlling Defects in Tool Steels*. Berlin, Springer-Verlag

Sourmail, T. 2001. Literature Review : Precipitation in Creep Resistant Austenitic Stainless Steels. *Materials Science and Technology,* 17**,** 1-14.

Speich, G. R. 1969. Tempering of Low Carbon Martensite. *Transactions of the Metallurgical Society of AIME,* 245**,** 2553-2564.

Speich, G. R., Cuddy, L. J., Gordon, C. R. and DeArdo, A. J. 1984. Formation of Ferrite from Control-Rolled Austenite. *Proceedings Phase Transformations in Ferrous Alloys, Edited by Marder, A. R. and Goldstein, J. I., TMS-AIME, Warrendale, PA***,** 341-390.

Speight, M. V. 1968. Growth Kinetics of Grain Boundary Precipitates. *Acta Metallurgica* 16**,** 133-135.

Steven, W. and Haynes, A. G. 1956. The Temperature of Formation of Martensite and Bainite in Low-alloy Steel. *Iron and Steel Institute,* 183**,** 349-359.

Sun, W. P. and Hawbolt, E. B. 1995. Prediction of the Onset of Static Recrystallization after Hot Deformation. *ISIJ International,* 35**,** 908-913.

Thewlis, G., Whiteman, J. A. and D.J.Segnoles 1997. Dynamics of Austenite to Ferrite Phase Transformation in Ferrous Metals. *Materials Science and Technology,* 13**,** 257–274.

Thompson, R. C. and Bhadeshia, H. K. D. H. 1992. Carbide Precipitation in 12Cr1MoV Power Plant Steel. *Metallurgical Transactions,* 23A**,** 1171-1179.

Thomson, R. C. and Bhadsehia, H. K. D. H. 1992. Carbide Compositions in 12Cr1MoV Power Plant Steel. *Metallurgical Transactions A,* 23A**,** 1171-1179.

Todd, J. A. 1986. The Early Stages of Tempering in a 3Cr-1. 5Mo Steel *Scripta Metallurgica,* 20**,** 269-274.

Tokizane, M., Matsumura, N., Tsuzaki, K., Maki, T. and Tamura, I. 1982. Recrystallization and Formation of Austenite in Deformed Lath Martensitic Structure of Low Carbon Steels. *Metallurgical Transactions A,* 13**,** 1379-1388.

Totten, G. E. 2006. *Steel Heat Treatment: Metallurgy and Technologies*. 2nd edition. New York, Taylor and Francis.

Totten, G. E. and Howes, M. A. H. 1997. Steel Heat Treatment Handbook, Marcel Dekker, New York, USA.

Trepczyńska-Łent, M. 2010. Rod and Lamellar Growth of Eutectic. *Archives of Foundry Engineering,* 10**,** 179-184.

Tunney, R. J. and Ridley, N. 1979. Tempering of High Purity and Commercially Based Steels Containing 10 wt% Tungsten or 5 wt% Molybdenum. *Metal Science,* 13**,** 585-590.

Van-Leeuwen, Y. and Sietsma, J. 2007. The Effect of Plastic Deformation on the Formation of Different Morphologies of Ferrite upon Cooling. *Materials Science Forum,* 539-543**,** 4572-4577.

Verhoeven, J. D. 2007. *Steel Metallurgy for the Non Metallurgist*. Ohio, ASM International, Materials Park.

Verlinden, B., Samajdar, J. D. I. and Doherty, R. D. 2007. *Thermo Mechanical Processing of Metallic Materials*. Amsterdam, Pergamon.

Vitek, J. M. and Klueh, R. L. 1983. Precipitation Reactions during the Heat Treatment of Ferritic Steels. *Metallurgical Transactions,* 14A**,** 1047-1055.

Wei, S., Zhu, J. and Xu, l. 2006. Effects of Vanadium and Carbon on Microstructures and Abrasive Wear Resistance of High Speed Steel. *Tribology International,* 39**,** 641-648.

Weiss, B. and Stickler, R. 1972. Phase instabilities during high temperature exposure of 316 austenitic stainless steel. *Metallurgical and Materials Transactions B,* 3**,** 851-866.

Wignarajah, S., Masumoto, I. and Hara, T. 1990. Evaluation and Simulation of the Microstructural Changes and Embrittlement in 21/4 Cr-1Mo Steel due to Long Term Service. *ISIJ International,* 1**,** 58-63.

Wilson, E. A. 1994. The $\gamma \rightarrow \alpha$ Transformation in Low Carbon lrons. *ISIJ International,* 34**,** 615.

Wilson, R. 1975. *Metallurgy and Heat Treatment of Tool Steel*. London, McGraw-Hill BookCompany.

Wittke, J. H. 2008. *Types of Signals* [Online]. Available: http://www4.nau.edu/microanalysis/Microprobe-SEM/Signals.html [Accessed 31th May 2013].

Wu, C., Sahajwalla, V. and Krauklis, P. 1996. The Effect of Austenitizing Process on the Hardening Behaviour of Cr-Mo-Mn-C Air-hardening Cast Tool Steel. *ISIJ International,* 36**,** 347-353.

Xiao, F., Liao, B., Qiao, G. and Guan, S. 2006. Effect of Hot Deformation on Phase Transformation Kinetics of 86CrMoV7 Steel. *Materials Characterization* 57**,** 306-313.

Yamamoto, S., Yokoyama, H., Yamada, K. and Nikura, M. 1995. Effects of the Austenite Grain Size and Deformation in the Unrecrystallized Austenite Region on Bainite Transformation Behavior and Microstructure. *ISIJ International,* 35**,** 1020-1026.

Yang, H. S. and Bhadeshia, H. K. D. H. 2009. Austenite Grain Size and the Martensite–Start Temperature. *Scripta Materialia* 60**,** 493-495.

Yang, J. R., Huang, C. Y., Hsieh, W. H. and Chiou, C. S. 1995. Mechanical Stabilization of Austenite Againts Bainite Reaction in Fe-Mn-Si-C Bainitic Steel. *Journal de Physique,* 05**,** C8-497 - C8-502.

Yaso, M., Hayashi, S., Morito, S., Ohba, T., Kubota, K. and Murakami, K. 2009. Characteristics of Retained Austenite in Quenched High C-High Cr Alloy Steels. *Materials Transactions,* 50**,** 275-279.

Yongtao, Z., Lede, M., Xiaojun, W., Hanqian, Z. and Jinfu, L. 2009. Evolution Behavior of Carbides in 2.25Cr-1Mo-0.25V Steel. *Materials Transactions,* 50**,** 2507-2511.

Yu-Kipelova, A., Belyakov, A. N., Skorobogatykh, V. N., Shchenkova, I. A. and Kaibyshev, R. O. 2010. Tempering-induced Structural Changes in Steel 10Kh9K3V1M1FBR and Their Effect on the Mechanical Properties *Materials Science and Heat Treatment,* 52**,** 100-110.

Zener, C. and Smith, C. S. 1948. Grains, Phases, and Interfaces,"an Interpretation of. Micro-Structure". *Transactions of the Metallurgical Society of AIME.,* 175**,** 15-51.

Zeng, Z., Chen, L., Zhu, F. and Liu, X. 2011. Static Recrystallization Behavior of a Martensitic Heat-resistant Stainless Steel 403Nb. *Acta Metallurgica Sinica* 24**,** 381-389.

Zhang, R. Y. and Boyd, J. D. 2010. Bainite Transformation in Deformed Austenite. *Metallurgical and Materials Transactions A,* 41A**,** 1448-1459.

Zhao, B., Gottstein, G. and Shvindlerman, L. S. 2011. Triple Junction Effects in Solids. *Acta Materialia,* 59**,** 3510-3518.

Zhou, Q., Wu, X., Shi, N., Li, J. and Min, N. 2011. Microstructure Evolution and Kinetic Analysis of DM Hot-Work Die Steels during Tempering. *Material Science and Engineering A,* 528**,** 5696-5700.